Simulation of Partially Premixed Turbulent Flames

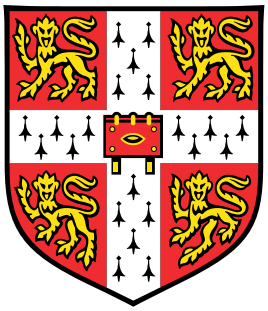

Zhi Chen

Darwin College

Department of Engineering

University of Cambridge

A thesis submitted for the degree of

Doctor of Philosophy

04 July 2016

Abstract

Simulation of Partially Premixed Turbulent Flames

Zhi Chen

This work numerically investigates the turbulent partially premixed flames, which are ubiquitous in combustion powered devices. This combustion mode involves many physical complexities such as flame propagation in unevenly premixed mixture of fuel and oxidiser, turbulence/flame interaction in presence of mixture fraction gradients, triple flame configuration, etc. The fundamental mechanisms of these physical processes are yet to be further understood, posing significant modelling challenges.

These issues are addressed in this thesis using a presumed joint probability density function (PDF) approach with both Reynolds Averaged Navier Stokes (RANS) and Large Eddy Simulation (LES) methodologies. This joint PDF is described by a parameter, mixture fraction, describing mixing and a reaction parameter, progress variable. The laminar flamelet concept is adopted to decouple chemistry and turbulence calculations for high computational efficiency. This modelling framework is validated using two experimental test cases in this study including a canonical lifted jet flame and a practical swirling flame, both exhibiting strong partial premixing features. The simulation results obtained for these validation cases show a robust model performance for a broad range of flow and mixing conditions with an attractive computational cost for practical interests.

For the lifted jet flame case, two-dimensional (2D) axisymmetric steady RANS approach is used to compute the flame lift-off height showing very good agreement with the experimental measurements for a range

of jet velocities and air-dilution levels. However, a substantial difference is found between the 2D unsteady RANS (URANS) results and experimental data for the flame transient evolution from its initial ignition to final stabilisation. The comparison for this transient evolution is improved significantly in the 3D URANS simulations suggesting that the third physical dimension, the azimuthal direction, plays an important role during the flame transient evolution. The following LES study further shows that the flame most-leading point appears to be in different azimuthal positions exhibiting a *spiral*-like trajectory as the flame propagates upstream towards the final lift-off height. The temporal variation of this leading point during this process is captured very well by the LES model in comparison with the experimental data. The validity of this LES model is then further assessed for a confined swirling flame with practical flow conditions. The simulation results are compared against an extensive experimental dataset including velocity, mixture fraction, temperature and major species mass fraction measurements, showing an overall good agreement at various locations inside the combustion chamber. The intermediate species mass fractions are also predicted reasonably well by the LES model despite that a general over-estimation is observed. Moreover, it is found that in the transport equation for the SGS variance of progress variable, the reaction and dissipation terms are predominant, substantially greater than the terms representing turbulent diffusion and production processes.

Furthermore, the statistical correlation between mixture fraction and progress variable is found to be important for the RANS closure. However, this correlation is observed to be negligible for the sub-grid scale (SGS) of LES showing reasonably good model predictions for both simulated experimental configurations.

Declaration

I, Zhi Chen, hereby declare that the contents of this dissertation are my own original work conducted at the University of Cambridge during the period from October 2012 to June 2016, and include nothing which is the outcome of work done in collaboration except as declared in the Acknowledgements and specified in the text.

No part of this dissertation has already been, or, is being concurrently submitted for any such degree, diploma or other qualification at the University of Cambridge or elsewhere.

This dissertation contains approximately 55,000 words, 85 figures and 9 tables.

Name: Zhi Chen

Date: 04 July 2016

Signature:

Acknowledgements

During this dramatic Ph.D. journey, there have been many people who held me through the rough roads and without their help, I would never have made to the finish line and thereby writing this thesis.

First and foremost, I would like to sincerely express my gratitude to my supervisor, Prof. N. Swaminathan, for his generous, patient and inspiring guidance. It has been a honour for me to have him as a teacher, mentor and friend. I will always be grateful for the priceless opportunity and support that he offered me when I was struggling at the beginning stage of my Ph.D. His knowledge, passion and persistency on combustion science has deeply influenced me and my choice to pursue an academic career in the future.

I also acknowledge the invaluable advice and encouragement from Prof. E. Mastorakos during my Ph.D. study. I would like to thank Drs. S. Ruan and H. Zhang for their generous help and useful suggestions while I was learning the research methodology and computational codes at the beginning. I am also very grateful for the inspiring discussions with my colleagues and also friends at the Cambridge Hopkinson Laboratory: Drs. I. Langella , I. Ahmed, A. Giusti, Mr. N.A.K. Doan, J. Massey, M.P. Sitte and Ms. G. Ghiasi, just to name a few. I have truly enjoyed being a member of this amazing group and it will be a precious memory for the rest of my life. My gratitude is expressed to our IT expert, Mr. P. Benie, for his tremendous help on the various computational difficulties I have had during my study. I would like to acknowledge Dr. W. Meier from the German Aerospace Centre (DLR) for providing the experimental data.

The last but not the least, I owe a great deal to my family for their unconditional love and everlasting support in the past and the future days to come. Little would have been accomplished without them always standing behind me.

This Ph.D. work has been funded by the Cambridge Overseas Trusts and the China Scholarship Council. Several travel grants have also been received from the Department of Engineering, Darwin College, the British Section of the Combustion Institute and the UK Turbulent Reacting Flows Consortium. These financial supports are greatly acknowledged.

Dedicated to my dear wife Wanlin and loving parents ...

Contents

List of Figures

List of Tables

Nomenclature

Acronyms/Abbreviations

1D	one-dimensional
2D	two-dimensional
3D	three-dimensional
ATF	artificially thickened flame
CD	central differencing
CFD	computational fluid dynamics
CFL	Courant-Friedrichs-Lewy
CMC	conditional moment closure
CV	control volume
DLR	German Aerospace Centre
DNS	direct numerical simulation
EDC	eddy dissipation concept
F-TACLES	filtered tabulated chemistry for large eddy simulation
FGM	flamelet generated manifold
FPI	flame prolongation of intrinsic low-dimensional manifolds

FPV flamelet/progress variable

FSD flame surface density

FTT flow-through-time

FVM finite volume method

GTMC gas turbine model combustor

IRZ inner recirculation zone

JAXA Japan Aerospace Exploration Agency

LDV Laser Doppler Velocimetry

LEM linear eddy model

LES large eddy simulation

LES-PPF large eddy simulation with partially premixed flamelets

LHS left-hand side

MFM multi-dimensional flamelet-generated manifolds

MILD moderate or intense low-oxygen dilution

MMC multiple mapping conditioning

OMA order of magnitude analysis

ORZ outer recirculation zone

PDF probability density function

PLIF planar laser-induced fluorescence

PVC precessing vortex core

r.m.s. root mean square

RANS Reynolds averaged Navier Stokes

RHS right-hand side

SDR scalar dissipation rate

SGS sub-grid scale

SMLD statistically most likely distribution

TVD total variation diminishing

UD upwind differencing

UDF used-defined function

UDS used-defined scalar

UHC unburnt hydrocarbons

URANS unsteady Reynolds averaged Navier Stokes

Greek Symbols

α thermal diffusivity

χ scalar dissipation rate

Δ LES filter width

δ Zel'dovich thickness

$\dot{\omega}$ chemical reaction rate

η Kolmogorov length scale

Γ Gamma function

Λ integral length scale

λ thermal conductivity

μ dynamic viscosity

ν kinematic viscosity

ω vorticity

$\overline{\dot{\omega}_{\mathrm{c}}^{*}}$ partially premixed reaction rate

$\overline{\dot{\omega}}_{\mathrm{cdr}}$ cross dissipation contribution

$\overline{\dot{\omega}}_{\mathrm{c}}$ premixed mode contribution

$\overline{\dot{\omega}}_{\mathrm{np}}$ non-premixed mode contribution

ϕ equivalence ratio

ψ sum of CO and CO_2 mass fractions

ρ density

Σ flame surface density

$\sigma_k,\ \sigma_\varepsilon$ k-ε model constants

τ_η Kolmogorov time scale

τ_Λ integral time scale

τ_c chemical time scale

τ_L laminar flame time scale

Θ progress variable based on temperature

θ azimuthal coordinate

ε dissipation rate of turbulent kinetic energy

$\widetilde{\chi}_{c,\,\mathrm{sgs}}$ sub-grid dissipation rate of progress variable

$\widetilde{\chi}_{Z,\,\mathrm{sgs}}$ sub-grid dissipation rate of mixture fraction

ξ sample space variable for mixture fraction

ζ sample space variable for progress variable

u'_η Kolmogorov velocity scale

$\boldsymbol{\tau}$ viscous tensor

$\boldsymbol{\varphi}$ thermo-chemical property vector

Non-dimensional Numbers

Re Reynolds number

Da Damköhler number

Ka Karlovitz number

Le Lewis number

Sc Schmidt number

Operators

$()'$ Reynolds fluctuation

$()''$ Favre fluctuation

$(\cdot)^{\mathcal{T}}$ matrix transpose

$(\cdot)_s$ surface average

$\langle\cdot\rangle$ time average

$\overline{(\cdot)}$ Reynolds average or filtered

$\overline{(\cdot)''^2}$ Reynolds variance

$\widetilde{(\cdot)}$ Favre average or filtered

$\widetilde{(\cdot)''^2}$ Favre variance

Roman Symbols

$\boldsymbol{x}$ Cartesian coordinate vector

$\mathcal{F}$ flamelet quantity

Δh_f^0 formation enthalpy

Δt time-stepping size

δ_L^0 laminar flame thickness

$\dot{m}$ mass flow rate

$\mathcal{Q}$ second invariant of the velocity gradient tensor

$\overline{S}_{\mathrm{d}}$ flame-brush displacement speed

$\overline{S}_{\mathrm{net}}$ net flame-brush propagation speed

$\overline{S}_{\mathrm{n}}$ normal diffusion component of displacement speed

$\overline{S}_{\mathrm{r}}$ reaction component of displacement speed

$\overline{S}_{\mathrm{t}}$ tangential diffusion component of displacement speed

$\mathbf{k}$ unit vector in z-direction

$\mathbf{n}$ unit normal vector of flame brush surface

$\widetilde{g}$ normalised Favre variance

$\widetilde{S}_{\mathrm{OH}}$ computed OH-PLIF signal

$\widetilde{c_{\mathrm{sgs}}''^2}$ sub-grid variance of progress variable

$\widetilde{c''^2}$ Favre variance of progress variable

$\widetilde{Z_{\mathrm{sgs}}''^2}$ sub-grid variance of mixture fraction

$\widetilde{Z''^2}$ Favre variance of mixture fraction

$\widetilde{Z''c''}$ Favre covariance

c progress variable

C_p^{e} effective specific heat capacity

$C_Z,\ C_c$ linear relaxation model constants

$C_\mu,\ C_{\varepsilon 1},\ C_{\varepsilon 2}$ k-ε model constants

C_{S}	Smagorinsky model constant
C_p	specific heat capacity
D	mass diffusivity
d	diameter
F	flame thickening factor
h	total enthalpy
I	turbulent intensity
k	turbulent kinetic energy
L_{f}	flame lift-off height
p	pressure
r	radial coordinate
R_0	universal gas constant
R_ρ	density ratio
S	swirl number
S_d	flame displacement speed
S_G	flame burning velocity for G-equation approach
S_L^0	laminar flame speed
T	temperature
t	time
T_0	reference temperature 298.15 K
U	axial velocity component
u'_Δ	sub-grid velocity scale

u'_Λ integral velocity scale

V radial velocity component

V volume

W molar mass or swirl velocity component

X mole fraction of air dilution

x, y, z Cartesian coordinates

Y mass fraction

Z mixture fraction

$\boldsymbol{q}$ heat flux vector

$\boldsymbol{U}$ velocity vector

$\mathcal{A}$ Arrhenius pre-exponential constant

$\mathcal{F}_K$ fraction of resolved kinetic energy

$\mathcal{L}^{\varphi}$ flamelet library matrix

$\mathcal{M}^{\widetilde{\varphi}}$ lookup table matrix

$\mathcal{N}$ number of discretisation points in the lookup table

$\mathcal{TV}$ total variation of numerical solution

$\mathcal{U}$ normalised mean axial velocity

$\mathcal{U}_{\text{r.m.s.}}$ normalised axial velocity fluctuation

$\mathscr{G}$ filter function

$\mathbf{I}$ identity matrix

N_{cc} scalar dissipation rate of progress variable

N_{Zc} cross dissipation rate of mixture fraction

N_{ZZ} scalar dissipation rate of mixture fraction

Superscript

b burnt mixture

u unburnt mixture

$*$ sample space variable

$+$ normalisation

Eq chemical equilibrium

Subscript

β Beta function

i species i

st stoichiometry

c co-flow

j jet

l lean flammability limit

mix mixture

q quenching

r rich flammability limit

t turbulent quantity

Chapter 1

Introduction

1.1 Motivation and challenge

The capability of manipulating combustion benchmarks the evolutionary breakthroughs in the entire human history of more than two million years [Stavrianos, 1999]. In the earliest days of mankind, the primitive utilisation of fire originated the migration of our ancestors from caves to river basins, leading to the generation of many great agricultural civilisations all around the world. During this time about two thousand years until the 18th century, combustion energy were mainly used for domestic needs (cooking, heating, etc.), and also for metallurgy to produce agricultural facilities as well as military cold weapons. As hand production was dominant in the manufacturing processes, human productivity remained quite low in that period. However, our understanding of the essence of nature including combustion phenomena became deeper and deeper, eventually led to a major turning point in human history − the Industrial Evolution [Lucas Jr., 2002].

The Industrial Evolution began in the United Kingdom from the 1760s with numerous technological innovations developed in the following 100 years, which dramatically improved the production efficiency and living standards of human beings. The steam engine invented by British pioneer James Watt was one of the most remarkable inventions in human history, and since then thermal energy started to be used as the primary source of power for all kinds of activities in

human lives. As reported by a major oil and gas company, BP [BP, 2014], in 2014, fossil fuel combustion supplies about 86% of the world's energy, which increases by an annual growth rate of 2% due to the expanding population and increasing energy demand per person. Though renewable energy resources have been largely developed in recent years, it is still believed that fossil fuels will remain as the major energy supply for human society in the foreseeable future.

On the other hand, largely burning fossil fuels has brought severe impact on the environment due to emissions of toxic pollutants and green-house gases. As a result, stringent regulations for combustion systems leave combustion engineers no choice but to find effective approaches to improve the environmental friendliness of these systems without sacrificing the power efficiency. However, it is extremely challenging to understand the underlying physics of combustion phenomena in practical systems, which usually involve turbulent thermo-fluid flows and complex chemical kinetics of heavy hydro-carbon fuel reactions interacting with one another.

In the last half a century, extraordinary progress has been achieved in combustion research [Law, 2006]. Theories of two idealised combustion modes, the premixed and non-premixed mode, are established based on the premixing condition of reactants. In non-premixed combustion, the flame exists in a thin layer between fuel and oxidiser which are supplied separately to the system. The mixing is achieved through molecular diffusion of reactants and thus it is also referred to as diffusion flame. Non-premixed flames are safe and easy to control since reactions only take place in a limited region and therefore almost all the earliest combustion devices operate in this mode, such as torches, candles and lighters. For combustion systems that require high level of safety and reliability, e.g. aero gas turbines, non-premixed mode is still employed. The main drawback of non-premixed combustion is that uneven mixing causes formation of soot and incomplete combustion products including unburnt hydrocarbons (UHC) and carbon monoxide (CO). Furthermore, the inevitable high flame temperature results in increased emission of nitric oxides (NO_x), which heavily influences the natural chemistry in the environment. In premixed mode, fuel and oxidiser are perfectly mixed at the molecular level prior to combustion often involving a flame propagating from burnt to unburnt mixtures. One common example is spark ignition

gasoline engine. This combustion mode with fuel lean condition (low fuel-to-air ratio) provides a more complete burning process with relatively low flame temperature leading to reduced emission of nitric oxides (NO_x) and soot. Recently, lean premixed combustion has become a popular choice for energy generation because of its promising potential of achieving high thermal efficiency and low pollutant emission at the same time [Swaminathan & Bray, 2011]. However, controlling such flames remains challenging as it is highly susceptible to thermo-acoustic instabilities which are inevitable in combustion systems. For instance, a small perturbation at the burner inlet can significantly influence the local heat release rate leading to undesired pressure fluctuations in the combustion chamber [Poinsot & Veynante, 2005].

In fact, neither premixed nor non-premixed condition can be achieved in real-life practical systems and partial premixing condition is ubiquitous. However, the "partially premixed mode" combustion is not as well defined as the two classical modes and can be sometimes ambiguous [Peters, 2000]. There also exists the "stratified" or "inhomogeneous" combustion referring to similar premixing conditions. In a recent review of partially premixed flames, Masri [2015] proposed a clarification that the term "partially premixed" refers to inhomogeneous composition of fluid parcel covering a wide range of mixture fractions including both flammable and non-flammable fluid, whereas "stratified flames" only contain mixtures varying within the flammability limits. This definition is followed hereafter in this thesis. Unlike the well established premixed or non-premixed mode combustion, partially premixed combustion is a relatively new subject and its flame structure and burning features are yet to be understood fully. Recent experimental studies [Barlow *et al.*, 2015; Li *et al.*, 2009; Meares & Masri, 2014] have shown that providing partially premixed (or inhomogeneous) inlet mixture can greatly enhance the flame stability and the blow-off velocity is increased by nearly 40%. These findings greatly motivate the combustion engineers to employ the advances in partially premixed flames for next generation of combustion systems.

The rapid development in Computational Fluid Dynamics (CFD) greatly boosts the use of numerical simulations in today's combustion research for both academic and industrial purposes [Poinsot & Veynante, 2005]. Compared to ex-

perimental measurements that are limited by the existing diagnostic techniques, computational simulations can provide more insights to the underlying physical phenomena at a significantly reduced cost, provided the models used are consistently accurate, meaningful and robust. Along with the advancement of combustion theory and computing power, combustion modelling has evolved from purely qualitative in 1970s to quantitative and predictive in recent days [Law, 2006]. However, most of current modelling methodologies have been established based on either premixed or non-premixed combustion while combustion models for partially premixed flames are scarce. Robust models with low computational cost are still to be developed for turbulent partially premixed flames under various operating conditions in complex practical combustion systems.

1.2 Approach and objectives

In practice, most combustion applications involve turbulent reacting flows. Modelling these flows is very challenging because both turbulence and chemistry have wide ranges of time and length scales, and these scales interact with one another resulting in a highly non-linear system, which is challenging for numerical simulation. Based on the scales solved in the simulation, three main paradigms have been established for turbulent combustion simulation: Direct Numerical Simulations (DNS), Large Eddy Simulations (LES) and Reynolds Averaged Navier Stokes (RANS) simulations. DNS to resolves all the chemical and turbulence scales including the Kolmogorov scales [Kolmogorov, 1941], which are the smallest scales involved in turbulent flows. However, resolving such small scales requires extremely fine numerical grid in both time and space, leading to extremely expensive computations even for a laboratory-scale burner. Currently, DNS is still primarily used to study specific physical processes in a small fluid domain, $\sim \mathcal{O}(1\ \mathrm{cm}^3)$, and DNS data is widely used for hypothesis testing and model validations. To reduce the computational expense, Smagorinsky [1963] proposed LES approach originally to simulate atmospheric air currents. LES resolves only large dynamic scales in the flow by applying a filtering operation whereas the small sub-grid scale (SGS) scales are modelled. As LES results contain information of large-scale fluid motions, they are very useful to study transient effects in turbu-

lent reacting flows in both laboratory and industrial devices [Pope, 2000]. The general flame characteristics can also be reflected in LES by collecting statistics of filtered fields. Although LES has been increasingly used in recent years, it is still too expensive to use in practical combustor design cycle where a very high number of test cases need to be simulated. Therefore, RANS remains dominant for industrial CFD applications because of its low cost despite that it only solves for statistical quantities of the flow.

Except for DNS, modelling is required in numerical simulations to account for the effects of chemical reactions, turbulence and their interactions. Over the past several decades, various turbulent combustion models have been proposed and applied to a broad range of laboratory and practical flame configurations [Janicka & Sadiki, 2005; Pitsch, 2006; Veynante & Vervisch, 2002]. Among these models, the laminar flamelet model involving tabulated chemistry has been the most widely used approach for both research and practical purposes because of its computational economy. The fundamental idea behind the flamelet model is that the laminar flame structure is retained when the flame front encounters turbulence and the turbulent flame can be described as an ensemble of laminar flames using statistical models. The most attractive aspect of this approach is the decoupling of chemistry and flow calculations and thus the thermo-chemical state of the flame can be computed and stored in a lookup library prior to the flow calculation. This concept was first proposed by Williams [1975] and developed further by Peters [1984] for non-premixed flames. Various strategies such as G-equation, Artificially Thickened Flame (ATF), Flame Surface Density (FSD), Scalar Dissipation Rate (SDR), etc., were developed subsequently for premixed combustion [Bradley *et al.*, 1990; Peters, 2000; Poinsot & Veynante, 2005; Swaminathan & Bray, 2011]. Considerable progress has been made recently to extend these flamelet-based models for partially premixed combustion using both RANS and LES as reviewed in [Masri, 2015], however, none has shown fully satisfactory performance so far for partially premixed flames involving the complexity of different burning modes and their interplay in highly turbulent flows.

As a further attempt to address this, Ruan *et al.* [2014a] proposed a RANS modelling framework for partially premixed combustion based on the analytical derivation by Bray *et al.* [2005] and the DNS data of a lifted hydrogen jet

flame from Japan Aerospace Exploration Agency (JAXA) [Mizobuchi *et al.*, 2002, 2005]. This approach takes into account of the effects of both premixed and non-premixed mode as well as their mutual influences through a correlated joint Probability Density Function (PDF) method. The simulation results [Ruan *et al.*, 2014a] of the flame brush structure and lift-off height for the lifted jet flame agreed quite well with the experimental measurements and DNS data, showing promising potential of predicting partially premixed combustion. Therefore, the objective of this thesis work is to further assess the practical validity of this model for partially premixed hydrocarbon flames with a wide range of flow and air dilution conditions. In addition, the original RANS framework is extended to LES with further validations.

The specific objectives of this research work are:

1. To assess the model validity using steady RANS simulations of turbulent lifted methane jet flames in order to investigate the individual contribution of each combustion mode and their interaction effects. Also investigate the influences of jet velocities and air dilution levels on the lifted flame behaviour;

2. To perform unsteady RANS (URANS) simulations of a spark-ignited jet flame to evaluate the model capability in predicting transient flame behaviours, in order to analyse the partially premixed flame propagation and the role of physical dimensions on the propagation characteristics.

3. To establish an LES framework for partially premixed flames by extending the modelling of Ruan *et al.* [2014a] to sub-grid scales;

4. To investigate flame edge dynamics in a spark ignition sequence to understand the flame leading point trajectory behaviour from the ignition to final stabilisation and lift-off statistics using LES;

5. To apply the LES modelling methodology to a laboratory-scale gas turbine model combustor (GTMC) with complex geometry in order to study the partially premixed flame stabilisation and dynamics in this model combustor.

1.3 Thesis structure

The structure of this thesis is as follows. Chapter 2 introduces the fundamental theories of turbulent combustion and briefly reviews representative modelling studies in the past for premixed, non-premixed and partially premixed combustion. Recent advances in developing modelling strategy for partially premixed combustion using both RANS and LES methods are discussed in detail as the background for the present work.

Chapter 3 describes the governing equations and model implementation for both RANS and LES contexts. The parallel computing performance and code scalability on the ARCHER clusters at UK National Supercomputing Service for LES are also discussed.

In Chapter 4, validation cases of cold flows are computed to assess the numerical setup, turbulence models and grid sensitivity for the subsequent reacting flow simulations. Two main experimental studies are considered: (i) the turbulent lifted methane jet flame series investigated by Ahmed & Mastorakos [2006] and (ii) the dual-swirler GTMC configuration of [Meier *et al.*, 2006; Weigand *et al.*, 2006] the German Aerospace Centre (DLR). The computational results obtained in the thesis work are presented in Chapters 5 to 8.

Chapter 5 presents the simulation results of turbulent lifted methane/air jet flames using two-dimensional (2D) axisymmetric steady RANS approach. Different model combinations are used in the simulations to systematically investigate the individual contribution from premixed and non-premixed combustion modes and their correlation effects. Lifted flames with a broad range of jet bulk mean velocities and air dilution levels are simulated to evaluate the model capability of predicting the flame lift-off height under this range of conditions.

In Chapter 6, 2D and 3D unsteady RANS simulations of a spark-ignited turbulent methane/air jet flame evolving from ignition to stabilisation are conducted for two jet velocities. The transient evolution of flame brush leading edge is compared between 2D and 3D simulation results to study the influence of the third physical dimension during this transient process. Effects of flame displacement speed components are studied to gain further insight in the flame propagation behaviour.

LES realisations of two spark ignition sequences are investigated in Chapter 7. The flame leading edge formation and its propagation dynamics in 3D physical space are discussed. The statistical behaviour of the stabilisation point at the final lift-off height is also analysed.

Chapter 8 further evaluates the LES model performance for a complex geometry and flow in a DLR dual-swirler burner. Computed flame structure (e.g. temperature, species profiles) is compared with the experimental data in detail. The flame dynamics and stabilisation statistics are also studied.

Finally, Chapter 9 summarises the main conclusions of this study along with an outlook for future works.

Chapter 2

Research Background

Partially premixed combustion involves compositionally inhomogeneous mixtures which can be flammable or non-flammable. This is the common situation in technical applications where the mixing of reactants produce mixtures between pure premixed and non-premixed regimes [Peters, 2000]. As a result, turbulent flame propagation occurs in an inhomogeneous mixture involving interactions between many complex physical processes, which poses a major challenge to numerical simulations. This chapter first briefly reviews the state-of-the-art turbulent combustion in general, and then focuses on the recent advances of partially premixed combustion modelling.

2.1 Governing equations

In the context of turbulent combustion, special treatments to the common Naiver-Stokes equations for constant-density flows are necessary [Poinsot & Veynante, 2005]. Specifically, detailed thermodynamic and transport data for multiple species may be required and production or consumption rates at which chemical reactions between these species occur need to be modelled carefully with the consideration of multi-species kinetics. For the present work, which mainly focuses on subsonic combustion of gaseous-phase low hydrocarbon fuels at atmospheric pressure, several common assumptions are made as follows.

The reacting fluid is considered to be a mixture of Newtonian perfect gases.

Fickian diffusion is assumed for molecular diffusive flux. The typical speed at which the flame propagate is much smaller than the sound speed and hence the pressure variation across the flame is negligible [Williams, 1985]. Therefore, the terms for viscous heating and pressure change in the energy equation are neglected. The gravitational forces on gases and other external forces are also neglected and combustion is assumed to be adiabatic. With the above simplifications, the instantaneous equations governing the turbulent reacting flows for the present work are written using common notations as [Kuo, 1986; Poinsot & Veynante, 2005]

- Mass Conservation:

$$\frac{\partial \rho}{\partial t} + \nabla \cdot (\rho \boldsymbol{U}) = 0, \tag{2.1}$$

  where ρ is the mixture density and $\boldsymbol{U}$ is the velocity vector;

- Momentum Conservation:

$$\frac{\partial \rho \boldsymbol{U}}{\partial t} + \nabla \cdot (\rho \boldsymbol{U}\boldsymbol{U}) = -\nabla p + \nabla \cdot \boldsymbol{\tau}, \tag{2.2}$$

  where p is the pressure and

$$\boldsymbol{\tau} = \mu \left[\nabla \boldsymbol{U} + (\nabla \boldsymbol{U})^{\mathcal{T}} \right] - \frac{2}{3}\mu \mathbf{I} \cdot \nabla \boldsymbol{U} \tag{2.3}$$

  is the viscous tensor, with μ and $\mathbf{I}$ being the dynamic viscosity and the identity matrix respectively and symbol $\mathcal{T}$ denotes a transpose operation;

- Species Conservation:

$$\frac{\partial \rho Y_i}{\partial t} + \nabla \cdot (\rho \boldsymbol{U} Y_i) = \nabla \cdot (\rho D_i \nabla Y_i) + \dot{\omega}_i, \quad i = 1, 2, ..., N \tag{2.4}$$

  where Y_i is the mass fraction of species i, $\dot{\omega}_i$ is the chemical reaction rate in mass units and D_i is the mass diffusivity.

- Total Enthalpy Conservation:

$$\frac{\partial \rho h}{\partial t} + \nabla \cdot (\rho \boldsymbol{U} h) = -\nabla \cdot \boldsymbol{q}, \tag{2.5}$$

where heat flux $\boldsymbol{q}$ is usually expressed by Fourier's Law for heat conduction along with a molecular diffusion term [Poinsot & Veynante, 2005]. In common modelling practice where a unity Lewis number is assumed for all species, i.e. Le $= \alpha / D_i$, where α is the thermal diffusivity, Eq. (2.5) becomes [Swaminathan & Bray, 2011]

$$\frac{\partial \rho h}{\partial t} + \nabla \cdot (\rho \boldsymbol{U} h) = \nabla \cdot (\rho D \nabla h)\,, \tag{2.6}$$

where D is the mass diffusivity of the mixture. The total enthalpy (without the kinetic energy) consists of the sensible and chemical parts written as

$$h = \overbrace{\int_{T_0}^{T} C_{p,\mathrm{mix}}\ dT}^{\text{sensible}} + \overbrace{\sum_{i=1}^{N} Y_i \Delta h^0_{f,i}}^{\text{chemical}}, \tag{2.7}$$

where $C_{p,\mathrm{mix}}$ is the mixture specific heat capacity at constant pressure and $\Delta h^0_{f,i}$ is the formation enthalpy of species i. The reference temperature at which the sensible and chemical enthalpies are defined is $T_0 = 298.15$ K.

- Equation of State:

$$p = \rho\, T \frac{R_0}{W_{\mathrm{mix}}}, \tag{2.8}$$

where $R_0 = 8413.5$ J/kmol/K, is the universal gas constant and W_{mix} is the molecular mass of the mixture.

As these equations are highly unsteady and non-linear for turbulent reacting flows, it is rather difficult, if not impossible, to directly solve them for practical applications. The ultimate target of turbulent combustion research is to understand the underlying physics and obtain approximate but close enough solutions of these equations using modelling strategies. Various approaches have been es-

tablished in the literature for this purpose and are briefly discussed in the next section.

2.2 Overview of turbulent combustion modelling

2.2.1 Statistical description

Turbulent combustion exists in most practical devices. Unfortunately, at present there is still no analytical solution for turbulent flows and the chaotic fluid motions are mostly described through statistical approaches [Cant & Mastorakos, 2008]. For example, a fluctuating quantity $Q(\boldsymbol{x}, t)$ in the flow can be expressed through a Reynolds decomposition method:

$$Q(\boldsymbol{x}, t) \;=\; \overline{Q}(\boldsymbol{x}, t) + Q'(\boldsymbol{x}, t), \tag{2.9}$$

where the mean $\overline{Q}(\boldsymbol{x}, t)$ can be obtained using either time or ensemble-averaging of the data for $Q(\boldsymbol{x}, t)$ as

$$\overline{Q}(\boldsymbol{x}, t) \;=\; \frac{1}{t_1}\int_0^{t_1} Q(\boldsymbol{x}, t)dt \quad \text{or} \quad \overline{Q}(\boldsymbol{x}, t) \;=\; \frac{1}{N}\sum_1^N Q(\boldsymbol{x}, t_N) \tag{2.10}$$

with t_1 and N being the sample collecting time and number respectively. The fluctuation is reflected through the variance:

$$\overline{\sigma_Q^2} \;\equiv\; \overline{Q'^2} \;=\; \overline{Q^2} - \overline{Q}^2. \tag{2.11}$$

Thus, using $\overline{Q}(\boldsymbol{x}, t)$ and $\overline{\sigma_Q^2}$ the overall behaviour of quantity Q at any local point in a given flow field can be described on a statistical basis.

For combusting flows, the correlation between density and any other quantities is significant, which introduces a major difficulty for modelling [Poinsot & Veynante, 2005]. To avoid this, a density-weighted averaging (or Favre-averaging) method is introduced and is written as [Favre, 1964; Kuo, 1986; Williams, 1985]

$$\widetilde{Q} = \frac{\overline{\rho\, Q}}{\overline{\rho}} \quad \text{with} \quad \widetilde{Q} = Q - Q'', \tag{2.12}$$

where $\rho = \rho(\boldsymbol{x}, t)$ is the instantaneous mixture density and Q'' denotes the Favre fluctuation. As a result of applying Favre averaging, the balance equations of reacting flows appear in forms similar to those for non-reacting flows. These equations will be discussed further in Chapter 3.

As turbulent flows usually involve high level of randomness, the *probability density functions* (PDF) in statistics theory are very useful to describe the behaviour of random variables associated with the flow. For quantity Q, its PDF is defined in such a way that the probability for $\xi < Q < \xi + d\xi$ is $P(\xi)$, where ξ is the *sample space variable* of Q. According to statistics theory, the sum of probabilities accounting for all possibilities must be unity and thus

$$\int_{\xi_{\min}}^{\xi_{\max}} P(\xi)\, d\xi = 1, \tag{2.13}$$

where ξ is bounded by its minimum and maximum values, $\xi_{\min}$ and $\xi_{\max}$. Such PDFs describing single variable behaviour are called marginal PDFs. Obtaining the PDF distributions of flow variables is the focus of turbulent combustion modelling, and various methods have been proposed based on presumed, conditional or transported PDFs as recently reviewed by Pope [2013].

For combustion in many practical systems, PDF of a quantity of interest often has a more or less fixed shape and thus can be prescribed using only few parameters [Williams, 1985]. There are a large number of presumed distributions formulised in the literature of probability and statistics. The most widely used PDF shape in turbulent combustion is the *β-distribution*, which is parameterised using the first two moments of quantity Υ, the Favre mean ($\widetilde{\Upsilon}$) and variance ($\widetilde{\Upsilon''^2}$) [Poinsot & Veynante, 2005]:

$$\widetilde{P}_\beta(\xi; a, b) = \frac{\Gamma(a+b)}{\Gamma(a)\Gamma(b)}\, \xi^{a-1}(1-\xi)^{b-1} \tag{2.14}$$

with

$$a = \widetilde{\Upsilon}\left(\frac{\widetilde{\Upsilon}(1-\widetilde{\Upsilon})}{\widetilde{\Upsilon''^2}} - 1\right) \qquad \text{and} \qquad b = (1-\widetilde{\Upsilon})\left(\frac{\widetilde{\Upsilon}(1-\widetilde{\Upsilon})}{\widetilde{\Upsilon''^2}} - 1\right), \tag{2.15}$$

where the Γ-*function* is given by

$$\Gamma(x) = \int_0^{+\infty} e^{-t}\, t^{x-1}\, dt. \tag{2.16}$$

As β-*distribution* is defined between 0 and 1, Υ is normalised as $\Upsilon = Q/Q_{\max}$. Here $\widetilde{\Upsilon}$ and $\widetilde{\Upsilon''^2}$ are usually calculated through transport equations. Using the PDF of Υ, from Eq. (2.13) one obtains

$$\widetilde{\Upsilon} = \int_0^1 \Upsilon\, \widetilde{P}(\xi)\, d\xi \tag{2.17}$$

More importantly, the PDF is used to construct the average of other quantities that are related to Υ, for example:

$$\widetilde{\Phi(\Upsilon)} = \int_0^1 \Phi(\xi)\, \widetilde{P}(\xi)\, d\xi. \tag{2.18}$$

However, in multivariate problems such as turbulent combustion, Φ usually depends on more than one variable and these variables interact with one another involving statistical correlations, for which joint PDFs need to be used to describe the correlated distributions. If one includes another random variable Ω then Eq. (2.18) becomes

$$\widetilde{\Phi(\Upsilon,\Omega)} = \int_0^1 \Phi(\xi,\zeta)\, \widetilde{P}(\xi,\zeta)\, d\xi\, d\zeta, \tag{2.19}$$

where $\widetilde{P}(\xi,\zeta)$ is the joint PDF with ζ being the sample space variable for Ω. For the extreme case where Υ and Ω are statistically independent, the joint PDF is simply the product of the two marginal PDFs: $\widetilde{P}(\xi,\zeta) = \widetilde{P}(\xi)\widetilde{P}(\zeta)$, which is commonly assumed in many combustion models. However, this assumption may not be valid for situations where there is a strong interaction between the two quantities. Further details are discussed in §2.3 while reviewing these existing models.

2.2.2 Multi-scale nature

As noted in Chapter 1, both combustion and turbulence involve a large number of time and length scales. The mechanisms that control the evolution of these scales for the two separate problems still remain unclear, while the two-way interaction of chemistry and turbulence makes turbulent combustion as one of the most complex subject in engineering sciences [Peters, 2000].

Nearly a century after Richardson [1922] described turbulence using the famous *whorls*, the *energy cascade* theory remains as the footstone of today's turbulence research. The most prominent contribution towards this concept was made by Kolmogorov [1941] , who proposed the fundamental hypotheses for turbulent flow motions at high Reynolds number. In brief, the basic idea is that the energy-containing large eddies transfer energy to smaller eddies until reaching the smallest scales, the Kolmogorov scales, at which the energy is then dissipated through viscous effects [Batchelor, 1953]. The Kolmogorov scales are believed to have an uniform size and behaviour (*isotropy*), and determined by the kinematic viscosity ν and the dissipation rate ε, which represents the dissipating rate of the turbulent kinetic energy k. The large scales, however, are characterised by the mean flow geometry, for example, the diameter of the jet nozzle for a typical jet flow.

For turbulence study, it is intuitive to use length scales as they provide a direct impression for the size of eddies [Tennekes & Lumley, 1972]. The Kolmogorov length scale is given as $\eta \equiv (\nu^3/\varepsilon)^{1/4}$ and the dissipation rate can be estimated using $\varepsilon \approx u_\Lambda'^3/\Lambda$ where Λ is the characteristic length scale of large eddies, also called the integral length scale, and the integral velocity fluctuation u_Λ' is related to the turbulent kinetic energy by $u_\Lambda' = \sqrt{2/3k}$. Using these scales, one can define a turbulent Reynolds number as $\mathrm{Re}_t = u_\Lambda'\Lambda/\nu$, which provides an important relation between the small and large length scales: $\Lambda/\eta \sim \mathrm{Re}_t^{3/4}$. This indicates that the range of scales increases rapidly with $\mathrm{Re}_t^{3/4}$ at large Reynolds numbers, which makes it difficult to solve the instantaneous equations presented in §2.1 using DNS methods with all the scales resolved [Pope, 2000]. In order to overcome this difficulty, RANS method is used by modelling the averaged turbulence behaviour by resolving only the scale associated to the mean flow; whereas LES

is proposed to resolve a range of energy-containing large scales and small scales are modelled.

Except turbulence scales, chemical reaction scales are also difficult to handle numerically, because each species and reaction have their own scales depending on mass concentrations, temperature and chemical kinetics. Practical fuels such as gasoline can have thousands of species and tens of thousands of reactions during the combustion process. Furthermore, these scales spread in a broad range and several order of magnitude difference can be found between large and small scales resulting in computationally stiff systems [Poinsot & Veynante, 2005]. To avoid this, two main approaches are used in modelling practice: (i) simplified (or reduced) chemistry which retains only the high-impact species and reactions through sensitivity analyses; (ii) tabulated chemistry parameterised using few representative chemical scales, which can be computed either before the flow calculation (known as ILDM [Maas & Pope, 1992a,b] and FGM [Gicquel *et al.*, 2000; van Oijen & de Goey, 2000]), or on the fly during the simulation (ISAT [Pope, 1997]). More details of these numerical methods will be provided in §2.3.

As introduced in Chapter 1, turbulence-chemistry interaction remains as a major challenge in turbulent combustion, and this interaction highly depends on the relative scales between the local turbulence and chemistry [Peters, 2000]. Based on the scale comparison, turbulent flames can be categorised into different regimes having different reaction zone characteristics as discussed in the following section.

2.2.3 Classification and regimes

2.2.3.1 Non-premixed flames

In non-premixed (or diffusion) flames, even though fuel and oxidiser enter the combustion chamber separately, sufficient mixing at the molecular level is required for chemical reactions to occur[Glassman, 1987]. This mixing is achieved mainly through species diffusion and turbulence, and the mixing rate essentially controls the chemical reaction progress. In order to describe the mixing process, the concept of mixture fraction denoted by Z, was proposed (see [Bilger, 1976] for a review of definitions) using a combination of fuel, oxidiser mass fractions or

temperature (any two of the three), and its balance equation is written as

$$\frac{\partial \rho Z}{\partial t} + \nabla \cdot (\rho \boldsymbol{U} Z) = \nabla \cdot (\rho D \nabla Z)\,, \tag{2.20}$$

where Z is a conserved (or passive) scalar, which is balanced only by convection and diffusion processes. Bilger *et al.* [1990] later proposed a more general form of mixture fraction using carbon (C), oxygen (O) and hydrogen (H) elemental mass fractions written as

$$Z \equiv \frac{2Y_{\mathrm{C}}/W_{\mathrm{C}} + Y_{\mathrm{H}}/2W_{\mathrm{H}} + (Y_{\mathrm{O},2} - Y_{\mathrm{O}})/W_{\mathrm{O}}}{2Y_{\mathrm{C},1}/W_{\mathrm{C}} - Y_{\mathrm{O},1}/W_{\mathrm{O}} + Y_{\mathrm{H},1}/2\,W_{\mathrm{H}} + Y_{\mathrm{O},2}/W_{\mathrm{O}}}, \tag{2.21}$$

where the subscripts 1 and 2 denote the fuel and oxidiser streams respectively. This formula is organised in such a way that $Z = 1$ for fuel inlet boundary and $Z = 0$ for oxidiser stream. The primary advantage of this definition is that these elemental mass fractions are directly available from experimental measurements so that mixture fraction can be easily determined.

A schematic of mixture fraction distribution is shown in Fig. 2.1 for a laminar diffusion candle flame. The dashed line corresponds to the stoichiometric surface where chemical reactions take place. The vectors shown in Fig. 2.1 denote the normal ($\mathbf{n}_{st}$) and tangential ($\mathbf{n}_1$) directions of the Z_{st} surface. Since reactions occur only in a very thin layer, it is reasonable to argue that the temperature and species gradients in the $\mathbf{n}_{st}$ direction are much larger than in the $\mathbf{n}_1$ direction, suggesting that the local flame structure can be viewed as one-dimensional in the mixture fraction space. This is the fundamental hypothesis of the *flamelet* concept [Peters, 2000; Williams, 1985]. Applying this concept, Eq. (2.4) can be transformed using the Z coordinate as [Peters, 1984]

$$\frac{\partial \rho Y_i}{\partial t} = \frac{1}{2}\,\rho\chi\,\frac{\partial^2 Y_i}{\partial Z^2} + \dot{\omega}_i, \tag{2.22}$$

where the gradient terms with respect to the tangential directions are neglected and the scalar dissipation rate χ is defined as

$$\chi = 2D\,(\nabla Z \cdot \nabla Z)\,, \tag{2.23}$$

which is one of the most important parameters in non-premixed combustion as it reflects the molecular mixing rate through the mixture fraction gradient with the dimension of the inverse of time (1/s). In many applications, the scalar dissipation rate at stoichiometric conditions, χ_{st}, is used for Eq. (2.22) and $1/\chi_{st}$ is taken as a characteristic mixing time scale for diffusion flames.

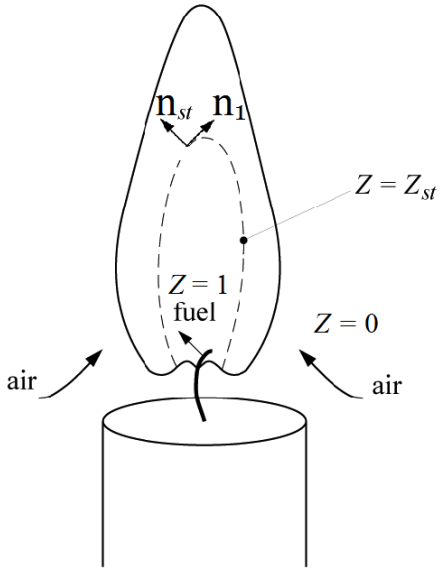

Figure 2.1: Schematic of a laminar diffusion candle flame [Peters, 2000].

Scalar dissipation rate is directly influenced by flow strain, a, as they have the same dimension (1/s) and high strain on a flame can lead to extinction at a quenching scalar dissipation rate χ_q. This process is illustrated using the classical S-shaped curve [Williams, 1985] in Fig. 2.2. The upper branch of the curve corresponds to burning flamelet, where the maximum flame temperature decreases as χ increases and eventually quenches at χ_q. Using these characteristic scales, Peters [2000] defined the thickness of flame and reaction zone in Z space, denoted as $(\Delta Z)_F$ and $(\Delta Z)_R$ respectively (see Chapter 3 of [Peters, 2000] for more detail).

In the presence of turbulence, the scalar fluctuation around stoichiometric mixture fraction can be significant and it is given by the r.m.s. of its Favre variance: $\widetilde{Z''_{st}} = \sqrt{\widetilde{Z''^2_{st}}}$. Figure 2.3 shows a regime diagram for turbulent non-premixed combustion described by mixture fraction fluctuation and scalar dis-

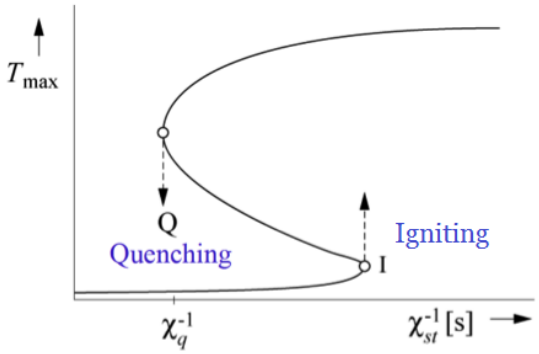

Figure 2.2: S-shaped curve for diffusion flame ignition and extinction [Williams, 1985].

sipation rate [Peters, 2000]. The vertical line corresponding to the condition of $\widetilde{\chi}_{st} = \chi_q$ separates the extinction and burning regions. In the top area of the burning side, where the turbulent fluctuation is larger than the flame thickness ($\widetilde{Z''_{st}} > (\Delta Z)_F$), the flamelets present as separate reaction zones; whereas if $\widetilde{Z''_{st}} < (\Delta Z)_R$, suggesting that Z fluctuation is smaller than the reaction zone thickness, the well-stirred reactor condition is reached. In between these two conditions, the flame is found to be continuous and affected by turbulence merely through wrinkling and stretching processes.

To apply the flamelet equations in a computational framework (RANS or LES), Eq. (2.20) needs to be averaged or filtered, and the mixture fraction variance require either modelling or solving a transport equation for it. Moreover, the scalar dissipation rate at stoichiometry also needs to be modelled and these modelling details will be discussed later in §2.3.

2.2.3.2 Premixed flames

Contrary to non-premixed systems where a quasi-stationary flame is established in the mixing layer of fuel and oxidiser, premixed flames tend to propagate from burnt products towards the unburnt reactants at a certain speed. One-dimensional laminar unstrained premixed flame is one of the most basic problems in combustion and it is relatively well understood based on a large amount of experimental, theoretical and numerical studies as summarised by Law [2006] and Poinsot & Veynante [2005].

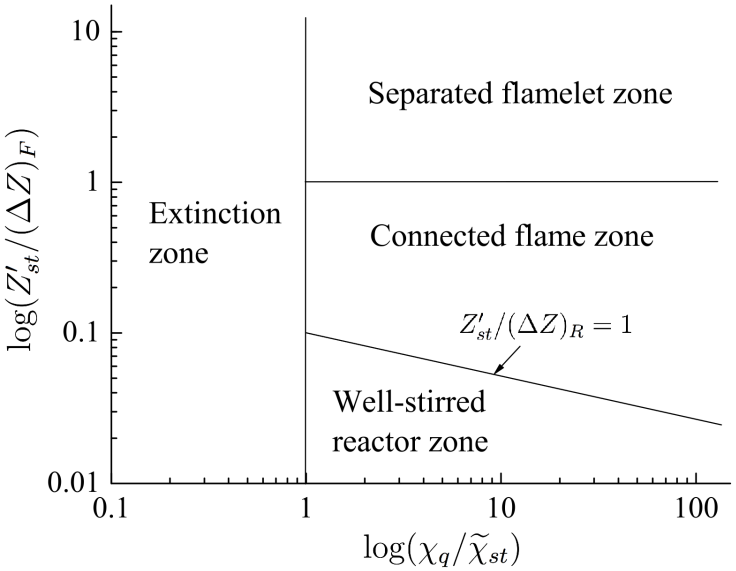

Figure 2.3: Regime diagram for turbulent non-premixed combustion [Peters, 2000].

A reactive scalar, progress variable, is commonly used to express the chemical reaction progress between fully unburnt and burnt mixtures. It can be defined either using temperature as $\Theta = (T - T^u)/(T^b - T^u)$, or a species mass fraction as $c = (Y_i - Y_i^u)/(Y_i^b - Y_i^u)$, where the superscripts ^{u} and ^{b} denotes fully unburnt and burnt conditions. Thus, the thermo-chemical structures across the premixed flame can be represented as function of this progress variable. However, care needs to be taken when defining the progress variable for a given problem since one value of progress variable can sometimes corresponds to two or more values of a certain quantity [Fiorina *et al.*, 2015b]. A good solution is to use a linear combination of several species mass fractions, for example, $c = (Y_{\mathrm{CO}} + Y_{\mathrm{CO_2}})/(Y^b_{\mathrm{CO}} + Y^b_{\mathrm{CO_2}})$ for hydrocarbon/air flames [Chen *et al.*, 2015; Fiorina *et al.*, 2003; Ruan *et al.*, 2015]. A systematic definition of progress variable has also been proposed by Najafi-Yazdi *et al.* [2012] based on *principal component analysis*.

Figure 2.4 presents a typical behaviour of the progress variable Θ (defined using temperature) in a freely propagating 1D unstrained laminar premixed methane/air flame calculated using CHEMKIN PRO[CHEMKIN, 2013]. The laminar flame speed denoted by S_L^0 signifies the fuel consumption rate and the

heat release rate at the flame front. Another important quantity, the laminar flame thickness δ_L^0 which provides a flame characteristic length scale, is often obtained using the maximum temperature gradient:

$$\delta_L^0 \equiv (T^b - T^u) \left(\frac{\partial T}{\partial x} \right)_{\max}^{-1} = \left(\frac{\partial \Theta}{\partial x} \right)_{\max}^{-1} \tag{2.24}$$

as illustrated in Fig. 2.4. In classical laminar flame theory [Glassman, 1987; Kuo, 1986], the flame structure is divided into two zones: the preheat zone where the reactants are heated by thermal conduction, and the reaction zone (or *the inner layer*), in which the ignition temperature is reached and chemical reactions take place. As can be seen in Fig. 2.4, the thickness of the reaction zone is much smaller than that of the preheat zone because chemical reactions usually occur at much faster rates compared to convective and diffusive processes. For stoichiometric methane/air mixture at room temperature and atmospheric pressure, the typical flame thickness is about 0.4 mm and the inner layer is approximately 1/10 of the flame thickness.

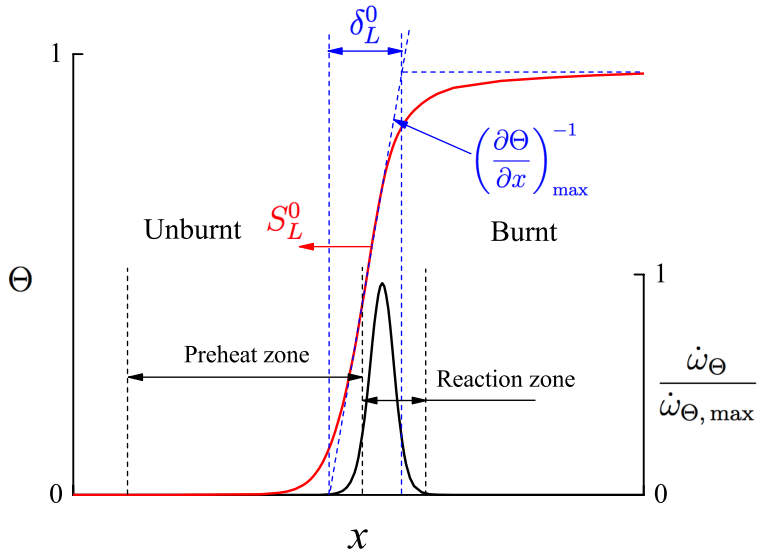

Figure 2.4: Computed typical variation of progress variable Θ (red line) and its reaction rate $\dot{\omega}_\Theta$ (black line) in a 1D unstrained laminar premixed flame for stoichiometric methane/air mixture.

The flame thickness defined in Eq. (2.24) is not often used in scale analy-

ses [Poinsot & Veynante, 2005] and instead an estimated thickness, $\delta = \lambda^u/\rho^u C_p S_L^0$ (known as the *Zel'dovich thickness*), is used to facilitate the derivation of turbulent premixed combustion regimes. A number of regime diagrams have been proposed by Borghi [1984], Abdel-Gayed & Bradley [1989], Poinsot *et al.* [1990], Peters [1999], etc. These diagrams are based on scale analysis and order of magnitude arguments to describe only some general behaviours of flame-turbulence interaction imposing many assumptions and approximations [Poinsot & Veynante, 2005]. Nevertheless, they provide physical insights of flame-turbulence interaction in premixed combustion, guiding many modelling methodologies proposed in the past. Here the widely used Peters' diagram [Peters, 1999] is shown in Fig. 2.5 and discussed for illustrative purpose below.

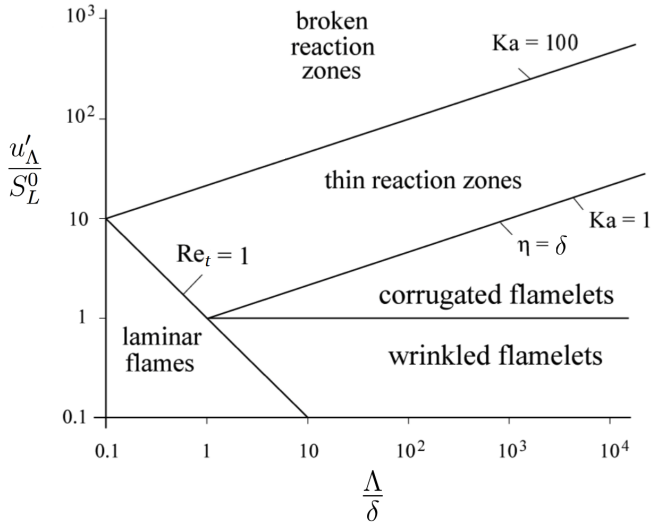

Figure 2.5: Regime diagram for turbulent premixed combustion [Peters, 1999].

First, two dimensionless numbers need to be introduced using the flame scales noted above and the turbulence scales noted earlier in §2.2.2. The Damköhler number defined as $\mathrm{Da} = \tau_\Lambda/\tau_c = (\Lambda/u'_\Lambda)/(\delta/S_L^0)$ represents the ratio of the integral time scale to the chemical time scale. The Karlovitz number corresponding to the ratio of the chemical time scale to the Kolmogorov time scale is given by $\mathrm{Ka} = \tau_c/\tau_\eta = (\delta/S_L^0)/(\eta/u'_\eta) = (u'_\Lambda/S_L^0)^{3/2}/(\Lambda/\delta)^{1/2}$, where u'_η is the Kolmogorov velocity scale defined as $u'_\eta \equiv (\nu\varepsilon)^{1/4}$. Using these two numbers along with the turbulent Reynolds number Re_t, the regime diagram can be constructed in terms

of the velocity, u'_Λ/S_L^0, and length, Λ/δ, ratios as shown in Fig. 2.5. Note that the diagonal of this diagram corresponds to $\mathrm{Da} = 1$ suggesting that $\tau_\Lambda = \tau_c$. The $\mathrm{Ka} = 1$ line distinguishes between the two main regimes:

(i) Flamelet regime ($\mathrm{Ka} < 1$), in which the flame is only slightly influenced by the turbulence as the chemical reactions are fast compared to the Kolmogorov time scale. If $u'_\Lambda < S_L^0$, which is rare in practical devices, flamelet structure is sustained since weak turbulence can only wrinkle the flame front; if $u'_\Lambda > S_L^0$ and $\delta < \eta$, the flame structure is thinner than the smallest eddies and thus cannot be perturbed by the turbulent fluctuations.

(ii) Thin or broken reaction regime ($\mathrm{Ka} > 1$), where the Kolmogorov length scale is smaller than the flame thickness and the chemical reactions can be substantially affected by the turbulent fluctuations. In extremely strong turbulence situations ($\mathrm{Ka} > 100$), the turbulent eddies can severely distort both the preheat zone and inner reaction layer resulting in broken (or distributed) reaction zones, possibly with flame extinctions [Peters, 2000]. As for the range in between ($1 < \mathrm{Ka} < 100$), which is similar to the operating conditions of most IC engines and aero gas turbines, turbulent eddies are able to enter and change the structure of the preheat zone but not the inner reaction layer. Therefore, the *flamelet-like* structure may still exist for this sub-regime but with strong turbulent fluctuations [Swaminathan & Bray, 2011].

2.2.3.3 Partially premixed flames

As mentioned in Chapter 1, neither premixed nor non-premixed condition can be perfectly achieved in practical combustion systems, where the mixing time or length is always a constraint due to the limited size of the device [Masri, 2015; Peters, 2000]. This is especially so in engines used for automobiles and aeroplanes. Some level of partial premixing is inevitable in most combustion situations, however, a clarification needs to be made before discussing further on this topic. The classical theories for fully premixed or non-premixed systems are still expected to hold for practical scenarios where a low level of "non-premixedness" or "premixedness" exists in forms of "holes" and "pockets" but does not significantly influence the flame behaviour [Peters, 2000]. In contrast, the partially premixed flames that

we consider here refer to situations where a relatively high level of partial premixing generates compositional inhomogeneity, which substantially changes the flame behaviour or even results in completely new features [Masri, 2015]. The *triple* or *tri-branchial* flame [Buckmaster, 2002; Echekki & Chen, 1997; Kioni *et al.*, 1993; Liñán, 1994] structure observed in laminar lifted jet flames is a good example. Some of these new features are quite advantageous and have been intentionally used in new generation of combustion devices such as direct injection gasoline engines and aero gas turbines involving lifted swirl flames [Peters, 2000].

Partially premixed flames can be further divided into two categories [Masri, 2015] depending on the range of mixture fraction. The first one is known as *stratified flames*, in which the mixture fraction only varies within the flammability limits. A typical configuration is the multi-slot burner, where the premixed mixtures with different equivalence ratios are injected through concentric annular nozzles as demonstrated in Fig. 2.6a. This type of configuration has been widely studied experimentally [Anselmo-Filho *et al.*, 2009; Seffrin *et al.*, 2010; Sweeney *et al.*, 2012a,b] and numerically [Fiorina *et al.*, 2015b; Kuenne *et al.*, 2012]. The second type of partially premixed combustion involves flame propagation in an inhomogeneous mixture, covering a broad range of mixture fraction including both flammable and non-flammable mixtures. This is mainly found in the flame base region of lifted non-premixed flame configurations, where the upstream partial premixing is introduced by the shear between the fuel and oxidiser streams. A canonical problem for this is turbulent lifted jet flame shown in Fig. 2.6b.

Turbulent lifted jet flames are quite common in many practical devices such as aero engines, gas flares, etc. These flames have been investigated in the past using analytical methods by Peters & Williams [1983] and Broadwell *et al.* [1984], experiments by Wohl *et al.* [1949], Vanquickenborne & van Tiggelen [1966], Eickhoff *et al.* [1984], Kioni *et al.* [1993], Schefer & Goix [1998], Kalghatgi [1984], Mansour [2003], Cessou *et al.* [2004] and Su *et al.* [2006], as well as using numerical simulations by Bradley *et al.* [1990], Müller *et al.* [1994], Favier & Vervisch [1998], Mizobuchi *et al.* [2002], Devaud & Bray [2003], Domingo *et al.* [2002], Ferraris & Wen [2007] and Ruan *et al.* [2014b]. These studies are reviewed critically by Pitts [1988], Buckmaster [2002], Peters [2000], Lyons [2007] and Lawn [2009] highlighting the importance of this topic and challenges involved in com-

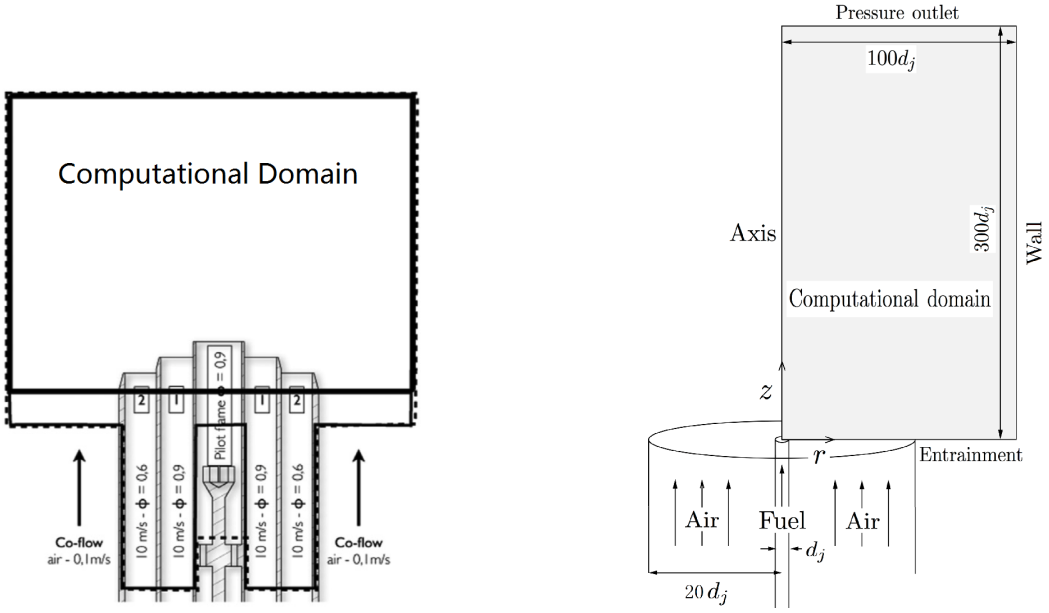

(a) (b)

Figure 2.6: Schematic of (a) Darmstadt lean premixed stratified burner [Seffrin *et al.*, 2010] and computational domain used in [Fiorina *et al.*, 2015b] (permission for reuse of figure has been granted by Elsevier). (b) Cambridge lifted jet flame experiments [Ahmed & Mastorakos, 2006] and computational domain used in [Chen *et al.*, 2015].

puting these flames. The flame stabilisation at the base of a turbulent lifted flames involves a fine balance among many complex physical processes such as partial premixing between fuel jet and entrained ambient air, flame propagation [Vanquickenborne & van Tiggelen, 1966], interaction between flame leading edge and large-scale flow structure [Broadwell *et al.*, 1984; Miake-Lye & Hammer, 1989; Yoo *et al.*, 2009], edge-flame propagation [Favier & Vervisch, 1998], triple-flames [Mizobuchi *et al.*, 2002; Su *et al.*, 2006; Upatnieks *et al.*, 2004; Watson *et al.*, 2003] and possibly extinction of non-premixed flamelets due to high scalar dissipation rate near the leading edge [Peters & Williams, 1983]. Autoignition [Domingo *et al.*, 2005, 2008; Yoo *et al.*, 2009, 2011] plays an important role when there is a heated co-flow with sufficiently large temperature surrounding the fuel jet. These complexities offer considerable challenge in modelling turbulent lifted flames. These flames without hot co-flow, which is of interest for

the scope of this thesis, have been modelled in the past using various methodologies, such as the G-equation or level-set approach [Chen *et al.*, 2000; Müller *et al.*, 1994; Peters, 2000], flamelet models involving premixed and non-premixed flamelets [Bradley *et al.*, 1990, 1998; Domingo *et al.*, 2002; Ferraris & Wen, 2007; Ma *et al.*, 2002; Michel *et al.*, 2009; Vervisch *et al.*, 2004; Vreman *et al.*, 2008] and Conditional Moment Closure (CMC) [Devaud & Bray, 2003; Kim & Mastorakos, 2005; Navarro-Martinez & Kronenburg, 2011]. These flames have also been computed using large eddy simulation methodology [Domingo *et al.*, 2002; Ferraris & Wen, 2007; Jones & Prasad, 2011; Lacaze *et al.*, 2009b; Leigier *et al.*, 2000; Vervisch & Trouvé, 1998]. More details of these models are described later in §2.3.

Although numerous works have been conducted in the last 30 years, the physical processes responsible for lifted flame stabilisation and their relative importance remain unclear. Our experimental findings are mainly based on measurements obtained using 2D planar imaging techniques with relatively low temporal and spatial resolutions [Lyons, 2007]. Indeed, some important features have been observed using these techniques, such as partially premixed type of edge flame propagation [Buckmaster, 2002] and the effect of large-scale flow structures [Broadwell *et al.*, 1984]. Another important finding which has been observed by different research groups [Kelman *et al.*, 1998; Lyons & Watson, 2000; Tacke *et al.*, 2000] is that the flame stabilisation point appears mostly on the lean side of stoichiometry. The reason for this is arguably the lower local oncoming flow velocity resulting in a higher net flame propagation speed [Su *et al.*, 2006].

However, time-evolving data which would be useful to study the dynamic interaction between these processes is still highly unavailable. One exception is the experimental study by Ahmed & Mastorakos [2006], in which they measured temporal variation of flame most-leading edge from spark ignition to final stabilisation at lift-off height. Different flame evolution stages were identified using 2D line-of-sight images but further investigation is required to understand the flame evolution and stabilisation processes in the 3D space. Moreover, the flame leading edge propagation speed was also calculated by Ahmed & Mastorakos [2006] using the experimental data and empirical estimation of the mean velocity field. It was found that the propagation speed varies significantly in different flame evolution

stages. Again, more precise investigation using modelling approaches is necessary in order to shed more light on this physical problem.

Due to the ubiquitous nature of partial premixing in turbulent combustion applications, it is also necessary to investigate its influences on more complex and close-to-practical flame configurations involving confined geometry, swirling flow, and realistic operating conditions (high pressure, preheating, etc.). As an intermediate setup between simple laboratory jet flames and real-life practical devices, a number of gas turbine model combustors (GTMC) have been established recently to serve for both combustion physics study and numerical model validation [Gicquel *et al.*, 2012; Masri, 2015]. GTMC operating at lean premixed condition [Gregor *et al.*, 2009; Meier *et al.*, 2007] have been a primary focus in recent years, because of its promising features of high fuel efficiency and low NO_x emission[Swaminathan & Bray, 2011]. However, it was pointed out by Meier *et al.* [2007] that imperfect mixing exists inside the combustion chamber of the burner and even results in a particular type of thermo-acoustic instability under certain operational conditions. This is further confirmed in a recent numerical study conducted by Franzelli *et al.* [2012] showing that the self-excited instability phenomenon occurs only when the inhomogeneous mixture is considered.

To further investigate the partially premixing effects, Meier et al. [Meier *et al.*, 2006; Weigand *et al.*, 2006] built a dual-swirler GTMC configuration operating under partially premixed conditions (see Fig. 2.7 for illustration). Three flames, a stable flame designated as flame A and two unstable flames designated as flame B and C, were considered. The stable flame A is of interest here because it was observed to be lifted and stabilised at quite some distance from the fuel injector and involves strong partial premixing at the flame base. Also, there is a comprehensive dataset available for model validation. Due to the complexities involved in this burner, so far there has only been one computational study on this combustor using the Flamelet/Progress Variable (FPV) model [See & Ihme, 2015], which showed fairly good comparisons for mean values of velocity, temperature and major species. However, notable differences were found upstream near the inner swirler where strong partial premixing conditions are expected at the base of the lifted flame. In this region, the mean mixture fraction was substantially over-predicted by the FPV model. Therefore, further modelling investigations

are needed to gain further understanding of partially premixed combustion in GTMC configurations.

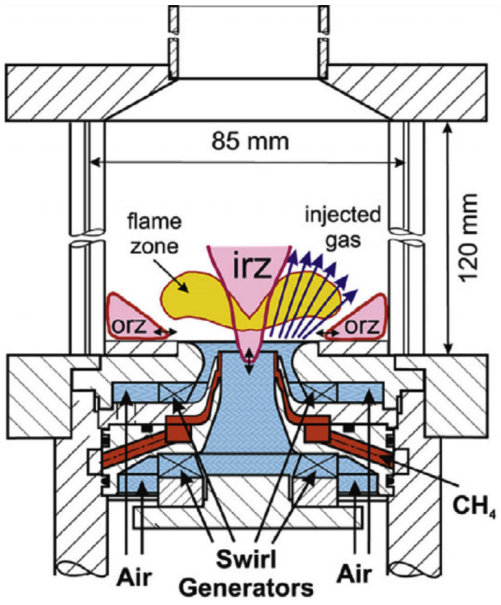

Figure 2.7: Schematic of DLR dual-swirler gas turbine model combustor [Meier *et al.*, 2006] (permission for reuse of figure has been granted by Elsevier).

2.3 Modelling of partially premixed flames

For problems involving turbulent reacting flows, computationally stiff systems are inevitable due to the multi-scale nature of both turbulence and combustion [Poinsot & Veynante, 2005] as noted in §2.2.2. To solve such problems, there are only two options available. We need to either apply some level of averaging to the instantaneous fields, or decrease the size of the computational domain. The former corresponds to RANS and LES (local averaging) approaches, and the latter is known as DNS, which directly solves the instantaneous quantities governed by Eqs. (2.1)-(2.6) and hence does not require turbulence modelling. However, it is computationally too expensive to be used for full-scale flames. In RANS or LES, those equations are averaged or filtered resulting in unclosed terms which need to be modelled. Many avenues to model these terms are proposed and investigated [Peters, 2000; Poinsot & Veynante, 2005; Swaminathan & Bray, 2011].

The existence of inhomogeneous composition in partially premixed flames poses even more challenges on top of this already complex problem [Masri, 2015; Peters, 2000]. A variety of models have been proposed to tackle this problem and these models are reviewed here in this section.

For turbulent combustion modelling in general, most existing models can be categorised into two main types, based on either flamelet or PDF methodology [Pope, 2013]. Applications of these two types of models for partially premixed flames are discussed separately below with a primary emphasis on the flamelet approaches. Exceptions that belong to neither types are the Eddy Dissipation Concept (EDC) [Magnussen & Hjertager, 1977] and Conditional Moment Closure (CMC) [Bilger, 1993; Kronenburg & Mastorakos, 2011]. All these models have been extensively reviewed by Klimenko & Bilger [1999], Peters [2000], Veynante & Vervisch [2002], Poinsot & Veynante [2005], Janicka & Sadiki [2005], Pitsch [2006], Haworth [2010], Echekki & Mastorakos [2010] and Swaminathan & Bray [2011].

2.3.1 Flamelet-type models

As noted in Chapter 1, flamelet-type models decouple the flow and chemistry calculations resulting in a high computational efficiency. These models are mostly based on either the "thin flame sheet" topology or presumed PDF methodology [Pope, 2013].

2.3.1.1 Flame topology methods

This category of flamelet models views the turbulent flame as a continuous surface integrated by laminar flame elements with wrinkling and stretching effects, etc. Various approaches proposed in the past to include these effects are briefly described next.

G-Equation

This modelling approach introduces a non-reacting scalar $G(\boldsymbol{x}, t)$ and the isosurface $G(\boldsymbol{x}, t) = G_0$ represents the flame front surface. It is also often referred to as the *level-set approach*, for which a transport equation for G is solved and a

general form is written as [Peters, 2000; Williams, 1985]:

$$\frac{\partial G}{\partial t} + \boldsymbol{U} \cdot \nabla G = S_G |\nabla G|, \tag{2.25}$$

where the flame burning velocity, S_G, requires a closure model, for which many approaches are proposed as reviewed by Peters [2000] and Poinsot & Veynante [2005] for premixed combustion. Müller *et al.* [1994] and Chen *et al.* [2000] proposed a RANS formulation of S_G for partially premixed combustion accounting for premixed propagation, partial premixing, flamelet quenching and flow straining effects. Their results shows that these effects play different roles as the flame propagates from its ignition location to final stabilisation height in a lifted jet flame.

The level set approach has also been used in LES for a turbulent stratified flame using a coupled G-equation/flamelet progress variable formulation by Trisjono *et al.* [2014]. The coupling is realised through the progress variable source term, which is modelled using the level-set solution when close to the flame surface and the flamelet progress variable method is used for the rest of the domain. It was argued by Knudsen *et al.* [2010] that this combination of approaches is used because the turbulent flame propagation cannot be predicted well by an unresolved progress variable field in LES and thus a level-set approach is required to determine the flame location. Strictly, LES resolves neither the flame front nor brush and thus one needs a due care while analysing LES results.

Flame Surface Density

Flame Surface Density (FSD) models are mathematically similar to the G-equation but employ different closure models [Vervisch & Veynante, 2000]. The concept of FSD was first proposed by Marble & Broadwell [1977] in the Coherent Flame Model for non-premixed flames and then was adopted for premixed flames (see for example in [Darabiha *et al.*, 1987]). The FSD commonly denoted by Σ is defined as the flame surface area per unit volume, which is directly related to the reaction-diffusion balance through a source term in the kinematic transport equation of progress variable [Vervisch *et al.*, 2011]. The exact transport equation for Σ was derived by Pope [1988] and also by Candel & Poinsot [1990] and

a generalised form is written as [Vervisch *et al.*, 2011]

$$\frac{\partial \Sigma_{\text{gen}}}{\partial t} + \nabla \cdot \overline{(\boldsymbol{U})}_s \Sigma_{\text{gen}} = \overline{(\rho S_d)}_s \Sigma_{\text{gen}}, \tag{2.26}$$

where $()_s$ denotes surface-averaging and Σ_{gen} is the generalised FSD [Boger *et al.*, 1998]. The surface-averaged displacement speed, $\overline{(\rho S_d)}_s$, can be approximated as $\overline{(\rho S_d)}_s \approx \rho^u S_L^0$ [Bray & Libby, 1994]. For the closure of Σ_{gen}, both algebraic and transport equation models have been used with both RANS and LES, and these models were compared in detail by Ma *et al.* [2013]. Recently, FSD models have also been applied to stratified flames with an extension in the mixture fraction space [Cavallo Marincola *et al.*, 2013; Fiorina *et al.*, 2015a] showing reasonably good comparisons with the experimental results. In these LES works, a transport equation for the filtered mixture fraction, $\widetilde{Z}$, is solved along with the filtered progress variable, $\widetilde{c}$, transport equation to account for the mixture stratification effects, and the laminar flame speed, $S_L^0 = S_L^0(\widetilde{Z})$, depends on the local mixing conditions. However, the sub-grid turbulent fluctuations of Z and c, and their correlation which can be significant when a relatively large LES grid size is used, are ignored in this modelling approach.

Artificially Thickened Flame

The ATF method is specific of LES and seems quite attractive especially for chemistry modelling as the reaction rate can still be expressed in an Arrhenius form without having to apply any model [Poinsot & Veynante, 2005]. The basic concept is to artificially increase the flame thickness by a factor of F so that it can be resolved by the LES computational grid. This is achieved by multiplying the thermal diffusivity α by F while dividing the Arrhenius pre-exponential constant $\mathcal{A}$ by F and thus one obtains $F\delta \sim \sqrt{(F\alpha)/(\mathcal{A}/F)}$. The laminar flame speed remains unaffected because $S_L^0 \sim \sqrt{(\mathcal{A}/F)(F\alpha)}$. However, the drawback of this approaching is that the turbulence-flame interaction is artificially changed through the decreased Damköhler number as $\text{Da} = (\Lambda S_L^0)/(u'_\Lambda F\delta)$. To address this issue, Colin *et al.* [2000] derived an ATF formulation using an *efficiency function* to compensate the erased sub-grid wrinkling resulting from the decreased Damköhler number. Both static and dynamic procedures have been proposed

[Charlette *et al.*, 2002a,b] to obtain this sub-grid wrinkling factor. Although the ATF approach seems to be "regime-independent" since the chemistry is explicitly solved using the Arrhenius law, it is still quite expensive to use detailed chemistry mechanisms, given that the LES grid size needs to be smaller than but still of the order of flame thickness [Boger *et al.*, 1998; Mukhopadhyay *et al.*, 2014]. Thus, it has been used in conjunction with the tabulated chemistry approach for the Darmstadt stratified burner [Kuenne *et al.*, 2012].

Arguably, recent trend of LES seems to move towards DNS by using increasingly finer grid sizes, which are able to resolve a part or even most of the flame wrinkling, even though it significantly increases the computational cost of these simulations. In such cases, the classical ATF models introduced above are inadequate to recover the laminar flame speed when the flame is fully resolved [Auzillon *et al.*, 2012; Fiorina *et al.*, 2010]. To overcome this, a new modelling strategy called F-TACLES (Filtered Tabulated Chemistry for Large Eddy Simulation) has been proposed by Fiorina *et al.* [2010] for premixed combustion and then extended for stratified mixtures [Auzillon *et al.*, 2012; Fiorina *et al.*, 2015a; Mercier *et al.*, 2015]. In this approach, 1-D laminar premixed flames are explicitly filtered using a typical LES grid size and the SGS wrinkling effects are considered through an SGS winkling factor. The computational results of a lean premixed GTMC [Meier *et al.*, 2007] obtained using this model [Fiorina *et al.*, 2010] were found to agree quite well with measurements compared to the conventional ATF model [Roux *et al.*, 2005]. The F-TACLES model has also been used to compute the partially premixed DLR GTMC burner [Meier *et al.*, 2006; Weigand *et al.*, 2006] and a realistic helicopter engine chamber [Auzillon *et al.*, 2013], however, substantial discrepancies are found for the minor species mass fractions [See & Ihme, 2015]. At a more fundamental level, filtering a laminar flame may be inappropriate physically, because this flame does not have multiple scales and filtering is meaningful for a multi-scale phenomenon.

2.3.1.2 Presumed PDF approaches

In presumed PDF models, though no direct geometrical assumption about the flame front is made as in the above models, the fixed PDF shape and quasi-

laminar assumptions are only valid when a *flamelet-like* structure exists [Pope, 2013]. These models are usually based on a low-dimensional manifold in the composition space, parameterised by few species entries (i.e. mixture fraction, progress variable, etc.), while other species and thermo-chemical quantities are pre-computed and stored in look-up tables. Differing in the elementary laminar flame configuration, various presumed PDF models have been proposed as discussed below.

Flamelet/Progress-Variable

The FPV model was proposed by Pierce & Moin [2004] for LES based on the previous works of steady [Peters, 1984, 2000] and unsteady flamelet models [Pitsch & Steiner, 2000] for non-premixed combustion. A progress variable c was introduced to account for the effects of local extinction and re-ignition in a co-axial jet diffusion flame showing good agreement with the experimental results, which is much improved from using the infinitely fast chemistry hypothesis and steady flamelets. The fluctuation of c was neglected in the original model [Pierce & Moin, 2004] and subsequently considered [Ihme & Pitsch, 2008a,b; Ihme *et al.*, 2005] by solving a transport equation for the sub-grid variance of progress variable, $\widetilde{c''^2_{\text{sgs}}}$. Using the first two moments of mixture fraction and progress variable, an SGS joint PDF is constructed by presuming shapes for the marginal PDFs, which are taken to be statistically independent, and all the thermo-chemical states can be represented by a four-dimensional manifold using Eq. (2.19) written as [Ihme & Pitsch, 2008b]

$$\widetilde{\mathcal{F}}_{\boldsymbol{\varphi}} = \int\int \mathcal{F}_{\boldsymbol{\varphi}}(Z^*, c^*)\ \widetilde{P}(Z^*)\,\widetilde{P}(c^*)\ dZ^*\ dc^*\ , \tag{2.27}$$

where the asterisk * denotes the sample space variable for the marked quantity and $\boldsymbol{\varphi}$ is vector of all thermo-chemical properties, which are calculated through the diffusion flamelet equations. As noted earlier in §2.2.3.1, the steady flamelet equations were derived based on the 1D counter-flow diffusion flame configuration, which is described as a convection-diffusion-reaction process [Peters, 1984]. However, it was argued by Pierce & Moin [2004] that the prescribed velocity profile for the convection terms in this configuration may not hold for turbulent

flows experiencing strong velocity fluctuations. Therefore, they proposed that the flamelet equations can be regarded as pure diffusion-reaction equations by assuming zero convective velocity. Hence, flamelet quantity in Eq. (2.27), $\mathcal{F}_{\boldsymbol{\varphi}}(Z^*, c^*)$, is obtained by solving the diffusion-reaction balance without having to impose an arbitrarily prescribed counter-flow configuration.

The statistical independence between the mixture fraction and progress variable has been shown to be invalid for flame regions when the partial premixing effects are strong as in the lifted flame base area [Chen *et al.*, 2015; Ruan *et al.*, 2012, 2014a]. A higher-moment (more than two) distribution model for the PDF of c conditioned in the Z space was also explored by Ihme & Pitsch [2008a], and the results were compared with the experimental data of the Sandia flames D, E and F [Barlow & Frank, 1998] as well as the distribution given by a β-PDF. However, only a marginal improvement was observed using this *Statistically Most Likely Distribution* (SMLD) approach.

Apart from the Sandia flames, the FPV model has been used for a range of flame configurations including auto-ignition [Ihme & See, 2010], Moderate or Intense Low-oxygen Dilution (MILD) combustion [Ihme *et al.*, 2012; Lamouroux *et al.*, 2014], piloted lean premixed jet burner [Chen & Ihme, 2013], gas turbine model combustor [See & Ihme, 2015] and dimethyl ether jet flame [Popp *et al.*, 2015] with partially premixed conditions. Overall satisfactory results were obtained in these studies compared with the experimental measurements. However, one needs to take due care while treating the scalar dissipation rate of $\widetilde{c''^2_{\rm sgs}}$, denoted as $\widetilde{\chi}_{c,\,\rm sgs}$, which is closely related to many important physical processes such as turbulent scalar mixing, thermal-expansion of reacting flow as well as multi-scale turbulence-chemistry interaction [Swaminathan & Bray, 2011]. In this FPV model [Ihme & Pitsch, 2008a,b], $\widetilde{\chi}_{c,\,\rm sgs}$ is modelled including only the SGS turbulent mixing effects, similar to the scalar dissipation rate modelling for the non-reactive scalar Z. This was found to be inadequate in a recent LES study by Langella & Swaminathan [2016] using *order of magnitude analysis* (OMA) for the terms in the $\widetilde{c''^2_{\rm sgs}}$ transport equation. It was concluded by Langella & Swaminathan [2016] that neglecting the combustion related effects on $\widetilde{\chi}_{c,\,\rm sgs}$ would result in an imbalance among various terms in the $\widetilde{c''^2_{\rm sgs}}$ equation and could lead to significant numerical issues.

Premixed flamelet approaches

As mentioned in §2.2.2, a reduction scheme can be applied to the complex chemistry system by cutting off the *very-fast-reactions* and only take account of the largest scales so that the system can be described by a reduced set of variables. This approach is known as the *intrinsic low dimensional manifold* (ILDM) proposed by Maas & Pope [1992a,b], and it provides very good solution for high temperature regions where the largest scales are dominant. However, prediction in low temperature region (i.e. the preheat zone) is approximated by linear interpolation, which is unable to capture the correct flame behaviour. Following Spalding [1979]'s pioneering turbulent combustion modelling works, another simple approach called the *mixedness/reactedness* model was suggested by Bradley *et al.* [1990, 1998] to combine the well-known 1D premixed laminar flame solutions with a range of equivalence ratios, and the mean reaction rate can be modelled using the formulation of Eq. (2.19) as

$$\overline{\dot{\omega}} = \int_0^1 \int_0^1 \dot{\omega}(\zeta, \xi)\ P(\zeta, \xi)\ d\zeta\ d\xi\ , \tag{2.28}$$

where $\dot{\omega}(\zeta, \xi)$ is the laminar flame burning rate at a given mixture fraction and progress variable. The statistical independence between two marginal β-PDFs was also implied by using $P(\zeta, \xi) = P(\zeta)P(\xi)$ in the work of Bradley *et al.* [1990] showing a good agreement between the simulated and measured flame lift-off heights for a range of jet velocities. Based on this concept, the so-called *flame prolongation of Intrinsic Low-Dimensional Manifolds* (FPI) and *flamelet generated manifold* (FGM) methods, were independently proposed by Gicquel *et al.* [2000] and van Oijen & de Goey [2000] respectively. These methods above are essentially based on the tabulated chemistry concept proposed by Bray [1980] to describe turbulent premixed flames using a lookup chemistry table parameterised by a few control variables.

A number of works have been conducted to apply the FGM and FPI methodology for partially premixed flames. Fiorina *et al.* [2003] performed simulations of a partially premixed laminar Bunsen-type flame using the FPI model integrated

with radiative heat loss. Good predictions of flame stabilisation due to the heat loss at the burner lip were observed using the FPI model. Subsequently, Fiorina *et al.* [2005] carried out a detailed study on the validity of FPI and FGM chemistry tabulations for premixed, partially premixed and diffusion steady laminar counterflow flames, in which they concluded that premixed flamelets failed to capture the diffusive fluxes across the iso-mixture fraction surfaces. As a follow-up work, the *multi-dimensional flamelet-generated manifolds* (MFM) method was proposed by Nguyen *et al.* [2010] to include scalar dissipation rates as one of the control parameters for the chemistry look-up table. Although the MFM approach seems promising when compared with laminar flame results, it involves further complexities of accurately obtaining the scalar dissipation rates for the look-up procedure in turbulent flames.

The *a priori* study by Ramaekers *et al.* [2009] assessed the RANS and LES FGM models based on both premixed and non-premixed flamelets for the partially premixed Sandia flames. It was shown that the non-premixed flamelet based FGM model was more accurate than the premixed based one. This is somewhat expected because the Sandia flames are essentially diffusion type of jet flames. Moreover, the LES results showed clear advancement in predicting the local extinction and re-ignition behaviours in the flame F compared to RANS, whereas the two FGM models seemed to have region-dependant (lean or rich) performances. Similar results were also observed in *a posteriori* LES investigation [Vreman *et al.*, 2008] on the same flame series. Furthermore, modelling of practical devices using the FGM approach was attempted by Bekdemir *et al.* [2011] for a high-pressure diesel engine and by de Souza *et al.* [2011] for a gas turbine combustor respectively. Although the simulation results shown in these studies compared well qualitatively with measurements (mainly pressure traces and high-speed camera images), more thorough modelling approaches and experimental data are still required before these flamelet based models can be confidently used in complex practical devices.

In the state-of-the-art FPI and FGM approaches, the progress variable variance is mostly either neglected or modelled using a simple algebraic model similar to the mixture fraction variance [Pitsch, 2006]. In the cases where a transport equation is solved for the variance of c, the modelling of its scalar dissipation rate

also lacks consistency with the underlying physics [Langella & Swaminathan, 2016] as mentioned previously while discussing the FPV model. These points provide motivation for further development of premixed flamelets approach using presumed PDFs.

2.3.2 Transported PDF models

The PDF method described in this section is fundamentally different from the presumed PDF approaches introduced in the previous sub-section and it is based on solving a transport equation for the joint PDF of a set of variables representing the thermo-chemical state of a reacting flow [Haworth, 2010]. Following the pioneering works of Dopazo & O'Brien [1974a,b], Pope [1985] proposed a Lagrangian-particle based solution for the transported PDF approach using *Monte Carlo* procedures, which has now become a main modelling stream and one of the attractive approaches for turbulent combustion. The multi-species joint PDF obtained by a conserved balance equation seems to provide a complete description for the turbulence-chemistry interaction in any flame configurations without having to invoke modelling assumptions based on the combustion regimes [Haworth, 2010; Poinsot & Veynante, 2005; Pope, 1985].

Starting from Eq. (2.18), if one takes into account all the thermo-chemical state variables, having their sample space variables: $\boldsymbol{\xi} = \xi_1,\ \xi_2,\ ...,\ \xi_N$, any averaged or filtered quantity, $\widetilde{\Phi}$, can be obtained as

$$\widetilde{\Phi} = \int_0^1 \int_0^1 ... \int_0^1 \Phi(\boldsymbol{\xi})\ \widetilde{P}(\boldsymbol{\xi})\ \ d\xi_1\ d\xi_2\ ...\ d\xi_N, \tag{2.29}$$

where the Favre joint composition PDF, $\widetilde{P}$, at any point in the fluid domain, is obtained using its modelled transport equation written as [Dopazo, 1994; Pope,

1985]

$$\overline{\rho}\frac{\partial \widetilde{P}}{\partial t} + \overline{\rho}\,\widetilde{\boldsymbol{U}} \cdot \nabla \widetilde{P} = \underbrace{-\nabla \cdot \left[\overline{\rho}\,\overline{(\boldsymbol{u}''|\boldsymbol{Y}=\boldsymbol{\xi})}\widetilde{P}\right]}_{\text{turbulent diffusion}} \tag{2.30}$$

$$\underbrace{-\overline{\rho}\sum_{i=1}^{N}\frac{\partial}{\partial \xi_i}\left[\overline{\left(\frac{1}{\rho}\nabla\cdot(\rho D\nabla Y_i)\,|\boldsymbol{Y}=\boldsymbol{\xi}\right)}\widetilde{P}\right]}_{\text{molecular mixing}}$$

$$\underbrace{-\overline{\rho}\sum_{i=1}^{N}\frac{\partial}{\partial \xi_i}\left(\frac{1}{\rho}\,\dot{\omega}_i(\boldsymbol{\xi})\widetilde{P}\right)}_{\text{chemical reaction}},$$

where $(\overline{Q|\boldsymbol{Y}=\boldsymbol{\xi}})$ represents a conditional averaging operation for Q over the sample spaces $\boldsymbol{\xi}$. Detailed derivation of this equation can be found in references [Haworth, 2010; Pope, 1985, 2000]. Here it is worthwhile to note that the chemical reaction term appears in a closed form and thus no model is required. However, the molecular mixing term due to the species diffusion is unclosed and its modelling is not straightforward. This is because the PDF only describes the statistics for one point in the physical space, while mixing usually needs length scale information which is not available in the PDF approach [Poinsot & Veynante, 2005].

Although this approach seems very promising since no statistical or geometrical assumptions are imposed for the turbulent flame structure, it is too expensive computationally to be applied for practical burners with detailed chemistry. The additional cost is mainly due to the large number of Lagrangian fluid particles which are solved by ODEs (Ordinary Differential Equations). To address this issue, an alternative approach based on Eulerian stochastic fields has been proposed [Jones & Prasad, 2010; Mustata *et al.*, 2006; Valiño, 1998] and the PDF equation is directly solved on the numerical grid along with the flow calculations resulting in a much improved computational speed. Other implementations of the PDF model include MMC (Multiple Mapping Conditioning)[Ge *et al.*, 2013; Kronenburg & Cleary, 2008; Wandel & Lindstedt, 2013], LEM (Linear Eddy Model) [Kerstein, 1988; Sen & Menon, 2010], Multi-environment approach [Fox,

2003], etc., as extensively reviewed by Pope [1990, 2000], Dopazo [1994] and Haworth [2010], and are not of direct interest within the scope of this thesis.

2.4 Summary

This chapter has briefly reviewed the fundamental theory and the state-of-the-art turbulent combustion modelling approaches and highlighted the importance of studying and modelling turbulent partially premixed flames. Various existing modelling approaches and their applications in both RANS and LES methodologies are reviewed briefly. A primary focus has been given on the flamelet-type models which have shown great potential for practical applications because of their simplicity, low computational cost and reasonably good accuracy. Although these models have been largely used in the literature for a broad range of flame configurations, their capabilities and limitations are yet to be fully understood. Further improvement needs to be made in order to deal with more complex combustion situations such as partially premixed flames envisaged for future generations of gas turbine and automobile engines.

Among the various flamelet based models discussed in this chapter, the presumed PDF approach seems quite attractive since it does not rely on any flame topology assumptions (i.e. thin flame sheet, thickened flame front, etc.). Moreover, the realisation of this approach is rather straightforward because it is only the PDF that needs to be modelled and then all the turbulent quantities can be calculated using laminar flame results and the presumed PDF. However, as noted in §2.3.1.2, quite a few issues are yet to be addressed in the existing presumed PDF models proposed for partially premixed combustion. A significant one is the modelling of the scalar dissipation rate of progress variable, $\widetilde{\chi}_c$. It is shown by Langella [2015] that $\widetilde{\chi}_c$ cannot be modelled simply using a mixing time scale alone as used in the *mixedness/reactedness* [Bradley *et al.*, 1990, 1998], FPV [Ihme & Pitsch, 2008a,b; Ihme *et al.*, 2005], FPI [Fiorina *et al.*, 2005] and FGM [Vreman *et al.*, 2008] models because this term is influenced by many combustion related processes such as thermal expansion and turbulence-chemistry interactions. Another important point is the modelling of the joint PDF. It has been assumed in the past that for all these models, the cross correlation between mixture fraction

and progress variable fluctuations is negligible for partially premixed combustion. However, Ruan *et al.* [2014a] found that this assumption was invalid for a lifted hydrogen flame and the effect of Z-c correlation made a substantial difference for the computed flame lift-off height. Further investigations are required to explore this effect for hydrocarbon flames. As discussed earlier in §2.2.3.3, partially premixed flame behaviour is influenced by many physical processes resulting from both premixed and non-premixed combustion modes and one should account for the effects of these processes while modelling this type of flames. The individual contributions of different combustion modes need to be included in the reaction rate closure model.

In order to address these issues, a revised flamelet methodology following the previous study of Ruan [2012] is introduced in the next chapter along with its implementation in common CFD codes such as Fluent and OpenFOAM. The performance of this model for partially premixed combustion are assessed for different flow and flame configurations in the Chapters 5 to 8.

Chapter 3

Modelling Methodology and Implementation

The modelling approach and numerical methods used for the studies presented in this thesis are described in this chapter. Both the LES and RANS methodologies are discussed along with the relevant turbulence and combustion models, followed by their corresponding implementation and coupling algorithms with the CFD solver. The Finite Volume Method (FVM) discretisation technique is also briefly introduced as well as the numerical schemes used for the present studies.

3.1 Balance equations

As noted at the beginning of §2.3, the exact form of the instantaneous governing equations, Eqs. (2.1)-(2.6), cannot be directly solved for laboratory and practical flames due to a very large range of time and length scales related to flow and chemical phenomena involved. Thus, these equations are averaged in RANS methodology to obtain the mean quantities, and filtered in LES to compute the resolved quantities. These procedures and the resulting averaged or filtered equations are respectively described in two separate sub-sections for RANS and LES frameworks as follows.

3.1.1 RANS framework

As combusting flows experience significant density change across the flame region, Favre averaging defined in Eq. (2.12) is usually preferred and the instantaneous quantity Q is decomposed as

$$Q = \widetilde{Q} + Q'' \quad \text{and} \quad \widetilde{Q''} = 0. \tag{3.1}$$

Applying this formulation to Eqs. (2.1), (2.2) and (2.6), one obtains the Favre-averaged mass, momentum and enthalpy conservation equations written as

$$\frac{\partial \overline{\rho}}{\partial t} + \nabla \cdot \left(\overline{\rho}\, \widetilde{\boldsymbol{U}} \right) = 0, \tag{3.2}$$

$$\frac{\partial \overline{\rho}\, \widetilde{\boldsymbol{U}}}{\partial t} + \nabla \cdot (\overline{\rho}\, \widetilde{\boldsymbol{U}} \widetilde{\boldsymbol{U}}) = -\nabla \overline{p} + \nabla \cdot \left(\overline{\boldsymbol{\tau}} - \overline{\rho}\, \widetilde{\boldsymbol{u}'' \boldsymbol{u}''} \right), \tag{3.3}$$

$$\frac{\partial \overline{\rho}\, \widetilde{h}}{\partial t} + \nabla \cdot (\overline{\rho}\, \widetilde{\boldsymbol{U}} \widetilde{h}) = \nabla \cdot \left(\overline{\rho D \nabla h} - \overline{\rho}\, \widetilde{\boldsymbol{u}'' h} \right), \tag{3.4}$$

assuming unity Lewis number for all species. The laminar diffusive enthalpy flux is usually approximated as $\overline{\rho D \nabla h} \approx \overline{\rho} \widetilde{D} \nabla \widetilde{h}$ and the turbulent enthalpy flux is generally closed using a gradient transport hypothesis:

$$\overline{\rho}\, \widetilde{\boldsymbol{u}'' h''} = -\frac{\mu_t}{\mathrm{Sc}_t} \nabla \widetilde{h} \tag{3.5}$$

where μ_t is the turbulent (or eddy) viscosity obtained from a chosen turbulence model, and Sc_t is the turbulent Schmidt number which is usually estimated as a constant value of 0.7 for RANS simulations [Poinsot & Veynante, 2005]. This hypothesis has also been shown incorrect for some premixed flames, especially when the fluctuation of turbulent velocity is of the order of the laminar flame speed, in which a counter-gradient transport of the scalar flux was observed [Bray *et al.*, 1981].

The Reynolds stresses term, $\widetilde{\boldsymbol{u}'' \boldsymbol{u}''}$, in Eq. (3.4) is unclosed and various turbulence models including the Prandtl mixing length, one-equation, two equation k-ω, and Reynolds stresses models, have been proposed in the literature as exten-

sively reviewed in [Pope, 2000; Wilcox, 2006]. The most widely used choice for the turbulent Reynolds stresses is the Boussinesq approximation written as [Poinsot & Veynante, 2005]

$$\overline{\rho}\,\widetilde{\boldsymbol{u}''\boldsymbol{u}''} - \frac{2}{3}\overline{\rho}\,\widetilde{k}\,\mathbf{I} = -\mu_t\left[\nabla\widetilde{\boldsymbol{U}} + (\nabla\widetilde{\boldsymbol{U}})^{\mathcal{T}} - \frac{2}{3}\mathbf{I}\cdot\nabla\widetilde{\boldsymbol{U}}\right], \tag{3.6}$$

where the turbulent kinetic energy is defined as

$$\widetilde{k} = \frac{1}{2}\,\widetilde{\boldsymbol{u}''\cdot\boldsymbol{u}''} \tag{3.7}$$

and the second term is rearranged to the LHS because it is usually embedded with the pressure for simplicity as a common practice (see [Pope, 2000] for more detail). Now the only remaining unclosed term is the turbulent viscosity μ_t, for which the widely used two-equation k-ε model proposed by Jones & Launder [1972] provides a closure:

$$\mu_t = \overline{\rho}\,C_\mu\frac{\widetilde{k}^2}{\widetilde{\varepsilon}}, \tag{3.8}$$

where $\widetilde{k}$ and its dissipation rate $\widetilde{\varepsilon}$ are obtained through their transport equations [Jones & Launder, 1972]

$$\frac{\partial\overline{\rho}\,\widetilde{k}}{\partial t} + \nabla\cdot(\overline{\rho}\,\widetilde{\boldsymbol{U}}\widetilde{k}) = \nabla\cdot\left[\left(\mu + \frac{\mu_t}{\sigma_k}\right)\nabla\widetilde{k}\right] + P_k - \overline{\rho}\widetilde{\varepsilon}, \tag{3.9}$$

$$\frac{\partial\overline{\rho}\,\widetilde{\varepsilon}}{\partial t} + \nabla\cdot(\overline{\rho}\,\widetilde{\boldsymbol{U}}\,\widetilde{\varepsilon}) = \nabla\cdot\left[\left(\mu + \frac{\mu_t}{\sigma_\varepsilon}\right)\nabla\widetilde{k}\right] + C_{\varepsilon 1}\frac{\widetilde{\varepsilon}}{\widetilde{k}}P_k - C_{\varepsilon 2}\overline{\rho}\frac{\widetilde{\varepsilon}^2}{\widetilde{k}}, \tag{3.10}$$

where the production term is modelled as [Swaminathan & Bray, 2011]

$$P_k = -\left(\overline{\rho}\,\widetilde{\boldsymbol{u}''\boldsymbol{u}''} : \nabla\widetilde{\boldsymbol{U}}\right) - \overline{\boldsymbol{u}''}\cdot\nabla\overline{p} + \overline{p'\nabla\cdot\boldsymbol{u}''}, \tag{3.11}$$

where the first term signifying the turbulent production is modelled using the Boussinesq approximation described in Eq. (3.6). The other two terms in Eq. (3.11) are the pressure dilatation terms, which are expected to be small for open flames. A common set of model constants for Eqs. (3.9) and (3.10) are [Poinsot & Vey-

nante, 2005]

$$C_\mu = 0.09\ , \quad C_{\varepsilon 1} = 1.44\ , \quad C_{\varepsilon 2} = 1.92\ , \quad \sigma_k = 1.0\ , \quad \sigma_\varepsilon = 1.3\ , \tag{3.12}$$

which have been validated for a wide range of flow configurations. However, modification of these constants is often required especially for compressible flows in order to accurately predict the flow field for a specific problem.

Apart from the conserved quantities described in Eqs. (3.2)-(3.4), two additional quantities, the mixture fraction Z and progress variable c, need to be considered to account for the fuel/oxidiser mixing and chemical reactions progress in partially premixed flames. Bilger's definition [Bilger *et al.*, 1990] of mixture fraction given in Eq. (2.21) is adopted for the methane/air flames studied in this work. As for the definition of progress variable, the sum of CO and CO_2 mass fractions is used as

$$c = \frac{\psi}{\psi^{\mathrm{Eq}}(Z)} \quad \text{with} \quad \psi = Y_{\mathrm{CO}} + Y_{\mathrm{CO2}}, \tag{3.13}$$

where $\psi^{\mathrm{Eq}}(Z)$ is the chemical equilibrium value of ψ for the local mixture fraction, Z, so that c is bounded between 0 and 1. This definition is chosen because it allows a unique mapping of flamelet quantities based on the normalised progress variable [Fiorina *et al.*, 2003, 2015b], which helps to clearly identify contribution of premixed and non-premixed modes to the mean reaction rate in partially premixed combustion as one shall see in §3.2.

The modelling approach previously developed for partially premixed combustion [Darbyshire & Swaminathan, 2012; Ruan *et al.*, 2014a] is followed here. The Favre-averaged transport equations for the first two moments of mixture fraction, $\widetilde{Z}$ and $\widetilde{Z''^2}$, and a reaction progress variable, $\widetilde{c}$ and $\widetilde{c''^2}$, are solved in addition to the previously discussed conservation equations. These four equations help us to characterise the scalar mixing and reaction progress at every point in the flow and they are written as

$$\frac{\partial \overline{\rho}\widetilde{Z}}{\partial t} + \nabla \cdot (\overline{\rho}\,\widetilde{\boldsymbol{U}}\,\widetilde{Z}) = \nabla \cdot \left(\overline{\rho D \nabla Z} \ - \ \overline{\rho \boldsymbol{u}'' Z''} \right), \tag{3.14}$$

$$\frac{\partial \overline{\rho}\widetilde{Z''^2}}{\partial t} + \nabla\cdot(\overline{\rho}\,\widetilde{\boldsymbol{U}}\widetilde{Z''^2}) = \nabla\cdot\left(\overline{\rho D\nabla Z''^2} - \overline{\rho \boldsymbol{u}'' Z''^2}\right) - 2\,\overline{\rho}\,\widetilde{\chi}_Z - 2\,\overline{\rho \boldsymbol{u}'' Z''}\cdot\nabla\widetilde{Z}, \tag{3.15}$$

$$\frac{\partial \overline{\rho}\,\widetilde{c}}{\partial t} + \nabla\cdot(\overline{\rho}\,\widetilde{\boldsymbol{U}}\widetilde{c}) = \nabla\cdot\left(\overline{\rho D\nabla c} - \overline{\rho \boldsymbol{u}'' c''}\right) + \overline{\dot{\omega}_c^*}, \tag{3.16}$$

$$\frac{\partial \overline{\rho}\widetilde{c''^2}}{\partial t} + \nabla\cdot(\overline{\rho}\,\widetilde{\boldsymbol{U}}\widetilde{c''^2}) = \nabla\cdot\left(\overline{\rho D\nabla c''^2} - \overline{\rho \boldsymbol{u}'' c''^2}\right) - 2\,\overline{\rho}\,\widetilde{\chi}_c - 2\,\overline{\rho \boldsymbol{u}'' c''}\cdot\nabla\widetilde{c} + 2\,\overline{c''\dot{\omega}_c^{*\prime\prime}}. \tag{3.17}$$

In order to account for the mutual influence between Z and c, the cross correlation (or covariance), $\widetilde{Z''c''}$, needs to be considered. Ribert *et al.* [2004] suggested a simple estimation: $\widetilde{Z''c''} \approx \sqrt{\widetilde{Z''^2}}\sqrt{\widetilde{c''^2}}$, which essentially implies that $\widetilde{Z''c''}$ holds the same sign across the flame. Robin *et al.* [2006] then noted that this may not always be the case especially for partially premixed flames involving different burning modes [Ruan *et al.*, 2012], and a transport equation is required for the covariance, which is written as

$$\frac{\partial \overline{\rho}\,\widetilde{Z''c''}}{\partial t} + \nabla\cdot(\overline{\rho}\,\widetilde{\boldsymbol{U}}\widetilde{Z''c''}) = \nabla\cdot\left(\overline{\rho D\nabla Z''c''} - \overline{\rho \boldsymbol{u}'' Z''c''}\right) - 2\,\overline{\rho}\,\widetilde{\chi}_{Zc} - 2\,\overline{\rho \boldsymbol{u}'' c''}\cdot\nabla\widetilde{Z} + \overline{\rho \boldsymbol{u}'' Z''}\cdot\nabla\widetilde{c} + 2\,\overline{Z''\dot{\omega}_c^{*\prime\prime}}, \tag{3.18}$$

where the turbulent scalar fluxes along with those in Eqs. (3.14)-(3.17) are modelled using the gradient assumption in a similar manner as described earlier in Eq. (3.5). The symbols $\widetilde{\chi}_Z$ and $\widetilde{\chi}_{Zc}$ in Eqs. (3.15) and (3.18) are respectively the Favre-averaged scalar dissipation rate of the mixture fraction fluctuations and cross dissipation rate. Following earlier studies [Darbyshire & Swaminathan, 2012; Ruan *et al.*, 2014a], these two dissipation rates are modelled as

$$\overline{\rho}\,\widetilde{\chi}_Z \equiv \overline{\rho D\left(\nabla Z''\cdot\nabla Z''\right)} \simeq C_d\,\overline{\rho}\left(\frac{\widetilde{\varepsilon}}{\widetilde{k}}\right)\widetilde{Z''^2}, \tag{3.19}$$

$$\overline{\rho}\,\widetilde{\chi}_{Zc} \equiv \overline{\rho D\left(\nabla Z''\cdot\nabla c''\right)} \simeq C_{cd}\,\overline{\rho}\left(\frac{\widetilde{\varepsilon}}{\widetilde{k}}\right)\widetilde{Z''c''}, \tag{3.20}$$

where the coefficients C_d and C_{cd} denote ratios of scalar to turbulence time scales and both of them are taken to be 1.0 for the studies presented in this thesis [Peters, 2000; Ruan *et al.*, 2012, 2014a].

These simple algebraic models were shown to be inadequate [Mantel & Bilger, 1995; Swaminathan & Bray, 2005] for the scalar dissipation rate of progress variable, $\widetilde{\chi}_c$. Many alternative models are proposed recently to overcome this and these are summarised in [Chakraborty *et al.*, 2011]. For this study, the model proposed by Kolla *et al.* [2009] for premixed combustion subsequently modified [Darbyshire *et al.*, 2010] to include mixture fraction stratification effects is used because of its simplicity and robustness. This model is written as

$$\overline{\rho}\,\widetilde{\chi}_c \equiv \overline{\rho D\left(\nabla c'' \cdot \nabla c''\right)} \simeq \frac{\overline{\rho}}{\beta'}\left(\left[2K_c^* - \tau\, C_4\right]\frac{S_L^0}{\delta_L^0} + C_3\frac{\widetilde{\varepsilon}}{\widetilde{k}}\right)\widetilde{c''^2}, \tag{3.21}$$

where $\beta' = 6.7$, $C_3 = 1.5\sqrt{\mathrm{Ka}}/(1+\sqrt{\mathrm{Ka}})$ and $C_4 = 1.1/(1+\mathrm{Ka})^{0.4}$ are model parameters. The Karlovitz number is defined as $\mathrm{Ka} = (\delta/S_L^0)\,/\sqrt{\nu/\widetilde{\varepsilon}}$, where ν is the local kinematic viscosity. The Zeldovich thickness, δ, heat release parameter, $\tau = (T^b - T^u)/T^u$, S_L^0 and δ_L^0 depend on the local mixture fraction value and these are obtained from unstrained planar laminar premixed flame calculation. The model parameter K_c^* is also obtained from the laminar flame calculation [Kolla *et al.*, 2009] and this parameter varies with Z for partially premixed flames .

The remaining unclosed terms in Eqs. (3.14)-(3.18) are the reaction rate related source terms. In RANS simulations, these terms cannot be obtained simply using the mean quantities since they are closely related to the two-way non-linear interaction between turbulence and chemistry involving effects from much smaller scales than the mean scales. Modelling these highly non-linear source terms has been a major challenge and it still remains as a vital part in turbulent combustion research. Detailed description of the reaction rate modelling approaches used for this thesis work is presented later in §3.2.

3.1.2 LES framework

In Large Eddy Simulation, the large scale dynamic fluid motions are directly solved. Their governing equations are obtained by low-pass filtering the instan-

taneous governing equations given in §2.1. For a given quantity $Q(\boldsymbol{x};t)$, the Favre-filtering procedure is described as [Poinsot & Veynante, 2005]

$$\widetilde{Q} = \frac{1}{\overline{\rho}} \int\int\int \rho\, Q(\boldsymbol{x}';t)\, \mathscr{G}(\boldsymbol{x}-\boldsymbol{x}';\Delta)\, d\boldsymbol{x}', \tag{3.22}$$

where $\mathscr{G}(\boldsymbol{x}-\boldsymbol{x}';\Delta)$ is the filter function with Δ being the filter width and $\boldsymbol{x}'$ the local spatial coordinate with respect to the filter centre. By definition, the integral of $\mathscr{G}$ over the entire domain is equal to unity: $\int_{-\infty}^{+\infty} \mathscr{G}(\boldsymbol{x}-\boldsymbol{x}';\Delta)\, d\boldsymbol{x}' = 1$. The value of $\mathscr{G}$ also depends on the filter type, for which a Gaussian shape is usually applied [Pope, 2000]:

$$\mathscr{G}(\boldsymbol{x}) = \left(\frac{6}{\pi\Delta^2}\right)^{1/2} \exp\left(-\frac{6\boldsymbol{x}^2}{\Delta^2}\right). \tag{3.23}$$

Note that the value of $\mathscr{G}$ decreases rapidly outside $\pm(\Delta/2)$ [Pope, 2000] so that $\int_{-\Delta/2}^{+\Delta/2} \mathscr{G}(\boldsymbol{x}-\boldsymbol{x}';\Delta)\, d\boldsymbol{x}' \approx 1$, suggesting a weighted local average within one filter width. The resulting quantity after filtering has two parts, namely the resolved and SGS components: $Q = \widetilde{Q} + Q''$. Although it is written in the same form as the RANS decomposition described in Eq. (3.1) for the sake of simplicity, the underlying implications are fundamentally different. Therefore, it is worthwhile to note here that:

- the residual part Q'' represents the sub-grid scale fluid motions that cannot be resolved by the filtered equations solved on the LES grid, and its typical size is several orders of magnitude larger than the Kolmogorov or diffusive scales;
- contrary to RANS, the SGS motions do not vanish after being filtered, and single-filtered and double-filtered values are not the same, i.e. $\widetilde{Q''} \neq 0$ and $\widetilde{\widetilde{Q}} \neq \widetilde{Q}$;
- the LES filtering operation is usually not explicitly conducted using Eq. 3.22 since no information of $Q(\boldsymbol{x};t)$ is available (except in *a priori* studies using DNS data), and instead filtered balance equations are solved with models for SGS quantities.

- particular care needs to be taken when comparing LES results with the experimental measurements. The former only represent the large-scale information, whereas the latter usually contain effects of all the scales when high-resolution diagnostic techniques are employed. The meaningful approach is to compute the time-averaged LES statistics and compare them with measured statistics [Haworth, 2010; Poinsot & Veynante, 2005].

Bearing these points in mind, one can easily obtain the filtered balance equations for mass, momentum and enthalpy conservations formally, similar to RANS Eqs. (3.2)-(3.4). These LES equations are written as follows:

$$\frac{\partial \overline{\rho}}{\partial t} + \nabla \cdot \left(\overline{\rho}\, \widetilde{\boldsymbol{U}} \right) = 0, \tag{3.24}$$

$$\frac{\partial \overline{\rho}\, \widetilde{\boldsymbol{U}}}{\partial t} + \nabla \cdot (\overline{\rho}\, \widetilde{\boldsymbol{U}} \widetilde{\boldsymbol{U}}) = -\nabla \overline{p} + \nabla \cdot \left[\overline{\boldsymbol{\tau}} - \overline{\rho} \left(\widetilde{\boldsymbol{U}\boldsymbol{U}} - \widetilde{\boldsymbol{U}} \widetilde{\boldsymbol{U}} \right) \right], \tag{3.25}$$

$$\frac{\partial \overline{\rho} \widetilde{h}}{\partial t} + \nabla \cdot (\overline{\rho}\, \widetilde{\boldsymbol{U}} \widetilde{h}) = \nabla \cdot \left[\overline{\rho D \nabla h} - \overline{\rho} \left(\widetilde{\boldsymbol{U} h} - \widetilde{\boldsymbol{U}} \widetilde{h} \right) \right], \tag{3.26}$$

where the unresolved (or residual) stresses $\overline{\rho} \left(\widetilde{\boldsymbol{U}\boldsymbol{U}} - \widetilde{\boldsymbol{U}} \widetilde{\boldsymbol{U}} \right)$ and enthalpy flux $\left(\widetilde{\boldsymbol{U} h} - \widetilde{\boldsymbol{U}} \widetilde{h} \right)$ are commonly modelled in a similar manner as for RANS through a turbulent viscosity hypothesis but at the sub-grid scale level denoted by μ_{sgs}. A turbulent Schmidt number of $\text{Sc}_t = 0.4$ [Pitsch & Steiner, 2000] is used for LES of methane flames. Accordingly, Eq. (3.6) can be rewritten for LES as

$$\overline{\rho} \left(\widetilde{\boldsymbol{U}\boldsymbol{U}} - \widetilde{\boldsymbol{U}} \widetilde{\boldsymbol{U}} \right) - \frac{2}{3} \overline{\rho}\, \widetilde{k}_{\text{sgs}}\, \mathbf{I} = -\mu_{\text{sgs}} \left[\nabla \widetilde{\boldsymbol{U}} + (\nabla \widetilde{\boldsymbol{U}})^{\mathcal{T}} - \frac{2}{3} \mathbf{I} \cdot \nabla \widetilde{\boldsymbol{U}} \right], \tag{3.27}$$

where the SGS kinetic energy on the LHS is expressed as

$$\widetilde{k}_{\text{sgs}} \equiv \underbrace{\frac{1}{2} \widetilde{\boldsymbol{U} \cdot \boldsymbol{U}}}_{\text{total}} - \underbrace{\frac{1}{2} \widetilde{\boldsymbol{U}} \cdot \widetilde{\boldsymbol{U}}}_{\text{resolved}}, \tag{3.28}$$

which is not modelled through SGS models but absorbed into the filtered pressure as noted earlier in §3.1.1. The RHS of Eq. (3.27) corresponds to the unresolved shear stresses appearing as the *off-diagonal* part of the stress tensor, which is

modelled using the filtered rate-of-strain defined as

$$\widetilde{\boldsymbol{S}} \equiv \frac{1}{2}\left[\nabla\widetilde{\boldsymbol{U}} + (\nabla\widetilde{\boldsymbol{U}})^{\mathcal{T}}\right]. \tag{3.29}$$

Thus, the implication behind this modelling approach is that the anisotropic residual stress tensor is aligned with $\widetilde{\boldsymbol{S}}$, which has been shown to be inaccurate [Meneveau & Katz, 2000] resulting in over-predicted residual stresses for SGS eddy-viscosity-based models. As a consequence, these models are overly dissipative in general. More advanced SGS stress models have also been proposed but mainly for incompressible flows as reviewed in [Ferziger & Perić, 1999; Pope, 2000]. Nevertheless, eddy-viscosity models are still the most widely used approach especially for turbulent reacting flows because they have the simplicity of using the already available filtered quantities from LES and meanwhile provide reasonable accuracy.

Among these models, the classical Smagorinsky model [Smagorinsky, 1963] and its invariants with dynamic procedures remain as a popular choice for SGS stress modelling. This model describes the eddy viscosity as

$$\mu_{\text{sgs}} = \overline{\rho}\,(C_{\text{S}}\Delta)^2|\widetilde{\boldsymbol{S}}|, \tag{3.30}$$

where $|\widetilde{\boldsymbol{S}}|$ is the characteristic filtered rate-of-strain defined as $|\widetilde{\boldsymbol{S}}| \equiv (2\widetilde{\boldsymbol{S}} : \widetilde{\boldsymbol{S}})^{1/2}$, and the common model constant is $C_{\text{S}} = 0.167$ [Pope, 2000]. This constant was found to depend on the local flow condition and thus a dynamic model was proposed first by Germano *et al.* [1991] for constant-density flows, which determines C_{S} using the accessible knowledge of local large eddy motions. This approach was then adopted by Moin *et al.* [1991] for variable-density flows and modified by Lilly [1992] using a localised formulation for an improved computational applicability. For the sake of simplicity, the static constant model is used for the LES studies in this thesis.

By analogy to Eqs. (3.24)-(3.26), the filtered scalar transport equations for reacting flows can be readily obtained as

$$\frac{\partial\overline{\rho}\widetilde{Z}}{\partial t} + \nabla\cdot\left(\overline{\rho}\widetilde{\boldsymbol{U}}\widetilde{Z}\right) = \nabla\cdot\left[\,\overline{\rho D\nabla Z} \;-\; \overline{\rho}\left(\widetilde{\boldsymbol{U}Z} - \widetilde{\boldsymbol{U}}\widetilde{Z}\right)\right], \tag{3.31}$$

$$\frac{\partial \overline{\rho}\widetilde{Z''^2_{\rm sgs}}}{\partial t} + \nabla\cdot\left(\overline{\rho}\,\widetilde{\boldsymbol{U}}\,\widetilde{Z''^2_{\rm sgs}}\right) \approx \nabla\cdot\left[\,\overline{\rho D\nabla Z''^2_{\rm sgs}} \;-\; \overline{\rho}\left(\widetilde{\boldsymbol{U}Z''^2_{\rm sgs}} - \widetilde{\boldsymbol{U}}\,\widetilde{Z''^2_{\rm sgs}}\right)\right] - 2\,\overline{\rho}\,\widetilde{\chi}_{Z,\,\rm sgs} - 2\,\frac{\mu_{\rm sgs}}{{\rm Sc}_t}\left(\nabla\widetilde{Z}\cdot\nabla\widetilde{Z}\right), \tag{3.32}$$

$$\frac{\partial \overline{\rho}\,\widetilde{c}}{\partial t} + \nabla\cdot\left(\overline{\rho}\,\widetilde{\boldsymbol{U}}\,\widetilde{c}\right) = \nabla\cdot\left[\,\overline{\rho D\nabla c} \;-\; \overline{\rho}\left(\widetilde{\boldsymbol{U}c} - \widetilde{\boldsymbol{U}}\widetilde{c}\right)\right] + \overline{\dot{\omega}^*_c}, \tag{3.33}$$

and

$$\frac{\partial \overline{\rho}\,\widetilde{c''^2_{\rm sgs}}}{\partial t} + \nabla\cdot\left(\overline{\rho}\,\widetilde{\boldsymbol{U}}\,\widetilde{c''^2_{\rm sgs}}\right) \approx \nabla\cdot\left[\,\overline{\rho D\nabla c''^2_{\rm sgs}} - \overline{\rho}\left(\widetilde{\boldsymbol{U}c''^2_{\rm sgs}} \;-\; \widetilde{\boldsymbol{U}}\,\widetilde{c''^2_{\rm sgs}}\right)\right] - 2\,\overline{\rho}\,\widetilde{\chi}_{c,\,\rm sgs} - 2\,\frac{\mu_{\rm sgs}}{{\rm Sc}_t}\left(\nabla\widetilde{c}\cdot\nabla\widetilde{c}\right), +2\left(\,\overline{c\,\dot{\omega}^*_c} - \widetilde{c}\,\overline{\dot{\omega}^*_c}\,\right), \tag{3.34}$$

where $\widetilde{Z''^2_{\rm sgs}}$ and $\widetilde{c''^2_{\rm sgs}}$ are the sub-grid scale variances signifying the local fluctuations within the LES grid for mixture fraction and progress variable respectively. These LES variances are to be distinguished with the RANS variances computed in Eqs. (3.15) and (3.17), which represent the total variance of the time or ensemble averaged samples. To relate the SGS variance to total, or RANS, variance, the resolved variance needs to be included, for example:

$$\langle Z''^2\rangle_{\rm total} \equiv \langle Z^2\rangle - \langle Z\rangle^2 = \underbrace{\langle\widetilde{Z}^2\rangle - \langle\widetilde{Z}\rangle^2}_{\rm resolved} + \underbrace{\langle\widetilde{Z''^2_{\rm sgs}}\rangle}_{\rm sub-grid}. \tag{3.35}$$

Since the physical meaning of the SGS variance differs fundamentally from its RANS counterpart, modelling of the scalar dissipation rate terms in Eqs. (3.32) and (3.34) requires different treatment to capture the sub-grid scale molecular mixing between not only the fuel and oxidiser but also the fresh and burnt gases. For the mixture fraction, as an inert mixing quantity, its SGS dissipation rate, can be modelled as in Eq. (3.19) using a SGS mixing time scale as used commonly [Pitsch, 2006]:

$$\widetilde{\chi}_{Z,\,\rm sgs} = C_Z\,\frac{\nu_{\rm sgs}}{\Delta^2}\,\widetilde{Z''^2_{\rm sgs}} \tag{3.36}$$

where $\nu_{\rm sgs} = \mu_{\rm sgs}/\overline{\rho}$ is the sub-grid kinematic turbulent viscosity obtained using the Smagorinsky model and the model coefficient $C_Z = 2.0$ [Ihme & Pitsch, 2008b;

Pitsch, 2006] is used for this work. However, for the progress variable which is a reactive scalar, the SGS variance is more significant than the resolved part because chemical reactions are mostly unresolved SGS phenomena when the grid size is coarse compared to the flame thickness. Thus, the SGS dissipation rate, $\widetilde{\chi}_{c,\,\mathrm{sgs}}$, plays an important role in turbulent flame burning process and cannot be simply modelled using mixing scale based approaches [Swaminathan & Bray, 2005]. To account for other influential effects such as dilatation, reaction and turbulence-flame interaction, Dunstan *et al.* [2013] proposed an algebraic model originally for premixed combustion and it is modified to include the effects of partial premixing for this work. This modified model is written as

$$\widetilde{\chi}_{c,\,\mathrm{sgs}} = \mathscr{F}\left[2K_c^*\frac{S_L^0}{\delta_L^0} + (C_3 - \tau C_4 \mathrm{Da}_\Delta)\left(\frac{2u'_\Delta}{3\Delta}\right)\right]\frac{\widetilde{c''^2}}{\beta'_c}. \tag{3.37}$$

This model has a similar form as Eq. (3.21), however, several points need to be noted in the context of LES:

- function $\mathscr{F} = 1 - \exp(-0.75\Delta/\delta_L^0)$ is introduced to ensure the model realisability that $\widetilde{\chi}_{c,\,\mathrm{sgs}}$ approaches 0 when Δ/δ_L^0 is small corresponding to a fully resolved flame.

- the characteristic SGS velocity scale u'_Δ is modelled using a scale-similarity assumption [Pope, 2000]: $u'_\Delta = |\,\widehat{\widetilde{\boldsymbol{U}}} - \widetilde{\boldsymbol{U}}\,|$ with a test filter width of $\widehat{\Delta} = 2\Delta$, which has been validated in previous studies [Langella, 2015; Langella & Swaminathan, 2016; Langella *et al.*, 2015] for various flame configurations.

- the model parameters C_3 and C_4 remain in their previously defined form (see §3.1.1), whereas the non-dimensional numbers are redefined at the SGS level. The SGS Damköhler number is given by $\mathrm{Da}_\Delta = (S_L^0\Delta)/(u'_\Delta\delta_L^0)$ and the SGS Karlovitz number is defined as $\mathrm{Ka}_\Delta = (u'_\Delta/S_L^0)^{3/2}(\Delta/\delta_L^0)^{-1/2}$.

- β'_c is the only tuneable model parameter, which is closely related to the strong interaction among spatial gradient of reaction rate, flamelet curvature as well as spatial variation of molecular diffusivity. To investigate the effects of this parameter in LES, Langella *et al.* [2015] conducted a parametric study and proposed an optimum value of $\beta'_c = 7.5$, for methane

combustion. A dynamic procedure was also proposed to determine the β_c' value depending on the local flame and flow conditions. In this thesis, only the static model is used for simplicity.

In LES, the cross correlation between mixture fraction and progress variable exists in sub-grid scales. Differing from $\widetilde{Z''c''}$ in RANS, this SGS correlation denoted here by $\widetilde{(Z''c'')}_{\text{sgs}}$ not only stems from the flame-flow interaction, but also is strongly influenced by the level to which the flow and flame are resolved by the LES grid. According to Pope's criterion [Pope, 2000], more than 80% of the kinetic energy should be resolved by the LES grid to obtain a good accuracy and this criterion yields

$$\mathcal{F}_K \equiv \frac{\langle K \rangle}{\langle K \rangle + \langle k_{\text{sgs}} \rangle} \geqslant 0.8, \tag{3.38}$$

where $\langle K \rangle$ and $\langle k_{\text{sgs}} \rangle$ are the resolved and average sub-grid scale kinetic energy respectively. The instantaneous SGS kinetic energy, k_{sgs}, is modelled through a relation with the SGS turbulent viscosity described in Eq. (3.30). If the criterion in Eq. (3.38) is satisfied, it is also expected to hold for the resolved mixture fraction field with the turbulent Schmidt number of an order of unity: $\text{Sc}_t \sim \mathcal{O}(1)$, which is so for methane combustion [Pitsch, 2006; Pitsch & Steiner, 2000]. In light of this assumption, the sub-grid part in Eq. (3.35) is much smaller than the resolved fluctuations. Consequently, the sub-grid cross correlation, $\widetilde{(Z''c'')}_{\text{sgs}}$, signifying the mutual influence between the SGS fluctuations of Z and c should have only marginal effects on the flame behaviour, especially for steadily burning flames. Moreover, modelling $\widetilde{(Z''c'')}_{\text{sgs}}$ is not straightforward for LES since it involves the complex interaction of Z and c fluctuations in different scales depending on the local LES filter size and flame thickness. Detailed analysis of the underlying physics using experimental or DNS data is required to examine the importance of $\widetilde{(Z''c'')}_{\text{sgs}}$ and to propose suitable modelling strategies. Therefore in this thesis work, it is postulated that the SGS cross correlation and its effect on combustion are negligible and so a statistical independence between SGS fluctuations of Z and c may be assumed for the sub-grid combustion modelling described next.

3.2 Reaction rate closure

The chemical reaction source terms appearing as the last term on the RHS of Eqs. (3.16)-(3.18) for RANS and Eqs. (3.33)-(3.34) for LES, require closure models to account for the mean and filtered reaction rate effects respectively. Although these terms have different physical interpretation for RANS and LES methodologies, a similar modelling approach can be applied using laminar flamelets with presumed joint PDF. From a statistical perspective, the mean reaction rate in RANS is seen as an averaged reaction rate based on samples collected over time or ensemble; whereas in LES, the filtered reaction rate can be estimated as the weighted average of the local samples within the filter width. Since the filter size is usually larger than the flame thickness, most of the chemical reaction effects are reflected through the SGS modelling of the filtered reaction rate in LES. Therefore, the RANS and LES reaction rates are closed in a statistically consistent manner as follows.

Starting from the conservation equation given in Eq. (2.4) for species Y_i, it is straightforward to derive the instantaneous transport equation for c as has been done by Bray *et al.* [2005] and here a brief derivation is shown for illustration. In partially premixed combustion, Y_i can be defined as a function of both the mixture fraction and progress variable as

$$Y_i(\boldsymbol{x};t) = Y_i\left[Z(\boldsymbol{x};t), c(\boldsymbol{x};t)\right]. \tag{3.39}$$

Substituting Eq. (3.39) into Eq. (2.4), after mathematical manipulation the LHS of Eq. (2.4) becomes

$$\text{LHS} = \frac{\partial Y_i}{\partial c}\left[\frac{\partial \rho c}{\partial t} + \nabla\cdot(\rho \boldsymbol{U} c)\right] + \frac{\partial Y_i}{\partial Z}\left[\frac{\partial \rho Z}{\partial t} + \nabla\cdot(\rho \boldsymbol{U} Z)\right] + Y_i\underbrace{\left[\frac{\partial \rho}{\partial t} + \nabla\cdot(\rho \boldsymbol{U})\right]}_{0}, \tag{3.40}$$

where the last term is equal to zero according to the continuity equation. The treatment for the RHS is relatively more complex and thus some details are

provided here. Using the linearity and chain rules for differentiation, one obtains

$$\begin{aligned}\text{RHS} \;=\; & \frac{\partial Y_i}{\partial c}\nabla\cdot(\rho D_i\nabla c)+\frac{\partial Y_i}{\partial Z}\nabla\cdot(\rho D_i\nabla Z)+\dot{\omega}_i \\ & +\frac{\partial^2 Y_i}{\partial c^2}\rho D_i(\nabla c\cdot\nabla c)+\frac{\partial^2 Y_i}{\partial Z^2}\rho D_i(\nabla Z\cdot\nabla Z)+2\frac{\partial^2 Y_i}{\partial c\partial Z}\rho D_i(\nabla Z\cdot\nabla c).\end{aligned} \tag{3.41}$$

Here if we assume the same molecular diffusivity for all species, i.e. $D_i \equiv D$, the second term in Eq. (3.40) cancels out with the second term in Eq. (3.41) due to the transport equation for mixture fraction given in Eq. (2.20). Finally, the instantaneous transport equation for c is obtained as [Bray *et al.*, 2005]

$$\begin{aligned}\frac{\partial\rho c}{\partial t}+\nabla\cdot(\rho\boldsymbol{U}c) \;=\; & \nabla\cdot(\rho D\nabla c)+\frac{1}{\partial Y_i/\partial c}\Bigg[\dot{\omega}_i+\frac{\partial^2 Y_i}{\partial c^2}\rho D(\nabla c\cdot\nabla c) \\ & +\frac{\partial^2 Y_i}{\partial Z^2}\rho D(\nabla Z\cdot\nabla Z)+2\frac{\partial^2 Y_i}{\partial c\partial Z}\rho D(\nabla Z\cdot\nabla c)\Bigg].\end{aligned} \tag{3.42}$$

This equation is in a general form, independent of the definition of progress variable. However, depending on the definition of c, Y_i needs to be substituted accordingly. For example, using the definition of progress variable given in Eq. (3.13), it is straightforward to obtain the expression of reaction rate, $\dot{\omega}_c^*$, written as [Bray *et al.*, 2005; Domingo *et al.*, 2002, 2005, 2008]

$$\dot{\omega}_c^* = \frac{1}{\partial\psi/\partial c}\left(\dot{\omega}_\psi+2\rho N_{cZ}\frac{\partial^2\psi}{\partial c\partial Z}+\rho N_{ZZ}\frac{\partial^2\psi}{\partial Z^2}+\rho N_{cc}\frac{\partial^2\psi}{\partial c^2}\right), \tag{3.43}$$

where $\dot{\omega}_\psi = \dot{\omega}_{\mathrm{CO}}+\dot{\omega}_{\mathrm{CO2}}$ is the reaction rate for ψ. The three instantaneous scalar dissipation rates are defined as $N_{ZZ} = \rho D(\nabla Z\cdot\nabla Z)$, $N_{Zc} = \rho D(\nabla Z\cdot\nabla c)$ and $N_{cc} = \rho D(\nabla c\cdot\nabla c)$. The derivatives in Eq. (3.43) become [Chen *et al.*, 2015; Ruan *et al.*, 2012, 2014a]

$$\frac{\partial\psi}{\partial Z} = c\frac{d\psi^{\mathrm{Eq}}}{dZ} \quad\Rightarrow\quad \frac{\partial^2\psi}{\partial Z^2} = c\frac{d^2\psi^{\mathrm{Eq}}}{dZ^2}, \tag{3.44}$$

$$\frac{\partial\psi}{\partial c} = \psi^{\mathrm{Eq}} \quad\Rightarrow\quad \frac{\partial^2\psi}{\partial c^2} = 0, \quad\text{and}\quad \frac{\partial^2\psi}{\partial Z\partial c} = \frac{d\psi^{\mathrm{Eq}}}{dZ}. \tag{3.45}$$

Substituting these derivatives into Eq. (3.43) and then averaging or filtering the resulting equation one obtains

$$\overline{\dot{\omega}_c^*} = \overline{\dot{\omega}}_c + \underbrace{\overline{\rho N_{ZZ} \frac{c}{\psi^{\mathrm{Eq}}} \frac{d^2\psi^{\mathrm{Eq}}}{dZ^2}}}_{\overline{\dot{\omega}}_{\mathrm{np}}} + \underbrace{\overline{2\rho N_{Zc} \frac{1}{\psi^{\mathrm{Eq}}} \frac{d\psi^{\mathrm{Eq}}}{dZ}}}_{\overline{\dot{\omega}}_{\mathrm{cdr}}}, \tag{3.46}$$

where the asterisk * appearing in $\overline{\dot{\omega}_c^*}$ denotes the partially premixed reaction rate. On the RHS, the first part signifies the contribution of premixed mode combustion with mixture fraction stratifications, the second part, $\overline{\dot{\omega}}_{\mathrm{np}}$, signifies the contributions from non-premixed mode and the third part, $\overline{\dot{\omega}}_{\mathrm{cdr}}$, denotes a contribution resulting from interactions of Z and c gradients. Previous studies [Domingo *et al.*, 2005; Ruan *et al.*, 2012] showed that the cross dissipation contribution is an order of magnitude smaller than the contributions from the other two terms and thus $\overline{\dot{\omega}}_{\mathrm{cdr}}$ is neglected from further consideration in this work. The other two terms are modelled as follows.

The first term on the RHS of Eq. (3.46) is modelled following the previous work by Ruan *et al.* [2014a] written as

$$\overline{\dot{\omega}}_c = \overline{\rho} \int_0^1 \int_0^1 \left[\frac{\dot{\omega}_c(\zeta,\xi)}{\rho(\zeta,\xi)} \right] \widetilde{P}(\zeta,\xi)\, d\zeta\, d\xi \tag{3.47}$$

where $\overline{\rho}$ is the mean or filtered local mixture density obtained as described in the later part of this section. The flamelet reaction rate, $\dot{\omega}_c(\zeta,\xi)$, and mixture density, $\rho(\zeta,\xi)$, are obtained from laminar unstrained premixed flame calculations. The Favre joint PDF, $\widetilde{P}(\zeta,\xi)$ is modelled differently for RANS and LES frameworks as noted earlier in §3.1.

In RANS simulations where the cross correlation between mixture fraction and progress variable is significant [Ruan *et al.*, 2012], the Z-c correlation is included in $\widetilde{P}(\zeta,\xi)$ through the *copula* method described in [Darbyshire & Swaminathan, 2012; Ruan *et al.*, 2014a]. This correlation is calculated using the two marginal β-PDFs and the covariance, $\widetilde{c''Z''}$, obtained from its transport equation given in

Eq. (3.18). Thus, the correlated joint PDF for RANS is expressed as

$$\widetilde{P}_{\mathrm{RANS}}(\zeta,\xi) = \widetilde{P}_{copula}\left(\zeta,\ \xi;\ \widetilde{Z},\ \widetilde{Z''^2},\ \widetilde{c},\ \widetilde{c''^2},\ \widetilde{Z''c''}\right). \tag{3.48}$$

For the LES sub-grid joint PDF, it is modelled as a product of two β-PDFs based on the SGS statistical independence:

$$\widetilde{P}_{\mathrm{LES}}(\zeta,\xi) = \widetilde{P}_{\beta}\left(\zeta;\ \widetilde{c},\ \widetilde{c''^2_{\mathrm{sgs}}}\right)\widetilde{P}_{\beta}\left(\xi;\ \widetilde{Z},\ \widetilde{Z''^2_{\mathrm{sgs}}}\right). \tag{3.49}$$

The second term in Eq. (3.46), $\overline{\dot{\omega}}_{\mathrm{np}}$, denoting contributions of non-premixed mode combustion is modelled as [Ruan *et al.*, 2014a]

$$\overline{\dot{\omega}}_{\mathrm{np}} \simeq \overline{\rho}\,\widetilde{c}\,\widetilde{N}_{ZZ}\int_0^1 \frac{1}{\psi^{\mathrm{Eq}}(\xi)}\frac{d^2\psi^{\mathrm{Eq}}(\xi)}{dZ^2}\,\widetilde{P}_{\beta}(\xi)\,d\xi, \tag{3.50}$$

where $\widetilde{N}_{ZZ}$ is the mean or filtered scalar dissipation rate of mixture fraction. For RANS simulations, $\widetilde{N}_{ZZ} \simeq \widetilde{\chi}_Z$ is approximated using Eq. (3.19) because the gradient of the mean is relatively small compared to gradient of the fluctuation [Ruan *et al.*, 2012]. In LES, however, the scalar dissipation rate of Z is largely resolved, and the filtered value is obtained using: $\widetilde{N}_{ZZ} = D(\nabla\widetilde{Z}\cdot\nabla\widetilde{Z}) + \widetilde{\chi}_{Z,\mathrm{sgs}}$, where the SGS part is obtained using Eq. (3.36).

Strictly, in order to close $\overline{c''\dot{\omega}_c^{*\prime\prime}}$, $\overline{Z''\dot{\omega}_c^{*\prime\prime}}$ and $\overline{c\,\dot{\omega}_c^{*}}$ in Eqs. (3.17), (3.18) and (3.34) respectively, one must include the contributions of three scalar dissipation rates in Eq. (3.43) at the flamelet level. This would need a multi-dimensional (in physical space) flamelet or alternatively the multi-dimensional flamelet generated manifolds with the three dissipation rates as controlling parameters [Nguyen *et al.*, 2010; Vervisch *et al.*, 2011]. This adds further complexity into the modelling and hence the approximations, $\overline{c''\dot{\omega}_c^{*\prime\prime}} \approx \overline{c''\dot{\omega}_c''}$, $\overline{Z''\dot{\omega}_c^{*\prime\prime}} \approx \overline{Z''\dot{\omega}_c''}$ and $\overline{c\,\dot{\omega}_c^{*}} \approx \overline{c\,\dot{\omega}_c}$ are made here for the sake of simplicity. The validity of this approximation can be adjudged using comparisons with experimental measurements to be discussed in a later chapter of this thesis. The closure models for the above three terms are

then written as [Darbyshire & Swaminathan, 2012; Ruan *et al.*, 2014a]:

$$\overline{c''\dot{\omega}_c''} \approx \overline{c''\dot{\omega}_c} = \overline{\rho} \int_0^1 \int_0^1 \left(\zeta - \widetilde{\zeta}\right) \frac{\dot{\omega}_c(\xi,\zeta)}{\rho(\xi,\zeta)} \, \widetilde{P}(\xi,\zeta) \, d\xi \, d\zeta, \tag{3.51}$$

$$\overline{Z''\dot{\omega}_c''} \approx \overline{Z''\dot{\omega}_c} = \overline{\rho} \int_0^1 \int_0^1 \left(\xi - \widetilde{\xi}\right) \frac{\dot{\omega}_c(\xi,\zeta)}{\rho(\xi,\zeta)} \, \widetilde{P}(\xi,\zeta) \, d\xi \, d\zeta, \tag{3.52}$$

$$\overline{c\dot{\omega}_c} = \overline{\rho} \int_0^1 \int_0^1 \zeta \, \frac{\dot{\omega}_c(\xi,\zeta)}{\rho(\xi,\zeta)} \, \widetilde{P}(\xi,\zeta) \, d\xi \, d\zeta. \tag{3.53}$$

Favre mean or filtered species mass fractions are computed in a similar manner using the joint PDF as

$$\widetilde{Y}_i = \int_0^1 \int_0^1 Y_i(\xi,\zeta) \, \widetilde{P}(\xi,\zeta) \, d\zeta \, d\xi, \tag{3.54}$$

where $Y_i(\xi,\zeta)$ is the flamelet mass fraction for species i. One could also obtain the temperature using the same approach. However, in order to be able to include non-adiabatic effects on the boundaries, the Favre temperature, $\widetilde{T}$, is calculated using the total enthalpy $\widetilde{h}$ computed in the simulation through its transport equation. By rearranging Eq. (2.7), under adiabatic conditions one obtains [Chen *et al.*, 2015; Ruan *et al.*, 2014a]

$$\widetilde{T} = \frac{\widetilde{h} - \Delta h^0_{f\,,\mathrm{mix}}}{C_{p\,,\mathrm{mix}}} + T_0, \tag{3.55}$$

where the mixture specific heat capacity $C_{p,\mathrm{mix}}$ and enthalpy of formation $\Delta h^0_{f\,,\mathrm{mix}}$ are calculated as

$$C_{p,\mathrm{mix}} = \int_0^1 \int_0^1 C_p^{\mathrm{e}}(\xi,\zeta) \, \widetilde{P}(\xi,\zeta) \, d\zeta \, d\xi, \tag{3.56}$$

$$\Delta h^0_{f,\mathrm{mix}} = \int_0^1 \int_0^1 \left(\sum_{i=1}^{N} Y_i(\xi,\zeta) \, \Delta h^0_{f,i} \right) \widetilde{P}(\xi,\zeta) \, d\zeta \, d\xi, \tag{3.57}$$

The $C_{p,\mathrm{mix}}$ term given in Eq. (3.55) includes its temperature dependence through Eq. (3.56) while simulating turbulent combustion. An effective specific heat ca-

pacity, defined as

$$C_p^{\mathrm{e}}(\xi,\zeta,T_1) = \frac{\int_{T_0}^{T_1} C_p(\xi,\zeta)dT}{T_1 - T_0} \tag{3.58}$$

is used to include the temperature dependence at the flamelet level and $T_1 = T(\xi,\zeta)$ is the local temperature at which $C_p^{\mathrm{e}}(\xi,\zeta)$ is calculated. The mixture molecular weight W_{mix} required for the state equation is calculated using

$$W_{\mathrm{mix}} = \int_0^1 \int_0^1 \left(\sum_i \frac{Y_i}{W_i} \right)^{-1} \widetilde{P}(\xi,\zeta)\, d\zeta\, d\xi. \tag{3.59}$$

The mean density is obtained using the ideal gas equation of state described in Eq. (2.8): $\overline{\rho} = \overline{p} W_{\mathrm{mix}} / \widetilde{T} R_0$, with $\overline{p}$ being the thermodynamic pressure obtained from the simulation.

The various sources and sinks terms related to combustion described above can be pre-computed and stored as a lookup table for turbulent flame simulation. The species mass fractions can also be recovered from this table through a post-processing step after the simulations are completed. The implementation of these procedures and its coupling with the CFD solver are described next.

3.3 Computation of lookup tables

One-dimensional freely-propagating laminar premixed flames for a number of equivalence ratios (ϕ) covering the flammable range are computed using CHEMKIN PRO [CHEMKIN, 2013]. An arbitrarily complex chemistry, GRI-Mech 3.0 involving 53 species and 325 reactions is considered. A typical flame solution has been shown earlier in Fig. 2.4 for a given ϕ, and all the thermo-chemical state variables (density, temperature, species, etc.) can be mapped onto a *one-dimensional array* parameterised by a discretised c, which is discretised with $\mathcal{N}_c$ points. Another dimension is added to the array by conducting this mapping for $\mathcal{N}_Z$ number of Z (converted from ϕ) points. Thus, a complete flamelet library can be described using a $(\mathcal{N}_Z \times \mathcal{N}_c)$ matrix: $\mathcal{L}^{\boldsymbol{\varphi}}$, where $\boldsymbol{\varphi}$ is the vector for all thermo-chemical quantities. The values of $\mathcal{N}_Z = 526$ and $\mathcal{N}_c = 501$ are chosen in such a way that the

Table 3.1: Number of discretisation points used for turbulent flame lookup tables.

	$\mathcal{N}_{\widetilde{Z}}$	$\mathcal{N}_{\widetilde{c}}$	$\mathcal{N}_{\widetilde{g}_Z}$	$\mathcal{N}_{\widetilde{g}_c}$	$\mathcal{N}_{\widetilde{g}_{Zc}}$
RANS	24	21	21	21	11
LES	46	75	25	40	1 (no correlation)

variations of $\boldsymbol{\varphi}$ in the Z-c spaces are well resolved for atmospheric methane/air combustion at room temperature (around 300 K) studied in this work. It has also been tested that these numbers are sufficient for the numerical integration using the *trapezoidal rule* [Press, 1996] for the turbulent flame lookup table generation, which is described next.

Before computing the double-integration in Eqs. (3.47), (3.51)-(3.54), (3.56), (3.57) and (3.59), the number of discretisation points needs to be assigned to the five control parameters for the turbulent flame lookup table. These parameters, for RANS calculations, are $\widetilde{Z}$, $\widetilde{c}$, $\widetilde{g}_Z \equiv \widetilde{Z''^2}/(\widetilde{Z}(1-\widetilde{Z}))$, $\widetilde{g}_c \equiv \widetilde{c''^2}/(\widetilde{c}(1-\widetilde{c}))$ and $\widetilde{g}_{Zc} \equiv \widetilde{Z''c''}/\sqrt{\widetilde{Z''^2}\widetilde{c''^2}}$, where the variances are normalised to facilitate the β-function computation. Details of the discretisation points are given in Table 3.1. Similar to the matrix construction described above for the flamelet library, a matrix $\mathcal{M}^{\widetilde{\boldsymbol{\varphi}}}$ with dimensions of $(\mathcal{N}_{\widetilde{Z}} \times \mathcal{N}_{\widetilde{c}} \times \mathcal{N}_{\widetilde{g}_Z} \times \mathcal{N}_{\widetilde{g}_c} \times \mathcal{N}_{\widetilde{g}_{Zc}})$ is established for the lookup table to be used during the turbulent flame simulations. A schematic of the table generation procedures is shown in Fig. 3.1 below. The numerical resolution of the table is refined around $\widetilde{Z}_{st}$ and $\widetilde{c} = 0.6$ because of large reaction rate near these locations. For the mixture fractions outside the flammable range, an linear interpolation approach is applied as described in [Ruan, 2012; Ruan *et al.*, 2014a]. In turbulent flame simulations, these tabulated values are interpolated using a five-dimensional linear interpolation function to obtain the various sources and sinks required for a spatial grid point and the error in this interpolation procedure was assessed to be about 1% [Ruan *et al.*, 2014a].

The formal procedure for the LES lookup table remains more or less the same except that a higher numerical resolution is required for LES. Similar to RANS, the five control parameters for LES are $\widetilde{Z}$, $\widetilde{c}$, $\widetilde{g}_Z \equiv \widetilde{Z''^2_{\text{sgs}}}/(\widetilde{Z}(1-\widetilde{Z}))$, $\widetilde{g}_c \equiv \widetilde{c''^2_{\text{sgs}}}/(\widetilde{c}(1-\widetilde{c}))$ and $\widetilde{g}_{Zc} \equiv \widetilde{(Z''c'')_{\text{sgs}}}/\sqrt{\widetilde{Z''^2_{\text{sgs}}}\,\widetilde{c''^2_{\text{sgs}}}}$. The lookup table for LES is similar to that shown in Fig. 3.1 for RANS, except for one attribute. Since

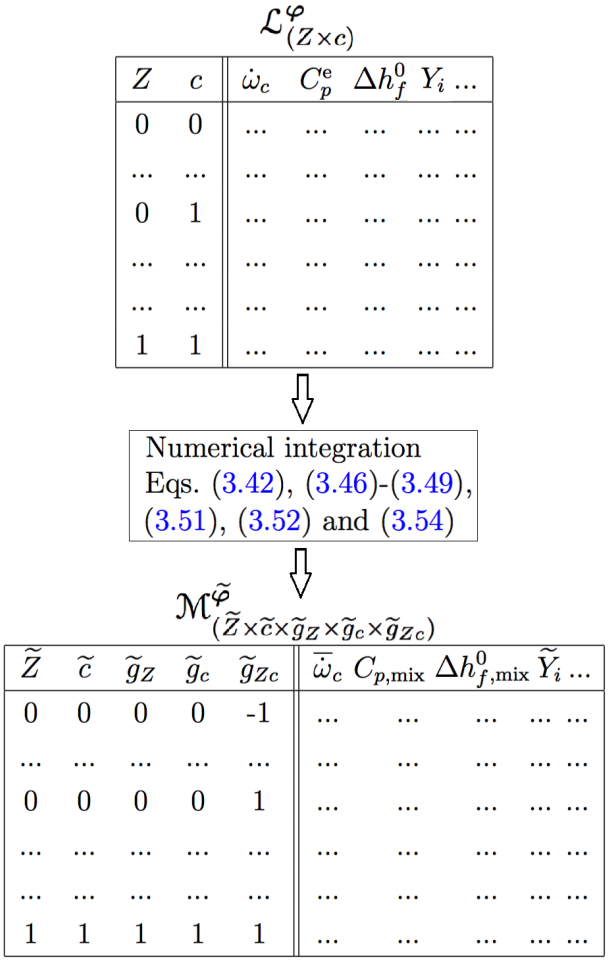

Figure 3.1: Demonstration of the flamelet lookup table generation procedures.

$\widetilde{(Z''c'')}_{\mathrm{sgs}}$ is taken to be zero (see §3.1.2), $\widetilde{g}_{Zc} = 0$ for LES.

3.4 Model implementation

The partially premixed combustion model described in §3.1 and §3.2 is implemented in two CFD solvers, Fluent [ANSYS-Fluent, 2012] and OpenFOAM [Open CFD, 2013], for RANS and LES respectively. As a continuation work of Ruan *et al.* [2014a], the RANS simulations presented in this thesis are performed using the Fluent implementation previously established by Ruan [2012]. However, for the high-fidelity LES calculations, the commercial codes are known to be too

dissipative to accurately resolve the large-scale dynamics in LES and so the open-source code OpenFOAM is used. Furthermore, as LES requires *massively parallel computing* for large computational grids and complex geometries, the license-free OpenFOAM code is chosen as the CFD solver for the LES calculations.

3.4.1 RANS-Fluent solver

The RANS modelling framework described in §3.1.1 is incorporated with the commercial CFD code ANSYS-Fluent 13.0 [ANSYS-Fluent, 2012]. The coupling between the solver and combustion model has been detailed by Ruan *et al.* [2014a], and only a brief description is given here. The mass and momentum conservation equations, Eqs. (3.2) and (3.3), are solved using the default setup in the Fluent package. The turbulence is modelled using the standard k-ε model available in Fluent. The scalar transport equations and combustion modelling equations are implemented through user defined scalars (UDSs) and functions (UDFs), and thus the default combustion modelling in Fluent is not used. A transport equation for $\widetilde{h}$ and those given in Eqs. (3.14)-(3.18) are solved using UDSs. The modelling of various sources and sinks of these equations discussed in §3.2 are included through UDFs. The fluid density is obtained using a user defined function involving $\widetilde{T}$ calculated from $\widetilde{h}$ as described in §3.2 (see Eq. (3.55)). The sources and sinks related to chemical reactions are obtained using the lookup table described in the previous section.

3.4.2 LES-OpenFOAM solver

The open-source CFD package OpenFOAM (v2.3.0) [Open CFD, 2013] is used to solve the LES balance equations described in §3.1.2. The object-oriented nature of this code allows us to establish a completely independent solver from the existing ones so that all the equations are coupled and solved according to a user preferences. It is only the discretisation methods and iterative solving algorithms that need to be called from the OpenFOAM Library while the solver is running. Thus, a stand-alone LES solver with a thermo-physical sub-library using the modelling framework described earlier in this chapter is developed for the partially premixed combustion, and this solver is referred to as the LES-PPF

solver hereafter in this thesis.

Another attractive feature of OpenFOAM is the high-efficiency Message Passing Interface (MPI) parallel computing for unstructured numerical grids, which is well-suited for LES of turbulent flames in practical burners with complex geometry. This shall be seen later in this subsection when investigating the scalability of LES-PPF.

Most OpenFOAM solvers are based on low-Mach number assumption, which solves the velocity and pressure equations, Eqs. (3.24) and (3.25), using a *pressure implicit with splitting of operator* (PISO) algorithm [Issa, 1986]. On top of the PISO iterative solving loop, a *Semi-Implicit Method for Pressure-Linked Equations* (SIMPLE) algorithm [Patankar, 1980] based outer iteration is added to introduce under-relaxation factors for improving numerical stability. This so-called *PIMPLE* algorithm is adopted for the reacting flows considered in this work. The standard Smagorinsky model with a static constant described in Eq. (3.30) is available in the OpenFOAM Library and hence it is adopted for the LES-PPF solver. No thermo-physical function from the OpenFOAM Library is used and all the thermo-physical quantities such as density, temperature, viscosity are computed through the in-house sub-library.

Figure 3.2 shows a flowchart of numerical solving procedure of the LES-PPF solver, in which the black coloured steps are inherited from the OpenFOAM Library and the red coloured sub-steps are implemented through combustion sub-library developed in this work. The lookup table discussed in §3.3 is preloaded into the Random-Access Memory (RAM) before the LES flow calculations. The five additional filtered scalar transport equations, i.e. Eqs. (3.26) and (3.31)-(3.34), are implemented and solved after the momentum-pressure coupling equations. These filtered scalars are then used as the control parameters to fetch the sources and sinks from the lookup table for next numerical iteration. After the table lookup procedure, the filtered temperature $\widetilde{T}$ and density $\overline{\rho}$ for the current time step are calculated and updated using Eqs. (3.55) and (2.8) respectively. The number of the outer PIMPLE loops is prescribed depending on the case, and typically, 1 to 2 loops are sufficient for non-reacting flow simulations and 3 to 5 loops are required for combusting flows due to the significant density change.

Parallelisation of the LES computation is implemented using the OpenFOAM

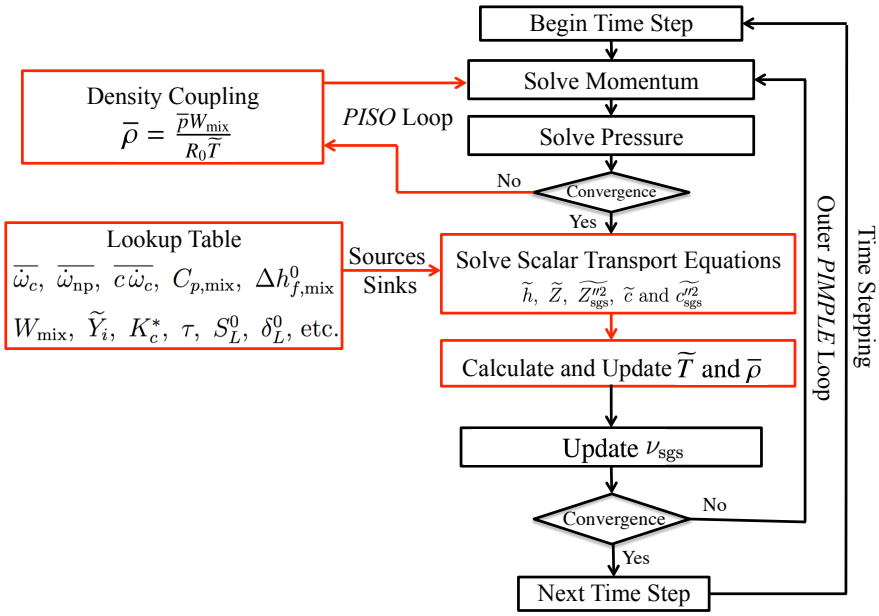

Figure 3.2: Flowchart of numerical solving procedure of the LES-PPF solver.

Utility (built-in function) called *decomposePar*, which performs the partitioning procedure of the computational domain in such a way that the solver can directly perform the MPI computations without having to call the MPI library in the solver. A *Parallel Threaded Scotch* [Pellegrini, 2006] decomposition approach from the OpenFOAM Library is used to minimise the interface communication between the partitions.

To assess the computational cost of the LES-PPF solver and its parallel computing performance, a scalability test is carried out using the UK National Supercomputing Service − ARCHER (Cray XC30 MPP) supercomputer consisting of 4920 compute nodes with a total of 118,080 processing cores. Details of the ARCHER hardware can be found online (http://www.archer.ac.uk/).

The lifted jet flame experiment by Ahmed & Mastorakos [2006] is chosen for the scalability test, and the computational domain consists of 7.3 million unstructured tetrahedral cells. A series of LES computations for the same test case are performed for 1000 time steps using the number of cores ranging from 48 to 7200. In order to highlight the computational cost of different physical processes, these LES computations are conducted on the same numerical grid

for three test cases: constant-density air flow, methane/air mixing and reacting flows. More numerical detail on the test cases are discussed in Chapter 7.

Figure 3.3 shows a comparison of the elapsed wall-clock time against the number of cores used for these three simulation series. It can be clearly seen that the code exhibits an excellent scalability up to 7000 cores suggesting that a good potential for heavy-duty LES computation of practical combustors. There is an approximately 60% increase in computational time for scalar mixing case compared to the air flow due to the additional scalar equations solved and more importantly the density variation resulting in a slower convergence process for the pressure-velocity equations. It is also evident that the additional computational cost due to combustion is less than 30% from mixing flow to reacting flow. For the LES computations performed in the present work, an optimum number of 1080 cores is chosen by considering both the computational speed and the subsequent post-processing procedures.

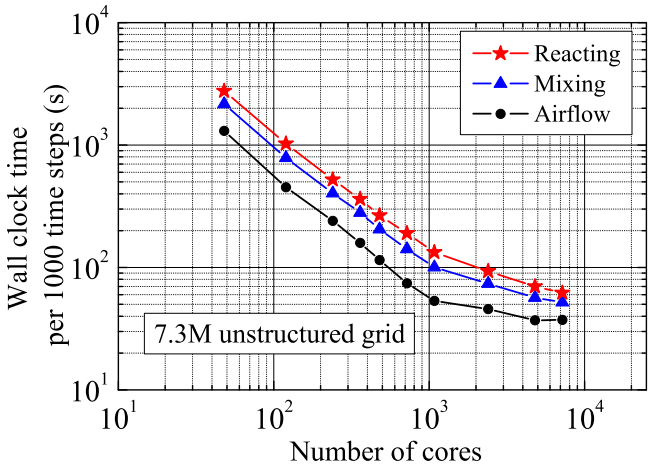

Figure 3.3: Elapsed wall-clock time as a function of the number of cores used for the LES computation of 1000 time steps. Three test cases are respectively the constant-density air flow, methane/air mixing and reacting flow simulations for a lifted methane/air jet flame with a bulk mean velocity of 25.5 m/s [Ahmed & Mastorakos, 2006].

To investigate the computational cost of the sub-processes in the code, their individual percentages of the total computational time shown in Fig. 3.3 for the reacting case are compared in Fig. 3.4. Three sub-processes are identified: solving

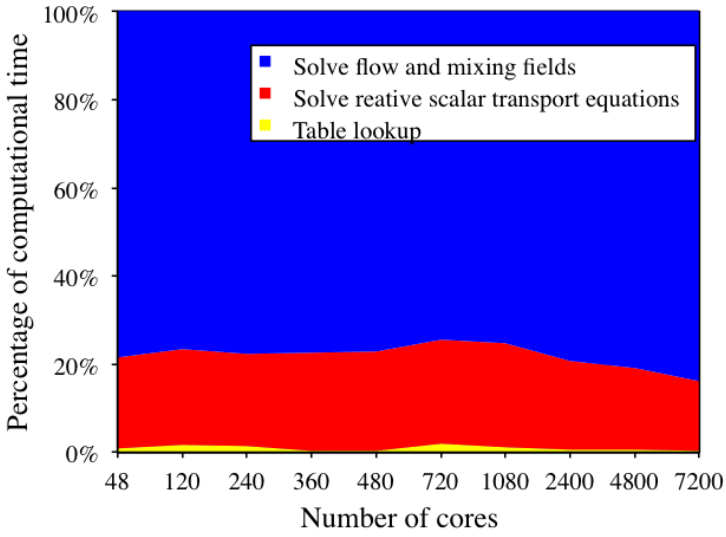

Figure 3.4: Computational time breakdown for different sub-processes in the LES-PPF solver. The shown case is the reacting flow presented in Fig. 3.3.

flow and mixing fields (Eqs. 3.24-3.26, 3.31 and 3.34), solving for reactive scalars (Eqs. 3.33 and 3.34) and table lookup (described in §3.3). It is shown in Fig. 3.4 that about 80% of the computational time is spent on solving the flow and mixing fields, whereas the combustion chemistry only accounts for 20%. The cost of obtaining the sources and sinks from the lookup table is negligible compared to the other costs. These percentages remain more or less the same for the number of cores ranging from 48 to 7200 suggesting that the combustion model is coupled with the flow solver in a consistent manner so that they have the same computational scalability and this model is computationally inexpensive.

3.5 Summary

The modelling framework used for this thesis work and its realisation in common CFD codes have been discussed in this chapter. A premixed flamelets based presumed PDF approach for partially premixed combustion is introduced, followed by its implementation for RANS and LES modelling methodologies. A particular emphasis is given on the LES-PPF model and its coupling with the OpenFOAM CFD Library. The code shows an excellent scalability up to 7000 cores for high-

performance parallel computation. These modelling and numerical approaches are evaluated using experimental test cases, which are presented in the following chapters.

Chapter 4

Non-reacting Flow Validation

Before applying the combustion models described in the previous chapter to reacting flow cases, cold flow simulations are performed to assess the validity of the computational approaches and numerical grids used. Two experimental test cases are chosen for this thesis work and the simulations results for the non-reacting flows are discussed in this chapter. The first one is the Cambridge methane/air lifted jet flame burner studied by Ahmed & Mastorakos [2006] and this configuration is simulated using 2D and 3D RANS as well as LES approaches. The second burner is the DLR dual-swirler gas turbine model combustor [Meier *et al.*, 2006; Weigand *et al.*, 2006] with confined geometry and mass flow conditions close to practical devices. LES is used to capture the complex fluid mechanical features in this geometry. These computational results are compared against the experimental measurements in two separate sections discussed below.

4.1 Cambridge non-piloted jet burner

4.1.1 Experimental configuration

The non-piloted lifted flames established in the downstream of a methane jet issuing into stagnant air were studied experimentally by Ahmed & Mastorakos [2006]. A detailed list of the geometrical and physical properties for this jet burner is presented in Table 4.1. The burner consisted of a round injection tube with an inner diameter of $d_\mathrm{j} = 5$ mm and a length of $128d_\mathrm{j}$ to ensure a fully

Table 4.1: Details of the Cambridge non-piloted jet burner.

Property	Value	Description
d_j	5 mm	Inner diameter of the fuel jet
d_c	200 mm	Inner diameter of the coaxial airflow
U_j	21 m/s	Bulk mean velocity of the air jet
Re_j	6800	Turbulent jet flow Reynolds number
U_c	0.1 m/s	Velocity of the laminar airflow
T	300 K	Temperature of inflowing and ambient fluids
p	101325 Pa	Operating pressure

developed turbulent flow at the jet exit. There were no turbulence generating devices inside the fuel nozzle and the turbulence in the downstream of the nozzle exit is mainly shear driven. In order to eliminate the disturbances from the room air currents, the fuel tube was surrounded by a coaxial laminar airflow having a diameter of 200 mm and a velocity of $U_\mathrm{c} = 0.1$ m/s [Ahmed & Mastorakos, 2006]. A non-reacting air jet with a bulk mean velocity of $U_\mathrm{j} = 21$ m/s was measured to assess the self-similarity flow behaviour and the corresponding Reynolds number based on the jet diameter is $\mathrm{Re}_\mathrm{j} = 6800$. The hot-wire measurement technique was used for this iso-thermal (300 K) air jet, and radial profiles of the mean and *root mean square* (r.m.s.) axial velocities were measured at five downstream axial positions ranging from $10d_\mathrm{j}$ to $50d_\mathrm{j}$. These experimental results are used in this study to validate the numerical setup for this jet burner, which is described next.

4.1.2 Numerical setup

A schematic of the numerical setup of the experiment is shown in Fig. 4.1. The grey-coloured half slice of the middle-plane represents the axisymmetric computational domain used for the two-dimensional (2D) steady and unsteady RANS simulations. This domain is $200d_\mathrm{j} \times 100d_\mathrm{j}$ in the axial, z, and radial, r, directions, which ensures a sufficient physical space for velocity and mixing fields to fully develop in the downstream of the jet nozzle without numerical disturbance from

the side boundaries. The third physical dimension, which is referred to as the azimuthal direction, θ, hereafter in this thesis, is included for the 3D URANS and LES computations resulting in a $200d_\mathrm{j}\times100d_\mathrm{j}\times2\pi$ cylindrical domain.

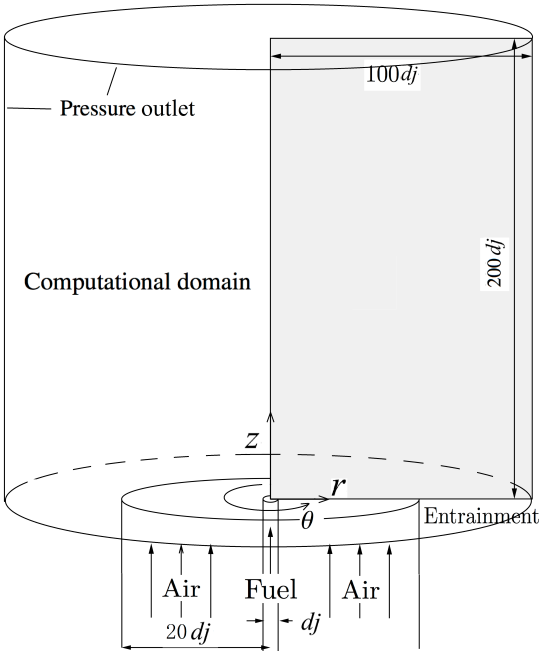

Figure 4.1: Schematic of the Cambridge jet burner setup for the experiments [Ahmed & Mastorakos, 2006] and computations.

The numerical boundary conditions used in the simulations are also shown in Fig. 4.1. At the jet exit, which is the inlet boundary for computations, the mean axial velocity is specified using the 1/7th power law for a fully developed turbulent flow as [Wilcox, 2006]

$$U_\mathrm{inlet} = 1.128\,U_\mathrm{j}\left(1-\frac{2r}{d_\mathrm{j}}\right)^{1/7}. \tag{4.1}$$

The turbulent velocity fluctuation at the inlet boundary was estimated using a correlation involving a Reynolds number, Re, based on the bulk mean velocity and pipe diameter for a fully developed turbulent pipe flow. This correlation is

given by [Wilcox, 2006]

$$I \equiv \frac{u'_\Lambda}{U_\mathrm{j}} = 0.16\,\mathrm{Re}^{-1/8}, \tag{4.2}$$

which is about 5.3% for the air jet considered here. For the RANS simulations, the turbulence integral length scale at the jet exit is approximated to be about $\Lambda = 0.7d_\mathrm{j}$. Using these values of I and Λ, the $\widetilde{k}$ and $\widetilde{\varepsilon}$ values are estimated to specify the inlet boundary conditions for the turbulence equations given in Eqs. (3.9) and (3.10). However, for the LES inlet, second-order velocity statistics (i.e. Reynolds stresses) are required to provide an accurate inlet turbulence condition and unfortunately such data is not available from the experiments [Ahmed & Mastorakos, 2006]. As an alternative approximation, a 5% White Noise random fluctuation is given for the LES inlet boundary. A laminar flow with a velocity of $U_\mathrm{c} = 0.1$ m/s is used for the co-flowing air as in the experiments [Ahmed & Mastorakos, 2006]. A pressure outlet condition is applied for the downstream outlet and also for the side boundary as shown in Fig. 4.1. These conditions are used for the RANS and LES computations in a consistent manner.

The computational domain shown in Fig. 4.1 is discretised using unstructured triangular and tetrahedral grids for the 2D and 3D (URANS and LES) simulations as presented in Figs. 4.2a and 4.2b respectively. The mesh is refined near the jet exit to resolve the large spatial gradient in the shear layer between the fuel jet and the ambient air. The total cell number is 76,000 for the 2D grid and 3.2 million for the 3D grid used for the RANS simulations. The near field and the shear layer region are further refined for the LES calculations to ensure that the resolved turbulent kinetic energy criterion described in Eq. (3.38) is satisfied. The resulting LES grid consists of 7.3 million cells.

The 2D and 3D RANS simulations are performed using the RANS-Fluent solver described earlier in §3.4.1. The hardwares used for these calculations are a multi-core desktop computer for the 2D computations and the DARWIN Cluster at the University of Cambridge consisting of 9600 compute cores (2.60GHz Intel Sandy Bridge) for the 3D simulations. For the LES computations, the LES-PPF solver based on OpenFOAM described in §3.4.2 is used on the UK national supercomputer ARCHER. The typical wall-clock time for a numerically converged

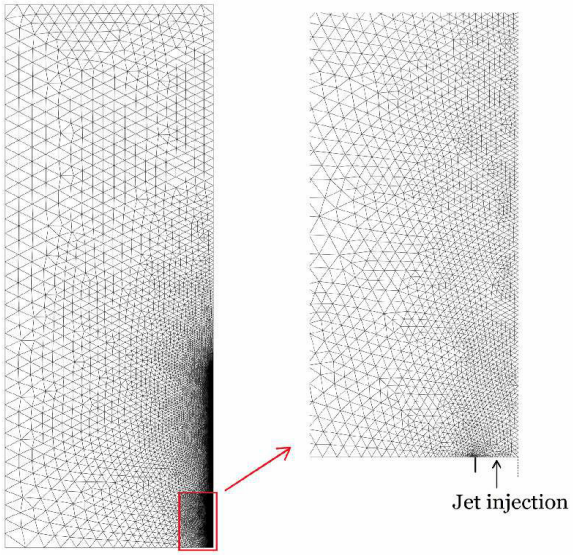

(a)

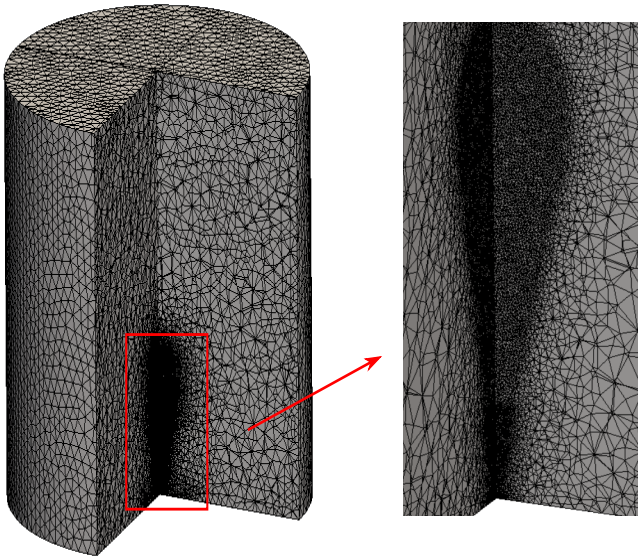

(b)

Figure 4.2: Typical computational grids for (a) 2D axisymmetric and (b) 3D simulations.

solution is about 30 minutes (2D RANS), 1 hour (3D RANS) and 10 hours (LES) using 8, 256 and 1080 cores respectively. The LES statistics are collected over a

physical time period of 0.2 s corresponding to about 20 flow-through-time, which is estimated using U_j and the distance from the jet exit to $50d_\mathrm{j}$ in the axial direction.

4.1.3 Cold flow results

4.1.3.1 Velocity field

The two-equation $\widetilde{k}$-$\widetilde{\varepsilon}$ turbulence model is used for RANS simulations of the free air jet described above. As suggested by Pope [1978], the model constants noted earlier in §3.1.1 require modification in order to accurately predict the spreading and penetration of round jet flows. Based on a previous study by Jones & Kakhi [1998], the model constants chosen for this study are $C_\mu = 0.065$, $C_{\varepsilon 1} = 1.44$ and $C_{\varepsilon 2} = 1.85$. For LES calculations, a standard model constant $C_\mathrm{S} = 0.167$ [Pope, 2000] is used for the Smagorinsky sub-grid stress model.

In order to assess the self-similar flow behaviour of this round jet, the mean axial velocity is scaled as $\mathcal{U} = \left(\langle\widetilde{U}\rangle - U_\mathrm{c}\right) / \left(\langle\widetilde{U}_\mathrm{cl}\rangle - U_\mathrm{c}\right)$, where $U_\mathrm{c} = 0.1$ m/s is the co-flow velocity and $\widetilde{U}_\mathrm{cl}$ is the centreline value at the respective axial location. Note that in RANS the mean velocity is directly computed: $\langle\widetilde{U}\rangle = \widetilde{U}$. In a similar manner, the r.m.s. of the axial velocity is scaled as $\mathcal{U}_\mathrm{r.m.s.} = \widetilde{U}_\mathrm{r.m.s.} / \left(\langle\widetilde{U}_\mathrm{cl}\rangle - U_\mathrm{c}\right)$, where the r.m.s. value is obtained as $\widetilde{U}_\mathrm{r.m.s.} = \sqrt{2\widetilde{k}/3}$ using the computed values of $\widetilde{k}$ in RANS and the resolved r.m.s. value in LES is calculated as

$$\widetilde{U}_\mathrm{r.m.s.} = \sqrt{\langle(\widetilde{U})^2\rangle - \langle\widetilde{U}\rangle^2}, \tag{4.3}$$

where the operator $\langle\cdot\rangle$ denotes a time average of the collected LES samples. The symbols in Fig. 4.3 are measured values reported in [Ahmed & Mastorakos, 2006] and the lines are computational results. Note that the radial position r is also normalised by the corresponding axial coordinate z in this figure to show the self-similar pattern of the radial profiles. The agreement seen in this figure is excellent for the 2D and 3D RANS simulations and supports the self-similar behaviour of the jet. The LES results for $\mathcal{U}$ also agree quite well with the experimental data, however, the r.m.s. values of the axial velocity is over-predicted by 5 to 10% in centre area ($r/z < 0.1$) of the near field ($z/d_\mathrm{j} < 30$)

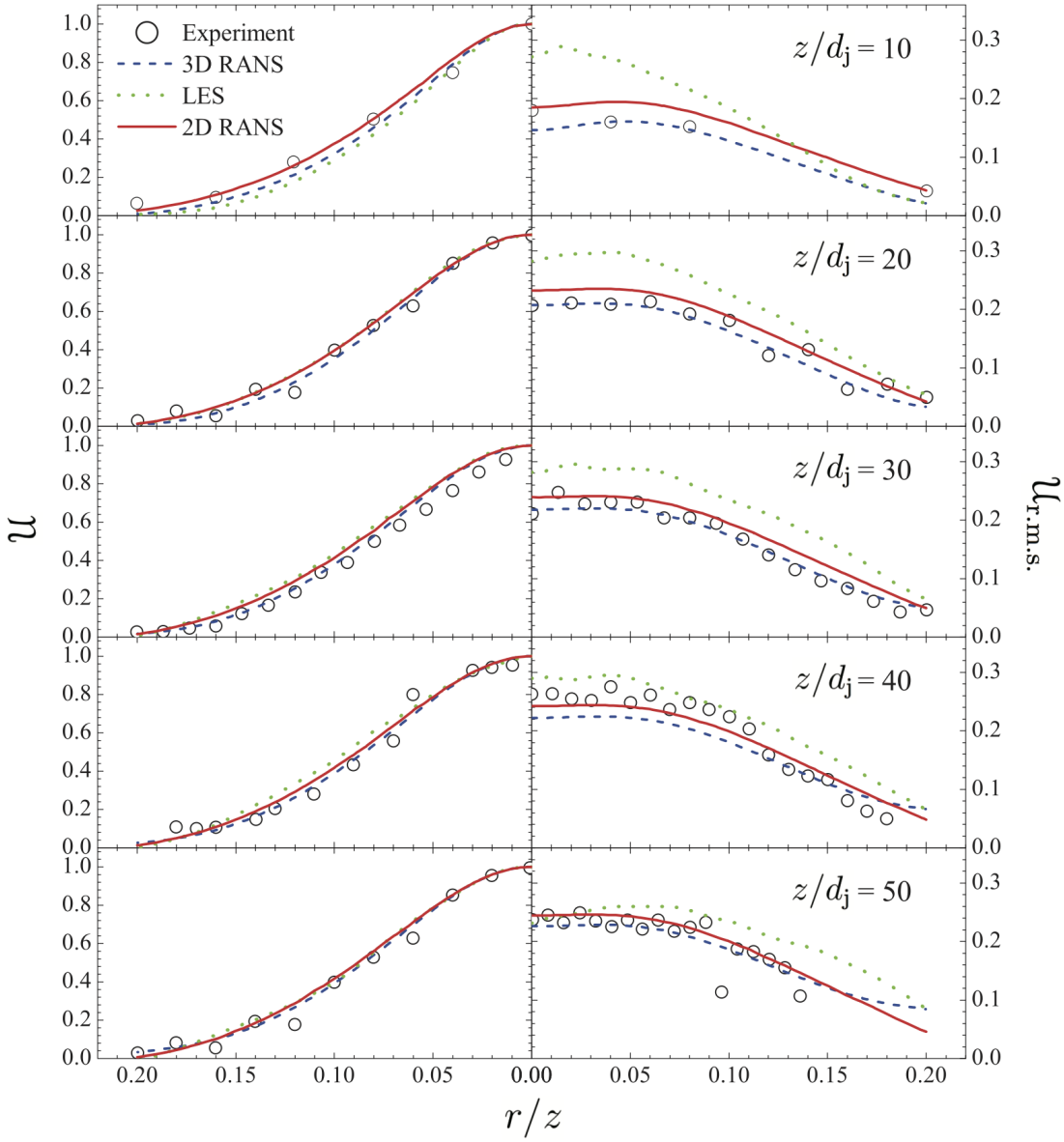

Figure 4.3: Comparison of the computed and measured [Ahmed & Mastorakos, 2006] radial variation of the mean axial velocity and turbulence r.m.s. values. Values are normalised as noted in the text. The jet velocity is $U_j = 21$ m/s and the co-flow velocity is $U_c = 0.1$ m/s.

of the jet. The difference between the LES and experimental results becomes smaller and eventually vanishes as one moves further downstream. This was also observed in the previous LES studies [Jones & Prasad, 2011; Lacaze *et al.*, 2009b]

and is possibly due to the under-specified inlet turbulence, which unfortunately was not characterised in the experiments [Ahmed & Mastorakos, 2006].

The computed axial variation of centreline velocity agrees quite well with the empirical relationship given by Tieszen *et al.* [1996] as shown in Fig. 4.4 for all three categories of simulations. This lends further support to the self-similar behaviour of the computed turbulent jets. The centreline value is over-predicted by about 5% for the LES, which again may be due to the inlet turbulence, in line with the previous observations in Fig. 4.3. The comparisons shown in Figs. 4.3 and 4.4 are very good, which support the values used for turbulence model parameters and thus they are adopted for the reacting flow simulations reported in the later chapters.

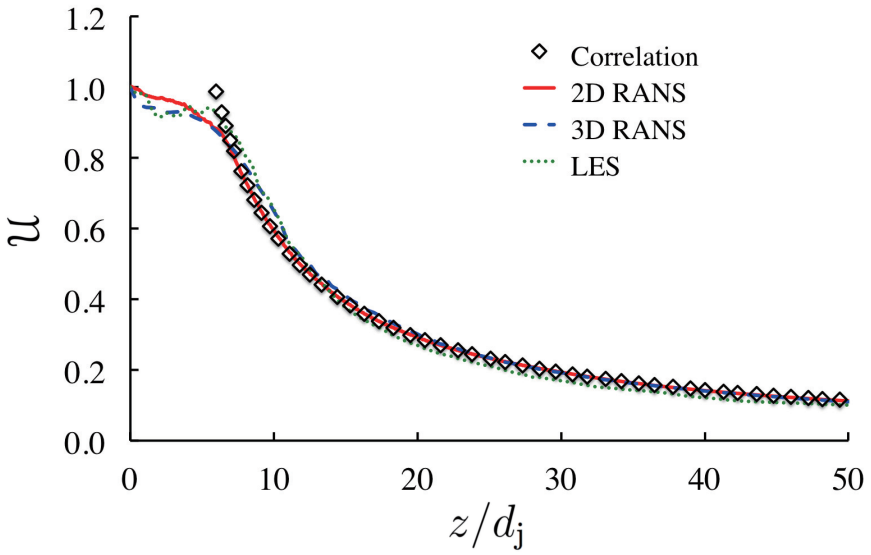

Figure 4.4: Axial variation of the scaled centreline velocity obtained from the simulations and an empirical correlation established in [Tieszen *et al.*, 1996].

To assess the LES grid quality, Pope's criterion for the resolved turbulent kinetic energy described in Eq. (3.38) is shown in Fig. 4.5. Overall, the fraction of the resolved part, $\mathcal{F}_K$, is larger than 0.8 suggesting a well-resolved LES flow field. Exception is found only close to the flow inlet boundaries within $10d_j$ because of the jet core, whereas for the downstream and shear layer regions where the jet flame propagates and stabilises, the value of $\mathcal{F}_K$ is close to 1. This shows further validity for the LES grid and chosen turbulence model, as well as for the various

boundary conditions described in §4.1.2.

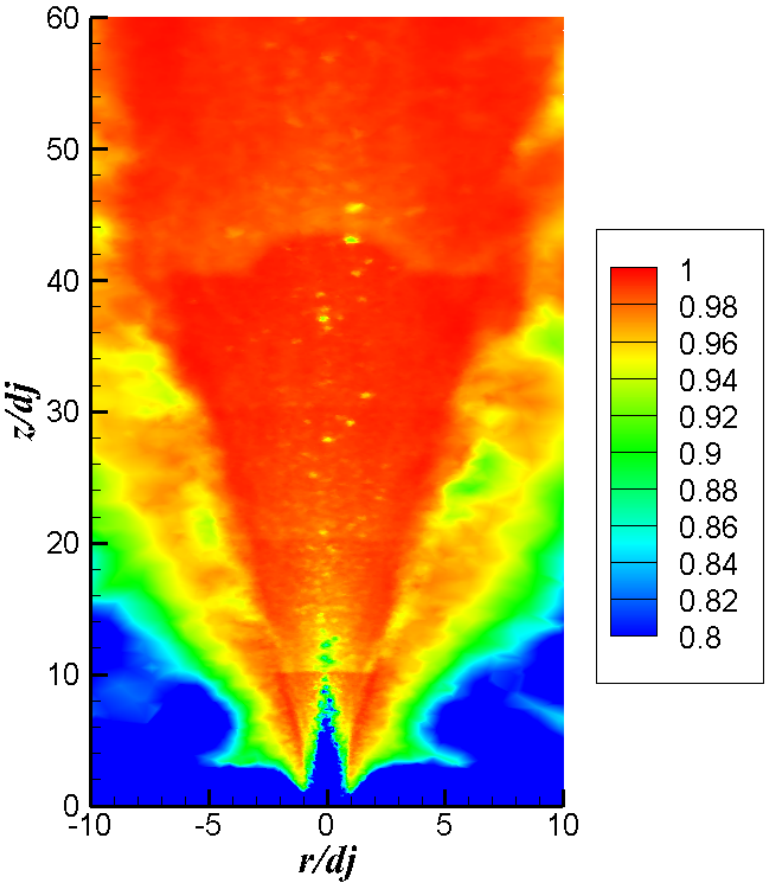

Figure 4.5: LES grid assessment using Pope's criterion [Pope, 2000] showing the fraction of resolved turbulent kinetic energy.

4.1.3.2 Mixing field

In common practice, a fully developed mixing field is required before performing the numerical initialisation of the reacting flow. Unfortunately, no measurements were reported for the mixture fraction field by Ahmed & Mastorakos [2006], however, it was argued that the variation of the mean mixture fraction, $\widetilde{Z}$, in these open jets can be approximated well using a correlation given by [Richards

& Pitts, 1993]:

$$\widetilde{Z}(\hat{z},\hat{r}) = 4.76\,\frac{\sqrt{R_\rho}}{\hat{z}}\exp\left(\frac{-59\,\hat{r}^{\,2}}{\hat{z}^{\,2}}\right), \tag{4.4}$$

where R_ρ denotes the density ratio of the jet fluid to air. $\hat{z} = (z/d_\mathrm{j} - 3.6)$ and $\hat{r} = r/d_\mathrm{j}$ are normalised axial and radial coordinates. Figure 4.6 shows a typical comparison of $\widetilde{Z}$ contours obtained from the correlation and computations for the jet velocity of $U_\mathrm{j} = 25.5$ m/s. The composition of the fuel jet is 70% methane and 30% air in volume. The steady RANS results shown are fully converged and and the LES results are time-averaged values. The equivalence ratio, ϕ, is calculated using $\phi = \widetilde{Z}(1-\widetilde{Z}_{st})/(\widetilde{Z}_{st}(1-\widetilde{Z}))$ and $\widetilde{Z}_{st} = 0.098$ is the stoichiometric mixture fraction. The three iso-lines shown in Fig. 4.6 represent the stoichiometry, lean and rich flammability limits, which are $\widetilde{Z}_\mathrm{l} = 0.05$ and $\widetilde{Z}_\mathrm{r} = 0.143$ respectively for methane-air mixture at 300K and atmospheric pressure.

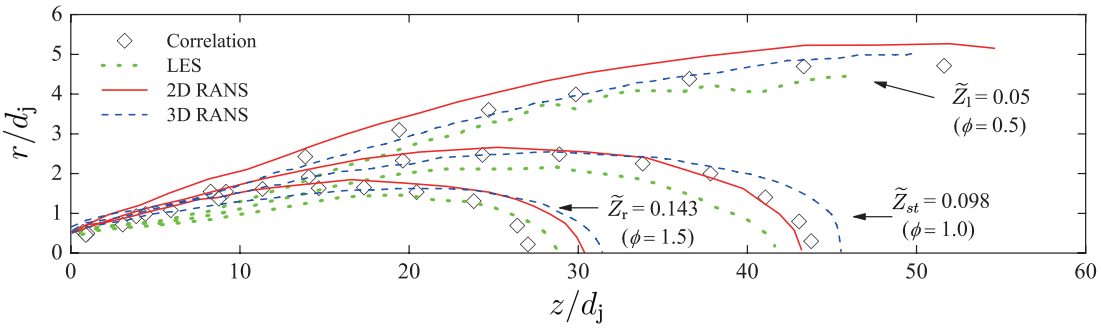

Figure 4.6: Comparison of mixture fraction fields obtained from the simulations and an empirical correlation proposed in [Richards & Pitts, 1993].

It is seen in Fig. 4.6 that the computational results agree well with the empirical correlation for the three critical mixture fraction values considered. As noted earlier in §4.1.3.1, the under-specified inlet turbulence in the LES can lead to an under-predicted spreading angle of the jet in the near field and this can be clearly observed here for $z/d_\mathrm{j} < 10$. However, for the further downstream where the turbulence is mainly driven by the shear, the spreading angle is recovered and a good agreement is obtained between the LES and correlation values. This ensures that the mixing field is well-established for the LES of the spark ignition sequence presented in Chapter 7. The final flame stabilisation height is found

to be in between $z/d_j = 10$ and 20 and thus is not expected to be significantly influenced by the near field turbulence. For the RANS simulations, both the 2D and 3D results are quite close suggesting that the axisymmetric assumption is valid for non-reacting flows as one would expect. Furthermore, these results also suggest that the 2D and 3D reacting flow simulations are initiated from an almost identical cold mixing scenario allowing one to directly investigate the effect of physical dimension on transient evolution of lifted flames, which will be discussed in Chapter 6.

4.2 DLR gas turbine model combustor

4.2.1 Experimental configuration

Figure 4.7a shows a schematic of the dual-swirler burner setup of the experiments conducted by Weigand *et al.* [2006] and Meier *et al.* [2006]. The geometrical and physical details are given in Table 4.2. The injector comprises two coaxial swirling air nozzles and an annular ring of fuel jet nozzles located in between. The exit plane of the inner swirling air and fuel jet is 4.5 mm below the outer swirling air exit, which is defined as $h = 0$ in the axial direction. Dry ambient air was supplied through the inlet located at the bottom of the plenum, and the inner and outer air nozzles have a diameter of 15 and 25 mm, respectively. Non-swirling methane fuel was supplied through 72 square channels (0.5×0.5 mm) as shown in Fig. 4.7b, and these small square geometries are retained in the numerical grid to capture the mixing between the fuel jets and swirling air. Instead of a continuous annular nozzle with a very small slit width (< 0.5 mm), these channel jet injectors were used to obtain a better realisation of the axisymmetric fuel injection so that it is well-defined for numerical simulations. The rectangular combustion chamber is 85 mm in width and 110 mm in height, and its top is connected to an exhaust duct having a diameter of 40 mm and a length of 50 mm.

To investigate the non-reacting flow characteristics in this burner geometry, the methane fuel was substituted by air as the fluid injected through the square injectors [Widenhorn *et al.*, 2009]. The air mass flow rates supplied through the plenum and square injectors are 19.74 and 1.256 g/s, respectively. For velocity

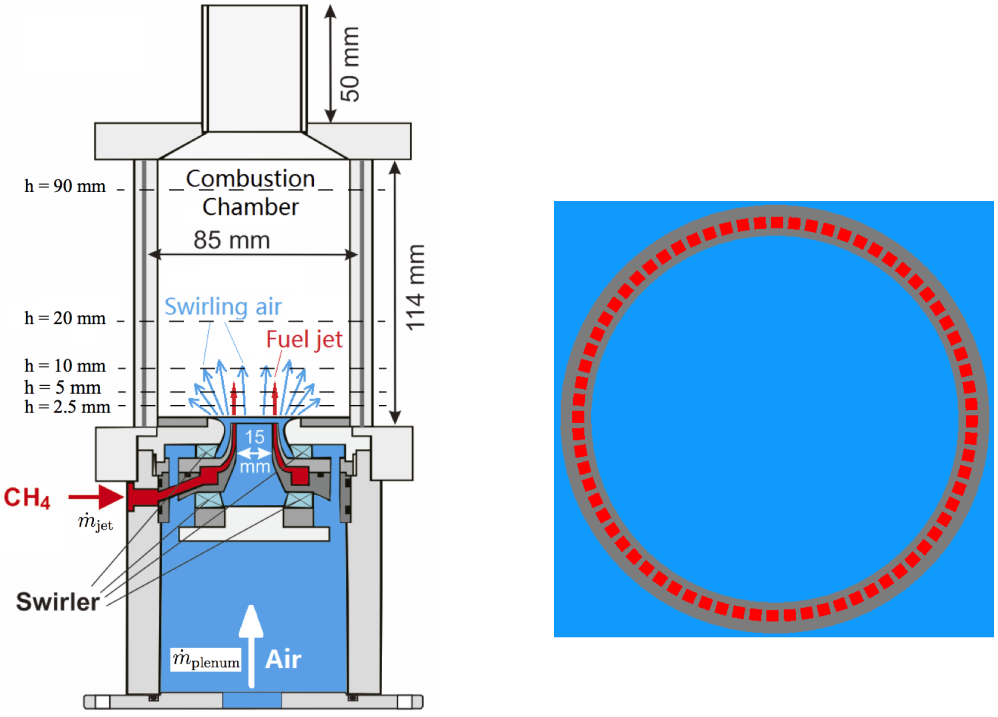

(a) (b)

Figure 4.7: Schematic of (a) the DLR dual-swirler burner setup and (b) the square fuel injectors [Meier *et al.*, 2006; Weigand *et al.*, 2006].

measurements, the Laser Doppler Velocimetry (LDV) technique was used at different axial heights in the chamber as marked in Fig. 4.7a and the lowest height was about $h = 1.5$ mm, providing good validation data for the inlet boundary conditions used in numerical simulations. The swirl number shown in Table 4.2 is calculated using the velocity measurements just above the $h = 0$ mm exit plane given by [Weigand *et al.*, 2006]

$$S = \frac{\int_0^{d_o/2} 2\pi UW\rho\, r\mathrm{d}r}{\int_0^{d_o/2} 2\pi U^2\rho\, r\mathrm{d}r} \approx 0.9, \tag{4.5}$$

where U and W are the axial and swirl (or circumferential) velocities respectively. The corresponding Reynolds number is about 58,000 based on d_o and the mass flow rates used for the cold flow. These cold flow conditions were chosen in

Table 4.2: Details of the DLR gas turbine model combustor for cold air flow.

Property	Value	Description
w_j	0.5 mm	Width of the fuel square jets
d_i	15 mm	Diameter of the inner air (fuel) nozzle
d_o	25 mm	Diameter of the outer air nozzle
$L_x \times L_y \times L_z$	$85 \times 85 \times 100$ mm	Dimensions of the cuboidal combustion chamber
$\dot{m}_\mathrm{jet}$	1.256 g/s	Total mass flow rate of the 72 air jets
$\dot{m}_\mathrm{plenum}$	19.74g/s	Total mass flow rate of air injected into the plenum
S	0.9	Swirl number based on the outer air nozzle diameter
T	295 K	Temperature of methane and air inflows
p	101325 Pa	Operating pressure

the experiments to have the similar flow field features as the mixing field before combustion, so that one can initialise the reacting flow simulation from validated flow and mixing fields. More details for this burner shall be given in Chapter 8.

4.2.2 Numerical setup

A schematic of the computational domain for the DLR burner described above is shown in Fig. 4.8. As in the experiments [Meier *et al.*, 2006; Weigand *et al.*, 2006], the streamwise direction is denoted as the h-direction and x-y is the transverse plane. It can be seen that the air is transported through 24 round tubes from the plenum to the outer swirler. The mass flow splitting between the inner and outer swirlers is driven purely by the plenum geometry and fluid hydrodynamics. For the downstream of the combustion chamber outlet, which is connected to the atmosphere in the experiments [Meier *et al.*, 2006; Weigand *et al.*, 2006], a large cylindrical far field domain is constructed to avoid the numerical issues caused

by the high velocity outflow at the boundary as shown in Figs. 4.8 and 4.9a.

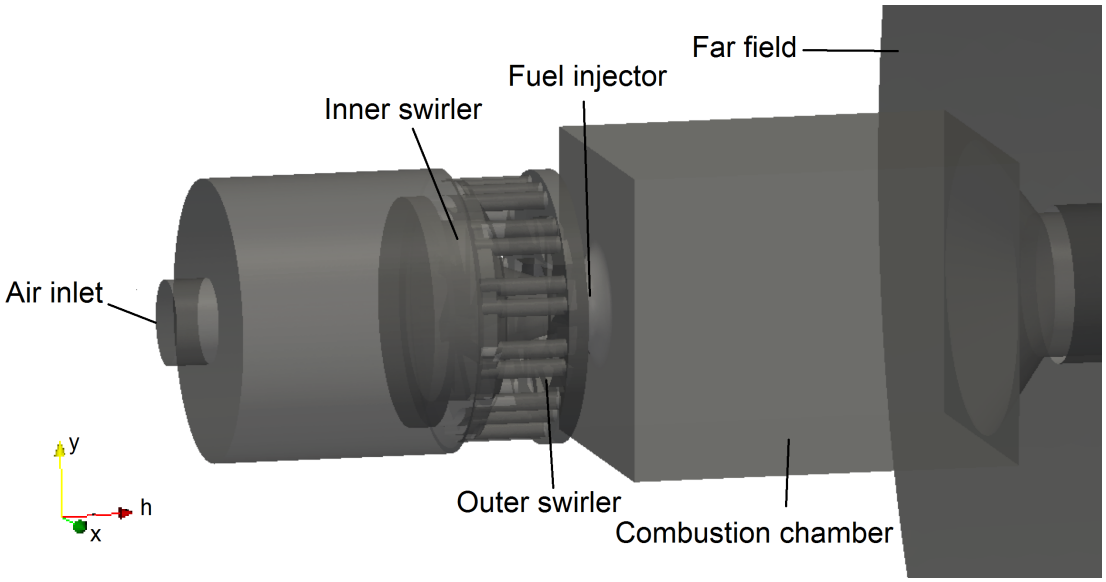

Figure 4.8: Illustration of the computational domain for the DLR burner [Meier *et al.*, 2006; Weigand *et al.*, 2006].

The numerical boundary conditions used for the LES of this burner are given in Fig. 4.9a. Top-hat mass flow rate profiles are specified for both the fuel and air inflow boundaries according to the values given in Table 4.2. No turbulent fluctuation is given for these inlet boundaries, which is consistent with previous studies [See & Ihme, 2014; Widenhorn *et al.*, 2009], since the turbulence inside the combustion chamber is mainly driven by the swirling flows. This is consistent with previous studies [See & Ihme, 2014; Widenhorn *et al.*, 2009]. No-slip and adiabatic wall conditions are employed for the plenum, swirler and combustion chamber walls. As noted above, the downstream of the computational domain is extended and the resulting cylindrical far field sub-domain has a diameter of 400 mm and length of 650 mm as marked in Fig. 4.9a. The entire computational domain is discretised using an unstructured tetrahedral grid and the mesh distribution inside the combustion chamber is shown in Fig. 4.9b. Three mesh zones have been identified and the grid size details are listed in Table 4.3 for three different refinement levels, designated as grid G1 (coarse), G2 (intermediate) and G3 (fine) respectively. These grids are tested for the cold flow experiment described in the previous section and the results of this sensitivity study are presented in §4.2.3.

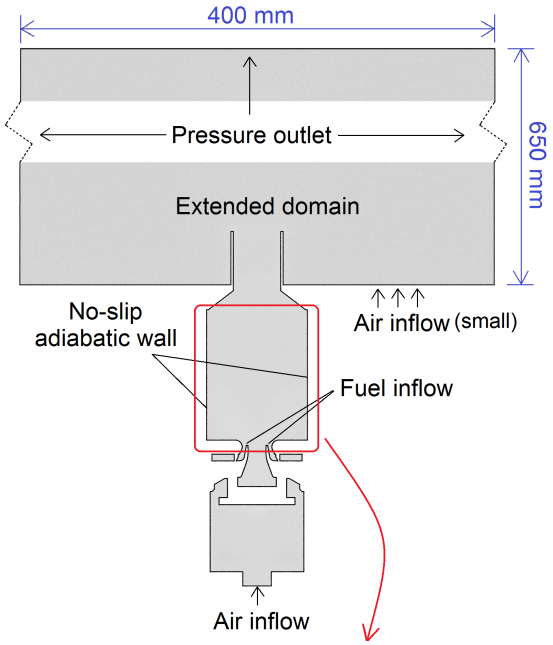

(a)

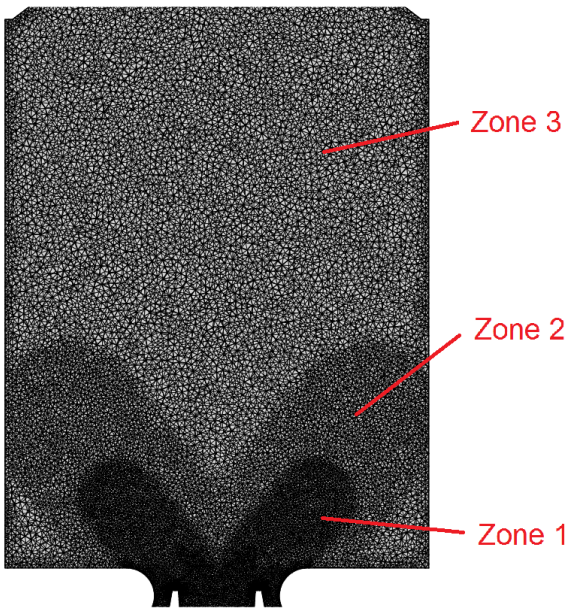

(b)

Figure 4.9: Schematic of (a) the numerical boundary conditions and (b) the mesh distribution inside the combustion chamber.

It should be noted here that for the region near the square jet nozzles where fuel is injected, only five grid points is used for the 0.5 mm nozzle width. This does not resolve the jet shear layer, which is only about 1 mm long before it merges into the swirling air streams and thus should not influence the main flow field. One shall see this in §4.2.3.2 while comparing the LES velocity results with experimental data.

Table 4.3: Numerical grid size details for the DLR burner.

units [mm]	G1	G2	G3
Zone 1	2	1.5	1
Zone 2	1.5	1	0.6
Zone 3	1.2	0.5	0.3
Total cell number	12M	15M	20M

The cold flow LES is performed using the LES-OpenFOAM solver described in §3.4.2. Equations (3.24) and (3.25) are solved for pure air flow simulation. The unresolved SGS stresses are modelled using the Smagorinsky model given in Eq. (3.30) with the model constant $C_S = 0.167$. The computation is conducted using 1080 2.7-GHz Intel Xeon E5-2697 (Ivy Bridge) cores on the UK's national supercomputer ARCHER. A time-step size of 2×10^{-7} s is used to satisfy CFL $<$ 0.3 for the entire computational domain. The Flow-Through-Time (FTT) for this burner is estimated as

$$\text{FTT} = \frac{h_{\text{chamber}}\ A_{h=0}\ \rho_{\text{air}}}{\dot{m}_{\text{total}}} \approx 2.6 \text{ ms} \tag{4.6}$$

where $h_{\text{chamber}} = 114$ mm is the height of the combustion chamber and $A_{h=0}$ is the fluid flowing area on the $h = 0$ mm exit plane. The total mass flow rate is obtained as $\dot{m}_{\text{total}} = \dot{m}_{\text{jet}} + \dot{m}_{\text{plenum}}$. In order to obtain a developed flow field, 8 FTT is first computed and then the LES statistics are obtained using samples collected over the next 15 FTT as in the previous studies [See & Ihme, 2014; Widenhorn *et al.*, 2009]. The wall-clock time required for this entire computation is about 24, 30 and 45 hours for grid G1, G2 and G2 respectively using 1680 cores.

4.2.3 Cold flow results

4.2.3.1 Swirling flow characteristics

The grid G2 with the intermediate refinement described in Table 4.3 is chosen as the base case to demonstrate the general flow characteristics in this sub-section. Figure 4.10 shows the two-dimensional x-h plane contours for axial (U), radial

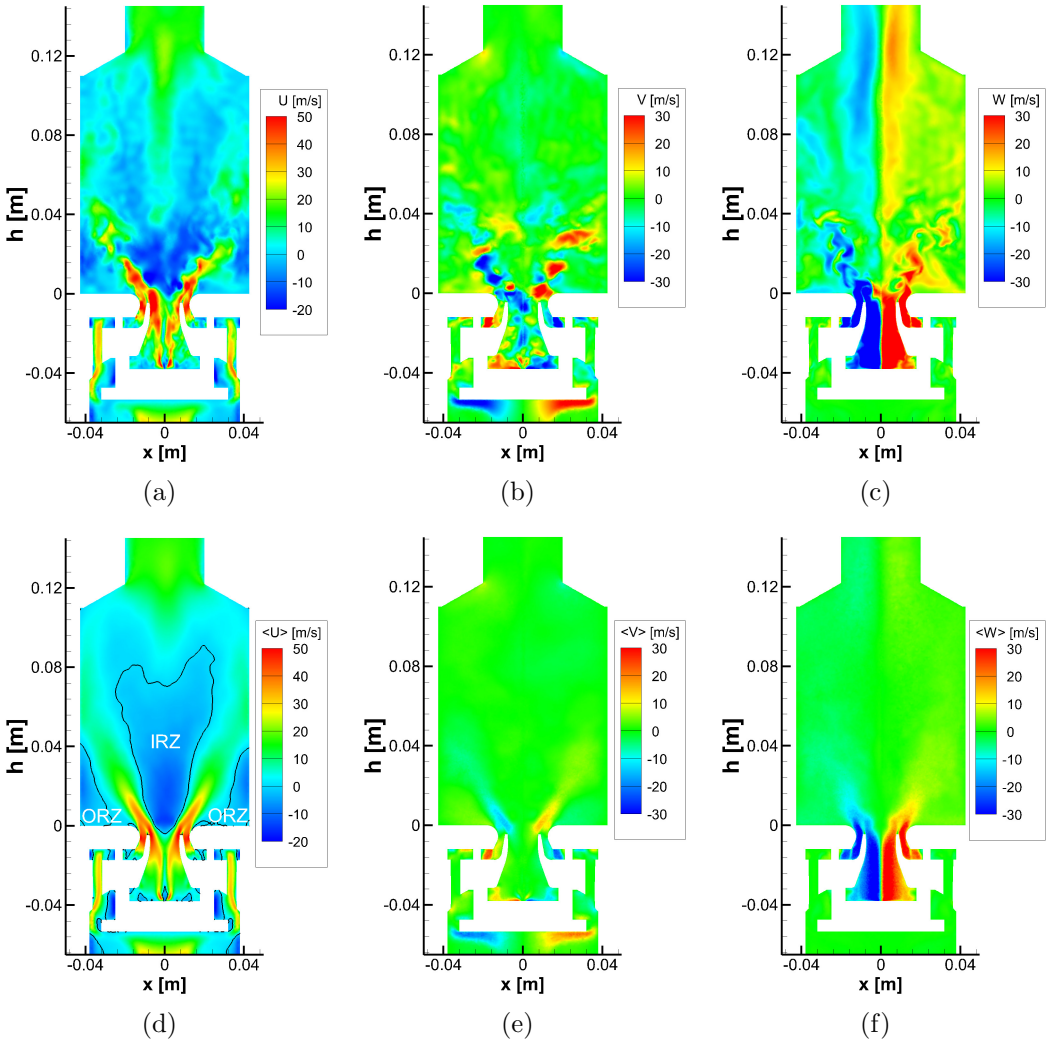

Figure 4.10: Two-dimensional x-h plane contours for instantaneous filtered (the top row) and time-averaged (the bottom row) axial (U), radial (V) and swirl (W) velocities. The black line corresponds to zero axial velocity iso-contour.

(V) and swirl (W) velocity components. The instantaneous filtered velocities are shown in Figs. 4.10a-4.10c (the top row), and the time-averaged values are plotted in Figs. 4.10d-4.10f (the bottom row) respectively. The black line in Figs. 4.10a and 4.10d corresponds to the zero axial velocity iso-contour marking the recirculation zones. A Y-shaped inner recirculation zone (IRZ) is seen in Fig. 4.10d, which is formed because of the converging geometry at the burner outlet. In the upstream region close to the nozzle exit, the IRZ extends to below $h = 0$ mm suggesting a strong flow recirculation. A outer recirculation zone (ORZ) is also observed in Figs. 4.10a and 4.10d. To see these recirculating flow motions more clearly, the two-dimensional streamline plots based on the axial and radial velocities are shown in Figs. 4.11a and 4.11b for the instantaneous and averaged fields respectively. Slight asymmetry is seen in Fig. 4.11b as also observed in the experimental data [Weigand *et al.*, 2006].

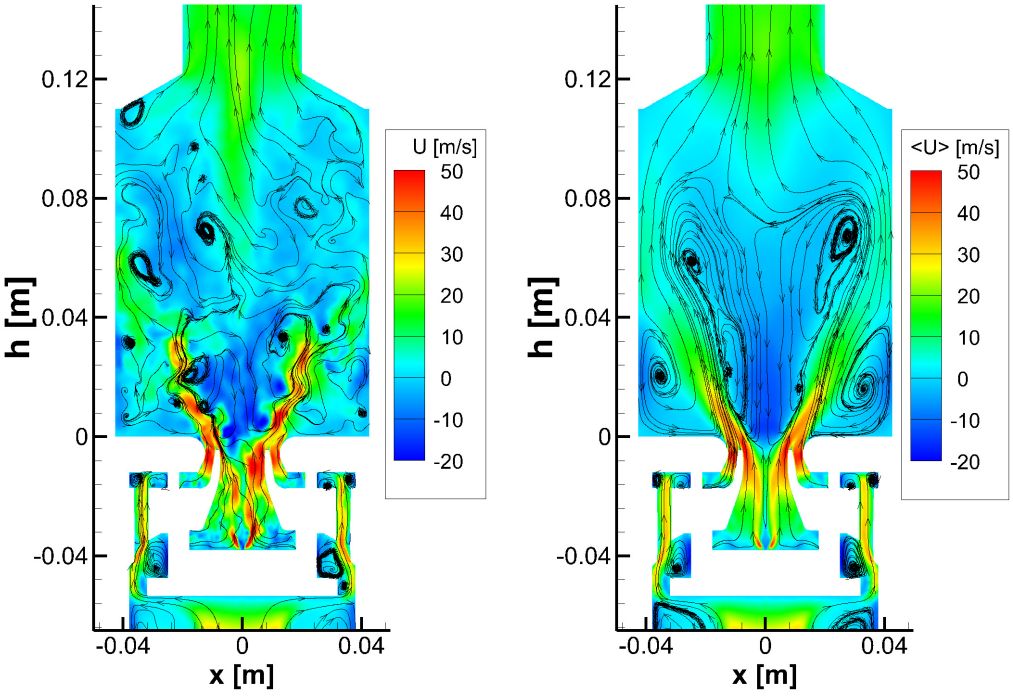

(a) (b)

Figure 4.11: Two-dimensional (x-h plane) streamlines for the (a) instantaneous and (b) averaged velocity fields.

For high swirl number flows (typically $S > 0.6$ [Candel *et al.*, 2014]), a he-

lical hydrodynamic instability appears in the form of a precessing vortex core (PVC) [Syred, 2006] as shown in Fig. 4.12. Here the PVC is visualised using a low pressure iso-surface with a typical dynamic pressure of −1425 Pa. The instantaneous axial velocity contour on a middle-plane is also plotted this figure along with the PVC, which is found to be in between the swirling flow stream and the IRZ as in previous studies [See & Ihme, 2014; Syred, 2006; Widenhorn *et al.*, 2009].

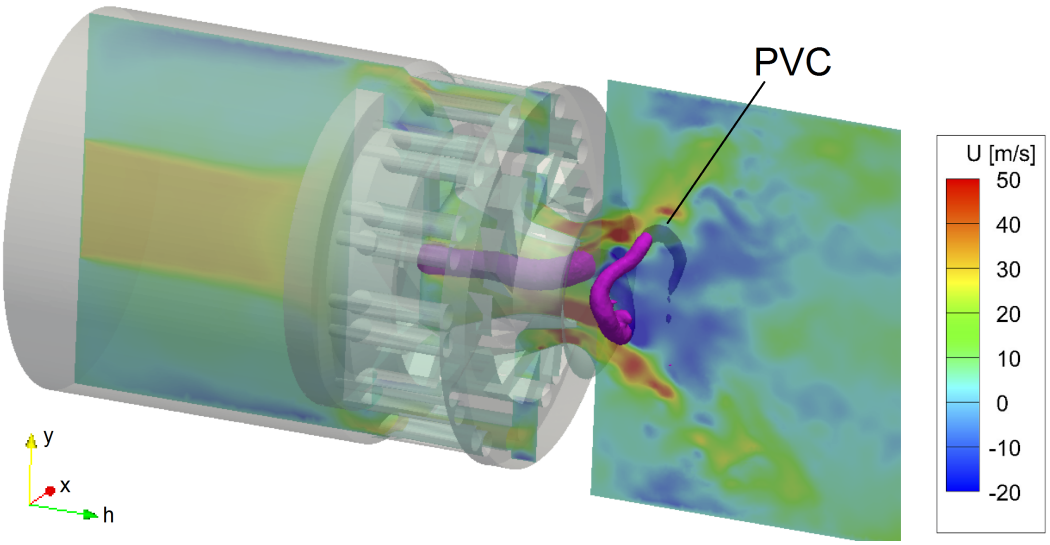

Figure 4.12: Visualisation of the PVC using a pressure iso-surface along with a middle-plane snapshot of axial velocity.

To show more turbulence structures, Figure 4.13 presents a typical iso-surface of the second invariant of the velocity gradient tensor (Q-criterion [Davidson, 2015]), $\mathcal{Q} = 2.5 \times 10^8$ s^{-2}. The colour shown corresponds to the magnitude of vorticity, $|\widetilde{\omega}|$, on the iso-surface. Although the grid refinement used here seems insufficient to resolve all the small turbulence structures in the swirlers, some large-scale vortex tubes are observed in the combustion chamber. It is also seen that the value of $|\widetilde{\omega}|$ is high for the flow in the outer swirler due to the small cross-sectional area of the swirler channels, compared to that for the inner swirler. As a result, the radial profile of the swirl velocity at the nozzle exit is expected to have a bimodal shape with a high outer peak and a low inner one, which can then be used to assess the accuracy of swirling flow computed using LES. One shall

see this while comparing the LES results with the experimental data in the next sub-section.

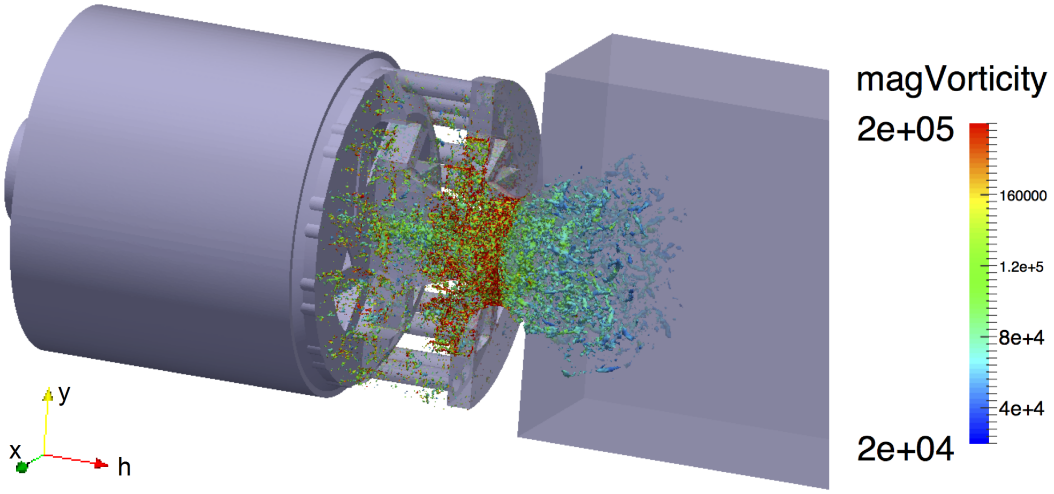

Figure 4.13: Iso-surface of the second invariant of the velocity gradient tensor (Q-criterion) for $\mathcal{Q} = 2.5 \times 10^8$ s^{-2}, coloured by the vorticity magnitude in units of s^{-1}.

4.2.3.2 Statistics and grid sensitivity

In the cold flow experiments [Widenhorn *et al.*, 2009], LDV measurements of velocity profile were taken in a chamber middle plane at five axial locations, h = 2.5, 5, 10, 20 and 90 mm, as marked in Fig. 4.7. These experimental measurements, both mean and r.m.s. values, are used to compare with the LES results in Figs. 4.13, 4.13 and 4.13 for the axial, radial and swirl velocities respectively. Three sets of LES results shown are for the three numerical grids detailed in Table 4.3. Note that the r.m.s. values in the LES are computed using the resolved velocity variance, for example, the r.m.s. axial velocity, $\widetilde{U}_{\text{r.m.s.}}$, is obtained using Eq. (4.3). As can be seen in Figs. 4.13, 4.13 and 4.13, a strong grid sensitivity is observed for all three velocity components when the grid size increases from G1 (12M) to G2 (15M). The comparison between the experimental data [Widenhorn *et al.*, 2009] and the LES results obtained for G2 is found to be very good, significantly improved from that for G1. However, the simulation results tend to

converge when further increasing the mesh refinement level from G2 (15M) to G3 (20M), both having a very good agreement with the measured values.

The measured data of the velocity profiles at a close-to-nozzle axial location of $h = 2.5$ mm allows us to examine the LES prediction of the swirling flow at the combustion chamber inlet. It is shown in Fig. 4.13a that at $h = 2.5$ mm the measured mean axial velocity peaks at around $|x| = 12$ mm with the value of about 40 m/s. Only one peak is observed in the radial direction suggesting that the two flow streams respectively coming from the inner and outer swirlers merge into one main inflow stream immediately after exiting the nozzle, which can be clearly seen in Fig. 4.10d. The computed LES profile agrees well with the experimental data at this close-to-nozzle axial location for grid G2 and G3 suggesting that the flow motions inside the swirlers, upstream of the combustion chamber, are captured quite well by the LES. However, the simulation based on

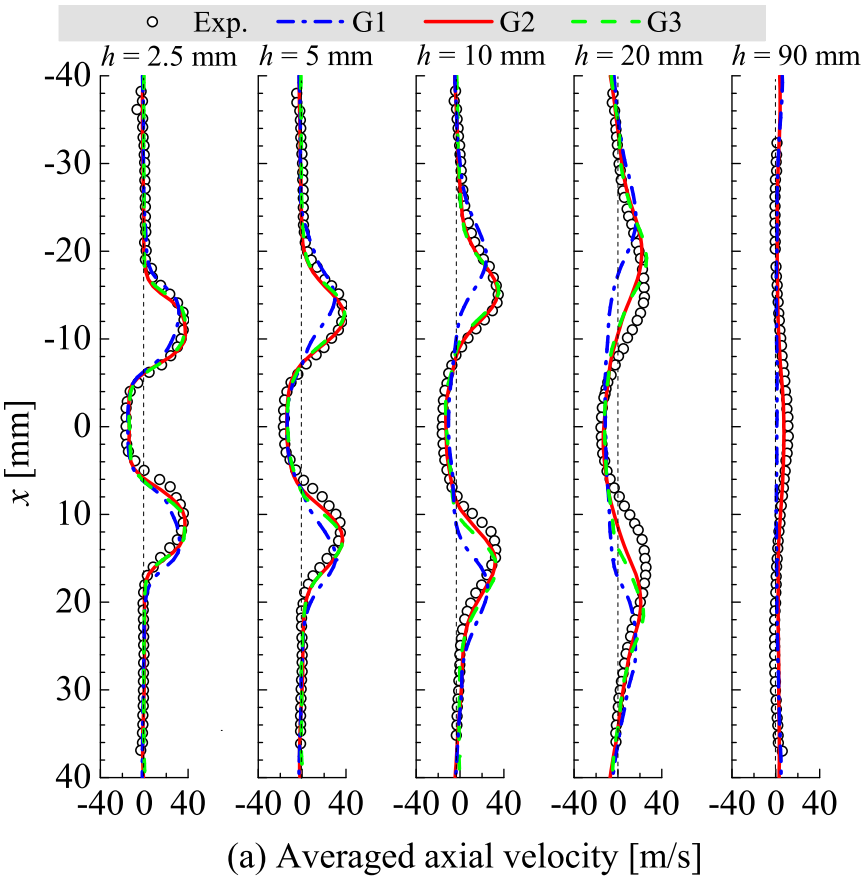

(a) Averaged axial velocity [m/s]

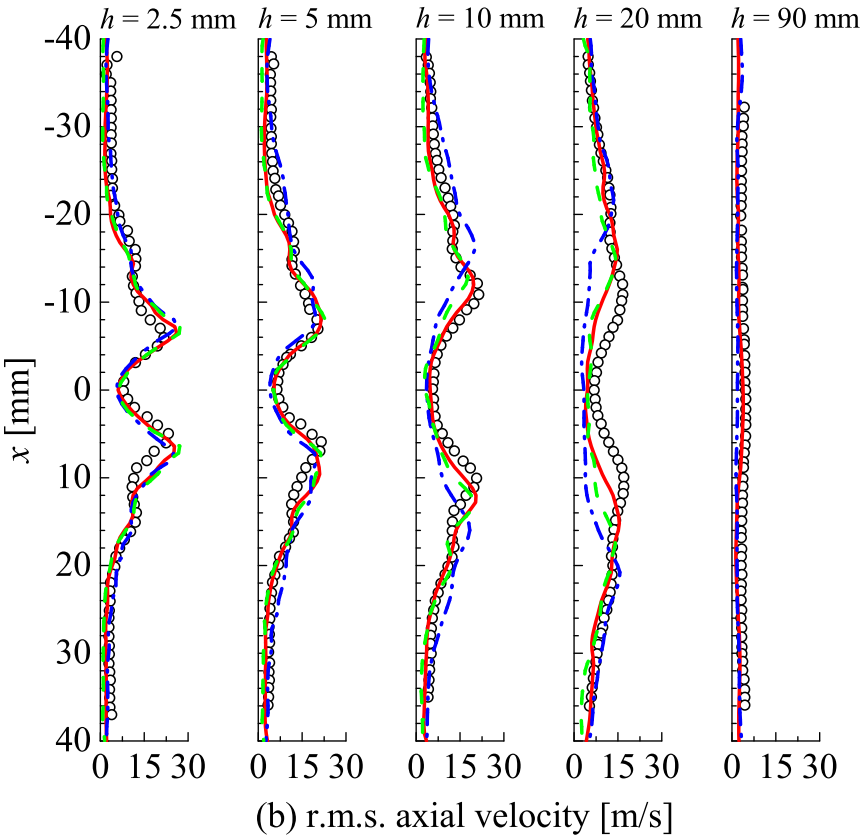

Figure 4.13: Cold flow comparison of axial velocity profiles: (a) mean values (b) r.m.s fluctuations, obtained from the experimental measurements [Widenhorn *et al.*, 2009] and the LES using grid G1, G2 and G3.

the coarse grid G1 under-predicts the peak mean axial velocity with the peak located further away from the centre axis of the chamber, i.e. $x = 0$ mm. This becomes more evident in Fig 4.13a for the downstream locations showing an approximately 80% over-prediction for the IRZ width at $h = 20$ mm for G1, as suggested by the $\langle \widetilde{U} \rangle = 0$ line (dashed). In contrast, this predicted IRZ width agrees reasonably well with the measured value for the refined grid G2 and G3.

The dislocated inflow streams for G1 can be also seen in Fig. 4.13a showing the mean radial velocity, $\langle \widetilde{V} \rangle$, profiles. The simulated maximum value of $\langle \widetilde{V} \rangle$ is found to be higher for G1 than that for the experimental data, which could be the reason for the under-predicted $\langle \widetilde{U} \rangle$ values. This may be caused the diverging geometry at the outer swirler nozzle exit, which results in a sudden expansion of

cross-sectional area in the streamwise direction forming a flow separation from the nozzle wall. One can see this in Fig. 4.14a showing the instantaneous axial velocity at a typical instant and the flow separation is illustrated using the $\widetilde{U} = 0$ iso-contour as highlighted. As this occurs in a relatively small scale, local mesh refinement is required in order to resolve the flow separation from the wall as presented in Fig. 4.14b for the G2 case. The refined grid size for the cells next to the wall is 0.1 mm and this treatment is also applied for grid G3. It is found that the spreading angle of the swirling flow in the combustion chamber is influenced quite significantly by this local mesh refinement as has been observed earlier in Fig. 4.13a.

As noted in the previous sub-section, the mean swirl velocity profile has two peaks in the near nozzle exit region for this dual-swirler burner, which is shown

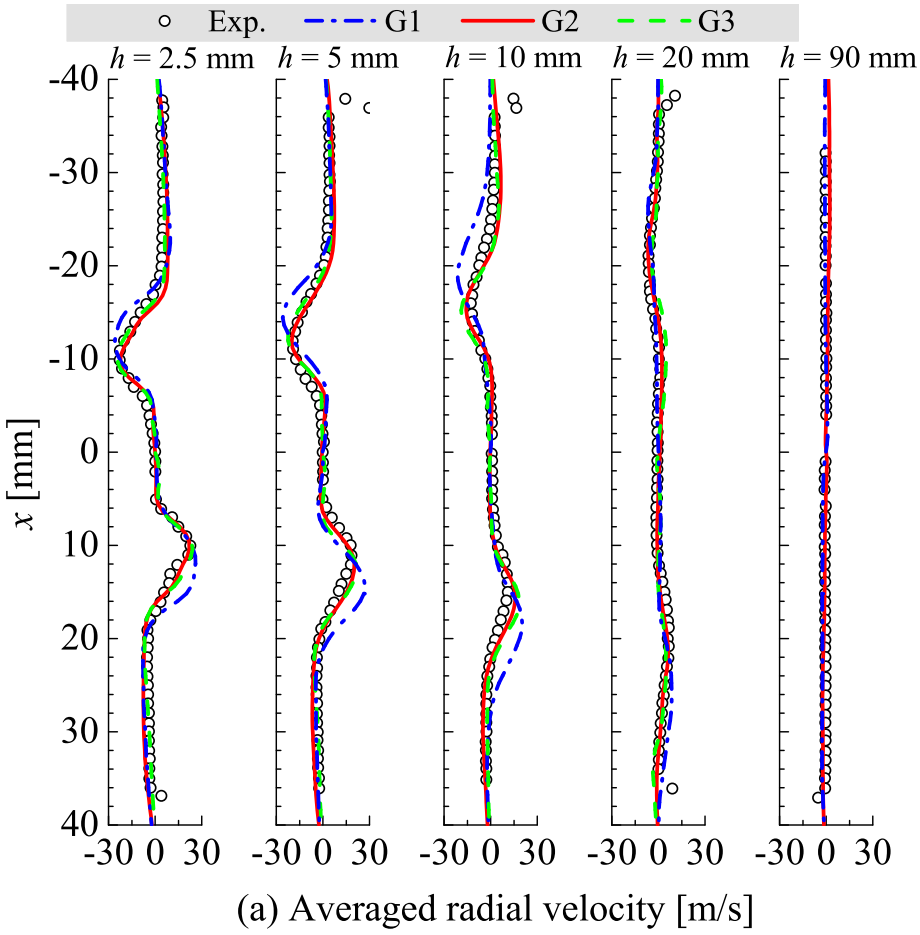

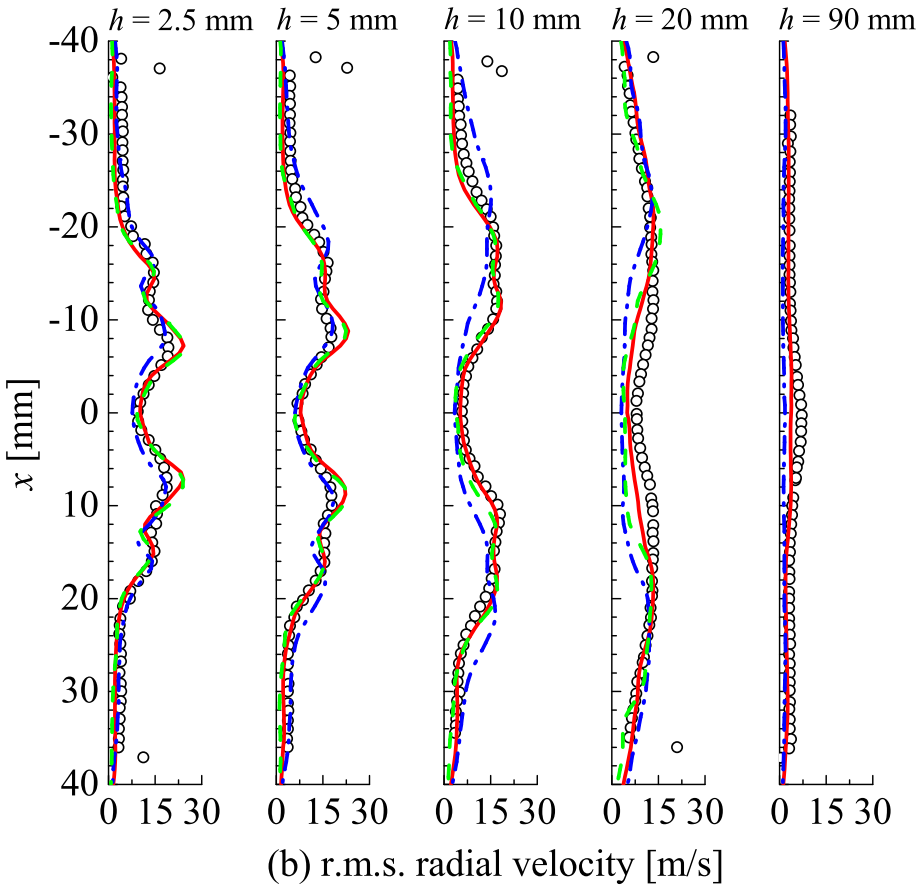

Figure 4.13: Cold flow comparison of radial velocity profiles: (a) mean values (b) r.m.s fluctuations, obtained from the experimental measurements [Widenhorn *et al.*, 2009] and the LES using grid G1, G2 and G3.

in Fig. 4.13a for $h = 2.5$ and 5 mm axial positions. The outer peak has a higher value of $\langle \widetilde{W} \rangle \approx 30$ m/s, compared to the inner one with $\langle \widetilde{W} \rangle \approx 20$ m/s at $h = 2.5$ mm. This is consistent with Fig. 4.13 showing higher flow vorticity in the outer swirler. It is also observed in Fig. 4.13a that the computed radial profile of $\langle \widetilde{W} \rangle$ at $h = 2.5$ mm agrees very well with the experimental measurements for all three cases. This further supports that the discrepancies found in Figs. 4.13a and 4.13a for the mean axial and radial velocities are caused by the flow separation discussed above. The flow field in the plenum and two swirlers, upstream of the inlet of the combustion chamber, is well predicted by the LES for all three grid sizes. Even so, the computed $\langle \widetilde{W} \rangle$ values for G1 start to deviate from the

measured data beyond $h = 5$ mm suggesting that grid resolution is inadequate inside the combustion chamber for G1.

As for the r.m.s. fluctuations, the axial velocity exhibits a pronounced peak fluctuation of $\widetilde{U}_{\text{r.m.s.}} \approx 25$ m/s in the inner shear layer between the inflow stream and IRZ at $h = 2.5$ mm as can be seen in Fig. 4.13b. In contrast, Figs. 4.13b and 4.13b show that $\widetilde{V}_{\text{r.m.s.}}$ and $\widetilde{W}_{\text{r.m.s.}}$ have a broader fluctuating region from the inner shear layer to the outer one with the maximum value between 15 and 20 m/s. The LES results (resolved r.m.s.) for case G1 under-predict the r.m.s. values at all axial positions suggesting a substantial unresolved sub-grid scale fluctuations. By increasing the refinement level for grid G2 and G3, the difference between the computed and measured values becomes quite small especially for the near nozzle regions ($h < 20$ mm).

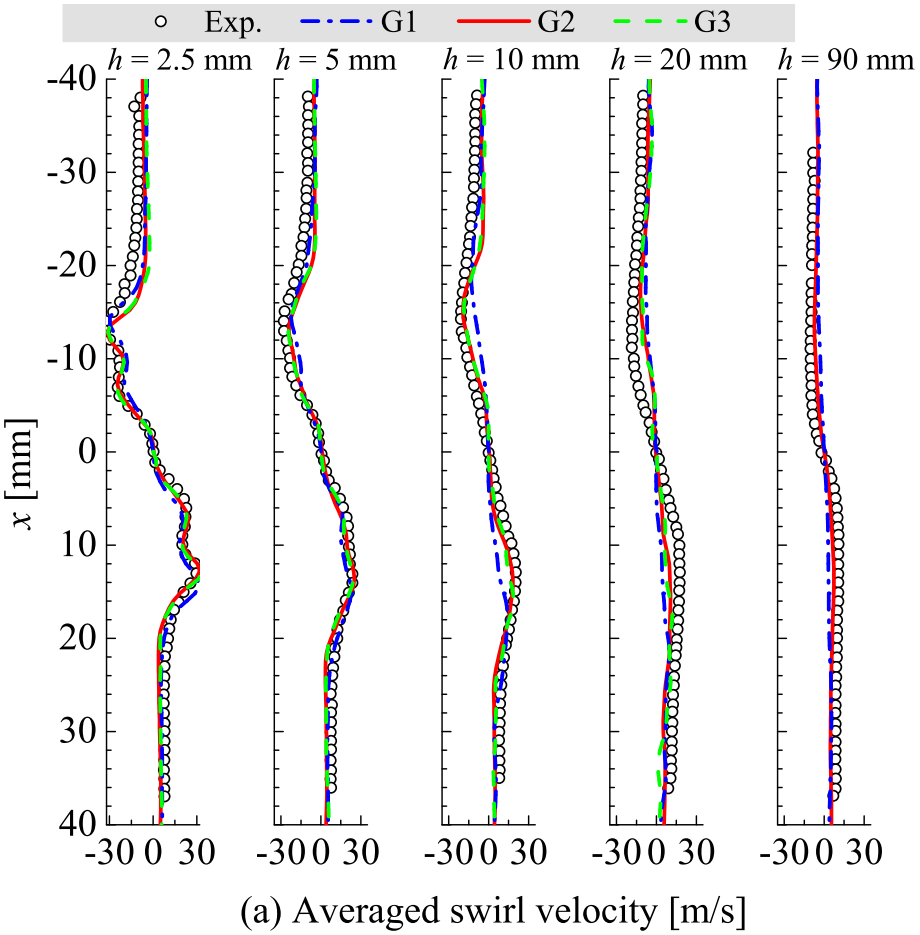

(a) Averaged swirl velocity [m/s]

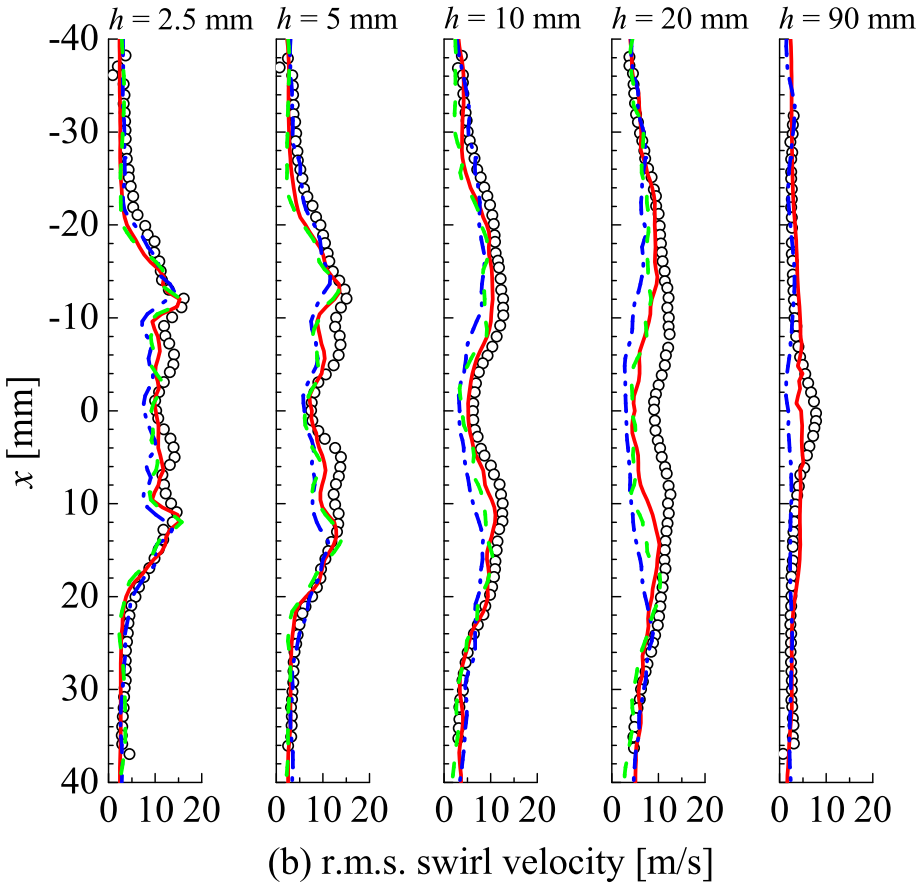

Figure 4.13: Cold flow comparison of swirl velocity profiles: (a) mean values (b) r.m.s fluctuations, obtained from the experimental measurements [Widenhorn *et al.*, 2009] and the LES using grid G1, G2 and G3.

In general, the grid sensitivity analysis above shows that the coarse grid G1 is insufficient for the LES of this DLR burner, while the simulation results obtained using the refined grid G2 are in overall good agreement with the experimental data [Widenhorn *et al.*, 2009]. No evident improvement is observed by using the further refined grid G3 and the results are found to be grid-independent between G2 and G3. Thus, grid G2 with 15 million unstructured tetrahedral cells is chosen for the subsequent reacting flow simulations, which will be discussed in Chapter 8.

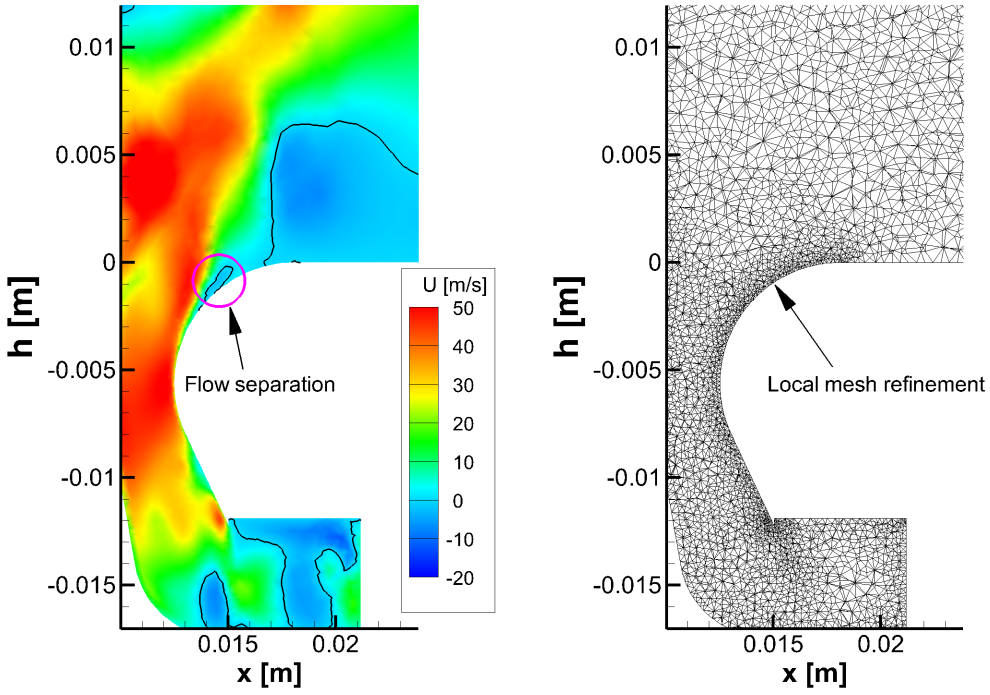

(g) (h)

Figure 4.14: Illustration of the (a) flow separation at the outer swirler nozzle exit and (b) the local mesh refinement near the nozzle outer wall for grid G2. The black line corresponds to the zero-velocity iso-contour.

4.3 Summary

The non-reacting flows for the two test cases considered in this thesis, namely the Cambridge non-piloted jet burner [Ahmed & Mastorakos, 2006] and the DLR dual-swirler gas turbine model combustor [Widenhorn *et al.*, 2009], are simulated in this chapter. The numerical models, grids and boundary conditions are validated using the experimental data and empirical approximations. The comparison between the computational results and measurements is very good for both cases. A grid sensitivity study is conducted for the DLR burner due to its complex flow and geometrical conditions, and an optimised grid size is chosen for good accuracy and reasonable computational cost. These cold flow studies serve as the preparatory work for the reacting flow simulations presented in the following chapters:

- Chapter 5 and 6: steady and unsteady RANS simulations of the Cambridge lifted jet flames.
- Chapter 7: Large eddy simulation of the Cambridge lifted jet flames.
- Chapter 8: Large eddy simulation of the DLR swirling flames.

Chapter 5

Turbulent Lifted Methane Jet Flames

The RANS modelling methodology described in Chapter 3 has been assessed for a lifted hydrogen flame in an earlier study [Ruan *et al.*, 2014a]. The simulation results agreed well with the experimental data for the flame brush structure and lift-off height for a range of jet velocities. To further evaluate the model capabilities for more realistic hydrocarbon flames, this chapter presents a numerical study of turbulent lifted methane jet flames investigated experimentally by Ahmed & Mastorakos [2006] for a range of air-dilution levels and inlet velocities. The simulation results are compared against the experimental measurements and the effects of various modelling approaches are discussed on a physical basis.

5.1 Experimental test case

Based on the experimental setup illustrated earlier in Fig. 4.1 (details listed in Table 4.1), Ahmed & Mastorakos [2006] investigated the effect of bulk mean velocity, U_{j}, at fuel jet exit ranging from 9 to 30 m/s with corresponding Reynolds numbers of 2938 to 9793. The influence of air dilution of the fuel jet on flame lift-off height, L_{f}, was also examined in the experiments for four different dilution levels and the mole fractions of dilution air in the fuel jet considered were X = 10%, 20%, 30% and 40%. A dilution level of 50% or more was reported

Table 5.1: Details of the lifted flame experiments [Ahmed & Mastorakos, 2006].

Flame	Air%	$\widetilde{Z}_{\mathrm{st}}$	Jet velocity range [m/s]
F0	0	0.055	$12.5 \sim 28.5$
F1	10	0.068	$12.5 \sim 28.5$
F2	20	0.08	$16 \sim 28.5$
F3	30	0.098	12.5 & 25.5
F4	40	0.12	$16 \sim 22$

to produce highly unstable flame and thus it was excluded in the experiments. These flames are denoted as F0 (0% dilution), F1, F2, F3 and F4 in this study and their details are listed in Table 5.1. Since the behaviour of F0 and F1 were found very similar in the experiments, three flames, F0, F2 and F4 listed in Table 5.3 are considered for steady RANS simulations. The transient evolution of flame position from its initial sparking location was reported for $X = 30\%$ case. Following the experiment, the F3 flame is used for URANS and LES methodologies to study the transient flame propagation and flame leading edge dynamics respectively in the later Chapters 6 and 7.

In the experiments [Ahmed & Mastorakos, 2006] for the pure methane jet case F0, a flame attached to the jet nozzle lip was first stabilised using a small fuel jet velocity of $U_{\mathrm{j}} = 6.3$ m/s. By gradually increasing U_{j}, the flame started to detach after U_{j} exceeding 13 m/s. At each velocity reported, the flame was kept for a long enough time to avoid the transition effects before measuring the flame lift-off height. The same procedure was conducted also for the diluted cases. Both the high-speed camera (line-of-sight image) and hydroxyl Planar Laser-Induced Fluorescence (OH PLIF) techniques were used to capture the flame stabilisation position and quantitatively similar results were found in the experiments [Ahmed & Mastorakos, 2006]. These measured values of L_{f} are compared with the computational results obtained using different models in this study and the numerical details of these models are described next.

5.2 Numerical modelling details

The steady RANS simulation approach is used to predict the quasi steady-state flame lift-off height in the present work. The Favre-averaged conservation equations for mass, momentum and total enthalpy respectively given in Eq. (3.2), (3.3) and (3.4) are solved eliminating the unsteady term on the LHS. The standard two-equation k-ϵ model is used for turbulence because it is simple and adequate for jet flows considered in this study. The modelled transport equations for the turbulent kinetic energy, $\widetilde{k}$, and its dissipation rate, $\widetilde{\varepsilon}$, are described in Eqs. (3.9) and (3.10). The modified model constants are validated using the cold flow results discussed in §4.1.3.1.

For the combustion modelling, the RANS model discussed in §3.1.1 using a presumed joint PDF with mixture fraction-progress variable correlation is applied to capture the partially premixed combustion process at the base of the lifted flames considered in this study. The scalar transport equations solved are Eqs. (3.14)-(3.18) and the total enthalpy equation given in Eq. (3.4). Here it is worthwhile to recall that the mean reaction rate, $\overline{\dot{\omega}_{\mathrm{c}}^{*}}$, described in §3.2, includes both contributions from the premixed, $\overline{\dot{\omega}}_{\mathrm{c}}$, and non-premixed, $\overline{\dot{\omega}}_{\mathrm{np}}$, combustion modes. The premixed contribution takes into account the statistical correlation between the mixture fraction and progress variable fluctuations. These separate models and their modularity allow one to systematically study their individual influences on the lift-off height by including one effect at a time. This consideration yields four possible combinations of these models as listed in Table 5.2. The case A has contribution from only premixed mode without the effects of Z-c correlation, i.e., the JPDF in Eq. (3.47) is modelled as the product of two marginal PDFs. The effect of this correlation is included in the case B. The cases C and D include contributions from premixed and non-premixed modes, and case C excludes the influences of Z-c correlation whereas case D includes this effect.

The numerical boundary conditions and computational grid used are the same as for the cold flow simulations discussed in §4.1.2 and their implementation in the RANS-Fluent solver is described earlier in §3.4.1 using UDSs and UDFs. For the scalar fields, $\widetilde{Z}$ is 1 at the jet exit and 0 for the air co-flow. The values of $\widetilde{h}$ obtained using species enthalpies and their mole fractions are specified for the

Table 5.2: Model combination detail for $\overline{\dot{\omega}_c^*}$.

Case	A	B	C	D
Modelling of $\overline{\dot{\omega}_c^*}$	$\overline{\dot{\omega}}_c$	$\overline{\dot{\omega}}_c$	$\overline{\dot{\omega}}_c + \overline{\dot{\omega}}_{np}$	$\overline{\dot{\omega}}_c + \overline{\dot{\omega}}_{np}$
Z-c correlation included or not?	No	Yes	No	Yes

respective inlet streams. The other scalars, $\widetilde{c}$, $\widetilde{Z''^2}$, $\widetilde{c''^2}$ and $\widetilde{Z''c''}$ are set to be zero at the inlet boundaries. For the side boundary, the normal gradient of these scalars are specified to be zero.

The flame is ignited numerically on a fully converged cold flow and scalar mixing solution. Following the experiments of Ahmed & Mastorakos [2006], the flame kernel is initialised on the jet axis at a downstream location of about 30 and $40d_j$ from the jet exit. This kernel has a size of 2×2 mm^2 and it is set to have $\widetilde{c} = 1$ representing fully burnt products. The energy in this kernel is about 100 mJ as provided by a spark in the experiments of Ahmed & Mastorakos [2006]. Different sizes and energy levels of this initial kernel are tested and it is found that the final lift-off height is not influenced by these parameters. Detailed modelling of the spark ignition and its plasma is beyond the scope of this work. Some attempt in this regard was made by Lacaze *et al.* [2009b] using one-step chemistry and an energy deposition ignition model in their LES study. However, only one case having $X = 30\%$ and $U_j = 25.5$ m/s was considered in their work because of the high computational cost. All of the RANS simulations reported in this study are started by initialising a kernel as described above in the respective converged cold flow and scalar mixing solutions.

5.3 Results and discussion

5.3.1 Mean flow fields

Figures 5.1, 5.2 and 5.3 show the computed mean flame patterns of the flames F0, F2 and F4 using colour contours for mixture fraction, progress variable and its mean reaction rate, $\overline{\dot{\omega}_c^*}$, which is computed using the case D described in Table 5.2.

This model includes both the non-premixed combustion mode contribution and Z-c correlation influence. The stoichiometric mixture fraction, $\widetilde{Z}_{st}$, iso-surface is highlighted in these figures using a black thick line.

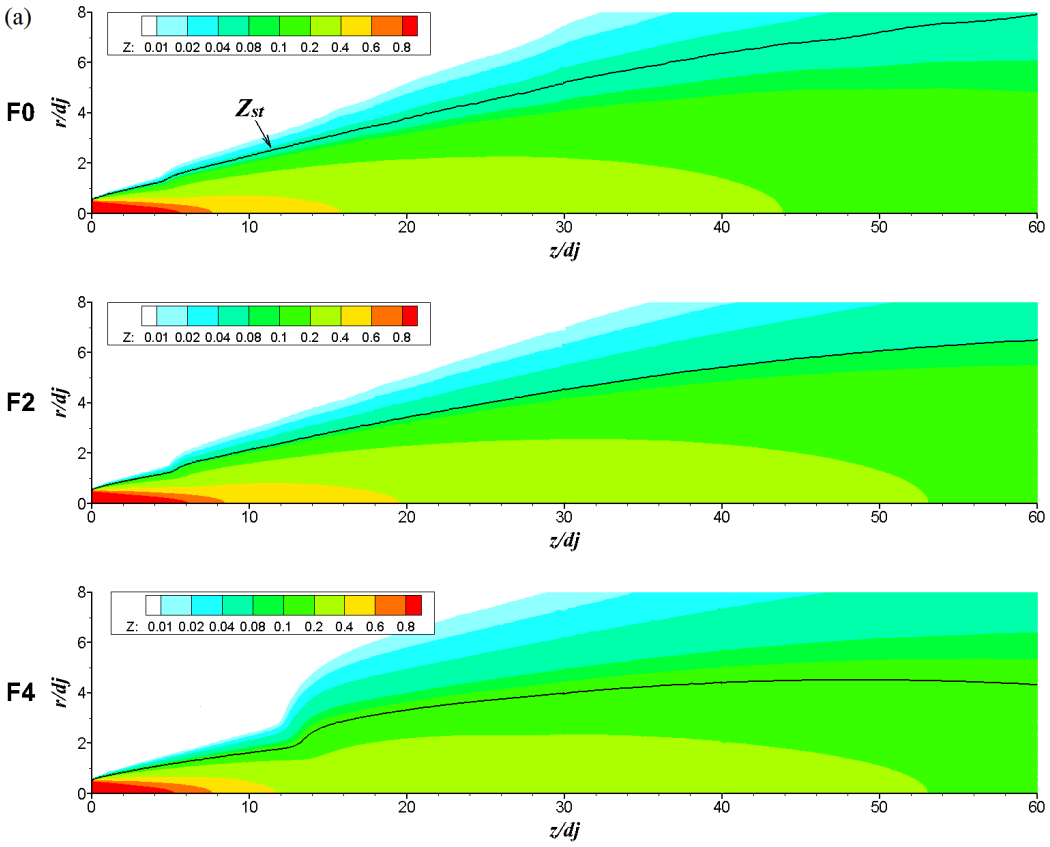

Figure 5.1: Computed mean mixture fraction field for flames F0, F2 and F4 using model D in Table 5.2. The thick black line corresponds to the stoichiometric mixture fraction. The jet exit velocity is $U_{\rm j} = 16$ m/s, and some relevant part of the computational domain is shown above.

It is seen in Fig. 5.1 that along the $\widetilde{Z}_{st}$ line the flow diverges in the radial direction after encountering the lifted flame base due to the heat expansion effects. As the air-dilution level increases from F0 in Fig. 5.1a to F4 in Fig. 5.1c, the flame is stabilised at a larger lift-off height with an increased flow divergence. This effect is further discussed in §5.3.5. For the progress variable contours shown in Fig. 5.2, the flame brush of F4 is broader than that of the non-diluted F0 and slightly diluted F2. This can be seen more clearly in Fig. 5.3 where the values

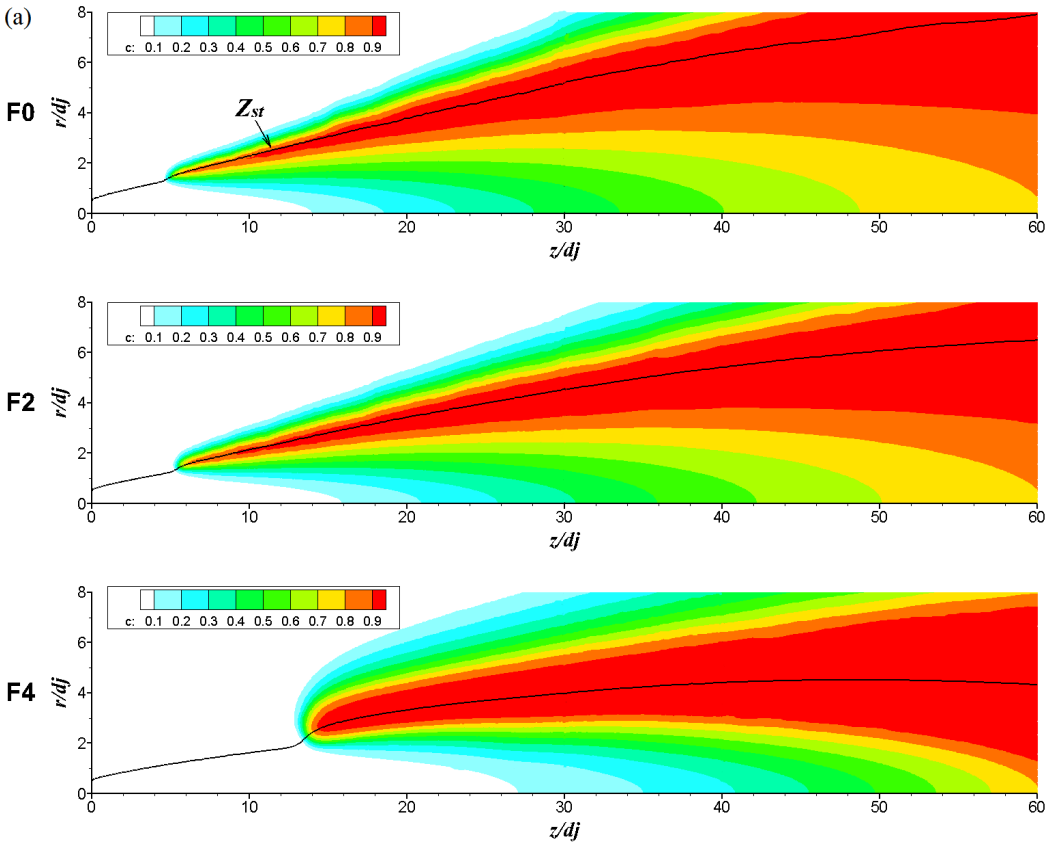

Figure 5.2: Computed mean progress variable field for the flames detailed in Fig. 5.1.

of $\overline{\dot{\omega}_c^*}$ are plotted for these three flames. In this figure, the highest reaction rates are found to be close to the stoichiometry in the flame base region for all cases as one would expect. For the less-diluted cases F0 and F2, the reaction zone is located in the vicinity of $\widetilde{Z}_{st}$ as illustrated in Figs. 5.3a and 5.3b respectively, which is similar to typical diffusion flames. This reaction zone ranges from the flame base region about $5-6d_{\mathrm{j}}$ to approximately $20-25d_{\mathrm{j}}$ downstream. However, for the highly diluted flame F4, two flame branches, one on the lean side and the other on the rich side, are identified in Fig. 5.3c exhibiting a typical triple-flame pattern.

These computed flame behaviours are compared with experimental observations of Ahmed & Mastorakos [2006] and are investigated to identify the individual importance of different modelling effects and their mutual influences in the

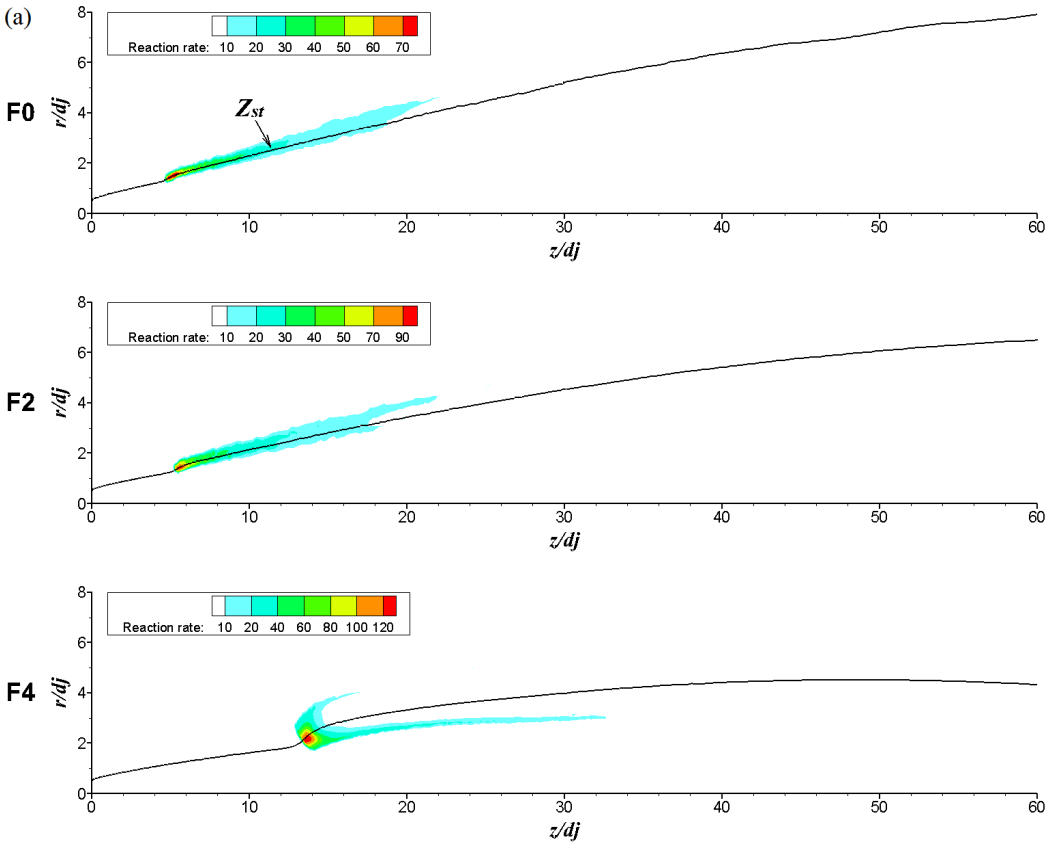

Figure 5.3: Computed mean reaction rate, $\overline{\dot{\omega}_c^*}$, in kg/m^3/s units. See details of the simulated flames in Fig. 5.1.

following sub-sections.

5.3.2 Flame lift-off height

The modularity of premixed and non-premixed combustion models and Z-c correlation allows four different model combinations to assess their individual effects and mutual dependencies, as noted in §5.2. The results of this assessment on the flame lift-off height for the four cases listed in Table 5.2 are shown in this sub-section. It is worth to remind ourselves here that case A has contribution only from premixed mode combustion and case B includes Z-c correlation effect along with premixed combustion through the joint PDF in Eq. (3.47). The other two cases include both the non-premixed and premixed combustion contributions,

but with Z-c correlation effect excluded in case C and included in case D.

Figure 5.4 shows the computed mean temperature field and mixture fraction contours for F0 (undiluted) and F4 (highly diluted) flames having the same jet velocity, $U_{\rm j} = 16$ m/s. Note that the two flames are plotted in two different scales, and the radial and axial distances are normalised using $d_{\rm j}$. The $\widetilde{Z}_{st}$ contour (as a thick line) and lift-off height ($L_{\rm f}$) are highlighted in this figure. The flame lift-off height is the most-upstream point of $\widetilde{T} = 1200$ K contour which corresponds to 5% of the maximum OH concentration as used in the experiment [Mansour, 2003]. The other two iso-lines (thin black lines) of $\widetilde{Z}$ correspond to the lean and rich flammability limits of methane ($\phi = 0.5$ and 1.5 respectively). It is shown that the highest temperature at the flame leading edge is close to the Favre-averaged stoichiometric mixture fraction, $\widetilde{Z}_{st}$, for both F0 and F4 flames as one would expect. The maximum temperature is found at further downstream where the $\widetilde{Z}_{st}$ contour intersects with the jet centre axis, approximately at about 130 to $150d_{\rm j}$ for flame F0; whereas for the diluted flame F4, it falls in between $70d_{\rm j}$ and $90d_{\rm j}$ because this intersection point is located more upstream due to the air dilution in the jet fluid.

Table 5.3 compares the computed $L_{\rm f}/d_{\rm j}$ of flames F0, F2 and F4 for the four cases listed in Table 5.2. The jet velocity is 16 m/s. The pure premixed case A excluding the Z-c correlation gives $L_{\rm f}/d_{\rm j} \approx 5$ and 5.5 for F0 and F2 respectively, lower than the measured values of 5.8 and 6.7. For the highly diluted ($X = 40\%$) flame F4, case A over-estimates the lift-off height by about $2d_{\rm j}$ as in Tables 5.3. The modelling case B includes the Z-c correlation and yields slightly larger values of $L_{\rm f}/d_{\rm j}$ for F0 and F2, whereas for F4 a decrease in $L_f/d_{\rm j}$ is observed. The reason for this will be discussed later in section 5.3.4 while examining the premixed mean reaction rate $\overline{\dot{\omega}}_c$. Case C includes contribution of non-premixed combustion and the lift-off height computed in this case is increased by about one diameter compared to the case A. This effect is further discussed in section 5.3.3. Finally, when both Z-c correlation and non-premixed combustion effects are included in the modelling case D, the computed lift-off heights are in excellent agreement with the experiments for F0 and F4 as seen in Table 5.3 for this case. The agreement is not as good for F2 but still within the 9% uncertainties noted in the experiments [Ahmed & Mastorakos, 2006]. The modelling case D is chosen for

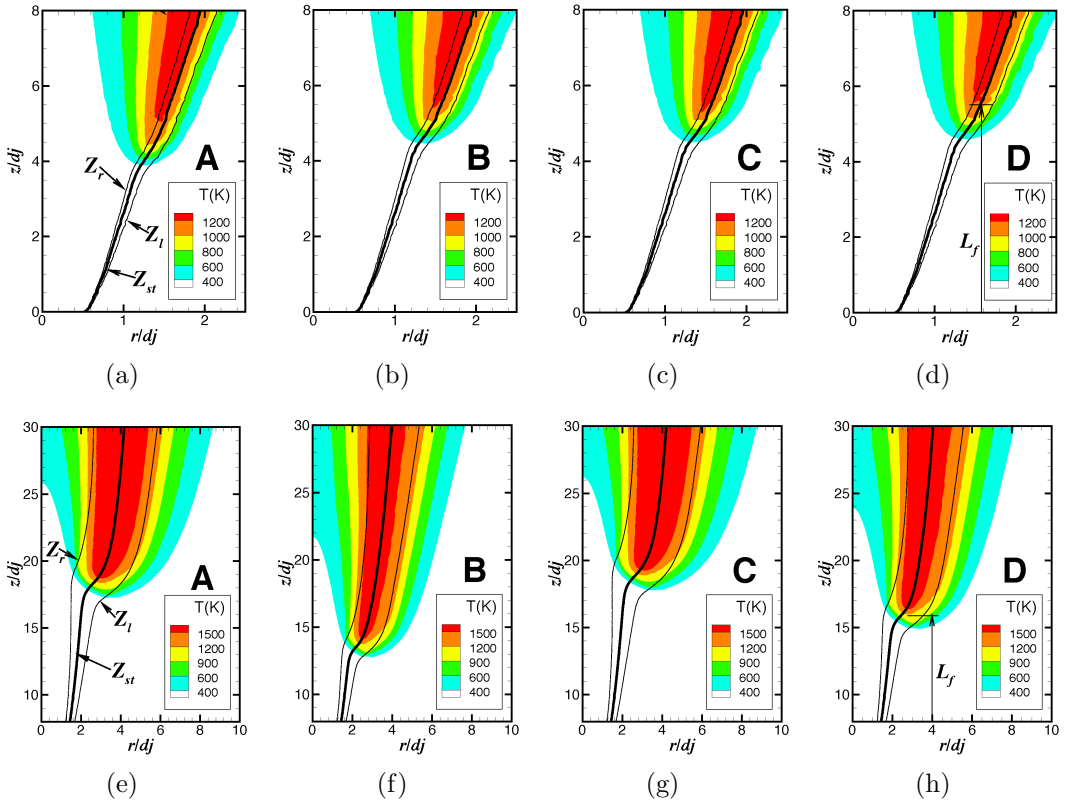

Figure 5.4: Temperature (dashed line) and mixture fraction (line) contours for flame F0 (top row) and F4 (bottom row). The jet exit velocity for these two cases is $U_{\mathrm{j}} = 16$ m/s.

further testing with different jet velocities and air-dilution levels in section 5.3.5.

5.3.3 Role of non-premixed combustion mode

The contributions of non-premixed combustion is given by Eq. (3.50), which involves the second derivative term, $d^2\psi^{\mathrm{Eq}}/dZ^2$. Thus, the contributions from $\overline{\dot{\omega}}_{\mathrm{np}}$ is expected to be important around $\widetilde{Z}_{st}$ contours. The variations of $\psi^{\mathrm{Eq}} = Y_{\mathrm{CO}}^{\mathrm{Eq}} + Y_{\mathrm{CO_2}}^{\mathrm{Eq}}$ and its derivatives with Z are shown in Fig. 5.5 for mixtures close to stoichiometry. Note that the derivatives are scaled appropriately to fit in the range of y-axis shown in this figure. As expected the second derivative peaks near the stoichiometric location and has a larger negative part than positive part. Hence, the overall contribution from $\overline{\dot{\omega}}_{\mathrm{np}}$ to $\overline{\dot{\omega}_c^*}$ in Eq.(3.46) is negative. The

Table 5.3: Comparison of computed and measured [Ahmed & Mastorakos, 2006] final lift-off heights, L_f/d_j, for $U_j = 16$ m/s.

Flame	Air%	$\widetilde{Z}_{st}$	Exp.	A	B	C	D
F0	0	0.055	5.5	4.9	5.3	5.4	5.6
F2	20	0.08	6.7	5.5	5.6	5.7	5.9
F4	40	0.12	16.3	18.4	13.7	18.8	16

diffusion effect of c in Z space, signified by $\partial^2\psi/\partial Z^2$, prevents the local chemical reactions to reach their equilibrium and thus decreases the flame propagation speed as noted by Bray *et al.* [2005] and Domingo *et al.* [2002]. This decrease in the flame propagation speed increases the lift-off height when non-premixed combustion contribution is included in the modelling, compare cases A & C and cases B & D in Table 5.3. This effects is observed for the range of velocities and dilution levels considered in this study.

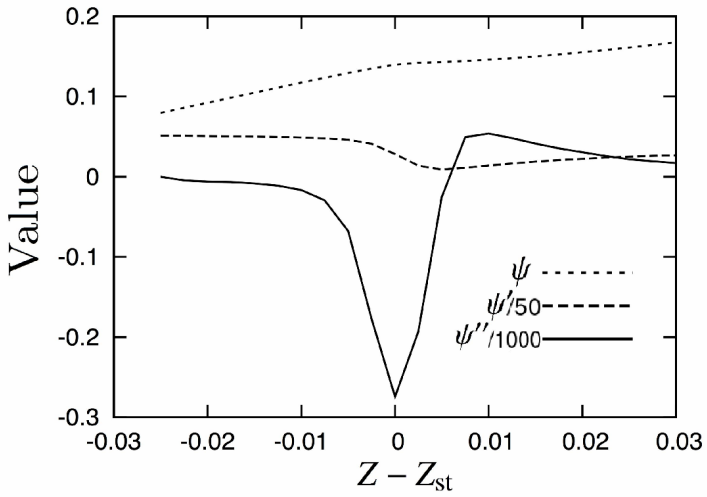

Figure 5.5: Variations of ψ^{Eq}, $\psi' = d\psi^{Eq}/dZ$ and $\psi'' = d^2\psi^{Eq}/dZ^2$ with Z in the vicinity of Z_{st}.

To further understand the relative role of non-premixed combustion contributions to the overall mean reaction rate, $\overline{\dot{\omega}_c^*}$, the spatial variations of $\overline{\dot{\omega}_c^*}$ and its components, $\overline{\dot{\omega}}_c$ and $\overline{\dot{\omega}}_{np}$, are shown in Fig. 5.6 for flames F0 and F4. This result

is shown for the modelling case D and for $U_{\rm j} = 16$ m/s. As one would expect, the significant reaction rates occur within the flammability limits and the peak rate is around the stoichiometric contour. The non-premixed mode contribution is significant only in the vicinity of $\widetilde{Z}_{st}$ as noted above, however its relative contribution varies significantly between the flames F0 and F4. Figures 5.6b and 5.6c show that the magnitude of peak $\overline{\dot{\omega}}_{\rm np}$ is about an order of magnitude lower than $\overline{\dot{\omega}}_c$ in the flame F0 and this difference becomes two orders of magnitude for the flame F4 as seen in Figs. 5.6e and 5.6f. This is because of the availability of oxygen in the jet fluid because of air-dilution. Despite the small contribution from non-premixed combustion mode, it is found to be important to obtain the correct lift-off height as noted in section 5.3.2. These observations on the localness of $\overline{\dot{\omega}}_{\rm np}$ supports the assumption of Müller *et al.* [1994] to account for partially premixed combustion effects in G-equation approach. The relatively larger contribution of $\overline{\dot{\omega}}_{\rm np}$ in the flame F0 compared to F4 results from larger values of $\widetilde{\chi}_Z$ because the flame F0 stabilises in regions relatively closer to the jet exit with larger shear and mixture fraction gradients. Thus, the oxygen transported by turbulence large-scale rollup leading to enhanced entrainment is likely to play an important role in the stabilisation of flame F0. In the flame F4, the effect of entrained oxygen is expected to be delayed downstream because of the presence of some oxygen in the fuel diluted with air. Thus, it is becoming imperative that the role of Z-c correlation signifying the mutual influences of scalar mixing and chemical reactions need to be understood and this is discussed next. The influence of this correlation on the flame lift-off height is observed already in Fig. 5.4 and Table 5.3.

5.3.4 Effect of Z-c correlation

The effects of Z-c correlation on $\overline{\dot{\omega}}_c$, Eq. (3.47), are shown in Fig. 5.7 for the flames F0 and F4 having $U_{\rm j} = 16$ m/s. The values of $\overline{\dot{\omega}}_c$ computed using models A and B (see Table 5.2) are compared to understand the role of Z-c correlation. In these two models, the influences arising from non-premixed combustion are excluded by omitting $\overline{\dot{\omega}}_{\rm np}$ given by Eq. (3.50) while calculating $\overline{\dot{\omega}^*_c}$. The computed covariance contours shown in Figs. 5.7b and 5.7d respectively for the flame F0 and F4 suggest that $\widetilde{Z''c''}$ changes its sign near $\widetilde{Z}_{st}$ which is consistent with a

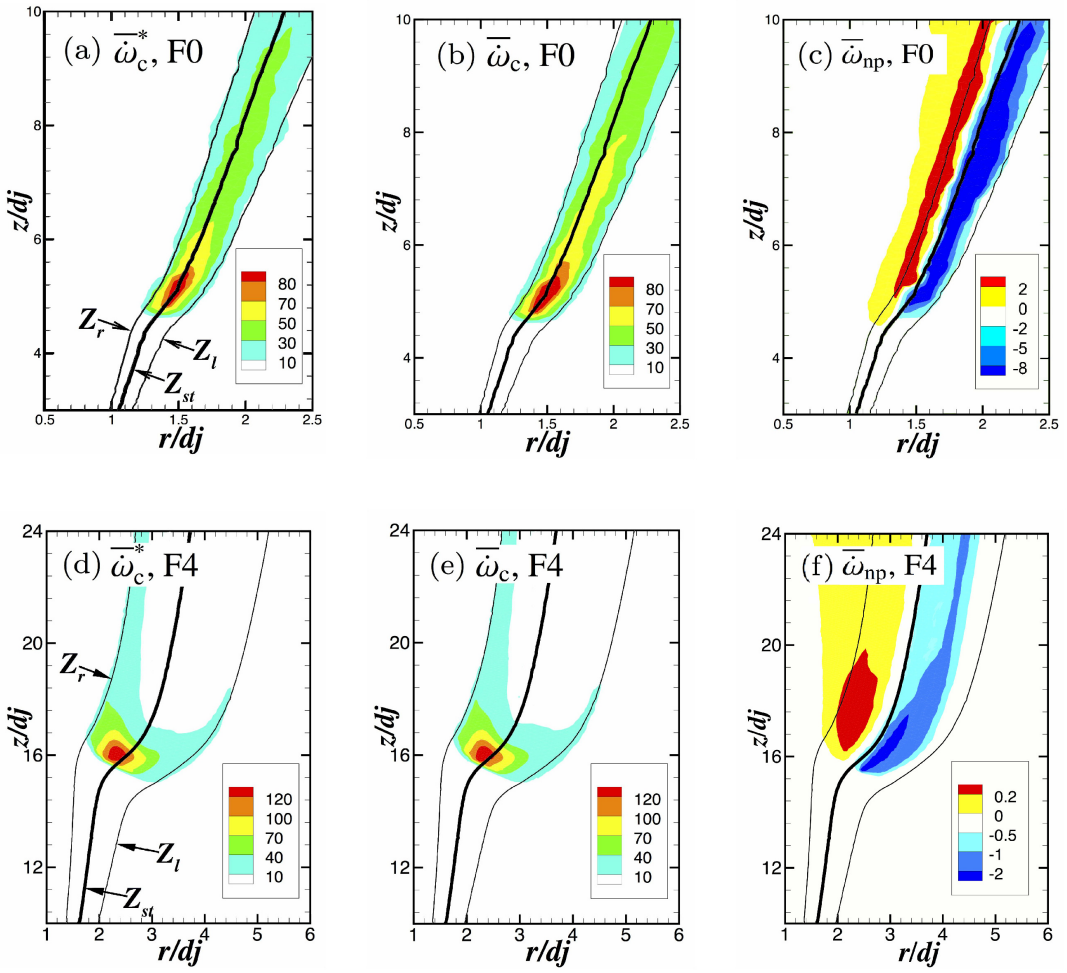

Figure 5.6: Spatial variation of mean reaction rate, $\overline{\dot{\omega}^*_c}$, and its components $\overline{\dot{\omega}}_c$ and $\overline{\dot{\omega}}_{\rm np}$ (kg/m^3/s) in flames F0 and F4. The jet exit velocity for these two flames is $U_{\rm j} = 16$ m/s.

previous DNS study by Ruan *et al.* [2012]. This sign change is because, locally richer mixture (positive Z'') in the lean side can promote combustion resulting in enhanced reaction rate (positive c''). This gives $\widetilde{Z''c''} > 0$ for the lean mixture. The locally richer mixture in the rich side can make the mixture difficult to burn reducing the overall reaction rate (negative c''). This yields $\widetilde{Z''c''} < 0$ for the rich side as seen in Fig. 5.7. These results are consistent with an earlier analysis of turbulent stratified combustion by Darbyshire & Swaminathan [2012].

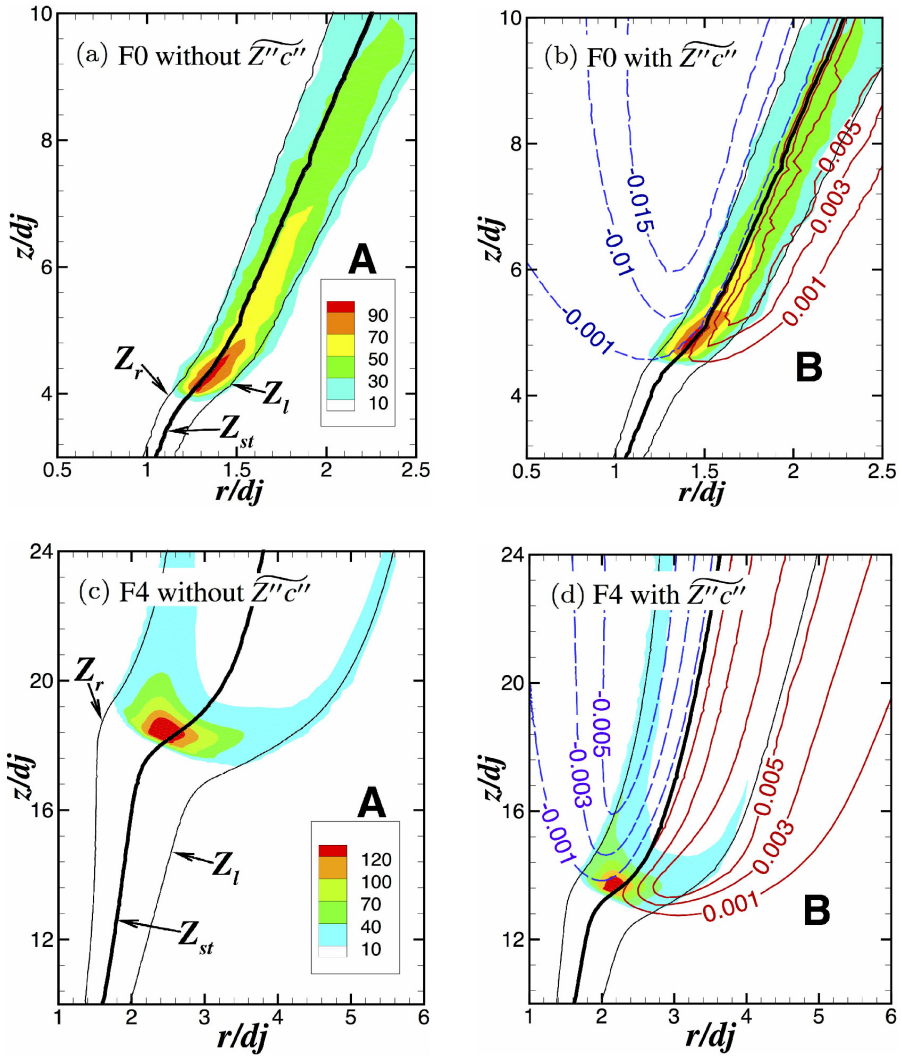

Figure 5.7: Effects of Z-c correlation on the premixed mean reaction rate, $\overline{\dot{\omega}}_c$. The mean reaction rate in kg/m^3/s is shown using pseudo colours and the iso-contours of $\widetilde{Z''c''}$ are shown as lines, solid line is for $\widetilde{Z''c''} > 0$ and dashed line is for $\widetilde{Z''c''} < 0$.

Including the Z-c correlation redistributes $\overline{\dot{\omega}}_c$ inside the flame brush as seen in Fig. 5.7. Two main effects can be observed by comparing Figs. 5.7a to 5.7b for flame F0 and 5.7c to 5.7d for flame F4. These two effects are as follows. (1) The region having high mean reaction rate near $\widetilde{Z}_{st}$ becomes smaller when Z-c correlation is included in the analysis and this is prominent for the air-diluted

flame F4. One could see a reduction in the reaction zone width near the lift-off height by about d_{j} for F4 by comparing Figs. 5.7c and 5.7d. (2) The two flame branches merge in downstream of the leading edge and the merged flame brush moves towards $\widetilde{Z}_{st}$ (radial squashing of the flame brush), which is more prominent for the flame F4. The first effect, a decrease in the reaction zone width, increases the lift-off height because of relatively weaker flame propagation along the $\widetilde{Z}_{st}$ contour. However, the second effect causing radial squashing of the flame brush moves the leading edge upstream. Thus, there is a fine balance between these two opposing effects at the leading edge for the flame brush to stabilise at the final lift-off height. The following is postulated here. As the rich flame branch typically located in relatively high velocity region moves away from the jet centreline because of radial squashing. Thus, the flame brush leading edge supported by the downstream chemical activity experiences a lower velocity at this axial position. This enables the leading edge to propagate towards its final stabilisation region. Therefore, the overall effect of Z-c correlation can be seen as a combination of the above two effects and their predominant role can vary depending on the turbulence and thermo-chemical conditions.

The effects of Z-c correlation also changes the relative importance of non-premixed combustion mode contribution. In the highly diluted flame F4, as the premixed lean and rich reaction zones merge and move towards $\widetilde{Z}_{st}$ contour where $\overline{\dot{\omega}}_{\mathrm{np}}$ tends to be large the non-premixed combustion plays an important role for the overall mean reaction rate. This substantially influences the lift-off height as given in Table 5.3. The difference in $(L_{\mathrm{f}}/d_{\mathrm{j}})$ is about 0.4 due to non-premixed combustion contribution (compare the values for A and C in Table 5.3) for flame F4, and this difference becomes 2.3 when Z-c correlation is included (compare B and D in Table 5.3 for F4). This supports the above observation on the role of Z-c correlation to obtain lift-off heights measured in experiments. This correlation effect is observed to be small for the undiluted methane flame F0 (see values in Table 5.3) whereas this effect was observed to be significant for an undiluted hydrogen jet flame by Ruan *et al.* [2014a]. These observations suggest that the flammability limits of the fuel can alter the importance of Z-c correlation effects - the effects are stronger when the flammability limit is wider. The level of partial premixing can also influence the Z-c correlation effects. In the lifted jet flames,

the partial premixing is affected by the entrainment influenced by the jet velocity and the dilution level. The influence of these two parameters on the flame lift-off height is discussed next.

5.3.5 Influence of jet velocity and air-dilution

To further assess and confirm the role of contributions from non-premixed combustion and Z-c correlation for other jet velocities, the flame F4 is computed using the four modelling cases, A to D in Table 5.2, for three different velocities. The flame lift-off heights obtained from these calculations are shown in Fig. 5.8a. The model A involving only the premixed combustion mode without Z-c correlation overestimates the lift-off height and including the correlation in model B leads to an underestimate. This underestimate seems to be significant for low jet velocity considered for this testing. When contributions of non-premixed combustion are included in model C then the overestimate of $L_{\rm f}/d_{\rm j}$ increases further by about 0.5 to 1. Including the contributions of both non-premixed combustion and Z-c correlation gives $L_{\rm f}/d_{\rm j}$ values close to the measured values for all the jet velocities and flames investigated in this study, supporting the observations made in the previous subsections on the roles of these contributions. Thus, the model D is used for further investigation of this study to address the air-dilution effects as below and transient evolution processes as discussed in the later chapters of this thesis.

The effect of air-dilution on $L_{\rm f}/d_{\rm j}$ is shown in Fig. 5.8b by considering F0, F2 and F4 flames. The computed and measured lift-off heights of these flames are compared in this figures for a range of jet velocities used in the experiments conducted by Ahmed & Mastorakos [2006]. As one can see in this figure, this comparison is uniformly very good for all the cases. For a given jet velocity, $L_{\rm f}/d_{\rm j}$ increases with dilution level. This is because an increase in the stoichiometric mixture fraction value resulting from dilution moves $\widetilde{Z}_{st}$ contour towards the jet centre where the local velocities are expected to be large. Thus, the diluted flame stabilises at a farther downstream location compared to the undiluted flame. For F4 flame, the highest jet velocity considered is 22 m/s and a higher velocity leads to flame blow-off in the simulation, which is consistent with observation in

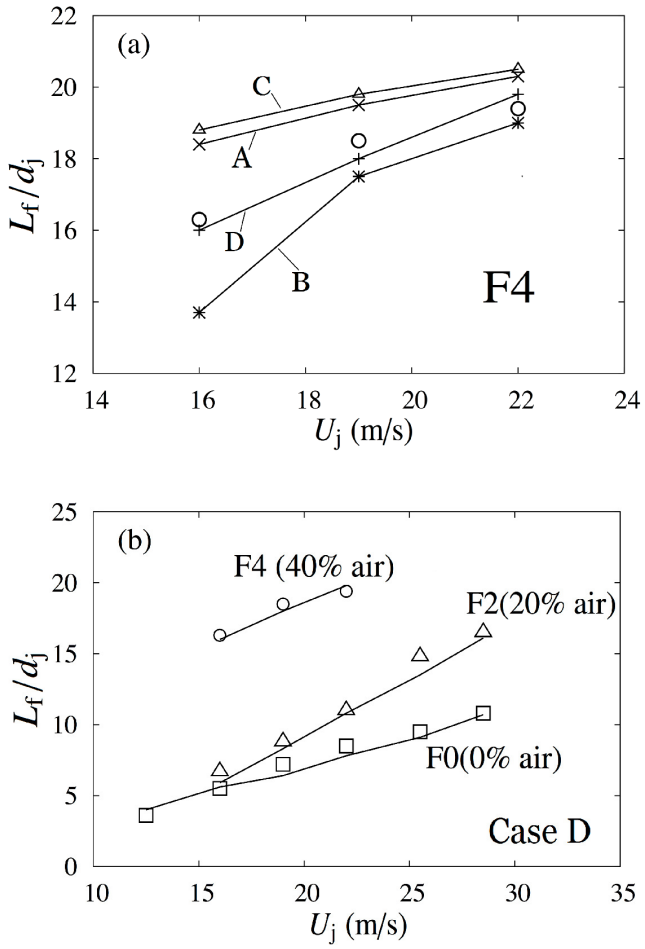

Figure 5.8: Computed flame lift-off height is compared to the measured [Ahmed & Mastorakos, 2006] values for various jet velocities and air-dilution levels.

the experiments [Ahmed & Mastorakos, 2006]. Thus, it seems that the modelling framework used in this study is able to capture the flame lift-off heights of a range of conditions, dilution levels, jet velocities ranging from 12 to 30 m/s and 500 to 900 m/s (computed by Ruan *et al.* [2014a] for undiluted hydrogen), without having to change the combustion modelling parameters. The reason for such robust and consistently good behaviour of the combustion model is because of close coupling of the model parameters to the underlying important physical processes controlling the local burning rate as discussed in [Kolla & Swaminathan, 2010; Kolla *et al.*, 2010; Ruan *et al.*, 2014a].

5.3.6 Stabilisation mechanism

Many theories [Lawn, 2009; Lyons, 2007; Pitts, 1988] for flame stabilisation mechanism at the leading edge have been proposed in past studies and they include premixed flame propagation [Eickhoff *et al.*, 1984; Pitts, 1988; Vanquickenborne & van Tiggelen, 1966; Wohl *et al.*, 1949], extinction of diffusion flamelets [Peters & Williams, 1983], triple flames [Favier & Vervisch, 1998; Kioni *et al.*, 1993], the large-scale eddy model [Broadwell *et al.*, 1984] as well as the edge flame concept [Buckmaster, 2002]. Detailed discussion of these theories is not the main objective here but some remarks can be made based on the results obtained from the RANS simulations conducted in this study. The two classical theories based on premixed flame propagation and extinction of diffusion flamelets are discussed as follows.

Figure 5.9 shows the velocity field in the region of flame stabilisation for flames F0 and F4 computed using the model D in Table 1. The flame brush leading edge in these two flames is located in low-velocity regions with a value of about 0.4 m/s in the immediate upstream of the leading edge. This value is close to the planar laminar premixed flame speed for stoichiometric methane/air mixture. This phenomenon is consistent with many previous experimental [Joedicke *et al.*, 2005; Schefer & Goix, 1998] and numerical [Ferraris & Wen, 2007] studies. Another notable point is that the main reaction zone with high heat release rate per unit volume is located relatively closer to the jet centre than the leading edge which is consistent with the experimental observation [Su *et al.*, 2006]. This is more evident in the highly diluted flame F4 depicting a strong flow divergence and streamline deflection as seen in Fig. 5.9b.

Peters & Williams [1983] suggested that the lifted flame stabilises due to extinction of diffusion flamelets at the leading edge resulting from high scalar dissipation rate. Although this concept was claimed to be inadequate [Peters, 2000; Schefer *et al.*, 1994; Stårner *et al.*, 1996; Watson *et al.*, 2003], the influence of flamelets extinction should not be overlooked in the stabilisation process as noted in [Lyons, 2007] and may be responsible for the hysteresis phenomenon observed for the lift-off height [Lawn, 2009]. The combustion model given by Eq. (3.46) supports this view since the scalar dissipation rate, $\widetilde{\chi}_Z$, plays a role for

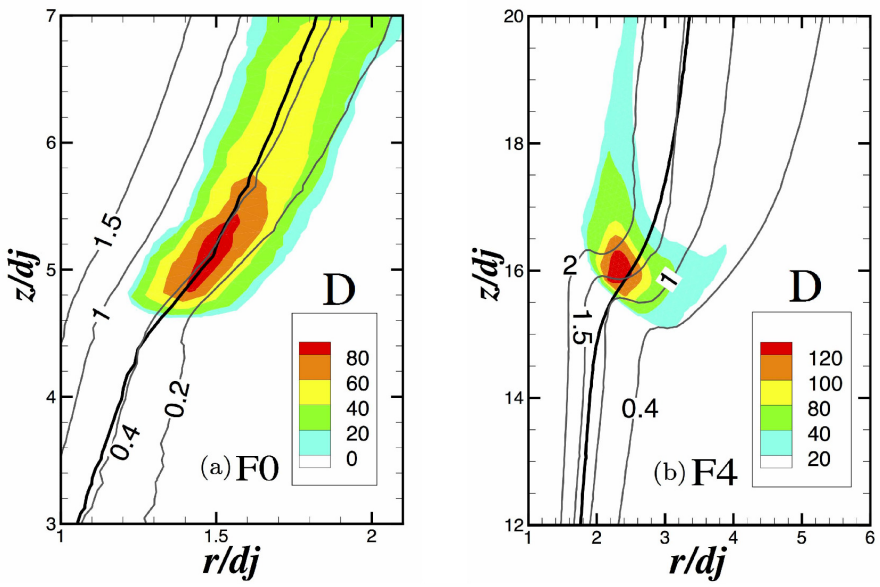

Figure 5.9: Contours of $\overline{\dot{\omega}_c^*}$ in kg/m^3/s (colour map) and $\widetilde{U}$ (m/s) (thin lines). The black bold line corresponds to $\widetilde{Z}_{st}$. The jet exit velocity for these two flames is $U_\mathrm{j} = 16$ m/s.

$\overline{\dot{\omega}_c^*}$ and thus on the turbulent flame propagation speed. Therefore, the normalised scalar dissipation rate, $\widetilde{\chi}_Z/\widetilde{\chi}_{Z,\mathrm{q}}$, in the flame stabilisation region computed using the model D is shown in Fig. 5.10 along with the mean reaction rate field. A typical extinction value of 5 s^{-1} for methane-air flame is used for $\chi_{st,\mathrm{q}}$ based on earlier studies [Ferraris & Wen, 2007; Peters, 2000]. It is observed that the normalised $\widetilde{\chi}_Z$ values in the stabilisation region are significantly smaller than 1, approximately 5% and 0.5% for F0 and F4 flames respectively. This considerably smaller value of $\widetilde{\chi}_Z/\chi_{st,\mathrm{q}}$ at the leading edge of the air-diluted flame is because of the smaller mixture fraction gradient in the flame F4 resulting from air-dilution. It is to be noted that $U_\mathrm{j} = 16$ m/s is the same for both F0 and F4 flames shown in Figs. 5.9 and 5.10. This suggests that the role of non-premixed flamelets extinction on flame stabilisation is relatively more important for undiluted flames compared to diluted flames. This is reflected in the $L_\mathrm{f}/d_\mathrm{j}$ values listed in Table 5.3. Including the non-premixed combustion effects in the model C moves the flame brush leading downstream by about 10% compared to the case A catering only

for premixed flamelets for the flame F0. This difference is only about 2% for the flame F4 as listed in Table 5.3. Thus, the role of contributions from premixed and non-premixed combustion must be included in the modelling of turbulent partially premixed flames. The influence of large-scale turbulence on the flow and scalar mixing is included inherently by solving the transport equations for the Favre-averaged momentum and scalar mass fraction conservations. Thus, the modelling framework used in this work seem to have the ability to include the relevant important physical processes. Also, the presence triple and edge flame structures in an averaged sense is also captured well by this modelling as has been evidenced in the mean reaction rate fields shown in Figs. 5.6, 5.7, 5.8 and 5.9.

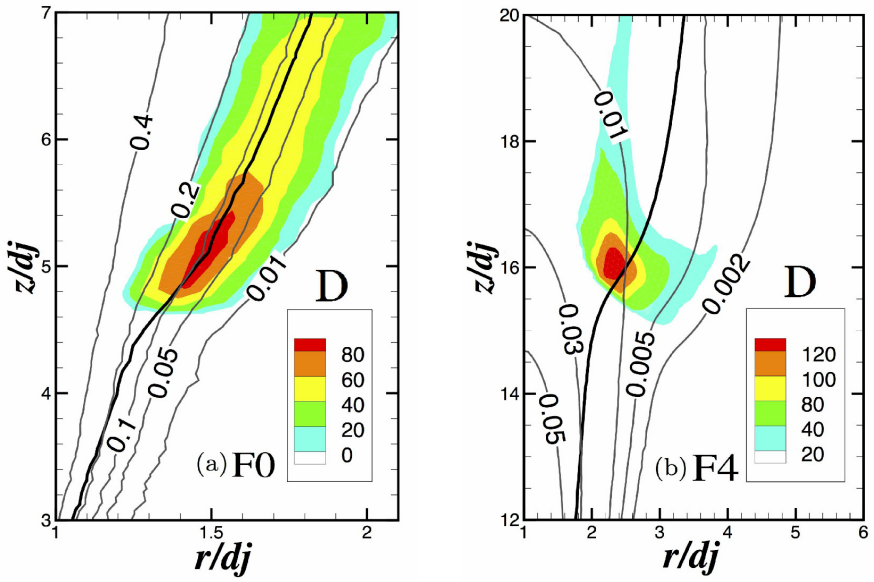

Figure 5.10: Contours of $\overline{\dot{\omega}_c^*}$ in kg/m^3/s (colour map) and $\widetilde{\chi}_Z/\chi_{st,\mathrm{q}}$ (thin line). The black bold line is for $\widetilde{Z}_{st}$. The jet exit velocity for these two flames is $U_\mathrm{j} = 16$ m/s.

5.4 Summary

Steady RANS simulation of turbulent lifted methane jet flames are conducted using a partially premixed combustion model involving unstrained premixed flamelets

and presumed PDF method in this chapter. The correlation between the mixture fraction and progress variable fluctuations is included in the analysis through a correlated joint PDF method. The contribution from non-premixed mode combustion is also included in the overall mean reaction rate modelling. These contributions appear in modular form in this approach allowing us to include and test one effect at a time. This modelling approach was developed in an earlier study and tested for undiluted hydrogen flames [Ruan *et al.*, 2014a]. The agreement between the measured and computed flame brush structure and lift-off heights was shown to be very good for the hydrogen flame [Ruan *et al.*, 2014a]. In this study, the abilities of this modelling approach to capture the undiluted and air-diluted methane jet lifted flames are tested as these flames involve relatively lower jet exit velocities compared to the earlier lifted hydrogen flames. The thermo-chemistry and its interaction with turbulence are well known to be different for methane and hydrogen mixtures. The ability of this combustion modelling approach, outlined in §3.1.1 and §3.2, is tested and validated without altering the combustion sub-modelling parameters used in [Ruan *et al.*, 2014a]. The main findings of this study are summarised as follows.

- Various jet exit velocities and air-dilution levels are tested for model validation. The calculated lift-off heights, L_{f}, agree very well with the measured values [Ahmed & Mastorakos, 2006] for the range of conditions tested here. This agreement is found to range from excellent to very good when the effects of both Z-c correlation and non-premixed combustion are included while calculating the mean reaction rate using the model D in Table 5.2. This clearly indicates that both of these two effects are important and required to capture the complex processes and their interactions involved at the stabilisation height of lifted flames.

- A systematic evaluation showed that the contributions from non-premixed combustion is predominantly negative to the mean reaction rate and thus shifts the flame brush leading edge downstream compared to the situation when these contributions are excluded. The effects of non-premixed combustion exists only in the vicinity of stoichiometry as one would expect. This contributions is observed to be more significant for the undiluted flame, F0,

because of relatively large $\widetilde{\chi}_Z$ values, resulting from mixing with entrained air, compared to that for the air-diluted flames.

- The Z-c correlation influences the flame stabilisation by redistributing the reaction rate inside the flame brush downstream of the leading edge. This results in changes in the flame-flow interaction causing two dominant effects on the flame brush. These effects are (1) the size of reaction zone with large reaction rate near $\widetilde{Z}_{st}$ is reduced and (2) the two flame, lean and rich, branches downstream of the leading edge are squashed towards $\widetilde{Z}_{st}$ contour. The former effect increases the lift-off height whereas the latter effect decreases L_{f}. The overall effect of the Z-c correlation is a resultant of these two opposing effects and the later effect is observed to be dominant and its relative role increases with dilution level. The relatively increased influence of the latter effect in the air-diluted flames is because the flame brush is thicker allowing the correlation to affect a larger part of the flame.

- The air-dilution increases the lift-off height for a given jet velocity because of an increase in the stoichiometric mixture fraction value, which usually resides in regions with higher velocity. The offset between the flame leading edge and the main heat releasing zone is found to be larger in the highly diluted case as has been observed in experimental [Su *et al.*, 2006] and LES [Ferraris & Wen, 2007] studies.

Although the modelling frame work used here seems robust to calculate the flame final lift-off heights over a wide range of flame and flow conditions for methane and hydrogen, the transient evolution of the flame leading edge from its ignition position to the final lift-off height is yet to be studied to further assess the combustion model. This transient process was investigated experimentally by Ahmed & Mastorakos [2006] for a diluted (30% air) fuel jet. To include the time-dependent effects in the simulations, the unsteady RANS modelling methodology is required and this study is shown in the next chapter.

Chapter 6

Transient Evolution of Lifted Jet Flames

As shown in the previous chapter, the steady-state flame final lift-off height is captured very well using the RANS modelling framework described in Chapter 3. Thus, the transient evolution of the lifted jet flames investigated experimentally by Ahmed & Mastorakos [2006] is of interest for the following study. The model D in Table 5.2 shows very good capability of predicting the lift-off height under various conditions and thus is used for this transient study. This model involves a correlated joint PDF and both premixed and non-premixed combustion mode contributions. Unsteady RANS simulations are performed in this chapter to capture the flame transient evolution from initial ignition to final stabilisation. Both two-dimensional axisymmetric and three-dimensional URANS methodologies are used and their computational results are compared with the experimental data to study the influence of the third physical dimension on the flame transient evolution.

6.1 Experimental test case

In the experiments of Ahmed & Mastorakos [2006], the transient evolution of flame position from its initial spark location to final stabilisation was investigated for a diluted methane jet with 30% air in volume. This flame refers to

the flame F3 denoted in §5.1. Two bulk mean jet velocities, U_j = 12.5 and 25.5 m/s, were recorded with corresponding Reynolds numbers of 3759 and 7669. The open flame was ignited at two downstream locations of 30 and $40d_j$ on the jet centreline. Both high-speed movies and OH PLIF techniques are used to visualise the flame evolution processes including from flame kernel growth, expansion, upstream propagation to its final stabilisation at lift-off height. During these processes, the temporal variation of the flame most-leading point axial position was examined by line-of-sight images at each elapsed time after ignition. This transient evolution was repeated in 10 experiments for each jet velocity condition and the axial position of the leading point was then ensemble-averaged using these 10 samples. A 9% maximum variation of this axial position was measured for a given elapsed time. It is worth noting here that the line-of-sight image captured by the high-speed movies is the flame evolution in 3D. Thus, the averaged measurements over 10 samples cannot be seen as the average in the azimuthal direction as for the 2D simulations. Therefore, a 3D numerical study is performed and compared with the 2D simulations to investigate the influence of the third physical dimension.

6.2 Numerical modelling details

The unsteady RANS methodology involving the time-dependent evolution of the mean flow fields is employed to study the transient flame evolution process. The time derivative term is considered for all the transport equations solved including Eqs. (3.2)-(3.4), (3.9), (3.10) and (3.14)-(3.18). The same set of modified constants for the $\widetilde{k}$-$\widetilde{\varepsilon}$ model described in §4.1.3.1 is used for the 2D and 3D URANS simulations for consistency in this study. For the combustion model, case D in Table 5.2 is chosen to include both the premixed and non-premixed mode combustion contributions as well as the correlation between mixture fraction and progress variable fluctuations in the URANS simulations.

The boundary conditions used in the earlier steady RANS study (see §5.2 for detail) are followed for this study as marked in Fig. 4.1. The mean axial velocity at the jet inlet is specified using the 1/7th power law and the turbulent velocity fluctuation is estimated using a Reynolds correlation [Wilcox, 2006]. A laminar

flow condition is used for the air co-flow with a small velocity of 0.1 m/s as in the experiments [Ahmed & Mastorakos, 2006]. The same condition with the velocity of 0.01 m/s is used for the air entrainment. For the side surface and outlet boundaries, far field boundary condition (pressure outlet) is used to simulate the open flames. The CFD package ANSYS FLUENT 13.0 [ANSYS-Fluent, 2012] is used for the simulations in this study and implementation of the modelling framework is detailed in §3.4.1 and the earlier study of [Ruan *et al.*, 2014a].

Following the experiments [Ahmed & Mastorakos, 2006], the numerical ignition is initiated on the jet axis at the location of 30 and $40d_{\mathrm{j}}$ downstream of the jet exit for both jet velocities of 12.5 and 25.5 m/s. Note that 3D URANS simulation is performed only for the $40d_{\mathrm{j}}$ cases due to the high computational cost. This location is chosen because it is further away from the jet nozzle, allowing us to study the influence of physical dimensions in a more complete flame propagation process with varying local mixing conditions. The flame kernel is initialised by setting $\widetilde{c} = 1$ in a spherical sub-domain with a diameter of 2 mm. The equivalent energy contained in this kernel is about 100 mJ as provided by the electrical spark in the experiments [Ahmed & Mastorakos, 2006]. It is found that the relative size of the kernel does not affect the final lift-off height and has only marginal influence on the transient flame leading edge evolution. A sensitivity test showed that there is minor influence only in the initial downstream convection stage and the overall flame leading edge evolution remains the same. Note that all the URANS simulations in this study are initialised using this approach on a fully converged cold flow and scalar mixing solution.

A time-step size of 5×10^{-5} s is used for both the 2D and 3D simulations, and it is much smaller than the laminar flame time-scale defined as $\tau_L \equiv (\delta_L^0 / S_L^0) \simeq 1.2 \times 10^{-3}$ s for stoichiometric CH_4/air mixture. The unsteady simulations are performed from the numerical ignition until a stable liftoff height is obtained. The typical wall-clock time required for computing this process (0.8 s of physical time) is about 6 hours for the 2D calculation using 8 cores on a desktop computer. For the same process, the 3D simulation requires about 72 hours using 256 cores on a high-performance computing cluster.

6.3 Results and discussion

6.3.1 Flame transient evolution stages

Figure 6.1 shows contours of the mean reaction rate, $\overline{\dot{\omega}_c^*}$, using pseudo colours at five different times noted in the figure. These times are normalised using a chemical time-scale τ_L noted in the previous section and are chosen to highlight the important stages of the flame-brush evolution. The results shown in Fig. 6.1 are typical for this evolution and it is shown for $U_\mathrm{j} = 25.5$ m/s with spark initiation at $z/d_\mathrm{j} = 30$ using 2D URANS simulations. The contours of $\widetilde{Z}_{st}$, lean and rich flammability limits are also shown as lines. Note t^* and t^+ are time scales normalised respectively using a jet flow time-scale defined as $(d_\mathrm{j}/U_\mathrm{j})$ and τ_L. The various stages of flame evolution discussed below compare very well with the experimental observations using high-speed movies in [Ahmed & Mastorakos, 2006].

1. Downstream convection:
   The flame kernel initialised at $z/d_\mathrm{j} = 30$ is first convected downstream very quickly by the mean flow as seen in the first frame of Fig. 6.1. In this early stage of flame development, the kernel growth is mainly due to both molecular and turbulent diffusion of deposited energy and thus it retains a spherical shape as seen in Fig. 6.1 for $t^* = 5$. This spherical evolution transitions into a second phase.

2. Radial expansion and downstream propagation:
   As the flame kernel moves into more flammable mixture bounded between $\widetilde{Z}_\mathrm{r}$ and $\widetilde{Z}_{st}$, the flame starts to propagate in the radial direction under the influence of streamwise convection by the mean flow. This results in the reaction zone shape as seen in the second frame of Fig. 6.1 shown for $t^* = 30$. The flame brush upstream edge remains at about the same position during this stage. From this second stage, the flame brush transitions into a third stage involving edge flame propagation.

3. Upstream propagation and Stabilisation:
   During the transition from the second stage, the flame brush positions itself

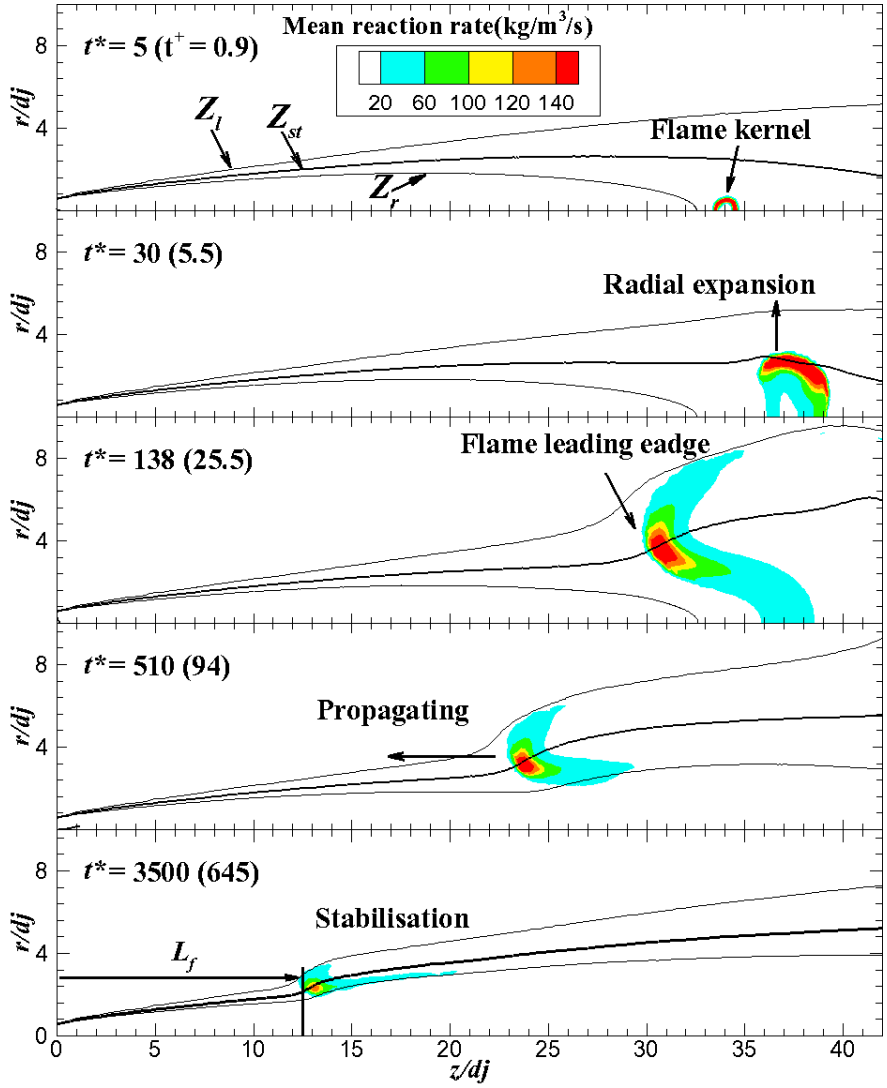

Figure 6.1: The flame brush evolution, computed using model D in Table 5.2 for flame F3 (30% air-dilution), towards its stabilisation height from its initial kernel location.

between the rich and lean flammability limits (in an average sense) with stronger reactions occurring near the stoichiometry. This gives a typical triple flame structure as shown in the third frame of Fig. 6.1 for $t^* = 138$. By this time, the total width of the flame brush reaches about $7d_{\mathrm{j}}$ in the radial direction as in Fig. 6.1. Once the flame brush attains this typical shape, then it starts to propagate upstream as an edge flame. This propagation is

led along $\widetilde{Z}_{st}$ contour until the final stabilisation height is reached as shown in the last frame of Fig. 6.1. A similar observation was also made by Müller *et al.* [1994] using a different modelling approach involving G-equation.

These three stages of flame brush evolution are clearly seen when the kernel is initialised in a mixture close to the rich flammability limit. When the kernel is initialised at $z = 40d_{\mathrm{j}}$ on the jet axis where the mixture fraction is close to stoichiometry, the second stage noted above becomes different. Instead of the radial expansion, the flame expands rapidly in the vicinity of $\widetilde{Z}_{st}$ iso-line and then starts to propagate upstream immediately. Similar behaviours are observed for other jet velocities, which are discussed next.

6.3.2 Temporal evolution of flame's leading edge

The temporal variation of flame leading edge was measured by Ahmed & Mastorakos [2006] using high speed movie techniques and 10 movies covering this transient evolution process from ignition to stabilisation were recorded for each of the two jet velocities of 12.5 and 25.5 m/s. The flame leading point was identified using line-of-sight imaging techniques and the 10 recorded movies were averaged frame by frame to obtain the transient evolution of the leading point of the flame brush. The experimental results for these two velocity cases are shown in Fig. 6.2 along with the computed results obtained from 2D and 3D URANS simulations. The error bar corresponds to the maximum variation of 9% observed in the experiments using limited samples of 10 frames for a given instant. The 3D simulations are performed only for the $40d_{\mathrm{j}}$ cases as noted in §6.2. The most-leading point in the simulations is identified using the axial coordinate of the most-upstream point of the $\widetilde{T} = 1200$ K iso-surface which corresponds to 5% of the maximum OH concentration as used in Chapter 5 to determine the flame final lift-off height as well as in a previous experimental study [Mansour, 2003].

In Figure 6.2, the y-axis is the axial coordinate normalised using the fuel jet diameter, and the x-axes are non-dimensional time axes corresponding to the elapsed time after ignition. The time axes, t^* and t^+, are scaled as noted in the previous section. After the ignition, the flame first moves downstream slightly due to the local flow convection in the experiments and this process is

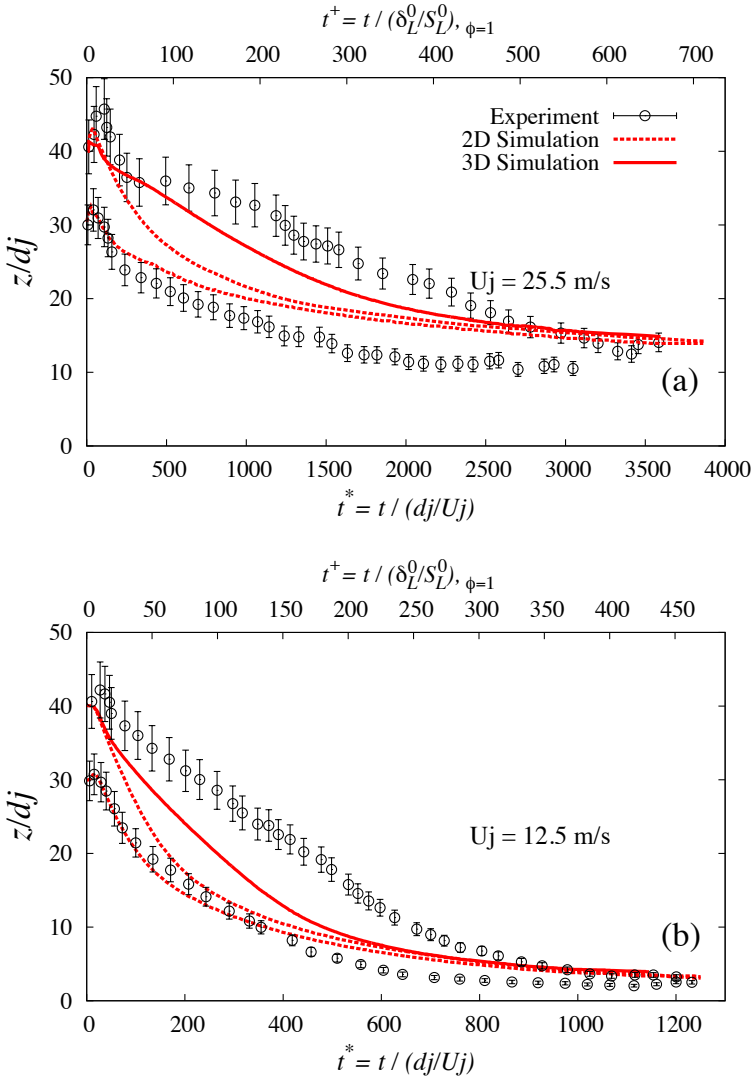

Figure 6.2: Temporal variation of axial location of flame leading edge, marked using the most upstream point of $\widetilde{T} = 1200$ K contour. Ignition was initiated at the instant $t = 0$. The error bar corresponds to 9% maximum error reported in [Ahmed & Mastorakos, 2006].

captured well in the computations, which is more apparent for the high velocity $U_j = 25.5$ m/s case shown in Fig. 6.2a. The flame then propagates towards its final stabilisation region against the flow. The convergence of flame tracks computed using 2D simulations for two different ignition locations suggests that the final lift-off height does not depend on the initial spark location for both $U_j = 25.5$ and

12.5 m/s cases shown respectively in Figs. 6.2a and 6.2b. Comparing these two figures also identifies that the flame takes longer to reach its final stabilisation height in the higher jet velocity case. The final lift-off height is reached within a few percent by $t^+ \sim 300$ for $U_\mathrm{j} = 12.5$ m/s as seen in Fig. 6.2b. This normalised time becomes about 700 for $U_\mathrm{j} = 25.5$ m/s suggesting that the time taken to reach the final lift-off height is proportional to the jet velocity when these are normalised using the stoichiometric flame scales, i.e., $t^+_\mathrm{final} \sim U^+_\mathrm{j}$, where U^+_j is U_j/S^0_L. This scaling suggests that the premixed flame propagation plays a vital role in the establishment of lifted flame from an initial kernel. Similar behaviour is observed for this scaling analysis between 2D and 3D simulations. The computed flame final lift-off heights for the two jet velocity cases agree quite well with the measured values for both the 2D and 3D computations suggesting that the final lift-off height, as a steady-state flame characteristic, is not influenced by the physical dimensions.

For the transient evolution, however, a substantial difference is observed between the 2D URANS and experimental results for the flame ignited at $40d_\mathrm{j}$ (upper branch) in both Figs. 6.2a and 6.2b. In contrast, the 3D computational results (solid line) show an improved agreement for the transient flame propagation process for both $U_\mathrm{j} = 25.5$ and 12.5 m/s cases. The flame brush propagation speed given by the slopes of these curves seems to agree better with the experimental data for the 3D cases compared to 2D results and this is further discussed in the next section. As one shall see in Fig. 6.1, after ignition at far downstream locations the flame first propagates in a fully flammable region before it encounters non-flammable mixtures from both rich and lean sides. This instant can be seen at $t^+ \sim 450$ in Fig. 6.2a and $t^+ \sim 250$ in Fig. 6.2b, where the experimental data points start to show horizontal bending suggesting a reduction in the propagation speed. This sub-process is well predicted by 3D simulations showing good agreement for the "bending point" for both jet velocities. In contrast, this appears much earlier in 2D simulations, at $t^+ \sim 200$ and $t^+ \sim 100$ for $U_\mathrm{j} = 25.5$ and 12.5 m/s respectively. This is due to a quicker propagation of the flame brush in 2D simulations as seen in Figs. 6.2a and 6.2b. This is more evident during the initial propagation in which the mixture surrounding the flame leading edge is within the flammability limits. This process is often referred to as stratified

flame propagation [Müller *et al.*, 1994; Peters, 2000] since the premixed combustion with varying equivalence ratios is found to be dominant. The influence of physical dimension observed here suggests that the third physical dimension plays an important role in flames propagating in partially premixed mixtures. To shed more light on this, the effect of the third physical dimension on flame brush propagation speed is studied next.

6.3.3 Flame-brush propagation characteristics

Flame displacement speed is known as the speed at which the flame front moves normal to its surface, relative to the local flow velocity [Peters, 2000]. Displacement speed has been extensively studied for turbulent premixed flames using scaling analysis, DNS, LES and RANS methods as reviewed in [Driscoll, 2008; Peters, 2000; Swaminathan & Bray, 2011]. However, the displacement speed behaviour in partially premixed mixture is not fully understood yet. A few 2D DNS studies have investigated laminar triple flames propagation [Im & Chen, 2001; Yoo & Im, 2004] and edge flame velocity in the event of turbulent diffusion flame extinction [Pantano, 2004]. These studies have shown that both premixed and non-premixed combustion modes contribute to the flame edge propagation and their contributions vary in the flame structure depending on the local mixing conditions. Furthermore, Im & Chen [2001] found that the correlation between displacement speed and scalar dissipation rate can be positive or negative. More recently, Chakraborty & Mastorakos [2006] conducted a further 3D DNS study on edge flame propagation in turbulent mixing layers and the results show similar behaviours as observed in laminar flame simulations. However, the behaviours of displacement speed, both overall and its components from reaction, normal and tangential diffusion [Chakraborty & Mastorakos, 2006], are observed to be non-monotonic with mixture fraction gradient. These complexities further increase the modelling challenge for flames propagating in turbulent partially premixed mixtures.

The flame displacement speed behaviour in response to these various parameters above can be studied both morphologically and statistically using DNS approaches. However, it is rather difficult to accurately identify the flame front in

experiments using the existing diagnostic techniques. For numerical simulations involving statistical models, namely RANS and LES, the flame front is theoretically unavailable. Because the flame front is not fully resolved but averaged as a "flame brush" (RANS) or filtered as a "filtered flame" (LES). Therefore, for clarification, the flame brush displacement speed, $\overline{S}_{\mathrm{d}}$, computed using unsteady RANS is investigated here.

6.3.3.1 Net flame propagation speed

In the experimental study of Ahmed & Mastorakos [2006], an ensemble averaged *net flame propagation speed*, $\overline{S}_{\mathrm{net}}$, with respect to the laboratory coordinates was calculated using differentiation of fifth-order polynomial curve fit based on the measured points as shown in Fig. 6.2. The same curve fitting method is used for the temporal variations obtained from the 2D and 3D simulations and these results are compared in Fig. 6.3 for both $U_{\mathrm{j}} = 25.5$ and 12.5 m/s cases. Note that this propagation speed accounts for the axial component of the flame brush displacement speed subtracted by the local flow axial velocity written as [Peters, 2000]

$$\overline{S}_{\mathrm{net}} = -\left(\,\overline{S}_{\mathrm{d}}\mathbf{n} + \widetilde{\boldsymbol{U}}\,\right)\cdot\mathbf{k}, \tag{6.1}$$

where the unit normal vector of the flame brush surface is defined as

$$\mathbf{n} = -\frac{\nabla\,\widetilde{c}}{|\nabla\,\widetilde{c}\,|}, \tag{6.2}$$

pointing towards the unburnt gas and $\mathbf{k}$ denotes the unit vector in z-direction, which points towards the downstream of the jet flow. In Fig. 6.2, the experimental results show that $\overline{S}_{\mathrm{net}}$ for the low jet velocity (12.5 m/s) case is approximately 2 times of that for high velocity (25.5 m/s) during the entire flame evolution process. This is consistent with the scaling analysis discussed in the previous section, showing that the time taken to reach the final lift-off height is proportional to the jet velocity using the normalised time-scale t^{+}. Therefore, it provides further support to the argument that the premixed flame propagation plays a vital role in the establishment of lifted flame from an initial flame kernel as also concluded

by Müller *et al.* [1994].

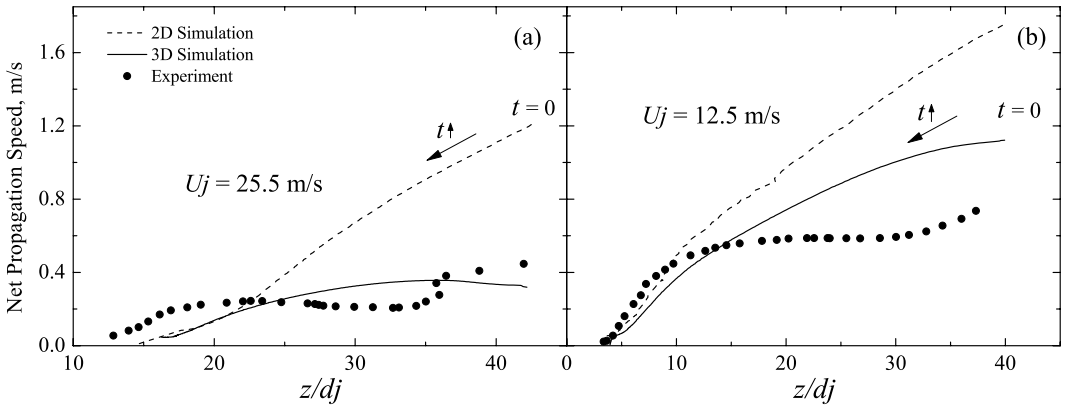

Figure 6.3: Comparison of net flame propagation speed vs. axial position, calculated from the results shown in Fig. 6.2 using best curve fits.

Figure 6.3 also shows that the 3D simulation results for $\overline{S}_{\text{net}}$ agree quite well with the experimental data, whereas significant discrepancies are observed for 2D simulations especially in the early stages (large z/d_{j} values). This is particularly apparent for the axial positions ranging from the ignition point, $z = 40d_{\text{j}}$ to about $20d_{\text{j}}$ for $U_{\text{j}} = 25.5$ m/s, and to about $10d_{\text{j}}$ for $U_{\text{j}} = 12.5$ m/s. These axial positions correspond to the "bending points" noted while discussing Fig. 6.2. After passing these positions, these three curves tend to converge towards the final lift-off height.

After the ignition, the flame brush tends to propagate towards the upstream at a nearly constant $\overline{S}_{\text{net}}$ initially and then slows down after encountering the region where the partial premixing with non-flammable mixtures starts to affect the leading edge propagation. This trend is captured reasonably well in 3D simulations as seen in Fig. 6.3, however, the net propagation speed computed in the 2D simulations shows a constant descending trend from the ignition to final stabilisation point.

These differences must stem from the influences of physical dimension on the displacement speed, $\overline{S}_{\text{d}}$, since $\widetilde{\boldsymbol{U}}$ is observed to be reasonably similar in 2D and 3D cases (see Figs. 4.3 and 4.4.). These effects are discussed next.

6.3.3.2 Displacement speed components

The transport equation of $\widetilde{c}$ given in Eq. (3.16) can be written in propagative form as [Peters, 2000]

$$\overline{\rho}\,\frac{\partial\,\widetilde{c}}{\partial t}+\overline{\rho}\,(\widetilde{\boldsymbol{U}}+\overline{S}_{\mathrm{d}}\mathbf{n})\cdot\nabla\,\widetilde{c}=0, \tag{6.3}$$

where the flame brush displacement speed, $\overline{S}_{\mathrm{d}}$, is

$$\overline{S}_{\mathrm{d}}=\frac{\nabla\cdot(\,\mu_{\mathrm{eff}}\nabla\,\widetilde{c}\,)+\overline{\dot{\omega}_{c}^{*}}}{\overline{\rho}\,|\nabla\,\widetilde{c}\,|}. \tag{6.4}$$

The effective dynamic viscosity is given as $\mu_{\mathrm{eff}}=\mu+(\mu_{\mathrm{t}}/\mathrm{Sc}_{\mathrm{t}})$, where μ and μ_{t} are the laminar and turbulent viscosity respectively and $\mathrm{Sc}_{\mathrm{t}}\approx 0.7$ is the turbulent Schmidt number.

The displacement speed is decomposed into three components as [Peters, 2000; Peters *et al.*, 1998]

$$\overline{S}_{\mathrm{d}}=\overline{S}_{\mathrm{n}}+\overline{S}_{\mathrm{t}}+\overline{S}_{\mathrm{r}}\ . \tag{6.5}$$

$\overline{S}_{\mathrm{n}}$ is the normal diffusion component written as

$$\overline{S}_{\mathrm{n}}=\frac{\mathbf{n}\cdot\nabla\,(\,\mu_{\mathrm{eff}}\ \mathbf{n}\cdot\nabla\,\widetilde{c}\,)}{\overline{\rho}\,|\nabla\,\widetilde{c}\,|}\ , \tag{6.6}$$

In the jet flame configuration of this paper, $\mathbf{n}$ at the leading edge of the flame brush points towards the upstream in the -z direction.

The tangential diffusion component is given by

$$\overline{S}_{\mathrm{t}}=-\frac{\mu_{\mathrm{eff}}\,(\nabla\cdot\mathbf{n})}{\overline{\rho}}\ , \tag{6.7}$$

where $(\nabla\cdot\mathbf{n})$ is the mean curvature of the flame surface which may also be written as the sum of the two principle curvatures, $(\kappa_1+\kappa_2)$, as in previous studies [Peters, 2000; Peters *et al.*, 1998].

Finally, $\overline{S}_{\rm r}$ is the the reaction component written as

$$\overline{S}_{\rm r} = \frac{\overline{\dot{\omega}_c^*}}{\overline{\rho}\,|\nabla\,\widetilde{c}\,|}\ . \tag{6.8}$$

The numerical values of these speeds depend on $\widetilde{c}$ iso-surface and their values at the leading edge marked using $\widetilde{c} = 0.05$ are of interest here. As the displacement speed is defined as the relative flame propagation speed normal to the local flame surface, the propagation direction of $\overline{S}_{\rm d}$ and its components vary across the flame brush during the lifted flame evolution. Figure 6.4 presents the colour map of the progress variable field and mixture fraction iso-contours obtained from the 2D and 3D computations at the same axial position of about $30d_{\rm j}$ for the flame brush leading edge. This corresponds to a time instant of $t^+ = 70$ for the 2D and $t^+ = 150$ for the 3D flames as can ben seen in Fig. 6.2. The leading edge is marked using the iso-surface of $\widetilde{c} = 0.05$ shown as a dashed line in Fig. 6.4. This value of $\widetilde{c} = 0.05$ has been used in earlier turbulent flame speed studies [Dunstan *et al.*, 2011, 2012] and is followed here. The arrows correspond to the local flame normal direction, $\mathbf{n}$, on the leading edge. Note that both cases are initialised at an axial distance of $40d_{\rm j}$ with the same jet velocity of $U_{\rm j} = 25.5$ m/s for comparison.

From this figure, one can see that the flame brush has similar shape between the 2D and 3D computations at the same axial position even with a different evolution in time from the ignition position. It is also shown that the flame normal direction, $\mathbf{n}$, varies along the leading edge suggesting different propagation direction locally. Note that $\mathbf{n}$ points towards exactly the upstream, (-z) direction, at the leading point which is located in the lean mixture with $\widetilde{Z} \simeq 0.08$ experiencing relatively low flow velocity. The leading edge with the stoichiometric mixture propagates towards the jet centreline as indicated in Fig. 6.4 and it experiences relatively high flow velocity. Thus, the leading point always has the highest net propagation speed and remains as the most upstream point on the leading edge. As a result, the net propagation speed defined in Eq. (6.1) at the leading point is determined by the leading point propagation characteristics such as the local flow velocity, displacement speed and their directions. This is further discussed later while examining $\overline{S}_{\rm d}$ and its components at the leading point.

The computed contours of $\overline{S}_{\rm r}$, $\overline{S}_{\rm n}$ and $\overline{S}_{\rm t}$ are shown in Fig. 6.5 for both the

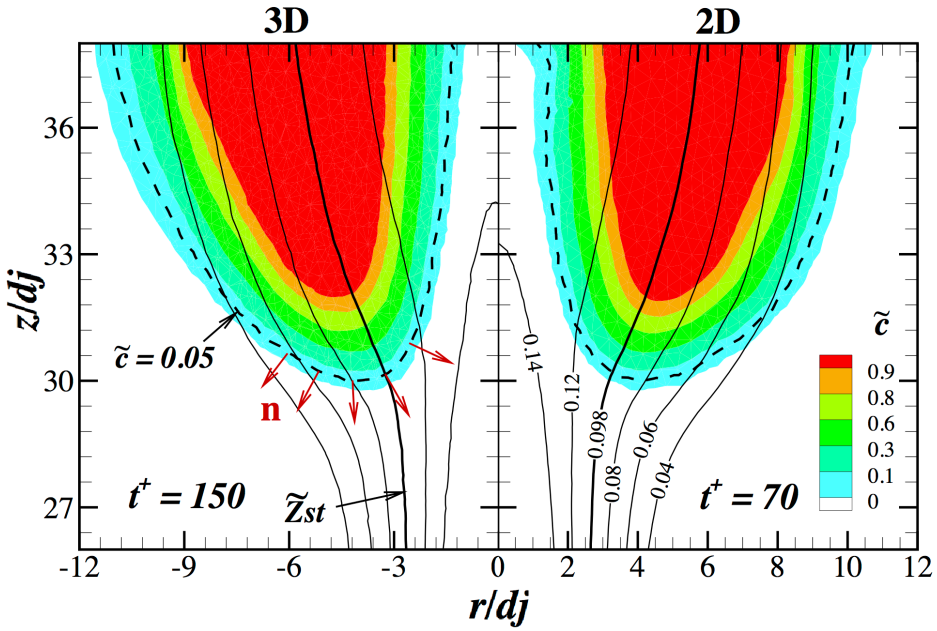

Figure 6.4: Computed 3D (left) and 2D (right) progress variable field at axial position, $z/d_{\rm j}$=30, for $U_{\rm j}$=25.5 m/s. The flame leading edge is marked using the iso-surface of $\widetilde{c} = 0.05$ shown as a dashed line. The solid lines are mixture fraction contours with stoichiometry, $\widetilde{Z}_{st} = 0.098$, being the thick line. The arrows correspond to local flame normal direction on the leading edge. Note the 3D contour is obtained from a slice on the middle plane of the domain.

2D and 3D cases at the same axial position as in Fig. 6.4. The mixture fraction contours (solid lines) correspond to the stoichiometry, $\widetilde{Z}_{st}$, and flammability limits for lean, $\widetilde{Z}_{\rm l}$, and rich, $\widetilde{Z}_{\rm r}$, methane-air mixtures. A progress variable iso-surface for $\widetilde{c} = 0.05$ (dashed line) representing the flame leading edge is also highlighted in this figure.

The reaction contribution to the propagation is concentrated at a downstream location of about $32d_{\rm j}$ as seen in Fig.s 6.5a and 6.5d, where the maximum value is about 6m/s $\sim 15S_L^0$ in both the 2D and 3D cases. The value of $\overline{S}_{\rm r}$ at the leading edge is much smaller, which is about $2.5S_L^0$. Therefore in this process, the diffusion (both laminar and turbulent) plays a rather important role by bringing the highly reactive radicals and heat from the downstream to the leading edge. Furthermore, no substantial influence of the physical dimension is observed at the leading edge between Figs. 6.5a and 6.5d as one would expect, however, the

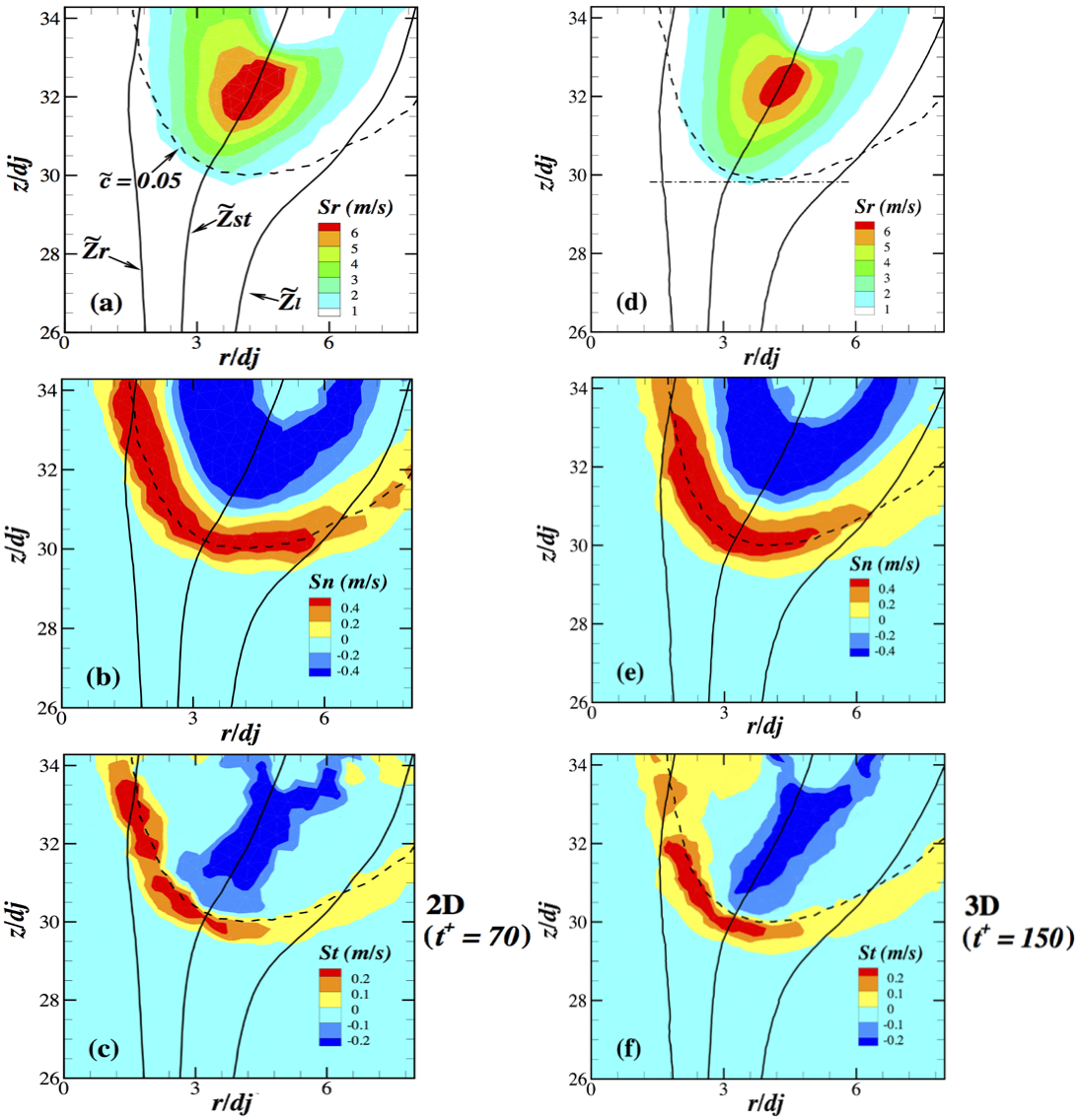

Figure 6.5: Spatial variation of displacement speed components, $\overline{S}_{\mathrm{r}}$ (reaction), $\overline{S}_{\mathrm{n}}$ (normal diffusion) and $\overline{S}_{\mathrm{t}}$ (tangential diffusion) obtained from 2D (left column) and 3D (right column) simulations. The 3D contour is obtained from a slice on the middle plane of the domain. Mean mixture fraction iso-contours are shown as black solid lines for stoichiometry ($\widetilde{Z}_{st}$), and flammability limits for lean ($\widetilde{Z}_{\mathrm{l}}$) and rich ($\widetilde{Z}_{\mathrm{r}}$) mixtures. The dashed line is the progress variable iso-surface of $\widetilde{c} = 0.05$. The jet exit velocity is $U_{\mathrm{j}} = 25.5$ m/s.

region with high $\overline{S}_{\mathrm{r}}$ values in the 2D case seems to be larger than that in the 3D case. Since $\overline{\dot{\omega}_c^*}$ does not depend on the physical dimension, the difference in

the scalar gradient magnitude, $|\nabla \widetilde{c}|$, between the 2D and 3D is the cause for the differences in $\overline{S}_{\mathrm{r}}$ (see Eq. (6.8)).

Figures 6.5b and 6.5e show the spatial variation of the normal diffusion component in the 2D and 3D simulations respectively. In both figures, $\overline{S}_{\mathrm{n}}$ varies from positive to negative values along the stoichiometric iso-line respectively from the upstream to downstream positions through the flame brush. The change of sign occurs in the middle of the flame brush at almost $\widetilde{c} = 0.5$. Note that positive value implies a positive contribution to the propagation towards the unburnt side and *vice versa*. The positive maximum values of $\overline{S}_{\mathrm{n}}$ are located around $\widetilde{c} = 0.05$ iso-contour, suggesting that this is an important contribution to the flame leading edge propagation. These maximum values are around $0.4 - 0.6$ m/s, which is close to the laminar flame burning velocity.

The tangential diffusion component, $\overline{S}_{\mathrm{t}}$, is plotted in Figs. 6.5c and 6.5f for the 2D and 3D cases respectively. Similar variation as for $\overline{S}_{\mathrm{n}}$ is seen, but with the maximum values of around 0.2 m/s, much smaller than that of $\overline{S}_{\mathrm{n}}$ and $\overline{S}_{\mathrm{r}}$.

In order to examine the displacement speed at the leading edge more quantitatively, the profiles of $\overline{S}_{\mathrm{d}}$ components are plotted against the mixture fraction, $\widetilde{Z}$, along the dot-dashed line shown in Fig. 6.5d at different axial positions. These profiles are presented in Fig. 6.6 for both velocities, U_{j} =25.5 and 12.5 m/s. The range of $\widetilde{Z}$ is shown from the lean limit, $\widetilde{Z}_{\mathrm{l}} = 0.05$, to the stoichiometric value, $\widetilde{Z}_{st} = 0.098$ and the leading edge is highlighted using a vertical dashed line. The axial velocity profiles are also presented to examine the balance between the displacement speed and the flow velocity shown in Eq. (6.3). Note that the y-axis is normalised using the laminar flame speed for stoichiometric methane-air mixture, S_L^0. Moving from the top to bottom in Fig. 6.6, the axial position, z/d_{j}, reflects the transient evolution of the leading edge propagation starting from the far downstream position of z/d_{j}=30 towards the upstream and finally stabilises at the lift-off height position.

As expected from the earlier discussion, it is more evident in this figure that the tangential diffusion component, $\overline{S}_{\mathrm{t}}$, is always less than $0.5S_L^0$, relatively small compared to the other two components throughout the flame evolution process for both velocities. Despite the difference between the 2D and 3D results for $\overline{S}_{\mathrm{t}}$, the contribution of this component is too weak to substantially influence the

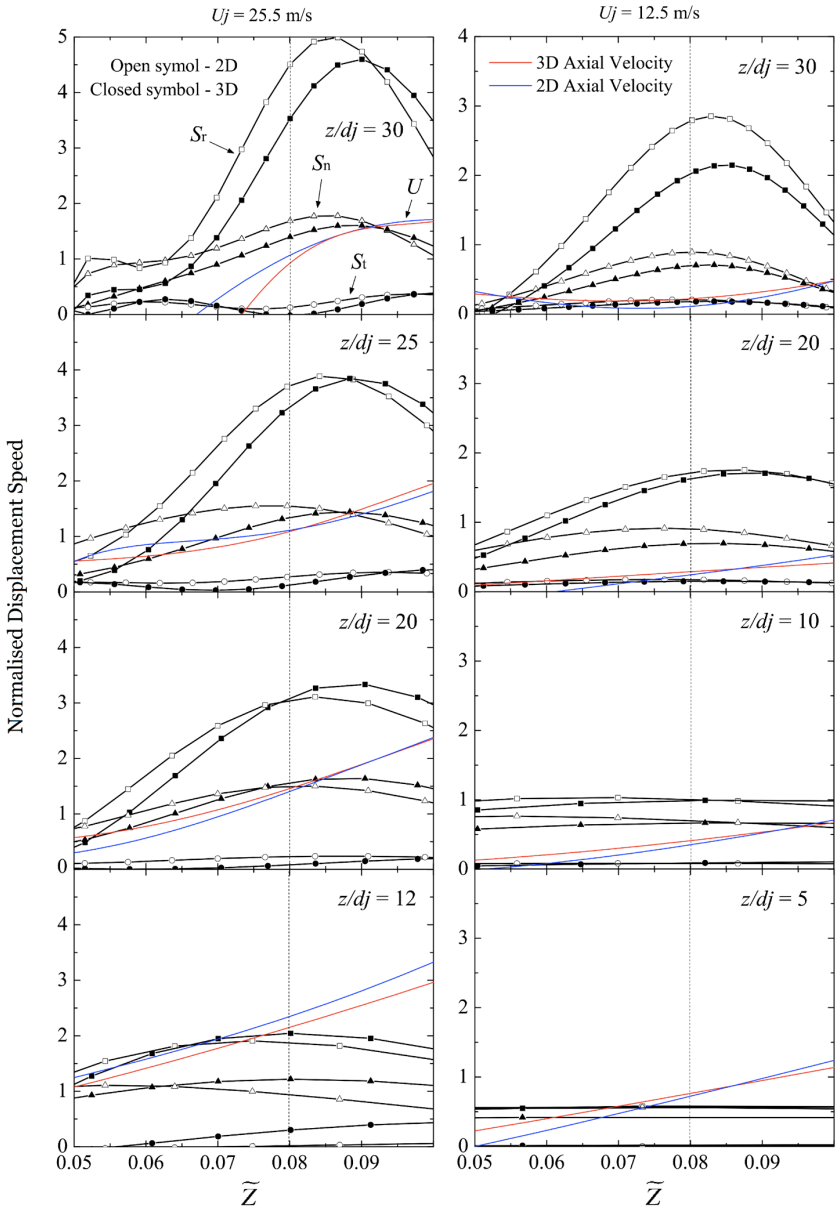

Figure 6.6: Comparison of computed 2D (open symbol) and 3D (closed symbol) displacement speed components in the $\widetilde{Z}$ space at different axial positions. The mean axial velocity is shown using blue (2D) and red (3D) solid lines. The y-axis is normalised using the laminar flame speed for stoichiometric methane-air mixture, S_L^0. Two jet velocities, $U_\mathrm{j} = 25.5$ m/s (left column) and 12.5 m/s (right column) are considered. The vertical dashed line corresponds to the flame most leading point marked in Fig. 6.5d.

flame propagation speed. The other two dominant components, $\overline{S}_\mathrm{r}$ and $\overline{S}_\mathrm{n}$, both have peaks located close to the leading point at all plotted positions. The values of both $\overline{S}_\mathrm{r}$ and $\overline{S}_\mathrm{n}$ at the leading point for the 2D cases are higher compared to that for 3D. For both velocity cases, this difference is substantial in the early stage of the transient evolution (top two rows in Fig. 6.6), whereas it vanishes as the leading edge approaches the final lift-off height region. As the local velocity is similar as shown by the coloured lines, the leading edge propagation speed in the 2D simulation is higher than that of 3D simulation in the early stage as has already been shown in Fig. 6.3. However, as the flame brush propagates upstream, the profiles of $\overline{S}_\mathrm{r}$ and $\overline{S}_\mathrm{n}$ spread over the mixture fraction space with smaller peak values near the leading edge and finally become more or less flat at the final lift-off height showing a fine balance between the flow velocity and the flame displacement speed for both 2D and 3D computations. The same trend is observed in Fig. 6.6 for both jet velocities. Thus, this change of influence of physical dimension during the transient evolution process is interpreted as that in the early-stage premixed propagation, since the surrounding mixture are fully flammable, the evolution of spatial gradients of scalars such as $\nabla \widetilde{c}$, plays a vital role in the flame propagation. As this spatial evolution occurs in the 3D physical space, one would expect 3D simulation for accurate prediction. However, these spatial gradients become less important to the leading edge propagation in the later edge flame propagation stage, involving many other physical processes such as strong flame/turbulence interaction, partial premixing with non-flammable mixtures, etc. In this stage, 2D simulation shows a reasonable prediction in the balance of these processes at the final lift-off height.

Another notable point in Fig. 6.6 is that the peak value of $\overline{S}_\mathrm{n}$ is nearly constant around S_L^0 throughout the flame evolution process, namely about 0.5 and 0.3 m/s for $U_\mathrm{j} = 25.5$ and 12.5 m/s respectively. In contrast, the maximum value of $\overline{S}_\mathrm{r}$ decreases quite significantly as the leading edge propagates towards its final stabilisation height. For both velocities, it drops from a value of several times of S_L^0 to around 0.4 m/s, which is very close to S_L^0. This is in line with the argument of Müller *et al.* [1994] using a G-equation approach showing that the premixed flame propagation dominates the early stage propagation process and the final stabilisation is controlled by a fine balance between many complex

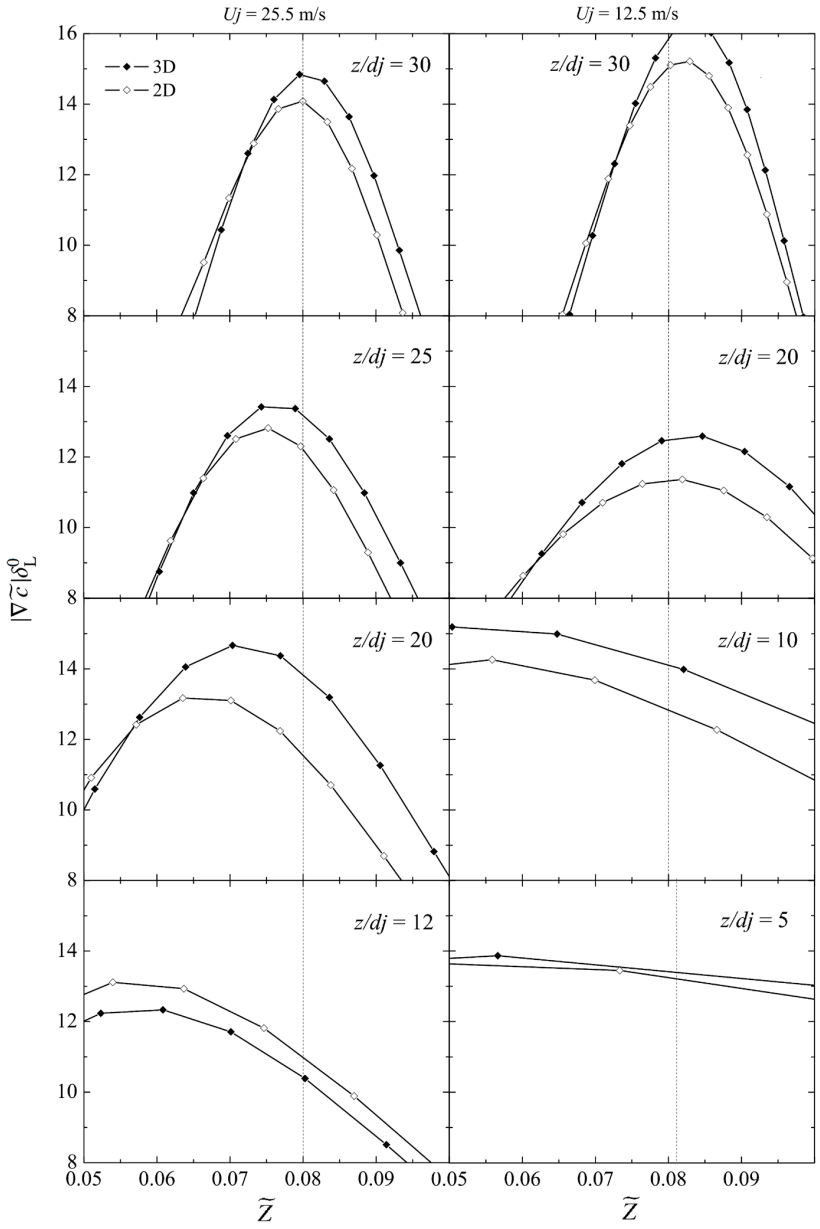

Figure 6.7: Comparison of computed 2D (open symbol) and 3D (closed symbol) profiles of scaled progress variable gradient magnitude, $|\nabla \widetilde{c}|\delta_L^0$, in the mixture fraction space. δ_L^0 is the laminar flame thickness for stoichiometric methane-air mixture. The vertical dashed line corresponds to the flame most leading point marked in Figure 6.5d.

physical processes.

Finally, to investigate the scalar gradients directly Figure 6.7 shows the profiles of $|\nabla \widetilde{c}|\delta_L^0$ in the $\widetilde{Z}$ space and δ_L^0 is the laminar flame thickness for stoichiometric methane-air mixture. It is seen that the value of $|\nabla \widetilde{c}|\delta_L^0$ at the leading point for the 3D computation is higher than that for the 2D case at most axial positions except those close to the final lift-off height. This is consistent with the previous findings in Figures 6.5 and 6.6, where the peak values of $\overline{S}_{\rm r} = \overline{\dot{\omega}_c^*} \ / \ \overline{\rho}\,|\nabla \widetilde{c}|$ at high axial positions, are smaller for the 3D simulation. It is also seen that for both velocity cases the maximum $|\nabla \widetilde{c}|\delta_L^0$ values vary only marginally throughout the transient evolution process. This suggests that the decrease of peak value $\overline{S}_{\rm r}$ shown in Figure 6.6 is caused by the decrease of maximum reaction rate at the leading edge, which may be due to the stronger turbulent fluctuations close to the jet nozzle corresponding to higher value of $|\nabla \widetilde{Z}\,|$, which agrees with a previous DNS study [Chakraborty & Mastorakos, 2006] showing that increase of mixture fraction gradient leads to decrease of $S_{\rm r}$. Furthermore, $|\nabla \widetilde{c}|\delta_L^0$ spreads over a wider range of mixture fraction at the leading edge as the flame propagates towards the upstream. In the stratified propagation stage (top two rows of Fig. 6.7), the gradient of $\widetilde{c}$ is mostly contained within the flammability limits suggesting that this scalar gradient is mainly driven by the chemical reactions. However, in the stabilisation stage (bottom two rows) the gradient covers a wider range beyond the flammability limits. This phenomenon indicates that in the stabilisation region, flame/flow interaction becomes much stronger and starts to influence the flame leading edge structure.

6.4 Summary

In this chapter, unsteady RANS simulations of spark ignited turbulent methane/air jet flames are performed using a partially premixed combustion model, which has shown good capability of predicting the flame final lift-off height in the previous chapter. A diluted jet with 70% CH_4 and 30% air by volume, injected into ambient air in the experimental study [Ahmed & Mastorakos, 2006] is tested for two jet bulk velocities, $U_{\rm j}$ = 25.5 and 12.5 m/s. 2D URANS computations are conducted first to study the flame transient evolution from ignition to stabili-

sation, and failed to capture the temporal variation of the flame's leading edge. Therefore, 3D URANS simulation is used for the same problem and the computed results are compared to the experimental and the 2D results. The main findings are summarised as follows.

- As one would expect, same final lift-off height is obtained from 2D and 3D computations for both jet velocities showing a good agreement with the experiments [Ahmed & Mastorakos, 2006]. This suggests that the influence of the third physical dimension on the flame stabilisation is negligible and hence the axisymmetric assumption is quite reasonable for computation of steady-state final lift-off height.

- Compared to the 2D results, the 3D computations show an evident improvement in comparison to the experimental data for the unsteady evolution of the most-upstream point of flame leading edge. The computed 3D net propagation speed is found to be much closer to the measured value. This is especially evident in the initial stage after ignition where the premixed flame propagation dominates for mixtures within the flammability limits. The third physical dimension plays an important role in this process by allowing the flame to evolve in the three-dimensional space, which leads to different flame propagation characteristics compared to 2D simulation. This influence of physical dimension is then found to be less significant after entering a region close to the final stabilisation height.

- Flame brush displacement speed, $\overline{S}_{\mathrm{d}}$, at the leading edge is investigated and it is found that for both 2D and 3D cases, the tangential diffusion component of $\overline{S}_{\mathrm{d}}$ is much smaller than the reaction, $\overline{S}_{\mathrm{r}}$, and normal diffusion, $\overline{S}_{\mathrm{n}}$, components throughout the transient flame evolution. The values of $\overline{S}_{\mathrm{r}}$ and $\overline{S}_{\mathrm{n}}$ in the 2D simulations are found to be larger than those of the 3D cases resulting in a higher net propagation speed. This effect of physical dimension is found to be more evident in the initial stratified flame propagation stage.

- The progress variable gradient $\nabla \widetilde{c}$ at the flame leading point is larger in the 3D cases compared to that for the 2D cases. From the initial ignition to

the final stabilisation, the maximum value of $|\nabla \widetilde{c}|\delta_L^0$ is found to be approximately the same, which implies that the higher mixture fraction gradient, $\nabla \widetilde{Z}$, resulting in the smaller reaction component of the displacement speed is responsible for the observed decrease of $\overline{S}_\mathrm{r}$.

Although the three-dimensional unsteady RANS simulation using a partially premixed combustion model seems to show quite good capabilities of predicting the transient evolution of the flame leading point, the instantaneous features of edge flame propagation and its interaction with the large structures of the oncoming flow are still to be examined. The influence of the third physical dimension is seen but still in an averaged manner in 3D URANS. Therefore, instantaneous behaviours of flame leading edge formation and propagation dynamics remain to be explored and more advanced approaches such as LES is well suited for this, which is explored in the next chapter.

Chapter 7

Spark Ignition and Flame Edge Propagation Dynamics

The LES modelling framework described in §3.1.2 and §3.2 for partially premixed combustion is tested in this chapter. The presumed joint PDF approach is used for the sub-grid combustion modelling which includes contributions from both premixed and non-premixed modes. The spark ignition experiments of Ahmed & Mastorakos [2006] are considered for the present work to study the transient behaviours of the most-leading flame edge in the ignition sequence of a methane/air jet using LES. This transient evolution has been simulated using URANS in the previous chapter, and the objective of this chapter is to apply LES to the same configuration to validate the model and to obtain further insights of the dynamic flame/flow interaction during this process, which is not available in URANS. Moreover, the statistics collected after the flame reaches its final lift-off height are analysed to shed more light on the lifted flame stabilisation mechanism.

7.1 Experimental test case

The schematic and geometrical details of the jet burner [Ahmed & Mastorakos, 2006] were shown earlier in Fig. 4.1 and Table 4.1 respectively. The experimental setup and measurement techniques used for the spark ignition sequence have been described in §6.1. The two jet bulk mean velocities, $U_{\mathrm{j}} = 12.5$ and 25.5 m/s, were

Table 7.1: Summary of the computed flame details.

Flame	Air	U_j [m/s]	Re	Ignition
F3-1	30%	12.5	3759	$30d_j$
F3-2	30%	25.5	7669	$30d_j$

investigated for the diluted flame F3 (30% air by volume) in the experiments and they are denoted as F3-1 and F3-2 respectively in this chapter. The details of these flames are given in Table 7.1. In previous LES studies on this ignition experiment, Lacaze *et al.* [2009b] computed the high-velocity (25.5 m/s) case using the artificially thickened flame model and found a quite good agreement with the measurements of both the final lift-off height and transient evolution of flame leading point. This evolution was studied by comparing LES snapshots and line-of-sight experimental images. Jones & Prasad [2011] calculated the low-velocity (12.5 m/s) flame of Ahmed & Mastorakos [2006] using a filtered PDF approach with Eulerian stochastic fields. A good agreement with the measurements was observed for the transient evolution but the final lift-off height was over-predicted by about 2 to $3d_j$. In the present study, both jet velocity cases ignited at $30d_j$ are computed to show the LES model performance under different flow conditions. The influence of jet exit velocity is investigated for the different flame stages identified earlier in Fig. 6.1 from the initial spark ignition to final stabilisation.

7.2 Numerical modelling details

The LES methodology for partially premixed combustion described in §3.1.2 and §3.2 is used for this study. The Favre-filtered conservation equations for mass, momentum and total enthalpy given in Eqs. (3.24), (3.25) and (3.26) are solved. The unresolved sub-grid stress tensor, $\boldsymbol{\tau}_{\rm sgs} \equiv \overline{\rho}(\widetilde{\boldsymbol{U}\boldsymbol{U}} - \widetilde{\boldsymbol{U}}\,\widetilde{\boldsymbol{U}})$, is closed using the Smagorinsky model [Smagorinsky, 1963] for the SGS eddy viscosity: $\mu_{\rm sgs} = \overline{\rho}\,(C_S\Delta)^2|\widetilde{\boldsymbol{S}}|$, where $C_S = 0.167$, $|\widetilde{\boldsymbol{S}}|$ is the magnitude of the filtered rate of strain as given in Eq. (3.29) and $\overline{\rho}$ is the filtered density calculated using the state equation. The filter width Δ is computed as the cube root of the local numerical

cell volume.

For the SGS combustion modelling, Bilger's formula [Bilger *et al.*, 1990] for mixture fraction and the progress variable definition given in Eq. (3.13) are used following the previous studies of Darbyshire & Swaminathan [2012] and Ruan *et al.* [2014a, 2015], and to be consistent with Chapters 5 and 6. The filtered values and sub-grid variances of Z and c are computed in LES using their transport equations as described in Eqs. (3.31)−(3.34). The unclosed reaction and dissipation terms appearing in these equations require modelling, and these models are detailed in §3.1.2 and §3.2. It is worthwhile to recall here that the filtered reaction rate, $\overline{\dot{\omega}_c^*}$, in Eq. (3.33) includes both the contributions from premixed and non-premixed combustion modes as in the RANS studies shown in Chapters 5 and 6. However, the Z-c correlation effect on $\overline{\dot{\omega}_c^*}$, which was found to be quite important in RANS, is not considered here at the sub-grid scale level because it is expected to be negligible in LES, where the fluctuation of Z is mostly resolved by the numerical grid. One shall see the validity of this hypothesis while comparing the LES results with the experimental measurements in the next section.

Figure 7.1 shows typical variation of the premixed part of the filtered reaction rate (see Eq. 3.46), $\overline{\dot{\omega}_c}$, as a function of the control parameters, $\widetilde{c}$ and $\widetilde{g}_c$, related to reaction progress for three representative filtered mixture fractions with a typical value of $\widetilde{g}_Z = 0.017$. This reaction rate is obtained using a sub-grid joint PDF as described in Eq. (3.47) and the tabulation procedure can be seen in §3.3. The contour values of $\overline{\dot{\omega}_c}$ shown in Fig. 7.1 are normalised by a laminar flame scale, $(\rho_u S_L^0/\delta_L^0)_{st}$, where ρ_u is the unburnt mixture density at stoichiometry. The marginal PDF of the mixture fraction, $P_\beta(\xi;\, \widetilde{Z},\, \widetilde{g}_Z)$, is also plotted in this figure, and it is computed using a β-function with the given $\widetilde{Z}$ and $\widetilde{g}_Z$ values. It can be seen that the distribution of $\overline{\dot{\omega}_c}$ is similar for these three mixture fractions and the only difference is the maximum value, which appears in the region around $\widetilde{c} = 0.7$ with very small $\widetilde{g}_c$ values. As one would expect, the maximum value (see colour bar) is larger for the stoichiometric case compared to the lean and rich cases. As $\widetilde{g}_c$ increases, the filtered reaction rate decreases because the burning part of the SGS PDF becomes smaller. The mixture fraction PDF has a monomodal shape peaking around the filtered value, marked using a dashed line, in all three cases because the mixture fraction variance is low. The effect of this distribution in

the mixture fraction space broadens the filtered reaction rate zone resulting in a smoother distribution compared to that for purely premixed flames (see Fig. 6.1 of [Langella, 2015]).

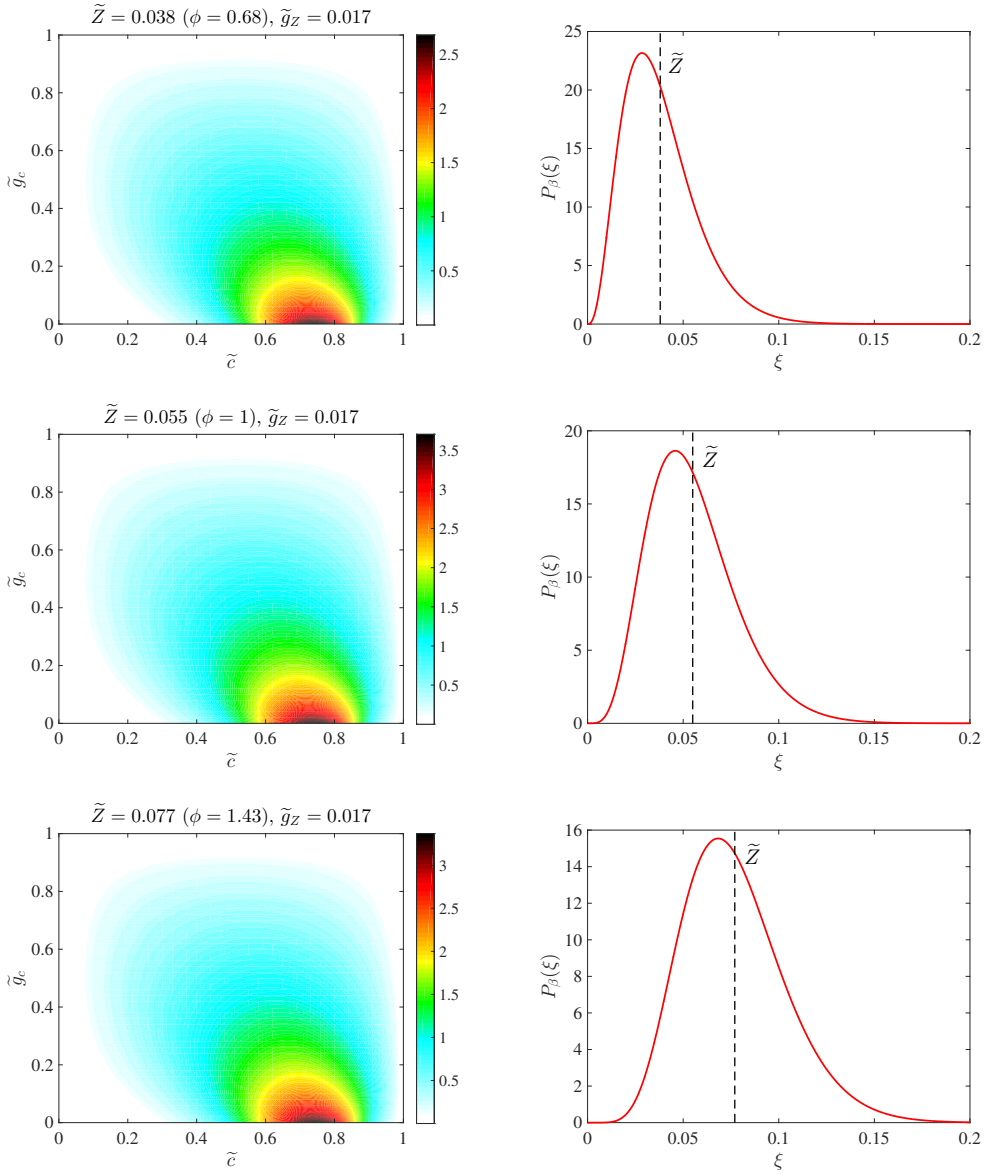

Figure 7.1: Typical variation of the normalised filtered reaction rate using a laminar scale, $(\rho_u S_L^0/\delta_L^0)_{st}$.

The computational domain illustrated in Fig. 4.1 for cold flow LES is adopted for reacting flow simulations. The velocity profile at the jet inlet is specified using

the 1/7th power law given in Eq. (4.1) and the turbulent fluctuation is described through a 5% random noise. Other flow field and scalar boundary conditions are similar as for RANS simulations and these are described in §5.2. The numerical grid used for cold flow LES (see Fig. 4.2) is refined in order to cover the entire the flame propagation region and the schematic of the resulting grid on a middle-plane slice is shown in Fig. 7.2a. The final LES grid for reacting flow simulations consists about 7.8 million tetrahedral cells. In order to show the relative mesh size with respect to the characteristic flame thickness, a normalised size defined as

$$\Delta^{+} = \frac{\Delta}{(\delta_L^0)_{st}} \tag{7.1}$$

is used, where $(\delta_L^0)_{st} \approx 0.4$ mm is the laminar flame thickness for stoichiometric methane/air mixture. Figure 7.2b presents a colour map of Δ^{+} in the enlarged refinement area marked in Fig. 7.2a. As one can see, the mesh in the spherical region around the ignition location is refined with $\Delta^{+} = 1$ to resolve the initial flame kernel expansion. Although it is not of interest, the downstream of this location up to the outlet also requires refinement to avoid numerical issues caused by the high temperature gradients. In the upstream mixing layer where the flame edge propagates towards the jet exit until reaching its final lift-off height, the grid size is about $\Delta^{+} = 2$ to 3 suggesting that the flame front is not resolved by the LES grid and it is computed using the sub-grid combustion model described in §3.2.

For the numerical ignition, imposing a constant value of $\widetilde{c} = 1$ for the entire flame kernel sub-domain is found to be numerically unstable for LES. This is because the temperature gradient is very high at the interface between the fully burnt kernel and surrounding unburnt mixtures. In order to overcome this issue, an empirical fit for the filtered progress variable profile is specified for the flame kernel, which is given by

$$\widetilde{c} = 1 - \left[\exp\left(8 - 16\frac{r_{\text{ig}}}{R_{\text{kernel}}}\right) + 1\right]^{-1}, \tag{7.2}$$

where r_{ig} is the distance from the kernel centre and $R_{\text{kernel}} = 1$ mm is the kernel

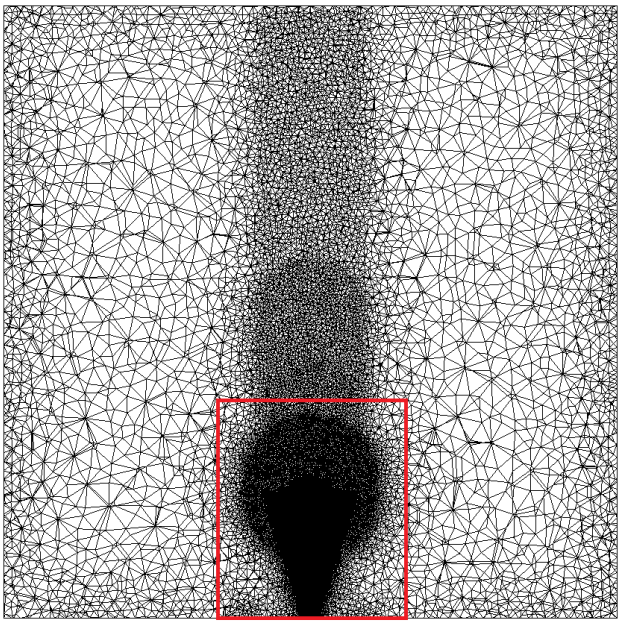

(a)

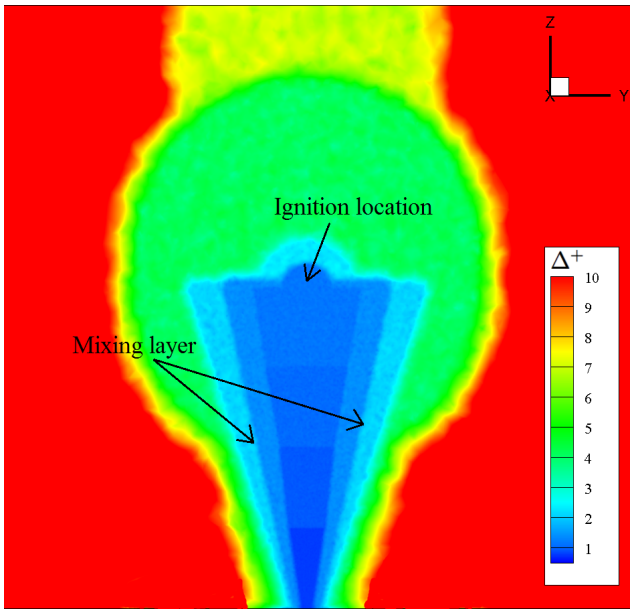

(b)

Figure 7.2: (a) Middle-plane of the LES numerical grid. (b) Distribution of the normalised filter size $\Delta^+ = \Delta/(\delta_L^0)_{st}$.

radius. This kernel is kept for a duration of 7.5 μs and the equivalent integrated energy deposition is about 100 mJ as in the experiments [Ahmed & Mastorakos, 2006].

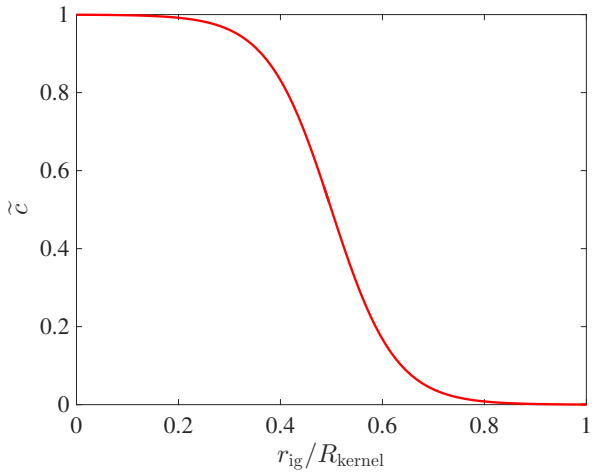

Figure 7.3: Progress variable profile for flame kernel initialisation. r_{ig} is the distance from the kernel centre and $R_{\mathrm{kernel}} = 1$ mm is the kernel radius.

In order to resolve the transient evolution of the spark ignition sequence, a relatively small time-step size of 4×10^{-7} s is used so that the CFL number (given in Eq. B.5) is below 0.3 for the entire LES domain. The computation is performed using 1080 cores on the ARCHER UK National Supercomputer and a typical ignition sequence of 600 ms in physical time requires about 60 hours of wall-clock time. Fully developed cold mixing flow is obtained before igniting the flame and the averaged mixture fraction for flame F3-2 agrees quite well with the an empirical correlation [Richards & Pitts, 1993] as has been shown in Fig. 4.6.

7.3 Results and discussion

7.3.1 General flame evolution characteristics

Figure 7.4 presents the instantaneous filtered temperature field evolution along with the stoichiometric mixture fraction iso-surface (shown as black line) for flame F3-2 from its initial ignition kernel to the final lift-off height. A series of eight

typical time instants are plotted in Figs. 7.4a to 7.4h. The overall flame typologies are very similar to the observations in the experiments [Ahmed & Mastorakos, 2006] and previous LES studies [Jones & Prasad, 2011; Lacaze *et al.*, 2009a]. Four flame evolution stages are identified in this ignition sequence, which is consistent with the RANS results presented earlier in Fig. 6.1.

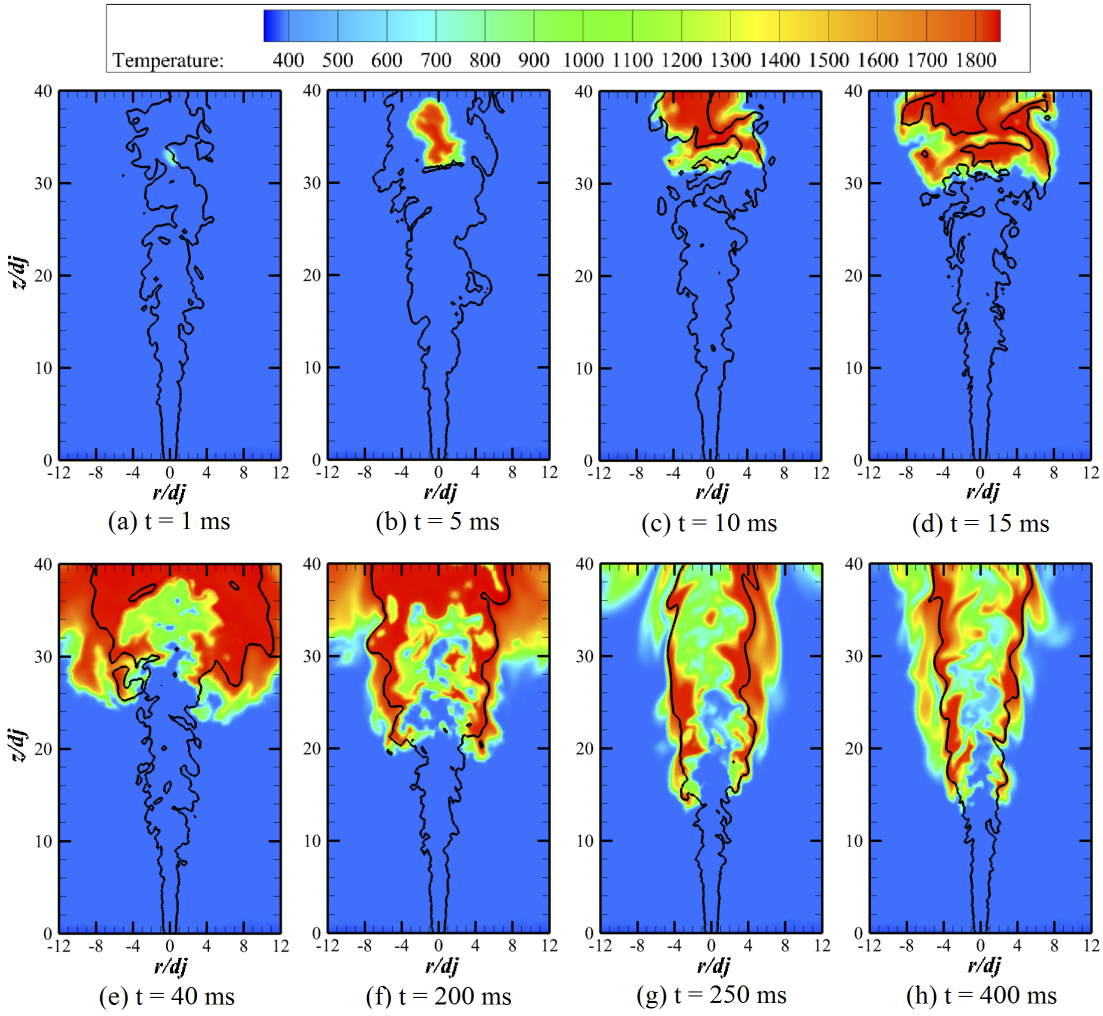

Figure 7.4: Typical LES middle-plane snapshots of the filtered temperature field for flame F3-2 at eight different time instants from initial ignition to final stabilisation. The thick line is the stoichiometric mixture fraction iso-surface.

After ignition, the flame kernel is first convected downstream by the oncoming turbulent flow and also diffuses in the spanwise directions leading to a decrease

of kernel temperature as seen in Fig. 7.4a. This process heats up the surrounding flammable mixtures and then forms an expanding flame kernel as in Fig. 7.4b. Subsequently, from Fig. 7.4b to 7.4d (t = 5 to 15 ms in physical time), the flame expands in the radial direction and propagates downstream along with the mean flow, but the most-upstream point remains at more or less the same axial position, about $32d_{\mathrm{j}}$. The upstream propagation starts when the flame reaches a certain radial position, about $8d_{\mathrm{j}}$ in this case, the most-leading point seems to be in quite lean regions. This can be seen in Fig. 7.4e where the flame most-leading point is approximately $2d_{\mathrm{j}}$ away from the $\widetilde{Z}_{st}$ line on the lean side. However, after the flame leading edge has propagated upstream for some distance, as seen in Figs. 7.4f and 7.4g, the most-leading point is found to be close to the stoichiometry line. A possible reason for this difference is that in the initial stage the flame radial expansion results in the flow divergence in the radial direction, which brings the burnable mixture from the upstream to the wide areas. Since the oncoming flow velocity is low in these wide areas, the resulting flame propagation speed is higher than that in the jet centre areas. However, there is no radial expansion occurring upstream and thus no flammable mixtures are supplied for the subsequent flame propagation in these areas. Therefore, these flame leading edges are quenched by the non-flammable lean mixtures and this can be seen in Figs. 7.4f and 7.4g, where the high temperature contour is convected downstream in the wide areas. Finally, in Fig. 7.4h an edge-flame is established in the vicinity of $\widetilde{Z}_{st}$ and stabilised at the final lift-off height.

To shed more light on the reaction zone evolution during the ignition sequence, Fig. 7.5 qualitatively compares the LES filtered reaction rate contours with the experimental OH-PLIF images for flame F3-2 at five different instants from 5 to 100 ms after ignition. It is shown that the overall reaction zone shapes computed by the LES are very similar to those indicated by the OH-PLIF images for the instants shown in Fig. 7.5. It can be observed that the reaction zone on the jet centreline disappears after 30 ms and the flame turns into a hollow cylindrical shape. Ahmed & Mastorakos [2006] argued that this is because the fuel pockets with mixture fraction higher than the rich flammability limit enter the central reaction zone as the flame moves upstream, which results in flame quenching in this area. This behaviour is also captured well by the LES as one can see in

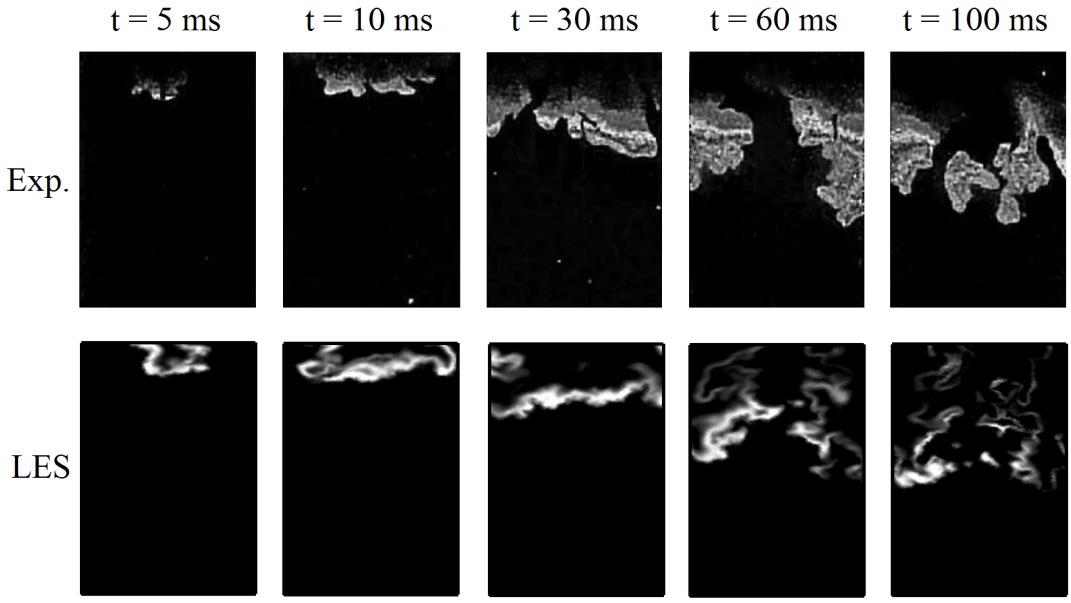

Figure 7.5: Comparison between experimental OH-PLIF images [Ahmed & Mastorakos, 2006] (the upper row) and computed reaction reaction rate $\overline{\dot{\omega}_c^*}$ contours (the lower row) at five typical time instants after ignition.

Fig. 7.5, at $t = 60$ and 100 ms.

The LES seems to predict the overall flame behaviours reasonably well suggesting good performance of the chosen turbulence and sub-grid combustion models. However, more quantitative comparison with the experimental measurements is required to demonstrate further validity of these models. Moreover, further investigation on the transient evolution of flame most-leading edge is required to obtain more insights of the flame ignition process. These are discussed next.

7.3.2 Kernel growth and flame edge formation

In the experiments, Ahmed & Mastorakos [2006] conducted the spark ignition using two electrodes with a gap of 1 mm in between. The total energy deposition was reported to be about 100 mJ. This procedure is followed in the LES through a numerical ignition approach as noted in §7.2. Figure 7.6 shows a comparison between the experimental high-speed camera images and the LES reaction rate contours for the initial flame kernel growth process. The flame kernel is observed

to be quasi-spherical during its early growing stage in the experiments, which is captured well in the LES.

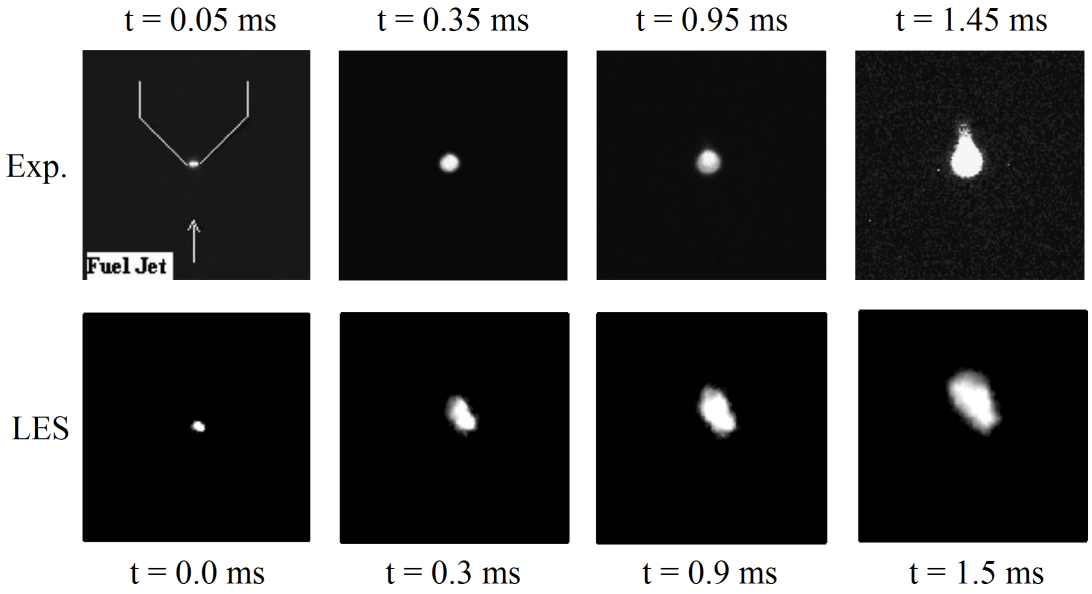

Figure 7.6: Visualisation of the flame F3-2 kernel growth: comparison between experimental high-speed camera images [Ahmed & Mastorakos, 2006] (the upper row) and computed reaction reaction rate $\overline{\dot{\omega}_c^*}$ contours (the lower row).

To quantify the growth rate of the kernel, Ahmed & Mastorakos [2006] obtained the temporal variation of the average kernel diameter using 10 high-speed images for each instant. These experimental results are shown in Fig. 7.7 along with the kernel diameter computed from the LES results. The kernel diameter in the LES is estimated as

$$d_{\text{kernel}} = \left(\frac{6V_{\text{b}}}{\pi}\right)^{1/3}, \tag{7.3}$$

where V_{b} is the volume of the burnt gas in the computational domain. It is seen in Fig. 7.7 that a very good agreement is obtained between the experimental and LES results for d_{kernel}. More importantly, the growth rate corresponding the slope, $d(d_{\text{kernel}})/dt$, is captured by the LES very well. This growth rate is mainly governed by the diffusive and reactive processes in the flame kernel region, suggesting that these processes are predicted well by the LES sub-grid

combustion and turbulence models.

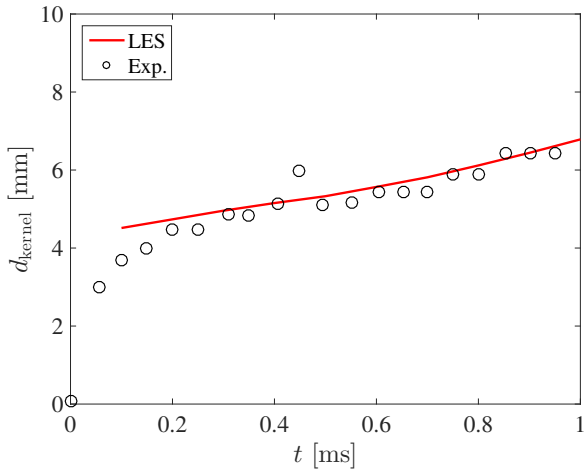

Figure 7.7: Temporal variation of the flame F3-2 kernel diameter obtained from the experiments [Ahmed & Mastorakos, 2006] and LES.

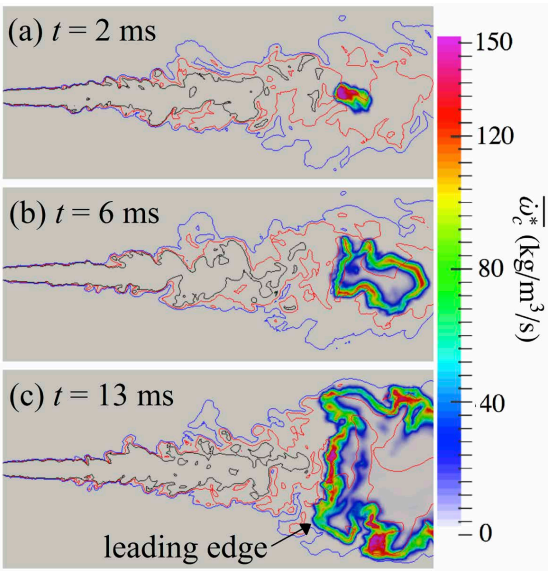

Figure 7.8: Middle-plane snapshots of the filtered reaction rate $\overline{\dot{\omega}_c^*}$ in flame F3-2. The iso-lines are stoichiometry (red), rich (black) and lean (blue) flammability limits.

After the spherical kernel has fully grown, an edge flame forms during the radial expansion stage as in Fig. 7.8, showing the filtered reaction rate of progress

variable along with the mixture fraction iso-lines. It is observed that the formation starts from a rich mixture on the jet centreline in Fig. 7.8a, and then expands radially across the stoichiometric line in Fig. 7.8b and finally establishes a leading edge in the relatively lean mixture as highlighted in Fig. 7.8c. Subsequently, this edge flame starts to propagate upstream interacting with the oncoming flow, shown by the wrinkled flame structure. During this process, the reaction rate is well contained within the flammability limits suggesting a good model prediction for the edge flame evolution. These flame edge formation behaviours are similar to those found in the previous URANS study as shown in Fig. 6.1. However, a wrinkled filtered flame front with dynamic interaction with the turbulent flow is seen in the LES. This helps to gather additional insights on the flame edge upstream propagation, which are discussed next.

7.3.3 Flame edge propagation dynamics

In the previous sections and earlier studies [Jones & Prasad, 2011; Lacaze *et al.*, 2009a], the LES slices and line-of-sight experimental images are compared qualitatively to study the flame edge propagation. To investigate this process further, the flame behaviour in the 3D space needs to be considered because the flame leading edge does not reside in the same z-r plane (see Fig. 4.1 for illustration) because of its evolution in the azimuthal direction. The influence of physical dimensions has been studied in Chapter 6 by comparing 2D and 3D URANS results showing substantial importance for the flame transient evolution but still in an averaged manner.

This influence is further investigated in Fig. 7.9 showing typical 3D evolution of the leading edge at four instants after ignition using $\widetilde{T} = 1200$ K iso-surface coloured by $\overline{\dot{\omega}_c^*}$. The iso-contour of the stoichiometric mixture fraction, $\widetilde{Z}_{st}$, is also shown to visualise the flow and mixing fields. As highlighted by the black circles in this figure, the leading point appears at different azimuthal positions at different times. The local reaction rate at these points seems to vary largely, with high values over 100 kg/m^3/s for $t = 19$ and 52 ms and lower values of around 75 kg/m^3/s for 91 and 151 ms. To shed more light on this, Fig. 7.10 plots a typical iso-surface of $\overline{\dot{\omega}_c^*} = 80$ kg/m^3/s coloured by $\widetilde{T}$ at the same instants

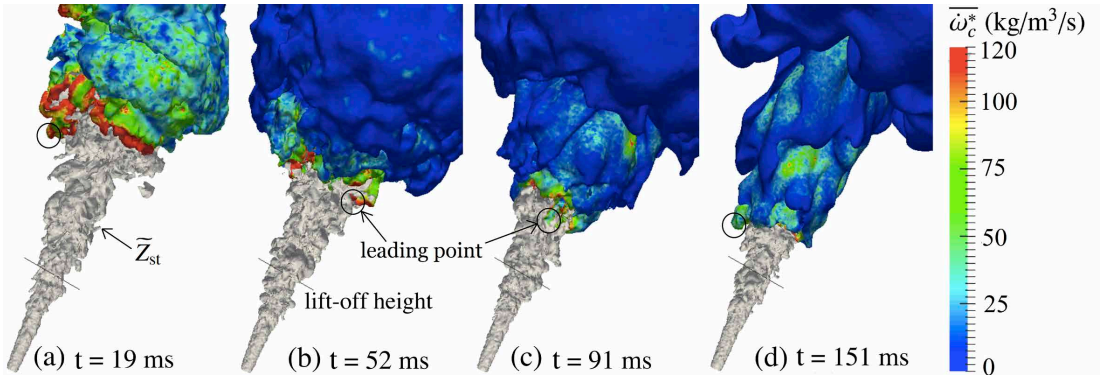

Figure 7.9: Transient evolution of flame F3-2 leading edge marked using $\widetilde{T}$=1200 K iso-surface coloured by $\overline{\dot{\omega}_c^*}$. The uncoloured iso-contour corresponds to stoichiometric mixture fraction

as in Fig. 7.9. Similar leading point locations are observed in these two figures suggesting that the leading point marker chosen using $\widetilde{T}$ can represent the flame leading edge quite well. In Fig. 7.10, the $\widetilde{Z}_{st}$ iso-surface is coloured by its filtered scalar dissipation rate, which is normalised as

$$\widetilde{\chi}_Z^+ = \frac{\widetilde{\chi}_Z}{\chi_{st,\mathrm{q}}}, \tag{7.4}$$

where $\chi_{st,\mathrm{q}} = 5\ \mathrm{s}^{-1}$ is the quenching dissipation rate obtained from laminar flame calculation using the chemical mechanism GRI-Mech 3.0, and it is found to be similar to the values used in the previous studies [Ferraris & Wen, 2007; Peters, 2000]. It is shown in Fig. 7.10 that $\widetilde{\chi}_Z^+ << 1$ for the downstream of flame lift-off height suggesting that the flamelet quenching effect on the flame leading edge propagation is negligible. The value of $\widetilde{\chi}_Z^+$ becomes visible in Fig. 7.10 when the flame leading edge approaches the final lift-off height, however, it is still smaller than 0.25. Therefore, flamelet quenching may be partly involved in the lifted flame final stabilisation mechanism, but is still not expected to have a crucial contribution. These findings are consistent with the observations from the previous studies [Chen *et al.*, 2015; Müller *et al.*, 1994; Ruan *et al.*, 2014a].

Furthermore, the radial position of the leading point identified in Figs. 7.9 and 7.10 also varies from one instant to another because of the difference in local mixing conditions. A *finger-like* shape at the leading point is observed

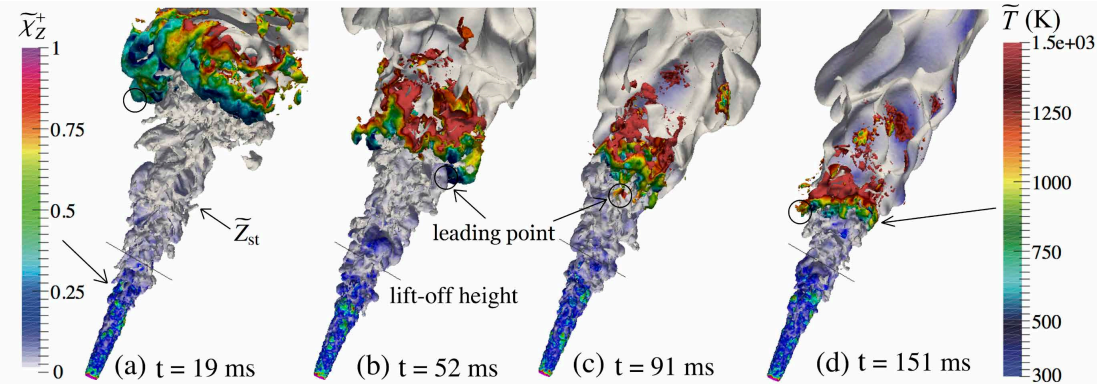

Figure 7.10: Transient evolution of flame F3-2 leading edge marked using $\overline{\dot{\omega}_c^*}$=80 kg/m^3/s iso-surface coloured by $\widetilde{T}$. The $\widetilde{Z}_{st}$ iso-contour is coloured by a normalised scalar dissipation rate $\widetilde{\chi}_Z^+$.

in Figs. 7.9a and 7.9d and this is outside the stoichiometric surface indicating lean mixture, whereas the leading point is found close to the stoichiometry in Figs. 7.9b and 7.9c. This is because the turbulent flow generates fuel pockets far from the jet centre and these ignited pockets propagate faster than the main flame as the local velocity is relatively small. Once the fuel in the pocket has been fully consumed, these branches extinguish and the leading point moves close to the stoichiometry. These flame propagation behaviours suggest that the large-scale flame/flow interaction plays an important role in the transient evolution of the leading edge.

The axial position of the most upstream point of the leading edge was measured by Ahmed & Mastorakos [2006] at various times covering the entire ignition sequence. The averaged results are obtained by ensemble averaging 10 samples for each of flames F3-1 and F3-2. These results are shown in Fig. 7.11 along with the computational results. An overall good agreement is observed for both flames, however, the final lift-off height of F3-1 is over-predicted by about $2d_j$, which is similar to that captured by Jones & Prasad [2011]. This is possibly due to the fast-decaying random fluctuation given at the inlet boundary yielding under-predicted turbulent mixing in the near jet exit region (about $3d_j$) where flame F3-1 is stabilised. The partially premixed combustion occurs in the stabilisation region and this small difference in the final lift-off height may be due to the assumption of statistical independence for the sub-grid fluctuations of Z and c.

The difference seen in Fig. 7.11 for the transient evolution may also be due to this assumption, although it is found to be quite small for both flames. Further investigations are required to obtain a clear understanding of the sub-grid fluctuation correlation but it is not within the scope of this thesis. Nevertheless, the transient evolution of the flame leading point during the entire ignition sequence is captured reasonably in the LES using the partially premixed combustion model proposed in §3.2 and is similar to the prediction obtained using thickened flame [Lacaze *et al.*, 2009a] and LES-PDF [Jones & Prasad, 2011] methods with significantly less computational cost.

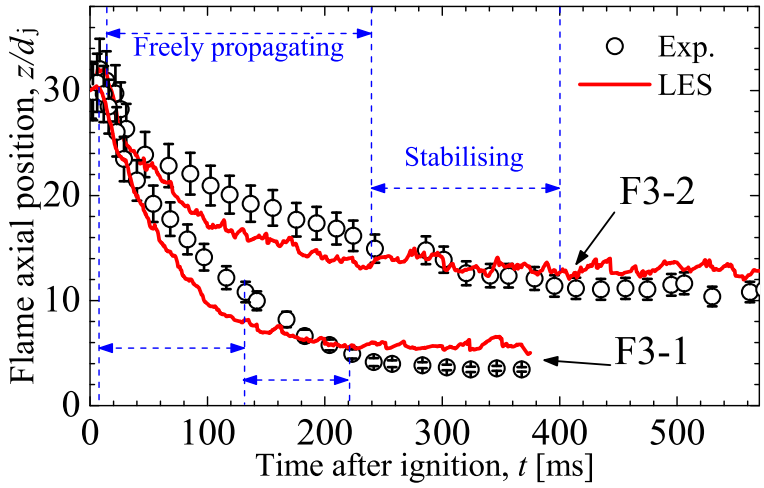

Figure 7.11: Transient evolution of measured and computed flame leading point. The error bars correspond to the 9% maximum scatter of the experimental data [Ahmed & Mastorakos, 2006].

Two sub-stages of flame propagation are noted in Fig. 7.11. In the beginning, the thermo-chemistry is stronger than the convection at the leading edge yielding a high net propagation speed and this process is called as the freely propagating sub-stage, which is from 5 to 130 ms for F3-1, and from 15 to 240 ms for F3-2 flames. The dominant thermo-chemical effect is reflected by the large $\overline{\dot{\omega}_c^*}$ in Fig. 7.9a and 7.9b. The second sub-stage is the stabilising process, in which the leading point enters the stabilisation region with high turbulence but still moves upstream slowly until the final lift-off height is reached. The flame propagation behaviour during these sub-stages is further discussed later in this section.

Figure 7.12 presents the 3D travel path of the leading point from the ignition location to final lift-off height for both flames F3-1 and F3-2. The trajectory shown is from single LES realisation of these two flames and different spiral trajectories are expected from different realisations. The scatters plotted on the stabilisation plane show the radial and azimuthal variation of the stabilisation location at the lift-off height. The arrows near the ignition plane demonstrate the initial downstream kernel convection and radial expansion stages, and the red arrows indicate the direction of increasing time.

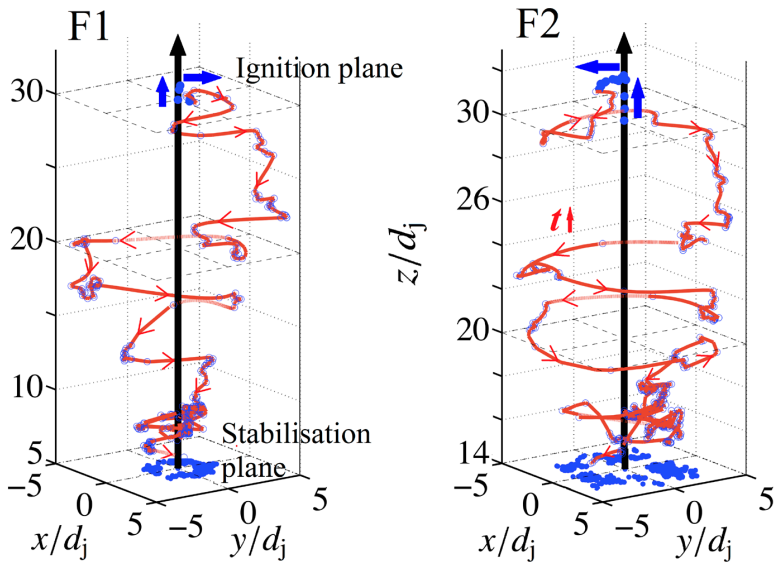

Figure 7.12: 3D visualisation of the flame leading point trajectory.

The leading point trajectory seems to follow a *spiral*-shaped trajectory during the evolution of both F3-1 and F3-2. The kernel is convected downstream initially almost along the jet axis which is clearer for F3-2 due to higher flow velocity. Different expansion directions are observed for F3-1 and F3-2 leading to different subsequent travel paths as in Figs. 7.12a and 7.12b. This is because of the difference in the local mixing conditions. However, there will be equal probability for the initial radial expansion of the flame to occur in any angle. After this expansion, the leading point moves upstream with further radial expansion until a maximum radial distance is reached. This distance seems to be independent of the jet velocity and it is about $5d_j$ in both Figs. 7.12a and 7.12b.

The flame propagation dominates during this phase, which corresponds to the freely propagating sub-stage identified earlier, and the flame/flow interaction is reflected through the mixing by directing the leading edge to the most reactive spots. These spots are controlled by the local conditions of the mixture and flow-straining dictated by large-scale motion. In the stabilising sub-stage, as the flame approaches the region close to the lift-off height below $10d_{\mathrm{j}}$ for F3-1 and $20d_{\mathrm{j}}$ for F3-2, the leading point move closer to the centreline. The large fluctuation seen there is caused by strong interaction between the leading edge and the oncoming flow with mixtures beyond the flammability limits creating local extinctions. In the final stage of stabilisation, the leading point randomly moves around the centreline. This random motion shown as scattered points projected on the final stabilisation plane suggests an approximate circular motion. This approximate circle diameter shown in Fig. 7.12b for flame F3-2 is evidently larger than that for F3-1 in Fig. 7.12a and this influence of the jet velocity is further discussed by examining the lift-off statistics next.

7.3.4 Lift-off statistics

The flame stabilisation location oscillates by about one to two jet diameters in both the axial and radial directions depending on the jet exit velocity. These oscillations are shown in Fig. 7.13 resulting from unsteadiness in the oncoming and entrained flows. The radial location moves outward as the flame leading edge moves downstream and *vice versa*. It is close to the $\widetilde{Z}_{st}$ iso-contour, about $r = 2d_{\mathrm{j}}$, at the first two instants in Fig. 7.13 ($t = 571$ and 611 ms), and the corresponding axial location is above $z = 14d_{\mathrm{j}}$. This axial location then moves upstream, below $z = 14d_{\mathrm{j}}$, in the two later instants ($t = 640$ and 667 ms), where the radial location of the flame leading edge is found to be in more outer regions with about $r = 3$ to $4d_{\mathrm{j}}$.

These correlated movements discussed above can be further seen in Fig. 7.14 showing the joint PDF of the axial, L_{f}, and radial, R_{f}, locations of the stabilisation point for both F3-1 and F3-2. This PDF is constructed using 500 samples collected over 250 ms. The iso-lines shown are the stoichiometry, lean and rich

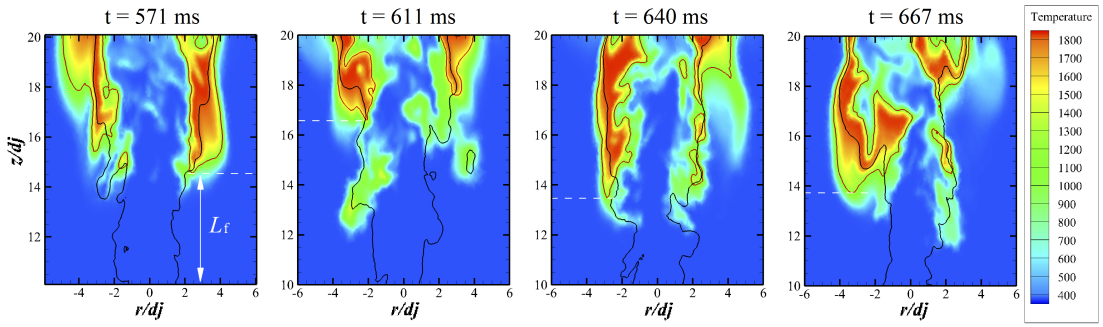

Figure 7.13: Illustration of flame F3-2 stabilisation location oscillations. The black line is the stoichiometric mixture fraction iso-contour and the red line corresponds to $\widetilde{T} = 1200$ K. The instantaneous lift-off height is marked using the white dashed line at each instant.

flammability limits based on the time-averaged mixture fraction field, $\langle\widetilde{Z}\rangle$. These radial and axial coordinates are normalised using the jet diameter, d_j, (the left and bottom axes) or a representative length scale, $U_\mathrm{j}\tau_L$, (the right and top axes) where $\tau_L = (\delta_L^0/S_L^0)_{st}$ for stoichiometric methane/air mixture. The stabilisation point with the highest probability in Fig. 7.14 is observed around $L_\mathrm{f} = 5.7d_\mathrm{j}$ and $R_\mathrm{f} = 1.7d_\mathrm{j}$ for flame F3-1. In contrast, flame F3-2 is stabilised at $L_\mathrm{f} = 13.2d_\mathrm{j}$ and R_f =$2.7d_\mathrm{j}$, further away from the jet exit and centreline. These axial and radial locations and also their fluctuations seem to collapse between F3-1 and F3-2 for the scaling using $U_\mathrm{j}\tau_L$ suggesting a possibly strong correlation with the jet exit velocity. Also, the most probable locations are observed to be on the lean side of stoichiometry, very close to the lean flammability limit for both flames. However, it is less probable for the stabilisation point to appear on rich side because of high local flow velocity, which is similar to previous study on lifted jet flame in vitiated co-flows [Ihme & See, 2010].

To further explore this correlation between the radial location and mixture fraction, Fig. 7.15 shows the joint PDF of R_f and $\widetilde{Z}$ for both flames F3-1 and F3-2. It is clear that both flames are mostly stabilised in the lean mixtures ($\widetilde{Z}_\mathrm{l} < \widetilde{Z} < \widetilde{Z}_{st}$), having the most probable location at about $\widetilde{Z} = 0.08$ for F3-1 and $\widetilde{Z} = 0.06$ for F3-2. However, no evident correlation is observed between R_f and $\widetilde{Z}$ fluctuations suggesting that the radial stabilisation location may also depend on other physical processes such as large-scale flow structure and flame/turbulence

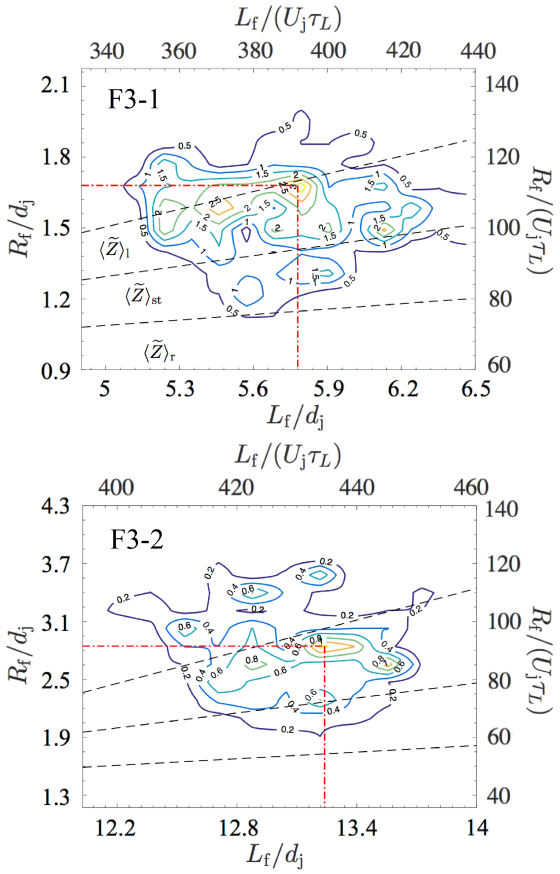

Figure 7.14: Joint PDF of the stabilisation axial and radial locations. $\langle\widetilde{Z}\rangle_{st}$, $\langle\widetilde{Z}\rangle_l$ and $\langle\widetilde{Z}\rangle_r$ correspond to stoichiometry, lean and rich flammability limits respectively.

interaction.

7.4 Summary

This chapter has numerically investigated the transient evolution of edge flame in a spark-ignited methane-air jet [Ahmed & Mastorakos, 2006] using LES with a sub-grid model for partially premixed combustion. Full sequence of ignition kernel development to final flame stabilisation is simulated for two jet velocities with the same initial ignition location. Good agreement is obtained between the LES results and measurements for the flame initial kernel growth, leading edge

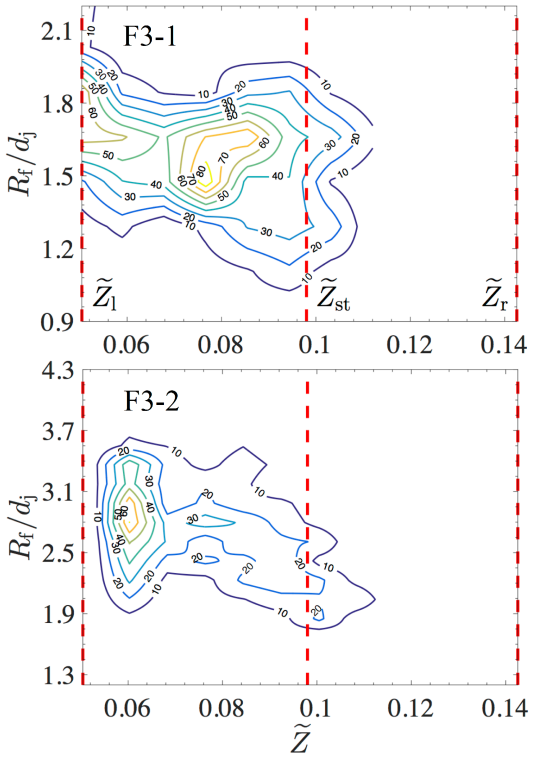

Figure 7.15: Joint PDF of the mixture fraction and radial stabilisation location.

propagation and final stabilisation processes. This suggests that the sub-grid combustion model, which is extended from previous RANS works [Chen *et al.*, 2015, 2016b; Darbyshire & Swaminathan, 2012; Ruan *et al.*, 2014a] as outlined in §3.1.2, also performs quite well for the LES of this lifted flame test case. Complementary to the RANS works presented in Chapters 5 and 6, the main findings of this LES study are

- In the early stages of flame kernel expansion process, a quasi-spherical flame shape is obtained in the LES, similar to that observed from the experimental images. Within about 1 ms after the ignition, the growth rate of the kernel diameter was measured to be almost linear [Ahmed & Mastorakos, 2006], which is also captured by the LES.

- The flame most-leading point is found to be in different azimuthal positions as the flame propagates from the initial ignition location to its final lift-off height. This lends further support for the importance of the flame edge

evolution in the azimuthal direction as concluded from the URANS study discussed in Chapter 6.

- The flame leading point trajectory is *spiral*-like during the edge flame propagation stage, in which two sub-stages are identified showing different propagation behaviours. These two stages are (i) the freely propagating stage and the stabilising stage respectively.

- The PDF of flame stabilisation location at the final lift-off height shows that both the axial and radial location are correlated to the jet exit velocity. The most probable radial stabilisation location is found to be in lean mixtures, however, no correlation is found between the radial location and mixture fraction fluctuations, suggesting that the stabilisation is not only mixing-controlled but is a balance many physical processes.

So far in this thesis, the modelling approach for partially premixed combustion described in Chapter 3 has shown good capability for both RANS and LES methodologies. The test cases used are canonical jet flames with relatively simple geometry and well understood flow conditions. However, the validity of the model under complex practical conditions is yet to be assessed. Therefore, the DLR gas turbine model combustor involving a dual-swirler and confined flow configuration described in §4.2 is used. The results are presented and discussed in the next chapter.

Chapter 8

Gas Turbine Model Combustor

Swirling flame configuration is widely used for practical combustion applications such as aero engines and stationary gas turbines [Gicquel *et al.*, 2012; Gupta *et al.*, 1984]. It helps to achieve fast mixing between the injected fuel and air and the resulting swirl-stabilised flame is rather compact allowing for a relatively smaller combustor size. Swirling flows involve complex fluid mechanics including strong flow recirculation and its interaction with the incoming flow stream, vortex breakdown, precessing vortex core, etc [Syred, 2006]. The interaction between these fluid mechanical processes and the swirling flame is yet to be further understood and poses significant modelling challenge. For instance, the vortex breakdown in these swirling flows produces intense turbulence leading to strong turbulence-chemistry interaction in the inner recirculation zone (IRZ) where the flame is stabilised. It is worthwhile to test the SGS combustion model discussed in §3.2 for these conditions. Therefore, gas turbine model combustor experiments of Weigand *et al.* [2006] and Meier *et al.* [2006] under partially premixed conditions are used in this chapter. The LES is performed for the swirling flame in this combustor and the simulation results are discussed in comparison with the measurements.

8.1 Experimental test case

The schematic of the experimental setup of this combustor [Meier *et al.*, 2006; Weigand *et al.*, 2006] has been shown earlier in Fig. 4.7 and details of the burner geometry are listed in Table 4.2. For the reacting cases, non-swirling pure methane fuel is injected into the combustion chamber through the 72 square nozzle as shown in Fig. 4.7b. These fuel jets mix with the swirling air within a few jet widths resulting in partial premixing in the near-nozzle field, where the flame is stabilised as a lifted flame exhibiting a typical V-shape.

Three flames, designated as flame A, B and C respectively, were investigated experimentally by Weigand *et al.* [2006] and Meier *et al.* [2006] at atmospheric pressure and ambient temperature of 295 K. The stable flame A with operating parameters listed in Table 8.1 is considered for this study. This flame was observed to be stable burning with a globally lean equivalence ratio of $\Phi_{\text{glob}} = 0.65$ based on mass flow rate of $\dot{m}_{\text{CH}_4} = 0.697$ g/s for fuel (pure methane) and $\dot{m}_{\text{air}} = 18.25$ g/s for air. The corresponding global mixture fraction, $\widetilde{Z}_{\text{glob}} = 0.037$, is calculated using $\phi = \widetilde{Z}(1-\widetilde{Z}_{st})/(\widetilde{Z}_{st}(1-\widetilde{Z}))$, where the stoichiometric value is $\widetilde{Z}_{st} = 0.055$. The Reynolds number was based on the kinematic viscosity of air and outer air nozzle diameter, $d_{\text{o}} = 25$ mm, and the swirl number was calculated using Eq. (4.5) [Weigand *et al.*, 2006].

Table 8.1: Summary of the computed flame parameters.

Flame	Φ_{glob}	Z_{glob}	$\dot{m}_{\text{air}}$ [g/s]	$\dot{m}_{\text{CH}_4}$ [g/s]	Re	S
A	0.65	0.037	18.25	0.697	58,000	0.9

Laser diagnostic techniques were used in the experiments by Weigand *et al.* [2006] and Meier *et al.* [2006] to measure velocity and scalar fields. Laser Doppler Velocimetry (LDV) was used to measure velocities inside the chamber at various axial heights ranging from $h = 1.5$ to 90 mm marked in Fig. 8.1 along with the filtered reaction rate iso-surface of $\overline{\dot{\omega}_{\text{c}}^*} = 200\,\text{kg/m}^3\text{/s}$ coloured by temperature at a particular instant. It is clear that the swirling flame is contained in a rather short region, below $h \approx 40$ mm. The swirling flows produce intense turbulence, with

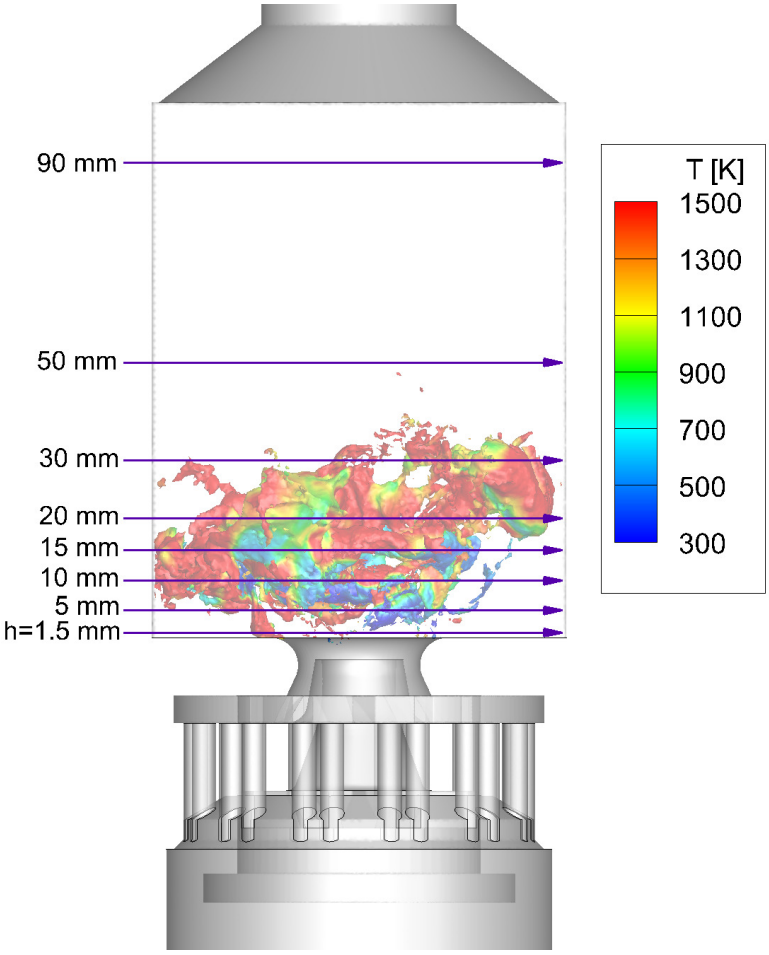

Figure 8.1: Iso-surface of the filtered reaction rate, $\overline{\dot{\omega}_c^*} = 200$ kg/m^3/s, coloured by temperature at a typical instant, $t = 30$ ms, after the numerical ignition. The axial positions for the laser measurements in the experiments [Meier *et al.*, 2006; Weigand *et al.*, 2006] are highlighted.

r.m.s. velocity ranging from 10 to 20 m/s, through vortex breakdown mechanism, which is a well-known phenomenon in swirling flows. This intense turbulence helps rapid fuel-air mixing resulting in a shorter flame compared to the combustor length.

Laser diagnostics were applied over this whole flame region ranging from 5 to 30 mm height above the fuel injector. The measurement locations also included two downstream positions, $h = 50$ and 90 mm. Temperature and concentrations of O_2, N_2, CH_4, H_2, CO, CO_2 and H_2O, were measured using the laser Raman

scattering technique. Both the mean and r.m.s. values constructed using single-shot data were reported by Weigand *et al.* [2006] and Meier *et al.* [2006] for combustion model validation. The temperature was deduced using the ideal gas law and the measured species concentration. The mixture fraction was constructed using concentrations of these species following Bilger's formulation [Bilger *et al.*, 1990] given in Eq. (2.21). It is worth noting that this definition includes elemental, C, H and O, mass fractions coming from minor species which were not measured. The implication of this difference are discussed in §8.3.

To visualise the reaction zone structures, planar laser-induced fluorescence (PLIF) imaging of OH and CH radicals were employed, and both instantaneous and mean planar images were reported in the experimental studies [Weigand *et al.*, 2006]. These results are used here to evaluate the LES model described in §3.2 for partially premixed combustion. The numerical setup used for the simulations of this study is discussed next.

8.2 Numerical modelling details

The LES modelling framework used in Chapter 7 for the lifted jet flames is followed for this study also. The Favre-filtered governing equations solved and the models used for the sources and sinks in these equation are detailed in §7.2. The same model parameters are used to be consistent with Chapter 7.

The computational domain and boundary conditions shown in Fig. 4.9 for non-reacting flow are adopted for reacting flows also. Since the equations related to mixture fraction and progress variable are solved for reacting flows, their boundary conditions are specified in the following manner. A fixed value of $\widetilde{Z} = 0$ and 1 is given for the air and fuel inlet boundaries respectively. The value for the filtered progress variable, $\widetilde{c}$, is specified to be zero for these boundaries. The zero-gradient condition is applied for the sub-grid scale variances, $\widetilde{Z''^2_{\text{sgs}}}$ and $\widetilde{c''^2_{\text{sgs}}}$, and this condition is also used for all of these transported scalars for the no-slip walls and far field boundaries marked in Fig. 4.9a.

Based on the grid sensitivity study in §4.2.3.2, the numerical grid G2 detailed in Table 4.3 comprising about 15 million unstructured tetrahedral cells is used for the reacting flow studied here. The smallest mesh size in the shear layers is

about 0.5 mm corresponding to the normalised filter size of about $\Delta^+ = 0.8$ (see Eq. 7.1). Figure 8.2 presents three histograms of Δ^+ for the reacting region of the computational domain, marked using $\overline{\dot{\omega}_c^*} > 0$. The histogram constructed using the cells below $h = 20$ mm is denoted using red colour and that for the cells above $h = 20$ mm is marked using green colour. The blue colour represents the histogram for the cells with $\overline{\dot{\omega}_c^*} > 0$ over the entire combustor. It is seen that in the reacting region, the LES filter width related to the numerical cell volume is about 1 to 2 $(\delta_L^0)_{st}$. For the upstream region ($h < 20$ mm) where a strong shear between the swirling streams and recirculation zones is expected, a fine mesh with $\Delta^+ \approx 1$ is used (red coloured bars) to resolve the large spatial gradients. The downstream grid size is relatively coarse with $\Delta^+ > 1$ in most regions shown as the green bars. Overall, the grid size used for this study does not resolve the flame front and thus the combustion is entirely at sub-grid scales, which is modelled as described in §3.2.

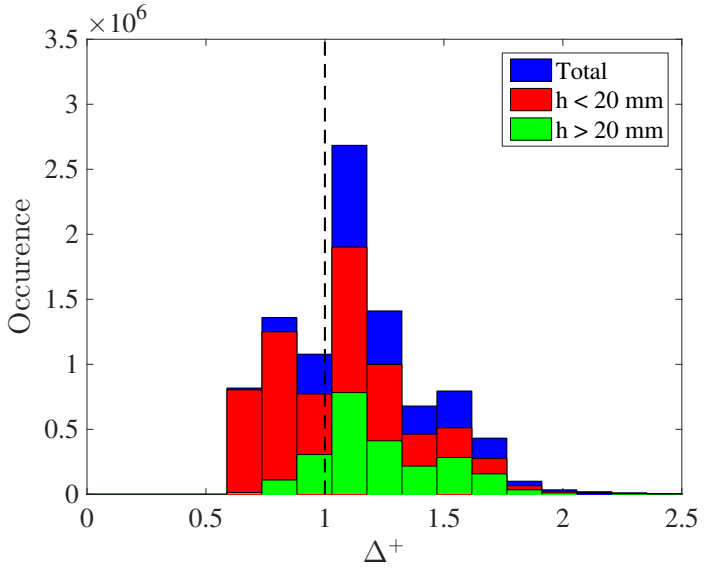

Figure 8.2: Histogram of the normalised filter size Δ^+ distribution. The cell samples are collected within the reaction region marked using $\overline{\dot{\omega}_c^*} > 0$. The dashed line highlights the filter size equal to the reference laminar flame thickness $(\delta_L^0)_{st}$.

Two different approaches are used to initialise the flame kernel in the fully converged scalar mixing field inside the combustion chamber. One approach is to initiate the flame kernel with fully burnt mixture ($\widetilde{c} = 1$) as used in the previous

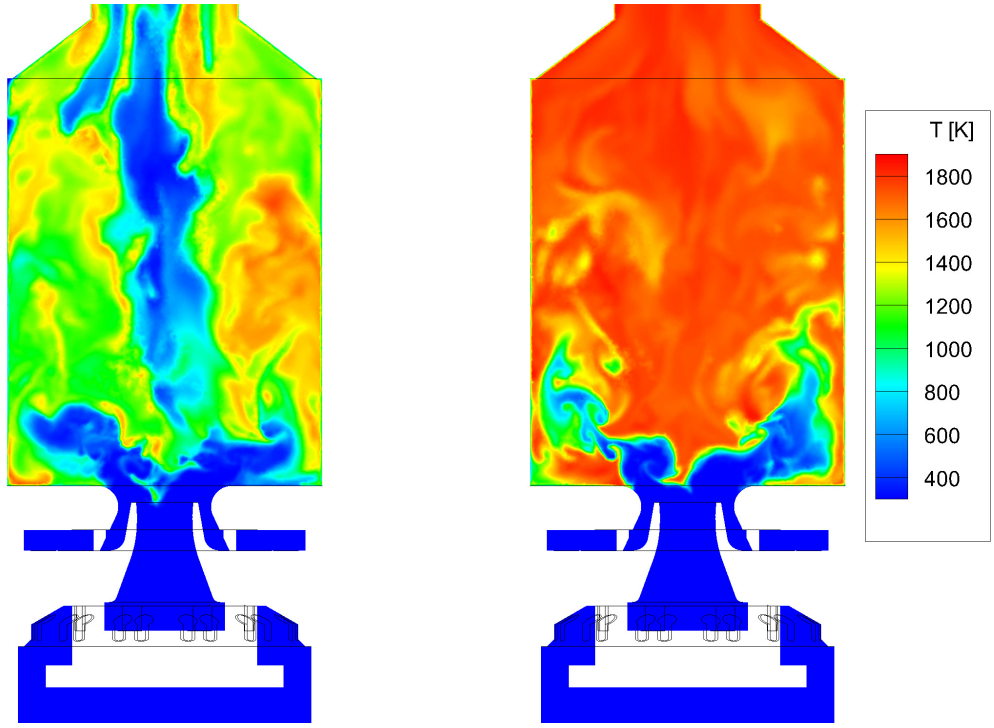

(a) (b)

Figure 8.3: Comparison of instantaneous temperature field computed using two different flame initialisation approaches: (a) flame kernel ignition and (b) entire-domain filled with hot products. The results are shown for $t = 18$ ms ≈ 7 FTT after the initialisation for both cases.

chapters, see Eq. (7.2), and let it evolve inside the chamber until a stably burning state is reached. The advantage of this method is that the ignition sequence follows a physical transient process which avoids undue numerical difficulties. However, this process takes a rather long physical time of about 40 ms, which corresponds to more than 15 FTT resulting in a high computational cost. The second approach is to impose $\widetilde{c} = 1$ for the entire the combustion chamber at the beginning of the reacting flow simulation. Although this can create some numerical issues in the beginning imposing a very small time-step, an order of magnitude smaller than that required for the first approach, the simulation can reach a fully burning state within about 8 FTT, quicker than in the first approach. A comparison between these two approaches is shown in Figs. 8.3a and 8.3b depicting

the temperature field at an arbitrarily chosen time of $t = 18$ ms ≈ 7 FTT. It is clear that the reacting flow filed is developed more in Fig. 8.3b employing the latter approach. In order to achieve a high computational efficiency, the second approach is used since the transient evolution is not of interest for this study.

The computation is performed on the ARCHER supercomputer using 1680 CPU cores. As noted above, a fully converged mixing field is computed first over 6 FTT using a time-step size of $\Delta t = 2 \times 10^{-7}$ s (CFL $\leqslant 0.3$), which requires about 15 hours of wall-clock time. For combustion simulations, the flow acceleration across the filtered flame dictates Δt to be 1.25×10^{-7} s to keep the same CFL condition. Starting from the flame initialisation, 8 FTT is simulated to allow for the flame evolution until it is fully evolved inside the combustion chamber. The LES statistics are then collected over a sampling time of 12 FTT. Thus, a total of 20 FTT is simulated, which took about 80 hours of wall-clock time.

8.3 Results and discussion

8.3.1 General flame features

Figure 8.4 shows the two-dimensional (x-h middle-plane) contours of the filtered and time-averaged axial, radial and swirl velocity fields. The black line in Figs. 8.4a and 8.4d is the zero axial velocity iso-contour denoting the recirculation zones. The IRZ and inflow stream are broadened in the radial direction compared to the cold flow results (see Figs 4.10a and 4.10d) because of the thermal expansion effects. The ORZ becomes smaller and is squashed into the chamber bottom corner. The Y-shape IRZ seen for cold flow is not present in the reacting flow. This widening effect is also seen for the radial and swirl velocities shown in Figs. 8.4b to 8.4f. Another notable point in these figures is that the outflow acceleration in the exhaust duct is further enhanced because of heat release inside the chamber. The resulting axial velocity at the outlet is over 50 m/s along with a high swirling velocity of over 30 m/s. It is found that this high-velocity flow at the outlet can cause numerical issues if the grid is not sufficiently fine in the extended far field domain (see Fig. 4.9a.). In order to avoid this unnecessary grid refinement in a region that is not of interest, the numerical schemes are locally downgraded

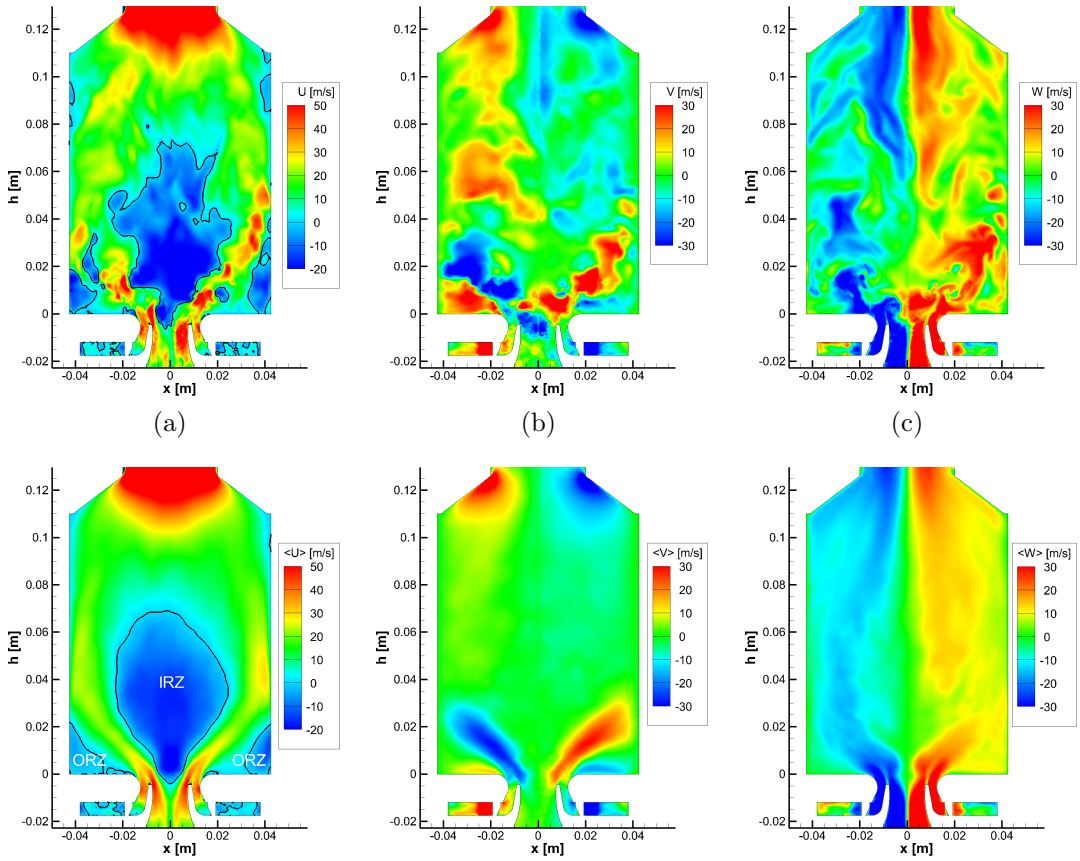

Figure 8.4: Two-dimensional x-h middle-plane contours of the filtered ($t = 30$ ms in the top row) and time-averaged (bottom row) axial (U), radial (V) and swirl (W) velocities. The black line corresponds to zero axial velocity iso-contour.

to first order upwind scheme for numerical stability. This procedure is realised in the CFD code using the built-in OpenFOAM function called as *localBlending scheme* [Open CFD, 2013] (see more details at http://www.openfoam.com/).

The filtered mixture fraction, $\widetilde{Z}$, and progress variable, $\widetilde{c}$, are plotted in Fig. 8.5 along with the stoichiometric mixture fraction, $\widetilde{Z}_{st} = 0.055$, marked using a black line. Both the instantaneous (top row) and time-averaged (bottom row) contours are shown in this figure. The $\widetilde{Z} = 1$ (pure fuel) contour is not seen here because of the fast-mixing occurring at above the fuel jet exit. The global mixture fraction is computed as $\langle\widetilde{Z}\rangle_{\text{glob}} = \left(\int_V \langle\widetilde{Z}\rangle dV\right) / V \approx 0.037$, where V is

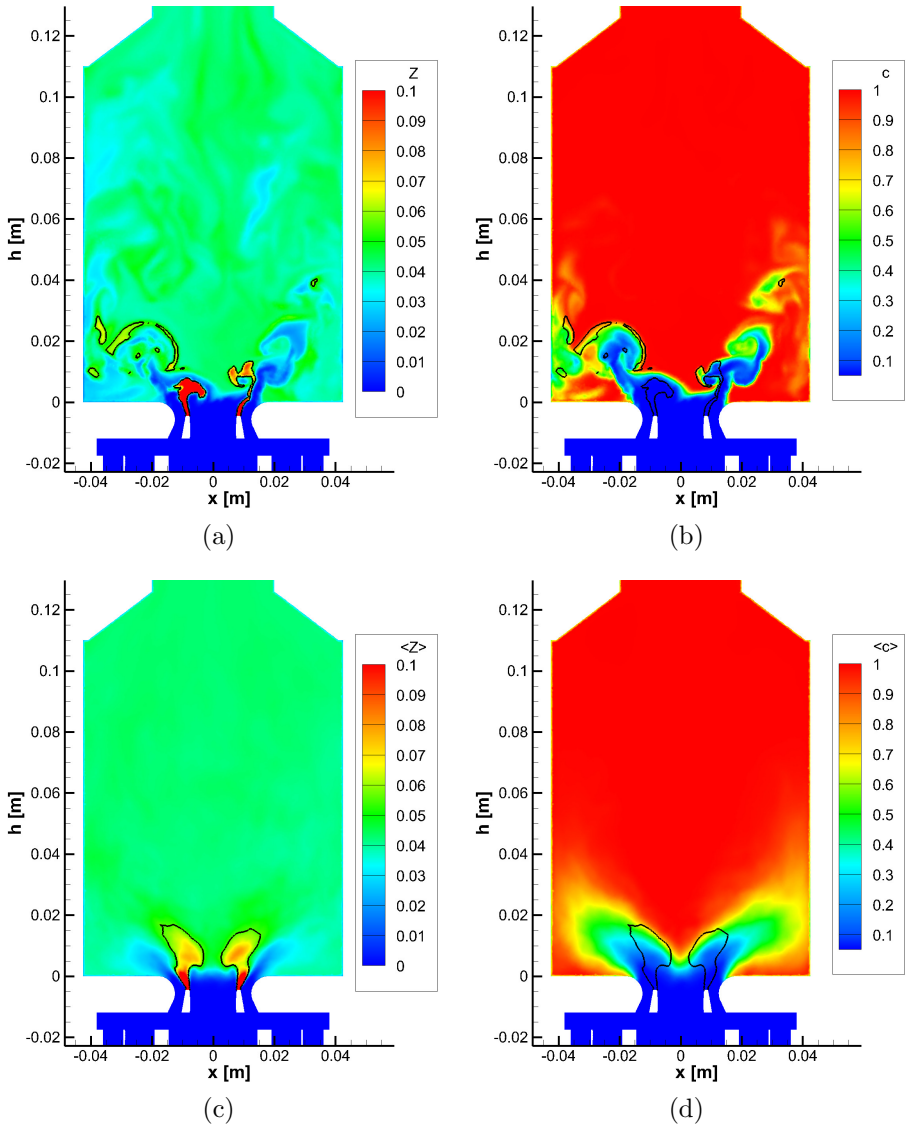

Figure 8.5: Two-dimensional x-h middle-plane contours of the filtered ($t = 30$ ms in the top row) and time-averaged (the bottom row) mixture fraction (Z), progress variable (c) and reaction rate ($\overline{\dot{\omega}_c^*}$). The black line corresponds to stoichiometric mixture fraction.

the volume of the combustion chamber and dV is the numerical cell volume. This is consistent with the value of Z_{glob} in Table 8.1 computed using $\Phi_{\text{glob}} = 0.65$. The stoichiometric mixture fraction contours are observed mainly below $h = 20$ mm in Figs. 8.5a and 8.5d, and combustion is completed (i.e. $\langle\widetilde{c}\rangle = 1$) by about

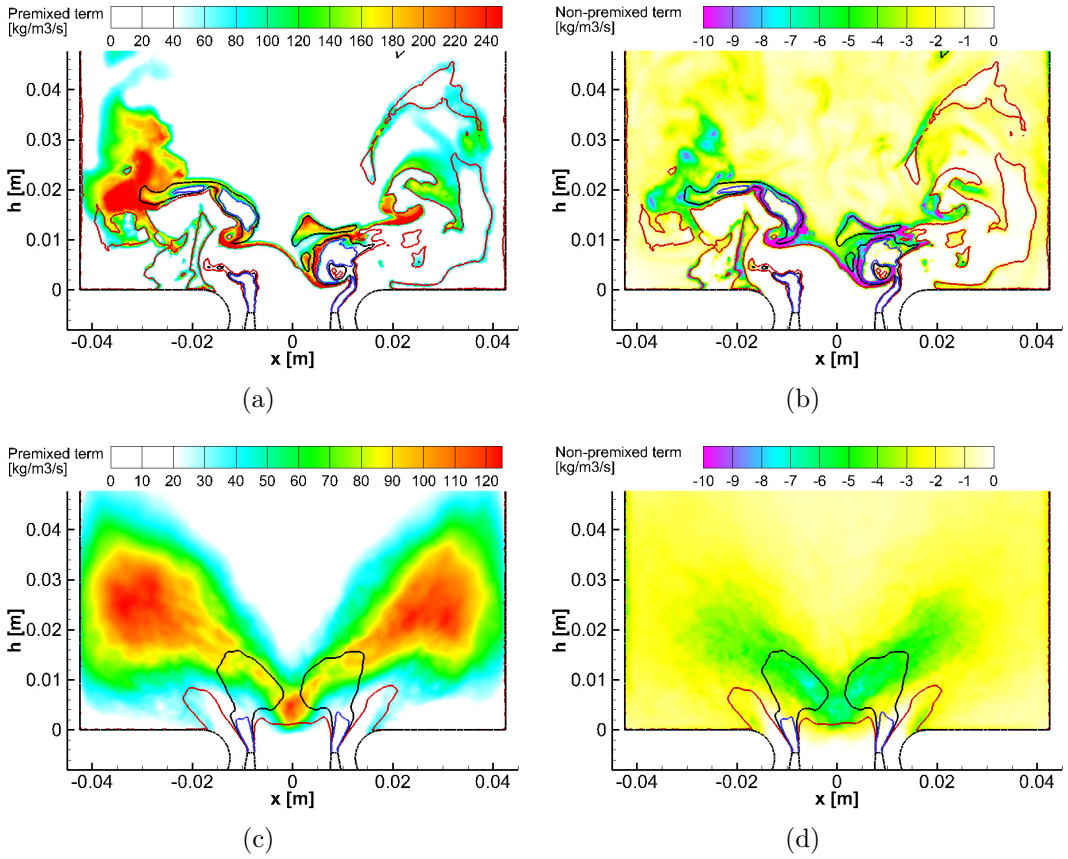

Figure 8.6: Two-dimensional x-h middle-plane contours of the filtered ($t = 30$ ms in the top row) and time-averaged (bottom row) $\overline{\dot{\omega}_{\mathrm{c}}}$ and $\overline{\dot{\omega}_{\mathrm{np}}}$, signifying the premixed and non-premixed mode contributions respectively. The mixture fraction iso-lines are the stoichiometry (black), lean (red) and rich (blue) flammability limits.

$h = 35$ mm, which is nearly one quarter of the combustor length as shown in Fig. 8.5d.

The contours of filtered and time-averaged reaction rate resulting from both the premixed ($\overline{\dot{\omega}_{\mathrm{c}}}$) and non-premixed ($\overline{\dot{\omega}_{\mathrm{np}}}$) mode contributions are shown in Fig. 8.6. These contributions are defined by Eqs. (3.47) and (3.50) respectively. The mixture fraction iso-lines shown are the stoichiometry, lean and rich flammability limits. The values of $\overline{\dot{\omega}_{\mathrm{c}}}$ are an order of magnitude larger than the $\overline{\dot{\omega}_{\mathrm{np}}}$ values which are mainly negative as observed in Chapter 5 for lifted jet flames. These negative values are significant only around the stoichiometry as seen in Fig. 8.6b.

The computed average reaction zone shown in Fig. 8.6c is mainly located in the shear layer between the IRZ and the main inflow stream within the flammability limits, showing a V shape with a small tip pointing towards the ORZ near the chamber wall. This tip is formed because of the flammable mixture pockets shedding from the main swirling flow, which first hit the side wall and then recirculate down into the ORZ creating a small reaction zone. This flow shedding can be seen clearly in Fig. 8.5a.

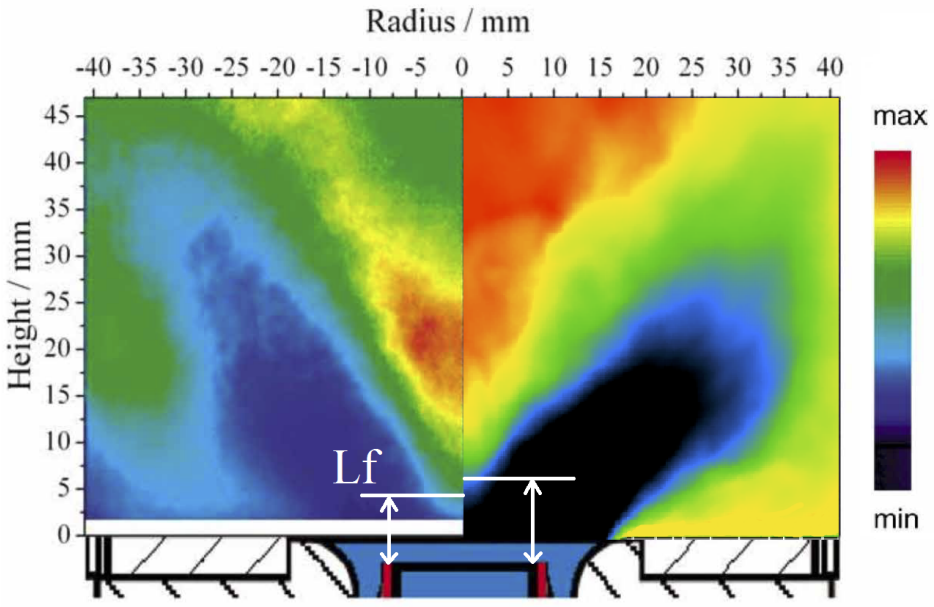

Figure 8.7: Qualitative comparison between the averaged OH concentration in the middle-plane obtained from the experimental (left) OH-PLIF images [Weigand *et al.*, 2006] and computed (right) signal $\langle \widetilde{S}_{\mathrm{OH}} \rangle$ using LES results.

Figure 8.7 compares the averaged OH-PLIF images [Weigand *et al.*, 2006] to the computed OH signals in the LES. The PLIF signal of OH is obtained using the computed local molar fraction, [OH], and temperature as [Minamoto & Swaminathan, 2014]

$$\widetilde{S}_{\mathrm{OH}} \propto [\mathrm{OH}]\, \widetilde{T}^{1-\beta}, \quad -2.0 \leqslant \beta \leqslant 1.0, \tag{8.1}$$

where the parameter β is taken to be zero for this study as used by Minamoto & Swaminathan [2014]. The overall V shape of the OH distribution with high con-

centration in the IRZ is captured reasonably well in the LES. OH is also observed in the ORZ with a relatively lower signal level compared to that in the IRZ. The high-signal zone is located at the bottom of the V shape in the experiments while in the LES this high OH concentration extends to the downstream. The reason for this is to be investigated further. The flame lift-off height, $L_{\rm f}$, defined as the distance between the fuel jet exit plane ($h = -4$ mm) and the most upstream point of the central reaction zone (bottom tip of the V shape), was reported to be about 10 mm by Weigand *et al.* [2006] as marked in Fig 8.7. The computed value of $L_{\rm f}$ is about 11.5 mm, in good agreement with the measurements.

Indeed, these qualitative comparisons suggest that the LES combustion model performs quite well for this dual-swirler combustor with complex flow fields. However, quantitative comparisons between the LES results and experimental data are required to further validate the combustion model. These comparisons are discussed in the next two sections.

8.3.2 Velocity field statistics

In the experiments of Weigand *et al.* [2006] and Meier *et al.* [2006], the LDV measurements were conducted at a number of axial positions starting from the nozzle exit plane up to the exhaust duct of the combustion chamber. A few typical locations covering the entire chamber are shown in Fig.8.1, and these locations are chosen for model evaluation. The averaged and r.m.s. values of the axial (U), radial (V) and swirl (W) velocities were obtained using typically 10,000 to 15,000 validated velocity data at each measurement point.

Figure 8.8 compares the computed and measured axial velocity variation along the chamber centreline. The r.m.s. values are computed using the resolved velocity fluctuations as $\widetilde{U}_{\rm r.m.s.} = \sqrt{\langle \widetilde{U}^2 \rangle - \langle \widetilde{U} \rangle^2}$, where the angle brackets denote the time averaging. For LES, these and other statistics are computed using samples collected over 12 FTT as noted earlier in §8.2. The averaged recirculation zone length, $L_{\rm r}$, is marked (60 mm) in Fig. 8.8a. An excellent agreement between the measured and computed (63 mm) $L_{\rm r}$ values is obtained. Starting from the nozzle exit plane, where the recirculating flow velocity is about -18 m/s, the $\langle \widetilde{U} \rangle$ value first decreases as one moves up along the centreline until reaching a minimum

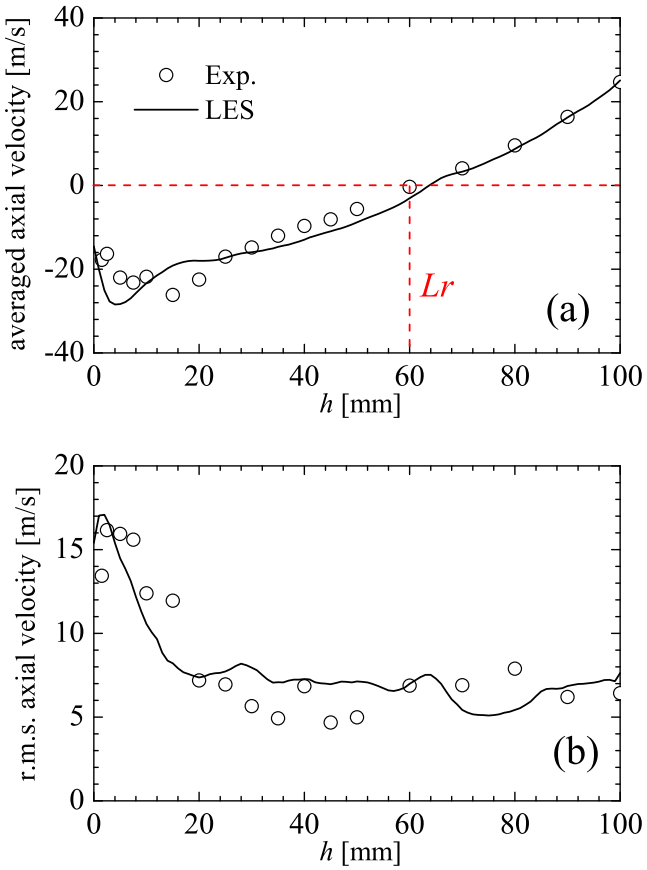

Figure 8.8: Centreline variation of axial velocity: (a) time-averaged values and (b) r.m.s. fluctuations. Symbols: experimental measurements [Meier *et al.*, 2006; Weigand *et al.*, 2006]. Lines: LES results.

velocity of -28 m/s. This is the same for both the experimental data and LES results. However, $\langle \widetilde{U} \rangle$ is found to decrease faster in the LES reaching the -28 m/s value at around $h = 6$ mm, whereas it is at $h = 15$ mm in experiments. This may be due to the over-predicted temperature in this near-nozzle region as one shall see in the next section while discussing the temperature fields. This could also be because of the missing turbulence in the inner swirling air stream. The relative role of these two causes need to be explored, which is a subject for future investigation. However, the agreement is quite good. The centreline variation of the r.m.s. fluctuation is plotted in Fig. 8.8b. Neither the experimental data nor the computational results seems to be statistically converged for this second

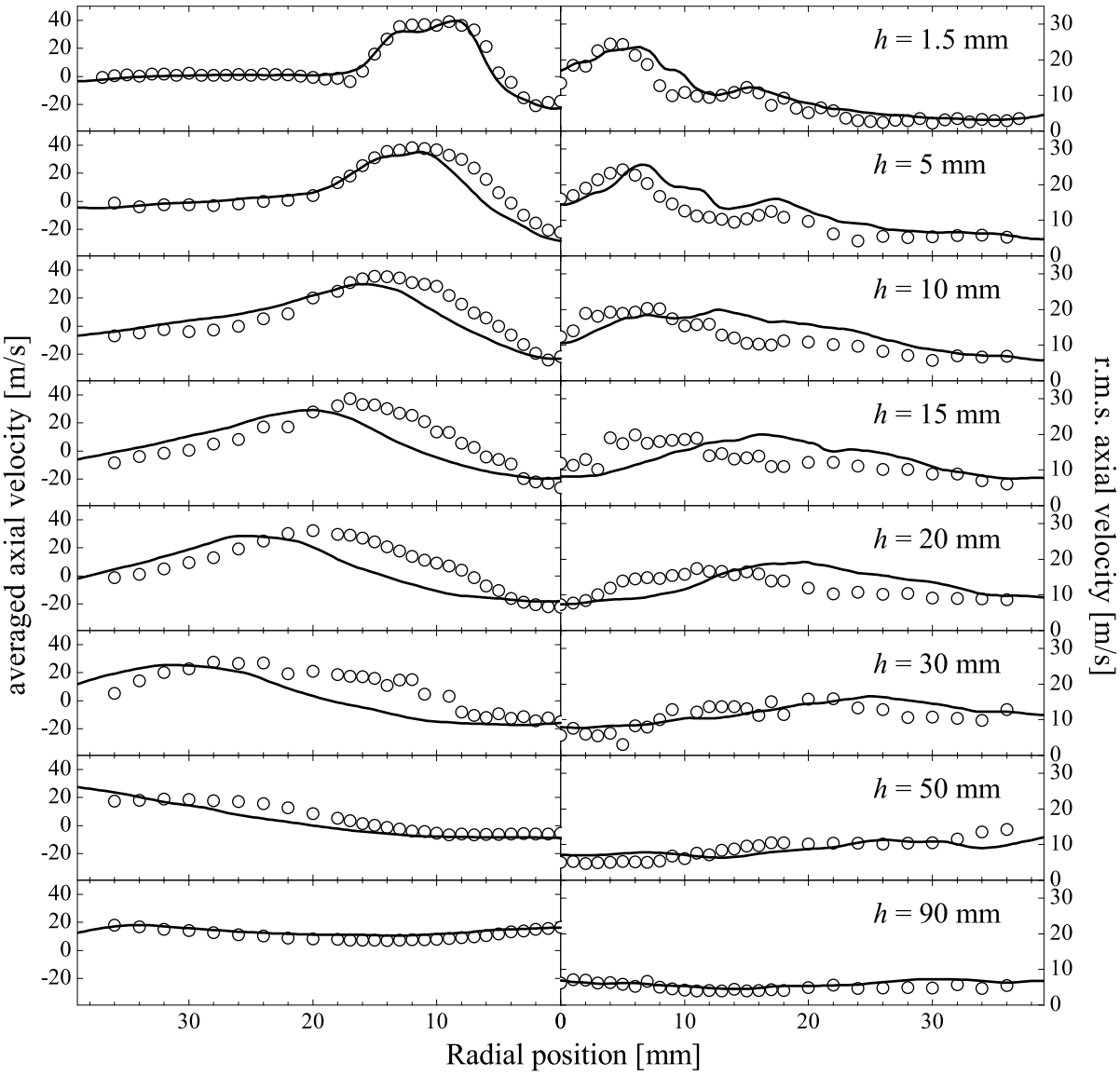

Figure 8.9: Radial profile of axial velocity: time-averaged values (left) and r.m.s. fluctuations (right). Symbols: experimental measurements [Meier *et al.*, 2006; Weigand *et al.*, 2006]. Lines: LES results.

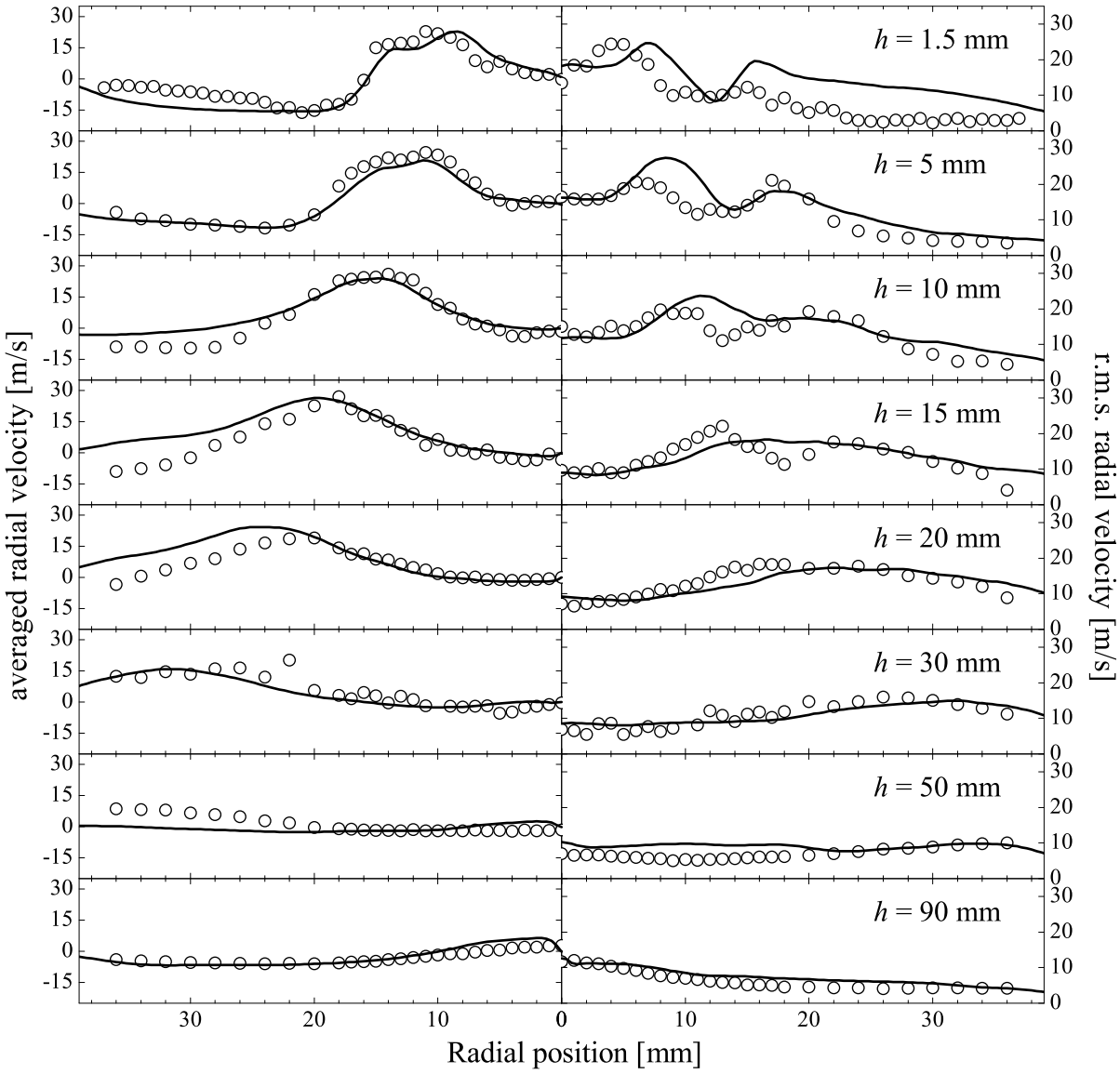

Figure 8.10: Radial profile of radial velocity: time-averaged values (left) and r.m.s. fluctuations (right). Symbols: experimental measurements [Meier *et al.*, 2006; Weigand *et al.*, 2006]. Lines: LES results.

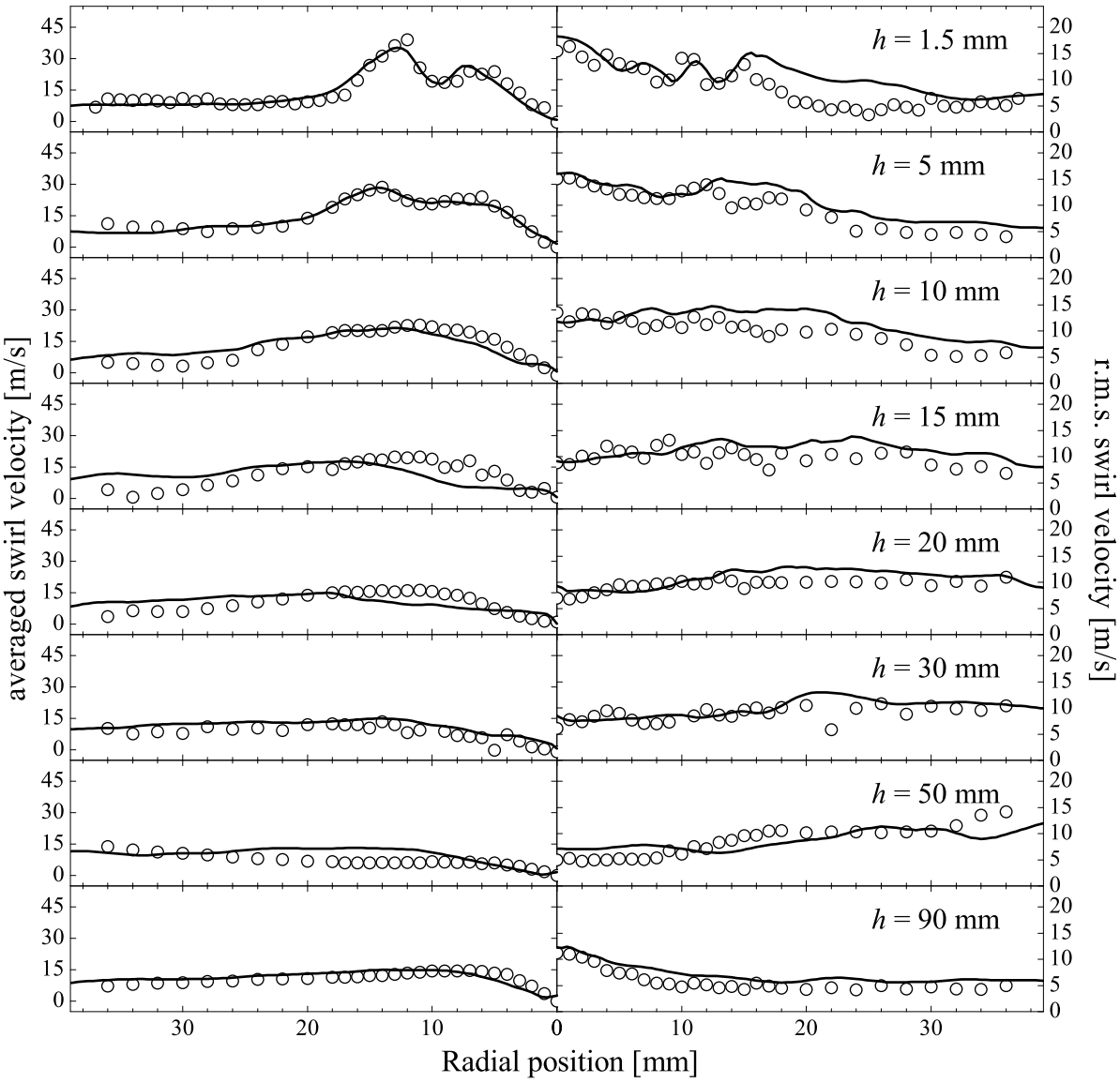

Figure 8.11: Radial profile of swirl velocity: time-averaged values (left) and r.m.s. fluctuations (right). Symbols: experimental measurements [Meier *et al.*, 2006; Weigand *et al.*, 2006]. Lines: LES results.

moment quantity. Nonetheless, the overall trend is captured quite well in the LES.

Figure 8.9 shows the radial variations of $\langle\widetilde{U}\rangle$ (the left column) and $\widetilde{U}_{\text{r.m.s.}}$ (right column) for the axial positions marked in Fig.8.1. The near-nozzle position, $h = 1.5$ mm, is plotted to show the LES prediction of the flow at the chamber inlet, which is expected to be free of combustion influence. The middle-plane contour of $\langle\widetilde{U}\rangle$ is plotted in Fig. 8.4d. The computed values of both $\langle\widetilde{U}\rangle$ and $\widetilde{U}_{\text{r.m.s.}}$ agree very well with the measurements for $h = 1.5$ and 5 mm positions as seen in Fig. 8.9. As one moves in the downstream direction, the computed $\langle\widetilde{U}\rangle$ values start to deviate from the measurements. An under-prediction is observed for the inner shear layer region while a small over-prediction is seen for the outer one. These differences are consistent with the difference in the spreading angle of the reaction zone shown in Fig. 8.7. Similar behaviour is also seen for the r.m.s. values. These differences vanish at further downstream locations of $h = 50$ and 90 mm.

Figures 8.10 and 8.11 respectively show the radial variation of the radial and swirl components of the velocity. A quite good agreement is obtained for both velocity components despite a slight over-prediction in the r.m.s. values at $h = 1.5$ and 5 mm. The two peaks in the $\langle\widetilde{W}\rangle$ variation at $h = 1.5$ and 5 mm seen is because of the two concentric swirling flows. A small shift in the peak location compared to the measurements in Fig. 8.10 reflects the large spreading angle of the computed flow. Similar to the axial velocity shown in Fig. 8.9, the LES recovers the correct velocities $\langle\widetilde{V}\rangle$ and $\langle\widetilde{W}\rangle$ for the downstream positions of $h = 50$ and 90 mm. Nevertheless, the comparison between the computed and measured velocity statistics is good showing that the LES model captures the reacting flow hydrodynamics in this complex burner geometry quite well.

8.3.3 Scalar field statistics

Weigand *et al.* [2006] and Meier *et al.* [2006] measured the concentrations of O_2, N_2, CH_4, H_2, CO, CO_2 and H_2O using laser Raman scattering as noted earlier in §8.1. The temperature was then calculated using these measured species concentrations and the ideal gas law. As all of these major species were measured

simultaneously, the corresponding mixture fraction was also deduced. Only 500 samples were used to obtain the average and r.m.s. values due to the inherent limitations of the Raman scattering technique [Keck *et al.*, 2002] such as the low signal intensities caused by the small scattering cross section and the short measuring time due to high average laser power required. The uncertainty for the averaged values of the measured temperature, mixture fraction as well as O_2, CO_2 and H_2O mole fractions was reported to be 3-4% [Weigand *et al.*, 2006]. To compare with these experimental measurements, the LES statistics (the average and resolved r.m.s. values), are computed using 600 samples.

8.3.3.1 Mixture fraction and temperature

As noted above, the mixture fraction was deduced using only the measured major species and the intermediate and minor species were ignored as they were not measured [Meier *et al.*, 2006; Weigand *et al.*, 2006]. This may result in a substantial error in the reaction zone where the mass fractions of these neglected species can be comparable to the measured ones. The laminar planar premixed flame results, which are used to construct the lookup table for turbulent flame simulation (see §3.3 for detail), are processed to make some assessment of the difference in the mixture fraction values computed with and without the intermediate and minor species. Here, one should recall that the Bilger's formulation for the mixture fraction as given in Eq. (2.21) includes the elemental mass fractions of C, H and O coming from all the possible species.

Figure 8.12 shows typical variation of the mixture fraction across the laminar flame for a range of equivalence ratios covering the entire flammable range. These methane-air laminar flames calculation are at atmospheric pressure (101325 Pa) and their reactants mixture has a temperature of 300 K as in the experiments [Meier *et al.*, 2006; Weigand *et al.*, 2006]. The progress variable, c, is defined based on CO and CO_2 mass fractions as in Eq. (3.13). If the mixture fraction remains the same across the flame then its variation would follow the dashed line. The mixture fraction values corresponding to the rich and lean flammability limits are 0.078 and 0.03, and thus the flammable range is $\Delta Z_{\text{flam}} = 0.048$, which is quite small, accounting for only about 5% of the entire mixture fraction range

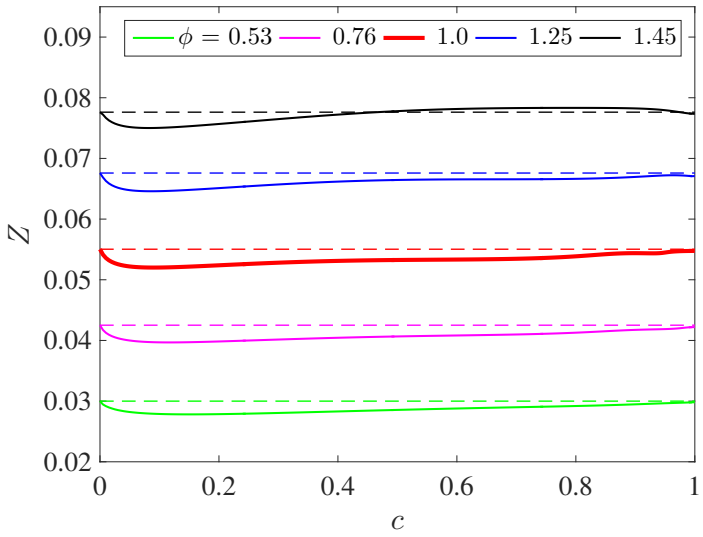

Figure 8.12: Mixture fraction variation across the premixed laminar flames of varing equivalence ratios. The progress variable, c, is defined using the sum of CO and CO_2 mass fractions. Solid lines: values computed using Bilger's formulation [Bilger *et al.*, 1990]. Dashed lines: the constant value for a given ϕ.

of 0 to 1. The stoichiometry value is $Z_{st} = 0.055$ for the methane-air mixture considered. A, for each equivalence ratio, The value of Z varies slightly across the flame as one would expect because of differential diffusion effects. However, this variation is fairly small ($< 2\%$) and hence is commonly neglected in the presence of high turbulence. The significance of these effects in a turbulent lean premixed methane-air flame was studied experimentally by Barlow *et al.* [2012] and about 10% difference was observed in the measured equivalence ratio and carbon-to-hydrogen atom ratio.

In order to investigate the relative error of mixture fraction introduced by considering only the measured major species [Meier *et al.*, 2006; Weigand *et al.*, 2006], a normalised difference, δZ^+, between the Z value obtained using the measured and all (53 for GRI-Mech 3.0) species is plotted against c in Fig. 8.13 for all the equivalence ratios shown in Fig. 8.12. This normalised difference is calculated as

$$\delta Z^+ = \frac{Z_{\text{all}} - Z_{\text{exp}}}{\Delta Z_{\text{flam}}} \times 100\%, \tag{8.2}$$

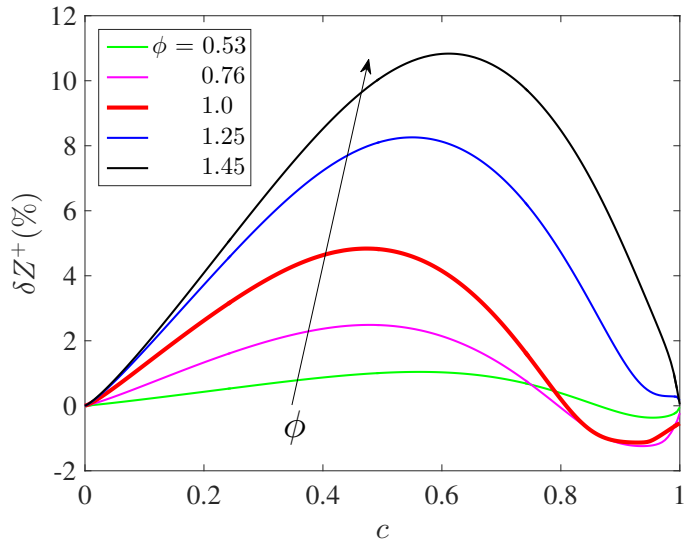

Figure 8.13: Difference between mixture fraction values obtained from all species and from the major species measured in [Weigand *et al.*, 2006] for different equivalence ratios. δZ^+ is a difference normalised using the flammable range for methane/air mixture.

where $\Delta Z_{\text{flam}} = 0.048$ is the flammable range. It is seen that the maximum δZ^+ increases monotonically with ϕ from the lean flammability limit to the rich limit. There is no difference at $c = 0$ and 1 as one would expect. This difference is almost negligible, less than 2%, for very lean mixtures ($\phi < 0.76$). However, it becomes rather large as high as 11%, for rich mixtures. The maximum difference occurs between $c = 0.5$ and 0.7 where the reaction rate is expected to peak. It is also noted in Fig. 8.13 that except for the rich mixtures, δZ^+ appears to be small negative values close to $c = 1$ and this is because of the dissociation of reaction products near chemical equilibrium.

Nevertheless, the above results show that the mixture fraction deduced from measured major species seems to provide a quite good accuracy of more than 90% in most cases and one should be mindful while comparing the simulated mixture fraction results with the experimental data especially for the fuel-rich regions.

The computed and measured [Meier *et al.*, 2006; Weigand *et al.*, 2006] radial variation of mixture fraction are compared in Fig. 8.14. The LES results for the averaged value, $\langle \widetilde{Z} \rangle$, are in very good agreement with the experimental data

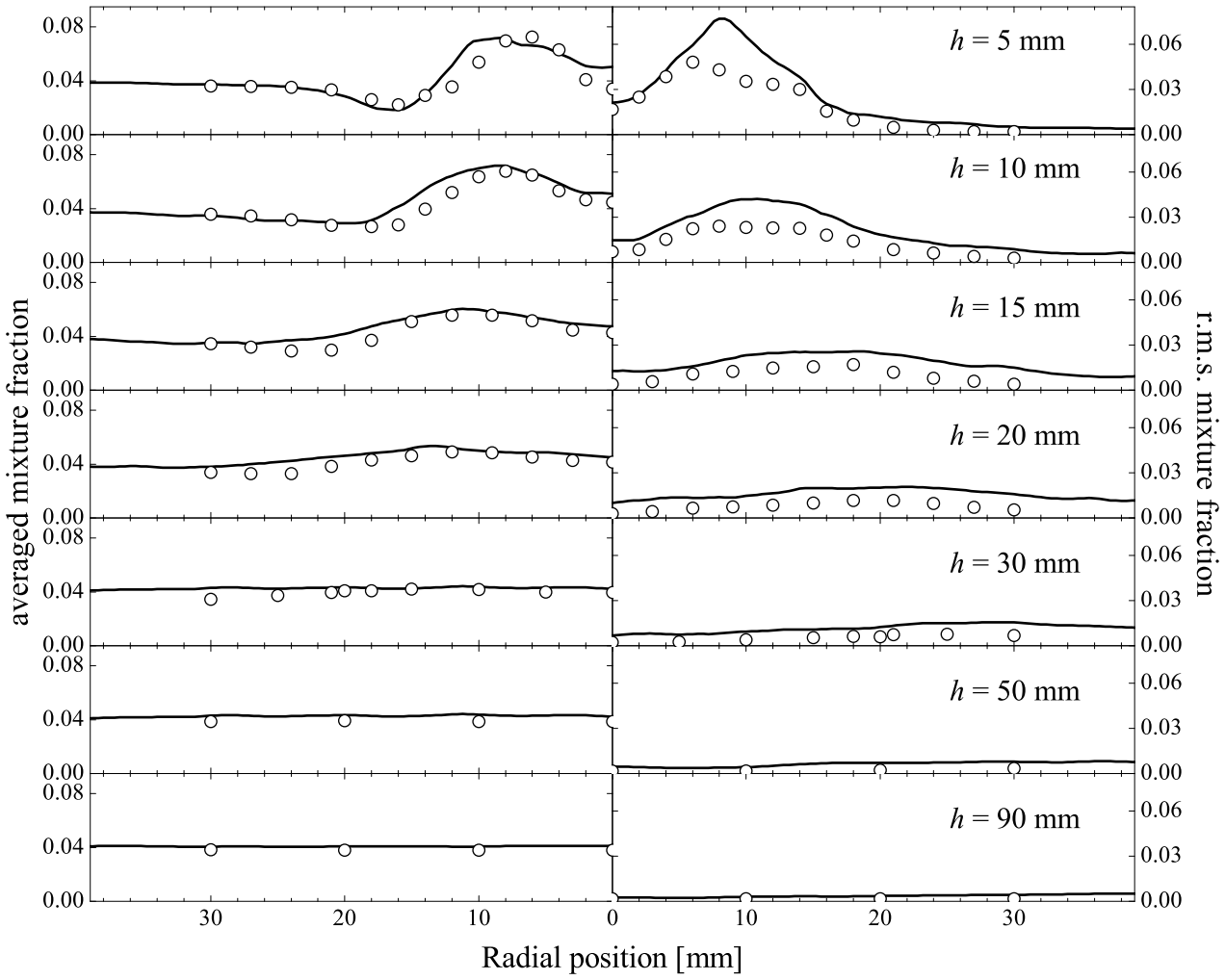

Figure 8.14: Radial profile of mixture fraction: time-averaged values (left) and r.m.s. fluctuations (right). Symbols: experimental measurements [Meier *et al.*, 2006; Weigand *et al.*, 2006]. Lines: LES results.

despite the over-prediction around the centreline. This over-prediction is about 20% at the $h = 5$ mm position and this difference becomes smaller as one moves in the downstream direction. Another notable difference observed in Fig. 8.14 is that the $\langle \widetilde{Z} \rangle$ values computed decrease slower than the measurements after the peak in the radial direction. The maximum difference is about 15 to 20% at $h = 5$ mm, which also becomes smaller if one moves downstream. These above differences may be because of the mixture fraction error caused by considering only the measured major species noted earlier, which could be as high as 11% (this error is defined in Eq. 8.2) in laminar flames. Also, these differences are more evident for relatively large $\langle \widetilde{Z} \rangle$ values (> 0.05), which is consistent with the observation in Fig. 8.13. The r.m.s. values of mixture fraction, $\widetilde{Z}_{\text{r.m.s.}}$, are over-predicted by about 30 to 60% between the radial positions of 8 and 14 mm at the $h = 5$ mm axial location. This is believed to be related to the over-prediction in the mean values discussed above. The computed $\widetilde{Z}_{\text{r.m.s.}}$ values agree quite well with the measurements at axial locations ranging from $h = 10$ to 90 mm as seen in Fig. 8.14. The overall agreement between the LES results and experimental data is good for the mixture fraction field.

Figure 8.15 compares the radial variation of temperature computed using Eq. (3.55) and the measured values [Meier *et al.*, 2006; Weigand *et al.*, 2006]. The averaged temperature, $\langle \widetilde{T} \rangle$, is predicted quite well for all the streamwise locations shown. The LES results are about 30% higher than the measured temperature for the radial positions, $10 < r < 20$ mm at $h = 20$ mm and for $15 < r < 30$ mm at $h = 30$ mm. The average burner outlet temperature was observed to be about 1900 K with very small fluctuations by Weigand *et al.* [2006] and Meier *et al.* [2006], which is captured very well by the simulations. On the centreline, $\langle \widetilde{T} \rangle$ is under-predicted by about 10% and 20% for $h = 5$ and 10 mm respectively. However, the agreement improves for the downstream locations of $h = 50$ and 90 mm, and overall it is good for this dual-swirler burner with relatively complex flow and geometry. The trend of temperature r.m.s. evolution in the radial and axial directions is captured reasonably in the LES.

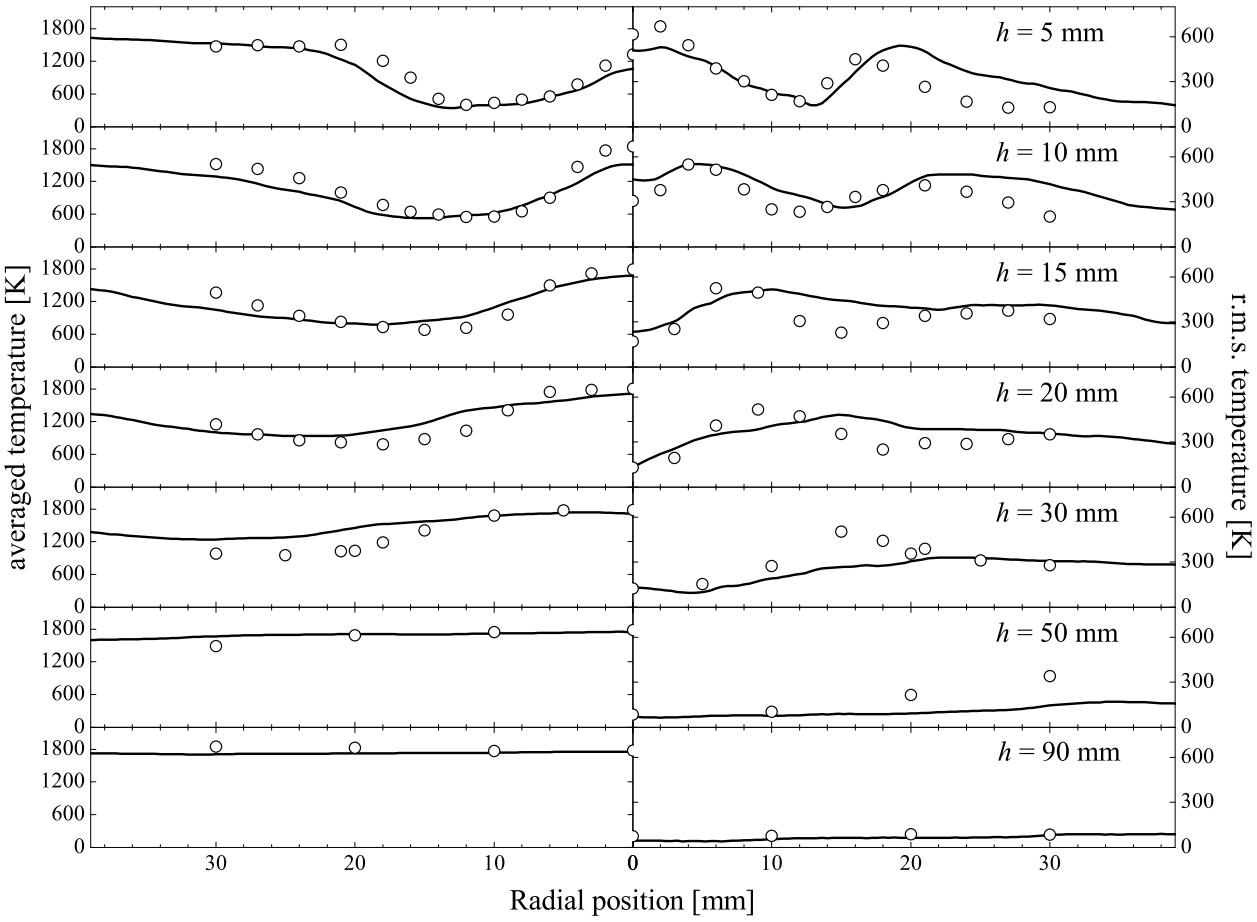

Figure 8.15: Radial profile of temperature: time-averaged values (left) and r.m.s. fluctuations (right). Symbols: experimental measurements [Meier *et al.*, 2006; Weigand *et al.*, 2006]. Lines: LES results.

8.3.3.2 Major species

The radial profiles of the major species mass fractions for CH_4, O_2, H_2O and CO_2 are shown in Figs. 8.16 to 8.19. These figures compare the respective computed

averages and r.m.s. values with the measured values.

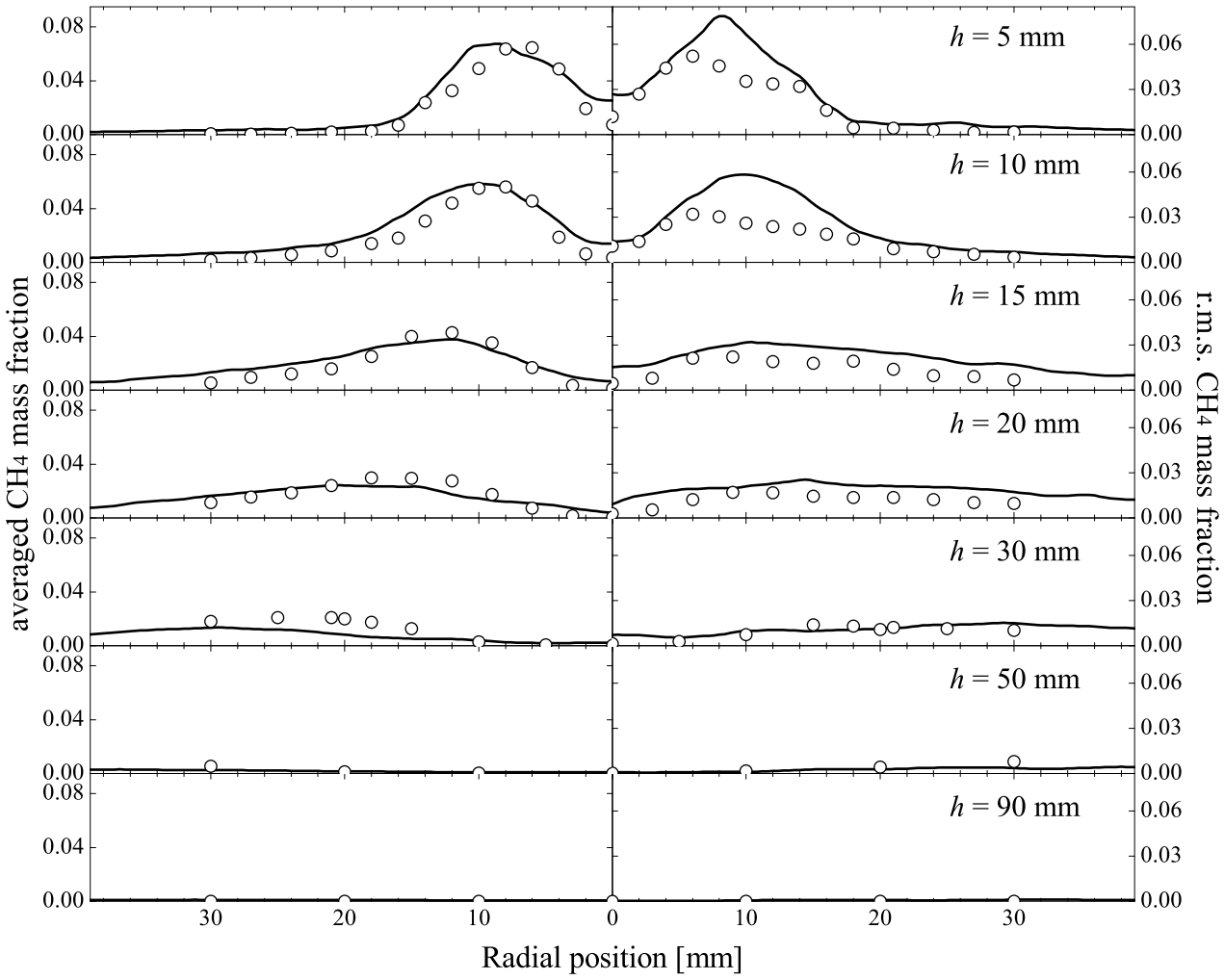

Figure 8.16: Radial profile of CH_4 mass fraction: time-averaged values (left) and r.m.s. fluctuations (right). Symbols: experimental measurements [Meier *et al.*, 2006; Weigand *et al.*, 2006]. Lines: LES results.

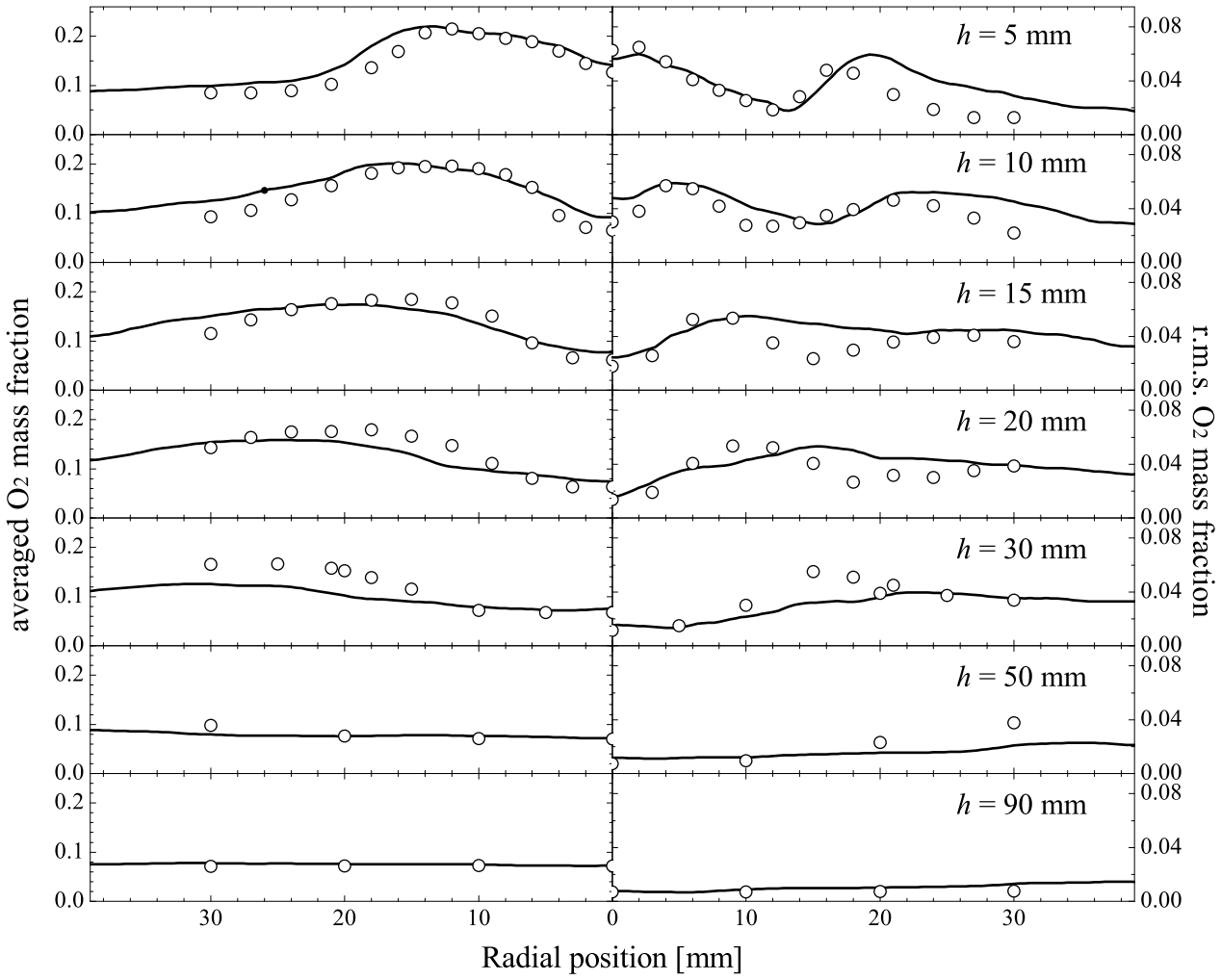

Figure 8.17: Radial profile of O_2 mass fraction: time-averaged values (left) and r.m.s. fluctuations (right). Symbols: experimental measurements [Meier *et al.*, 2006; Weigand *et al.*, 2006]. Lines: LES results.

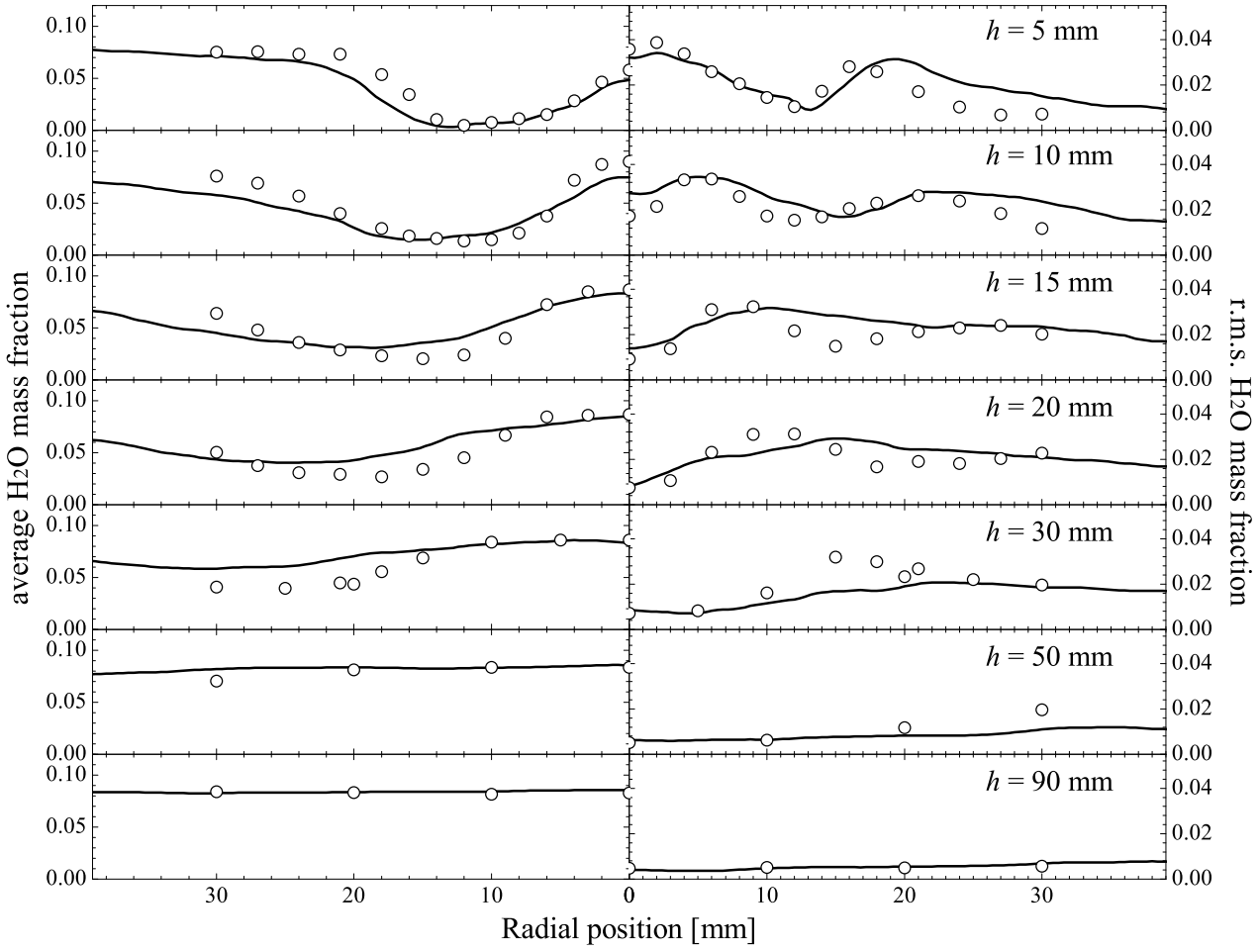

Figure 8.18: Radial profile of H_2O mass fraction: time-averaged values (left) and r.m.s. fluctuations (right). Symbols: experimental measurements [Meier *et al.*, 2006; Weigand *et al.*, 2006]. Lines: LES results.

For the methane fuel mass fraction presented in Fig. 8.16, the averaged values agree well with the measured data except that the centreline value is larger than

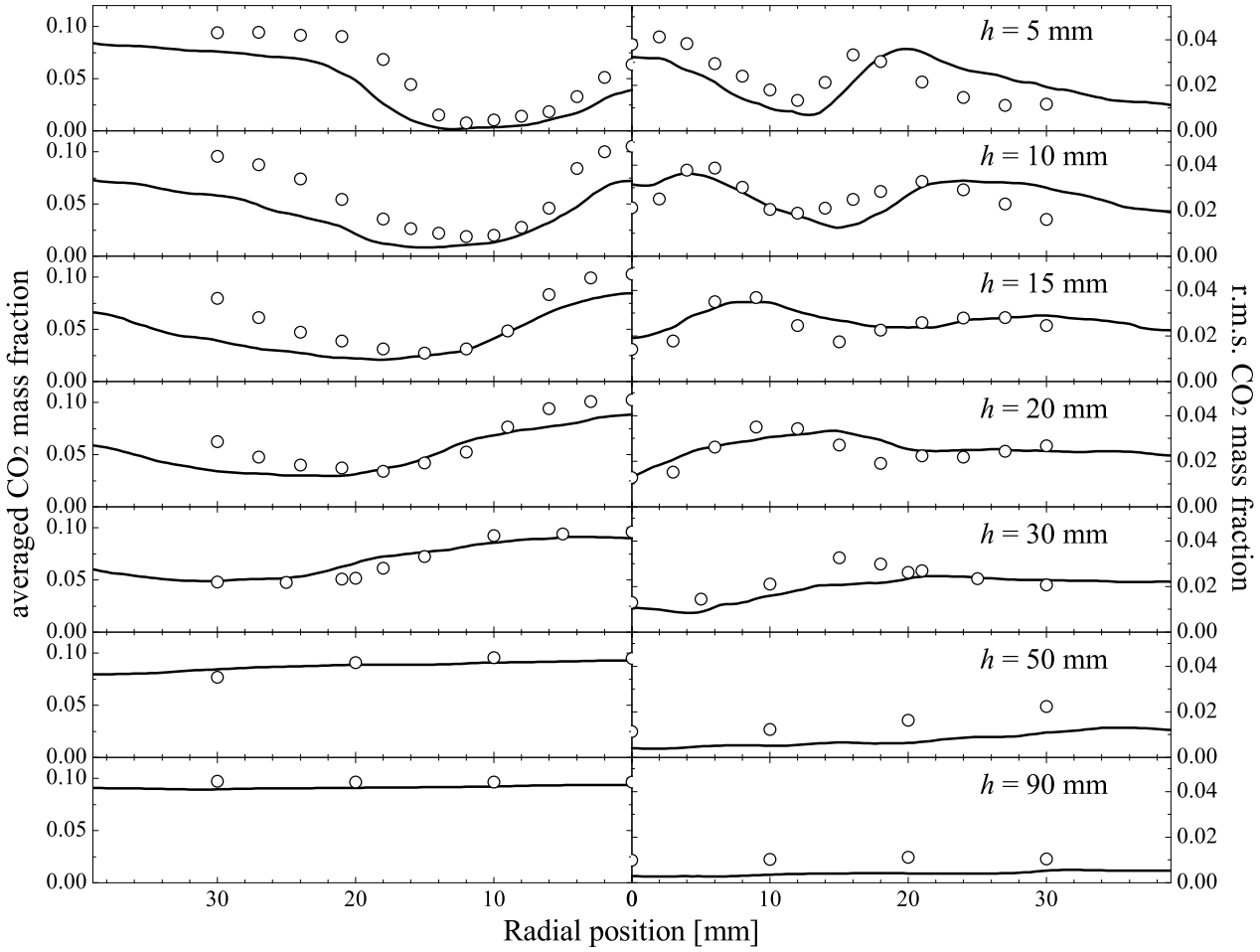

Figure 8.19: Radial profile of CO_2 mass fraction: time-averaged values (left) and r.m.s. fluctuations (right). Symbols: experimental measurements [Meier *et al.*, 2006; Weigand *et al.*, 2006]. Lines: LES results.

the measured one at the near nozzle location $h = 5$ mm. As a result, in Fig. 8.17 the corresponding O_2 mass fraction at this location is found to be over-predicted

and thus the mass fractions for the major products, H_2O and CO_2, are under-predicted as shown in Figs. 8.18 and 8.19, respectively. Similar to the prediction of mixture fraction r.m.s. (see Fig. 8.14), the computed r.m.s. fluctuation for the fuel mass fraction in the near-nozzle region is significantly higher than the measured values. The agreement is very good for the downstream locations from $h = 15$ to 90 mm. The fuel is fully burnt with zero CH_4 mass fraction at the outlet as one would expect for this overall lean burner.

The comparison between the computed and measured O_2 and H_2O mass fractions shown, respectively, in Figs. 8.17 and 8.18 is found to be very similar to that for the temperature observed in Fig. 8.15. Again, the average mass fractions of these species are captured well in the LES and some differences are found for the r.m.s. values for $h = 15$, 20 and 30 mm. The CO_2 mass fraction is observed to be under-predicted by about 30% as shown in Fig. 8.19. This under-prediction is seen for axial locations up to $h = 20$ mm. However, the agreement between the LES results and experimental measurements is very good for the further downstream locations.

8.3.3.3 Intermediate species

Two intermediate species, CO and H_2, are measured in the experiments [Meier *et al.*, 2006; Weigand *et al.*, 2006]. Due to the relatively low concentration of these intermediate species and their unstableness during the reaction process, the measurement uncertainty can be quite substantial, provided the weak signal detection of the Raman scattering technique compared to other techniques such as Rayleigh scattering ($>$ 1000 times stronger signal) [Keck *et al.*, 2002]. Unfortunately, the uncertainty and measurement errors for these two species were not reported by Weigand *et al.* [2006] and Meier *et al.* [2006].

It is seen in Fig. 8.20 that the CO formation in this partially premixed combustor is predicted very well in the LES very well. Both the averaged and r.m.s. values obtained from the simulations are in good agreement with the measurements. Notable over-prediction is seen in the regions close to the centreline and side wall, consistent with the earlier observation of under-predicted CO_2 mass fraction in these regions (see Fig. 8.19). Interestingly, this difference is not seen for temper-

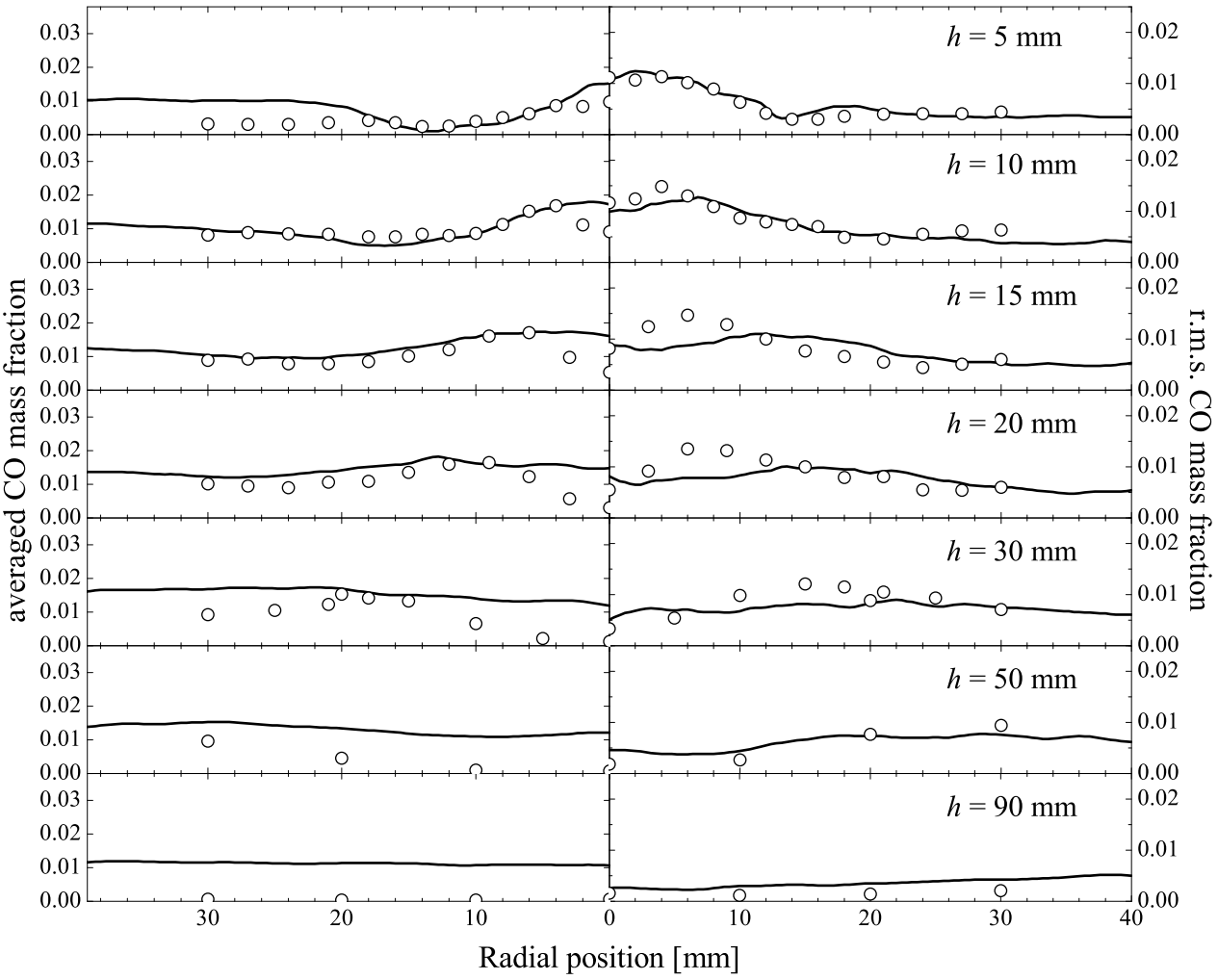

Figure 8.20: Radial profile of CO mass fraction: time-averaged values (left) and r.m.s. fluctuations (right). Symbols: experimental measurements [Meier *et al.*, 2006; Weigand *et al.*, 2006]. Lines: LES results. The error bars are plotted based on the corresponding r.m.s. values at each measurement location.

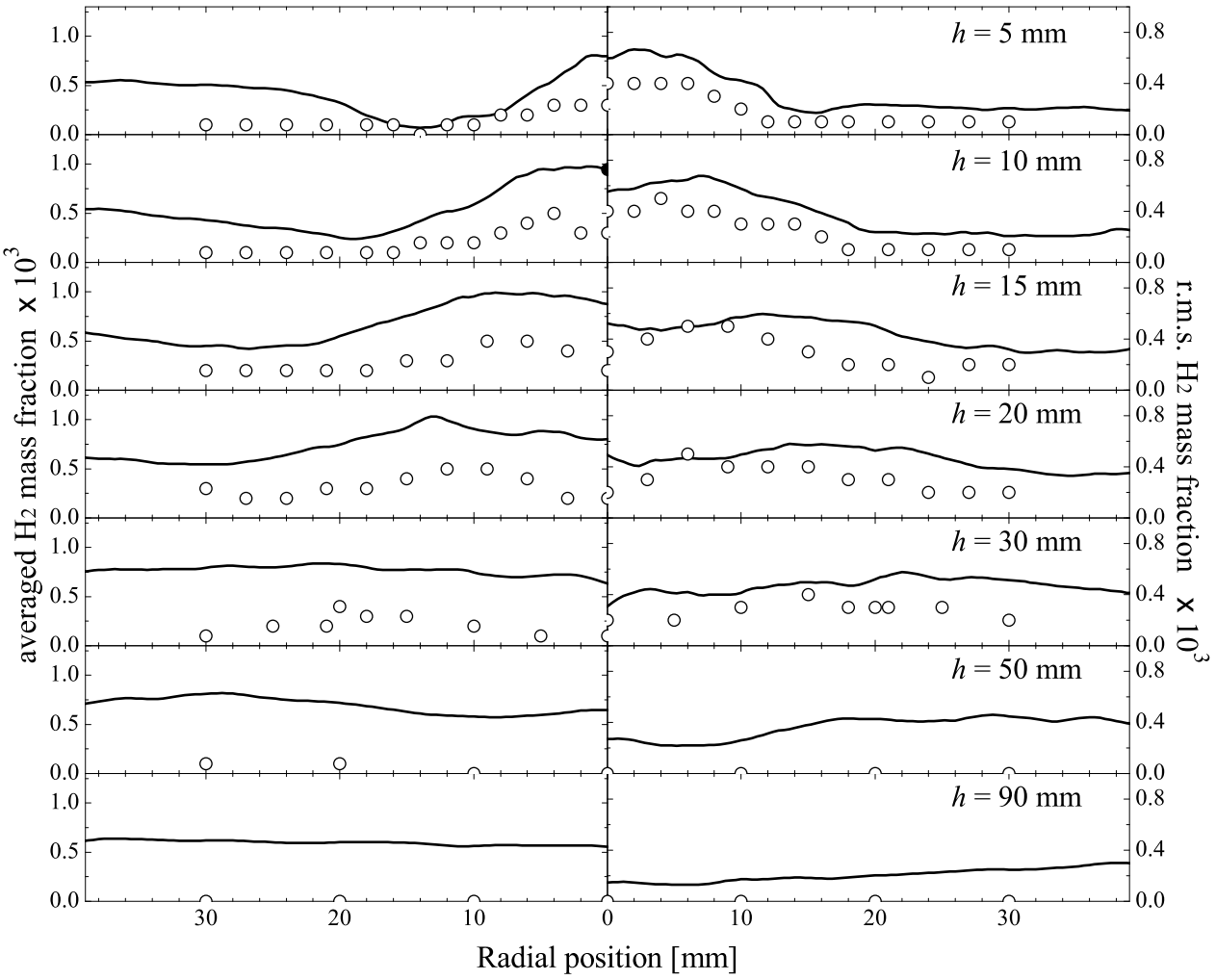

Figure 8.21: Radial profile of H_2 mass fraction: time-averaged values (left) and r.m.s. fluctuations (right). Symbols: experimental measurements [Meier *et al.*, 2006; Weigand *et al.*, 2006]. Lines: LES results. The error bars are plotted based on the corresponding r.m.s. values at each measurement location.

ature, CH_4, O_2 and H_2O mass fractions. One possible reason for this is that the chemical time scale for the reactions involving the reversible conversion between CO and CO_2 through the water-gas-shift reaction may not be captured well by the flamelet model using a single representative time scale. However, it is difficult to uncover the underlying physics using the statistics comparisons.

The LES results for the radial profiles of H_2 mass fraction is compared with the experimental data in Fig. 8.21. Note that both the averaged and r.m.s. values are scaled by a factor of 1000. The comparison shows that the computed H_2 average mass fraction is almost twice the measured values for all locations. The r.m.s. fluctuation is also over-predicted by about 20%. However, it should be noted that the resolution of the measured data for H_2 is 1×10^{-4}, which about 25% of the maximum H_2 mass fraction value measured in the experiments [Meier *et al.*, 2006; Weigand *et al.*, 2006]. Nonetheless, the overall trend is captured reasonably well for this intermediate species.

In comparison with the previous study by See & Ihme [2015] using the FPV model, the LES results obtained in this work are in better agreement with experimental data in terms of the length of the IRZ, mixture fraction and CO predictions. However, the axial velocity profiles were computed with about 10% less accuracy and this could result from the lower level of gird refinement used in the present study. Overall, both flamelet models are able to reproduce the main features of this burner such as mean flow and major species fields, whereas further modelling improvement is still to be made towards the minor species predictions.

8.3.4 Discussion

The LES statistics agree quite well with the measurements for the velocity and various scalar fields. Thus, the LES combustion model involving a presumed joint PDF approach for partially premixed combustion is quite good for the swirling flame of the DLR burner established in [Meier *et al.*, 2006; Weigand *et al.*, 2006]. Further insights on the two key variables, Z and c, their statistical behaviour, and the balance of the various terms in the $\widetilde{c''^2_{\rm sgs}}$ transport equation are given in this section.

8.3.4.1 Statistical behaviour of Z and c

The resolved and time-averaged sub-grid variances of mixture fraction and progress variable are plotted against their mean values in Fig. 8.22 for three different axial heights, h = 5, 15 and 30 mm. These chosen heights are the same as in the experimental analysis (see Figs. 2, 4 and 5 of [Meier *et al.*, 2006]). The SGS variances are obtained by time-averaging the instantaneous values computed using their transport equations, which are given in Eq. (3.32) for $\widetilde{Z''^2_{\rm sgs}}$ and Eq. (3.34) for $\widetilde{c''^2_{\rm sgs}}$ respectively. This time averaging is performed using more 100,000 samples collected over 12 FTT. Note that the progress variable variances plotted are conditioned on the stoichiometric mixture fraction, $\langle\widetilde{Z}\rangle = 0.055$.

It is seen that the mixture fraction variances, both the resolved (blue coloured) and SGS (red) parts, are very small at all three axial locations ranging from 0.001 to 0.008. This is because the injected fuel mixes with the strongly swirling air quickly. As a result, most of the samples collected have the mixture fraction value below 0.1, which is consistent with the experimental data reported by Meier *et al.* [2006] (see Figs. 2, 4 and 5 of this reference). The range of the mean mixture fraction, $\langle\widetilde{Z}\rangle$, becomes even smaller as one moves downstream in Fig. 8.22 and finally approaches the global mean mixture fraction, $Z_{\rm glob}$ = 0.037 [Weigand *et al.*, 2006]. The resolved variance, $\langle\widetilde{Z''^2}\rangle_{\rm res}$, is significantly greater than its SGS counterpart at h = 5 mm because of the grid refinement employed in the upstream regions. This difference vanishes in the downstream reaching a quasi-homogeneous mixing state for $h > 30$ mm.

As the flame front is not resolved in the LES, the sub-grid variance of progress variable, $\langle\widetilde{c''^2_{\rm sgs}}\rangle$, is quite significant compared to the resolved part as seen in Fig. 8.22. This becomes more evident as one moves in the downstream direction and the $\langle\widetilde{c''^2_{\rm sgs}}\rangle$ value is nearly twice the resolved part at the position of h = 30 mm. Thus, the sub-grid fluctuation of progress variable should not be neglected in the modelling approach in order to account for the flame/turbulence interaction at the SGS level. These statistical behaviours are found to be similar for lean and rich mixtures (not shown here) using different $\langle\widetilde{Z}\rangle$ values.

It has been shown by Langella & Swaminathan [2016] that using an simple algebraic model is for $\widetilde{c''^2_{\rm sgs}}$ is incorrect for premixed combustion as it largely

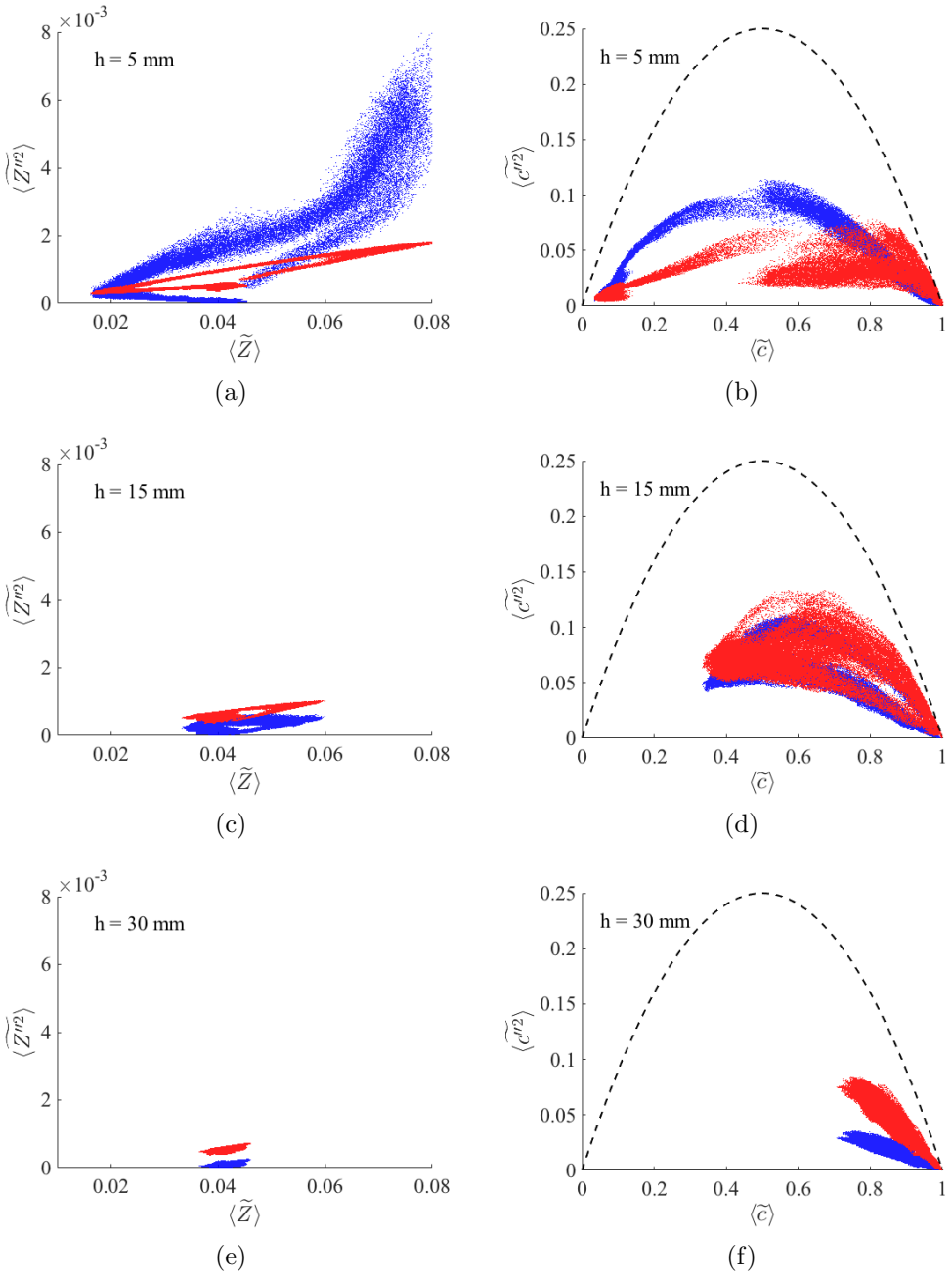

Figure 8.22: Scatter plots of resolved (blue) and sub-grid variance (red) for mixture fraction (left) and progress variable (right). The dashed line is the maximum possible total variance for progress variable.

under-estimates value of $\widetilde{c''^2_{\rm sgs}}$ by neglecting leading order combustion effects. A transport equation needs to be solved so that the correct $\widetilde{c''^2_{\rm sgs}}$ value can be obtained by balancing the physical processes involved. This is also expected to hold for partially premixed combustion. In order to investigate this, a balance analysis of the various terms in the $\widetilde{c''^2_{\rm sgs}}$ transport equation is discussed next.

8.3.4.2 Balance analysis of $\widetilde{c''^2_{\rm sgs}}$ equation

The transport equation for the sub-grid variance of progress variable noted earlier in Eq. (3.34) is rewritten for convenience as

$$\underbrace{\frac{\partial \overline{\rho}\,\widetilde{c''^2_{\rm sgs}}}{\partial t}}_{\text{unsteady}} + \underbrace{\nabla\cdot\left(\overline{\rho}\,\widetilde{\boldsymbol{U}}\,\widetilde{c''^2_{\rm sgs}}\right)}_{\text{convection}} \approx \underbrace{\nabla\cdot\left[\overline{\rho}\left(\frac{\widetilde{\nu}}{\mathrm{Sc}_t}+\frac{\nu_{\rm sgs}}{\mathrm{Sc}_t}\right)\nabla c''^2_{\rm sgs}\right]}_{T1} \underbrace{-\,2\,\overline{\rho}\,\widetilde{\chi}_{c,\,\rm sgs}}_{T2} + \underbrace{2\,\overline{\rho}\frac{\nu_{\rm sgs}}{\mathrm{Sc}_t}\nabla\widetilde{c}\cdot\nabla\widetilde{c}}_{T3} + \underbrace{2\left(\overline{c\,\dot{\omega}^*_c}-\widetilde{c}\,\overline{\dot{\omega}^*_c}\right)}_{T4}, \tag{8.3}$$

with the unsteady and convective terms in the LHS. The first term on the RHS of Eq. (8.3), denoted as $T1$, accounts for the molecular and SGS turbulent diffusion effects on the $\widetilde{c''^2_{\rm sgs}}$ transport. The term $T2$ including the negative algebraic sign signifies the dissipation of sub-grid variation. The last two terms, $T3$ and $T4$, are the turbulent production and SGS chemical reaction terms respectively. The relative importance of these RHS terms in premixed combustion has been discussed by Chakraborty & Swaminathan [2011]; Swaminathan & Bray [2005] for DNS and RANS, and has also been demonstrated for LES by Langella & Swaminathan [2016] using an *order of magnitude analysis* (OMA). These previous studies have clearly shown that all the RHS terms in Eq. (8.3) can have significant contributions depending on the flow/flame conditions and hence it is necessary to solve this transport equation in order to obtain the correct balance of these physical processes.

In particular, the chemical reaction term, T_4, and the scalar dissipation term, $T2$, were identified to be the predominant source and sink terms in the reaction zone [Chakraborty & Swaminathan, 2011]. The individual balance between these two terms is of primary importance for premixed combustion. To estimate the

SGS scalar dissipation rate (SDR), $\widetilde{\chi}_{c,\,\mathrm{sgs}}$, which is related to many physical processes such as turbulent staining, thermal dilatation, chemical reaction, etc., a common model used in the literature is the linear relaxation (LR) model, as it was suggested by Pierce & Moin [1998] for the mixture fraction (see Eq. 3.36). This model is based on the balance between the SGS turbulent scalar production and its dissipation rate, i.e., $T3 \approx T4$. However, for a reactive scalar such as the progress variable, this model was shown [Langella & Swaminathan, 2016] to severely under-estimate $\widetilde{\chi}_{c,\,\mathrm{sgs}}$ in premixed combustion by neglecting the important combustion induced scalar dissipation effects. This results in an unbalanced SGS variance equation and thus over-predicting the value of $\widetilde{c''^2_{\mathrm{sgs}}}$. In contrast, the algebraic model for $\widetilde{\chi}_{c,\,\mathrm{sgs}}$ recently proposed by Dunstan *et al.* [2013], described in Eq. 3.37, was used in [Langella & Swaminathan, 2016] showing good comparison between the LES results and experimental measurements for piloted premixed jet flames.

To investigate this balance of the $\widetilde{c''^2_{\mathrm{sgs}}}$ equation in partially premixed combustion, the RHS terms in Eq. (8.3) are plotted in Fig. 8.23 using the LES results obtained for the DLR burner [Meier *et al.*, 2006; Weigand *et al.*, 2006]. The dissipation term $T2$ computed using the LR model, denoted as $T2$-LR, is also shown for comparison and this model reads

$$\widetilde{\chi}_{c,\,\mathrm{sgs}} = C_c \frac{\nu_{\mathrm{sgs}}}{\Delta^2} \widetilde{c''^2_{\mathrm{sgs}}}, \tag{8.4}$$

where the common model constant $C_c = 2.0$ is used [Ihme & Pitsch, 2008b; See & Ihme, 2014]. The instantaneous data samples are taken from a thin slice (± 2 mm) at the axial location of $h = 5$ mm. The filtered reaction rate contour on the $h = 5$ mm transverse x-y plane is also presented in Fig. 8.23 along with the stoichiometric mixture fraction iso-line. All the terms shown in Fig. 8.23 are conditional average values in the $\widetilde{c}$ space as in [Chakraborty & Swaminathan, 2011] and these average values are normalised by a laminar flame scale $(\rho_u S_L^0/\delta_L^0)_{st}$, where ρ_u is the density of unburnt stoichiometric methane/air mixture. To separate the influence of mixture fraction variation, the samples are collected for a particular $\widetilde{Z}$ value. Three typical values, $\widetilde{Z} = 0.045$, 0.055 and 0.065, are chosen to represent the lean, stoichiometric and rich mixtures respectively.

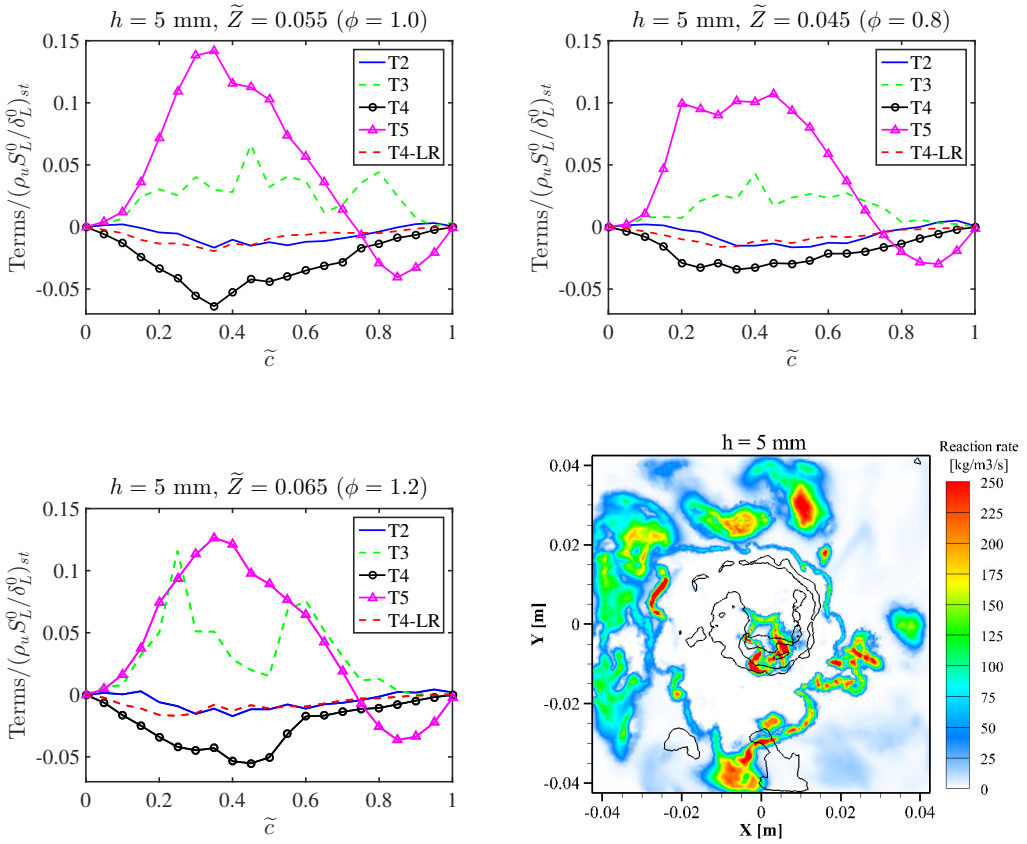

Figure 8.23: Variations of the RHS terms in the $\widetilde{c''^2_{\text{sgs}}}$ equation, Eq. (8.3), conditioned on $\widetilde{c}$ at $h = 5$ mm. The respective x-y plane contour for $\overline{\dot{\omega}_c}$ is plotted along with the $\widetilde{Z}_{st}$ iso-line.

The $\overline{\dot{\omega}_c}$ contour shown in Fig. 8.23 is mainly concentrated in the IRZ and ORZ regions. This is consistent with the experimental study [Meier *et al.*, 2006] showing that at this height ($h = 5$ mm) the flame exhibits strong partial premixing features. It can be seen that the reaction term $T4$ and dissipation term $T2$ are the leading order source and sink terms for all three mixture fraction cases. The diffusion term $T1$ is very small compared to the other terms. The turbulent production term $T3$ is relatively large because of the high-level turbulence at this near-nozzle axial location and it decreases with $\widetilde{Z}$ as the turbulence becomes less intense. The maximum value of $T4$ peaks around $\widetilde{c} = 0.4$ and it is higher for the most reactive $\widetilde{Z}_{st}$ mixture compared to the lean and rich cases as one would

expect. The behaviour of $T2$ closely follows this trend suggesting a good balance between the reactive and dissipative processes during combustion. However, the dissipation estimated using the LR model (red dashed line) appears to be an order of magnitude smaller than the reaction term $T4$, which would result in a significant over-prediction of $\widetilde{c''^2_{\text{sgs}}}$ production. This is consistent with previous findings in [Langella & Swaminathan, 2016]. A dynamic procedure was also proposed by Pierce & Moin [1998] to estimate the model constant C_c in Eq. (8.4) depending on the local flow conditions. However, this is expected to still under-estimate the SGS dissipation rate because the combustion related physics is missing in the dynamic filtering procedures.

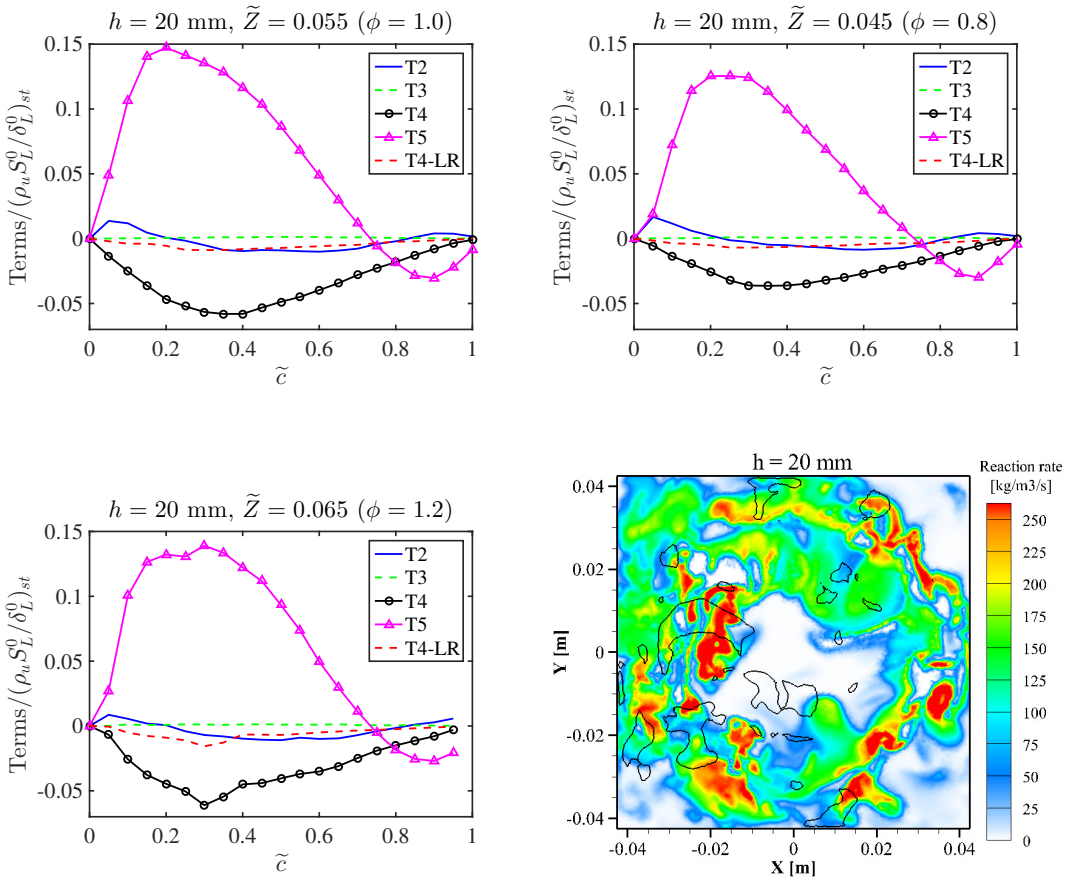

Figure 8.24: Variations of the RHS terms in the $\widetilde{c''^2_{\text{sgs}}}$ equation, Eq. (8.3), conditioned on $\widetilde{c}$ at $h = 20$ mm. The respective x-y plane contour for $\overline{\dot{\omega}_c}$ is plotted along with the $\widetilde{Z}_{st}$ iso-line.

Figure 8.24 shows the variation of these terms at a relatively downstream location at $h = 20$ mm. As seen, the reaction zone is more distributed compared to that at $h = 5$ mm indicating that the combustion takes place in a more premixed or stratified mixture. This is further reflected by the earlier peak position at about $\widetilde{c} = 0.3$ for $T4$. Similar to what has been seen in Fig. 8.23, the terms $T2$ and $T4$ remain predominant for different mixture fractions. As expected, the turbulent production term $T3$ drops significantly compared to that in Fig. 8.23, smaller than the diffusion term T1 because of the lower turbulence level at the downstream locations. Again, the LR model severely under-estimates the scalar dissipation rate suggesting that the SGS combustion related effects should be considered in the SDR model.

8.4 Summary

In this chapter, the LES modelling framework for partially premixed combustion proposed in Chapter 3 is further tested for complex flow conditions in a dual-swirler burner of Meier *et al.* [2006]; Weigand *et al.* [2006]. The computational results are compared against the experimental measurements showing a very good agreement for velocity, temperature and major species mass fractions at various axial locations. Although some discrepancies are found for the intermediate species, the overall trend is captured reasonably well, given the low computational cost of the combustion model. This suggests that the modelling framework is quite robust for a range of flow and mixing conditions existing in this burner with complex flow features and the important physical aspects involved are captured. The analysis of the progress variable SGS variance equation lends further support to this by showing that the modelled source and sink terms are balanced on a consistent physical basis. The reaction and dissipation terms are found to be predominant, an order of magnitude larger than the diffusion and turbulent production terms. This further supports that the SGS scalar dissipation models based on linear relaxation hypothesis is invalid, resulting in severely over-predicted SGS variance of progress variable, consistent with previous studies [Langella & Swaminathan, 2016]. In contrast, the SGS scalar dissipation model proposed by Dunstan *et al.* [2013], which is used in the simulations for this

work as described by Eq. (3.37), provides a correct balance to the SGS variance equation. This is because the ingredients of this model capture the underlying physics well.

Chapter 9

Concluding Remarks

The validity of the numerical modelling framework involving a presumed joint PDF closure for partially premixed combustion has been investigated in this thesis. This closure is based on planar unstrained premixed laminar flamelet with varying equivalence ratios, and its statistical description in turbulent flames using mixture fraction and progress variable. Both the Reynolds Averaged Navier Stokes (RANS) and Large Eddy Simulation (LES) methodologies have been used to test this modelling framework. The statistical correlation between mixture fraction and progress variable is considered for the joint PDF for RANS as has been found important by Ruan [2012]. This correlation is expected to be small for LES and thus is not included in the LES sub-grid joint PDF closure. This is because the mixture fraction variation is mainly resolved by the LES grid and the SGS part is too small to have a significant correlation with the progress variable variation at the sub-grid level. The test cases chosen include a canonical lifted jet flame configuration with a range of jet velocity and air-dilution conditions [Ahmed & Mastorakos, 2006]; and a model gas turbine combustor with complex geometry and flow conditions [Meier *et al.*, 2006; Weigand *et al.*, 2006]. The overall efficacy of the modelling framework has been shown to be quite good in these test cases by comparing the simulation results with the experimental measurements. The main findings in these studies are summarised below and then an outlook is given for the recommended future works.

9.1 Summary of findings

The first study of this thesis presented in Chapter 5 has focused on the steady RANS simulation of turbulent lifted methane jet flames [Ahmed & Mastorakos, 2006] as a continuation work of [Ruan, 2012], in which the RANS modelling framework was validated for a lifted hydrogen flame. Two-dimensional axisymmetric simulations have been performed to compute the flame lift-off height, L_{f}, for a broad range of jet velocities and air dilution levels. A systematic study has shown that the mixture fraction-progress variable (Z-c) correlation and non-premixed combustion mode contribution are both important to accurately predict the lift-off height. The Z-c correlation affects the reaction zone distribution inside the flame brush downstream of the flame leading edge and this effect has been found to increase with the air-dilution level because of the thicker flame brush allow for stronger interaction between Z and c. The non-premixed mode contribution to the mean reaction rate given in Eq. (3.46) has been found to be significant only close to the stoichiometric mixture with predominately negative values. Its relative role decreases as the air-dilution level increases resulting from the lower scalar dissipation rate of mixture fraction. The computed L_{f} value increases for higher jet velocity and air-dilution level showing an overall very good agreement with the measured data [Ahmed & Mastorakos, 2006].

Following the steady RANS study above, Chapter 6 has investigated the model efficacy by simulating the transient flame evolution from initial ignition to final stabilisation in a diluted methane/air jet [Ahmed & Mastorakos, 2006] using the unsteady RANS (URANS) approach. Both 2D and 3D URANS simulations have been performed for two jet velocities to explore the influence of the third physical dimension, the azimuthal direction, on the flame leading edge transient evolution. The calculated lift-off height has been found to be the same for the 2D and 3D simulations, both in good agreement with the measured value, suggesting that the influence of the third dimension is negligible if only the final stabilisation height is of interest. However, a substantial difference between the 2D and 3D computational results has been observed for the transient evolution of the flame most-upstream point. The flame net propagation speed computed in the 3D simulations shows a substantial improvement over the 2D case compared to the

experimental data. This improvement is found to be particularly evident during the initial propagation stage where the premixed flame propagation is dominant as has been found in an earlier study [Müller *et al.*, 1994].

The flame brush displacement speed and its components are investigated to shed further light on this. The tangential diffusion component, $\overline{S_\mathrm{t}}$, has been found to be small compared to the normal diffusion, $\overline{S_\mathrm{n}}$, and reaction, $\overline{S_\mathrm{r}}$, components for both the 2D and 3D cases. The influence of physical dimension results from these two predominant components and the computed values of $\overline{S_\mathrm{n}}$ and $\overline{S_\mathrm{r}}$ are larger in the 2D simulations leading to a higher propagation speed than that for the 3D case. This suggests that the third physical dimension plays a quite important role during the flame transient propagation process by allowing the leading edge to evolve and interact naturally with the oncoming flow in the three-dimensional physical space.

Large Eddy Simulation methodology has been employed in Chapter 7 to study the spark ignition and dynamic flame propagation characteristics, which cannot be captured in the RANS approach due to its averaged nature. The modelling methodology for partially premixed combustion has been tested and validated for the first time in the context of LES. It has been demonstrated that the different flame evolution stages observed in the experiments [Ahmed & Mastorakos, 2006] are reproduced well using the LES model. More quantitatively, computational results for the flame kernel growth rate after ignition, transient evolution of flame leading edge, and flame final lift-off height, agree very well with the measurements for two different jet velocities. However, the leading edge propagation speed has been found to be slightly over-predicted and the computed lift-off height is about $2d_\mathrm{j}$ above the measured value for the low jet velocity case. These discrepancies could result from the assumption of statistical independence between Z and c in the sub-grid joint PDF model and also possibly from the under-specified jet inlet turbulence. The flame propagation trajectory has been visualised by tracking the most-leading point movement, exhibiting a *spiral*-like shape starting from the ignition location to the final stabilisation height. This further confirms the important role of the flame propagation in the third physical dimension as has been demonstrated in Chapter 6 using URANS. Furthermore, the study on the final lift-off statistics has shown a correlation between the jet velocity and the stabil-

isation location through a scaling analysis. This correlation has been identified for both the axial and radial locations. It has also been observed that the most probable stabilisation location is located in the lean mixture, consistent with the RANS results discussed in Chapter 5. However, there is no clear correlation found between the radial stabilisation location and the mixture fraction implying that many other physical processes, apart from mixing, are also involved in the lifted flame stabilisation mechanism.

In order to demonstrate the model ability under more complex flow conditions, LES of a gas turbine model combustor investigated experimentally by Weigand *et al.* [2006] and Meier *et al.* [2006] has been conducted in Chapter 8. The flame A, which was featured as stably burning flame operating under partially premixed conditions, has been chosen for the model validation. The full burner geometry has been considered in the computation involving the air intake plenum, dual-swirler nozzle, 72-channel fuel jet injector and the combustion chamber. Given this complex burner geometry, the computed velocity field agrees well with the experimental data for various streamwise locations ranging from just above the nozzle exit plane (h = 1.5 mm) to the far downstream (h = 90 mm) near the chamber outlet. The predicted time-averaged inner recirculation zone (IRZ) length has been found to be in excellent agreement with the measured value, however, its width is over-predicted by the LES. The comparison has also been made for temperature, mixture fraction and species mass fractions showing overall satisfactory agreement. A balance analysis for the progress variable sub-grid variance transport equation has been conducted to show the relative importance of the various source and sink terms representing the different physical processes involved in the complex swirling flame. This analysis has clearly demonstrated that the reaction source and the scalar dissipation sink are the leading order terms balancing each other in the equation, consistent with a previous LES study [Langella & Swaminathan, 2016]. The commonly used linear relaxation model for the SGS scalar dissipation rate is inappropriate because it was derived based on the balance between the turbulent production and scalar dissipation terms, ignoring the reactions. The important combustion induced effects on the SGS variance of progress variable should not be neglected in the modelling approach.

To conclude, a simple, computationally inexpensive and yet robust modelling

framework for partially premixed combustion has been established and validated. A good model efficacy has been shown for a range of conditions in a canonical jet burner and a complex gas turbine model combustor. This modelling framework available for both RANS and LES paradigms is a promising predictive tool for various turbulent combustion problems of both academic and industrial interests.

9.2 Future work

Although the computational models used in this thesis seem to work reasonably well for a wide range of conditions in different burner configurations, there is still room for further improvement of this modelling framework. The specific future works recommended are as follows.

- The statistical independence of mixture fraction and progress variable has been assumed for the sub-grid joint PDF in this work. The validity of this needs to be demonstrated and one possible approach is to leverage a DNS database such as that used by Ruan [2012]. A *priori* investigation on the filtered reaction rate would reveal the importance of this SGS correlation.

- As one of the attractive aspects of LES, dynamic procedures can be used for determining the various model constants depending on the local scale similarity. For example, the Germano *et al.* [1991] dynamic approach for the Smagorinsky constant in Eq. (3.30), and the dynamic β_c' [Langella & Swaminathan, 2016] for the SGS scalar dissipation rate model described in Eq. (3.37), can be used in future studies.

- Since the modelling methodology used here does not rely on any flame topological assumption, it would be interesting to apply this methodology for other combustion regimes such as autoignition, Moderate or Intense Low-oxygen Dilution (MILD) combustion, multi-phase flames, etc. As a first attempt, it has been found quite successful for a Jet-in-Hot-Coflow configuration under MILD conditions using a Perfectly Stirred Reactor model [Chen *et al.*, 2016a].

- Extending this modelling framework to problems such as thermo-acoustic instabilities, flame blow-off phenomena and flame-flame interaction would be beneficial.

Appendix A. List of Publications

The results produced from this thesis work have been published, or are currently being prepared for publication, in

Journals:

1. Z. Chen, S. Ruan and N. Swaminathan. Simulation of turbulent lifted methane jet flames: Effects of air-dilution and transient flame propagation. *Combust. Flame*, 162:703-716, 2015.

2. Z. Chen, S. Ruan and N. Swaminathan. Numerical study of transient evolution of lifted jet flames: partially premixed flame propagation and influence of physical dimensions. *Combust. Theory Model.*, 20:592-612, 2016.

3. Z. Chen, S. Ruan and N. Swaminathan. Large eddy simulation of flame edge evolution in a spark-ignited methane-air jet. *Proc. Combust. Inst.*, 2016. doi: 10.1016/j.proci.2016.06.023.

4. Z. Chen, V. M. Reddy, S. Ruan, N. A. K. Doan, W. L. Roberts, N. Swaminathan. Simulation of MILD combustion using Perfectly Stirred Reactor model. *Proc. Combust. Inst.*, 2016. doi: 10.1016/j.proci.2016.06.007.

5. Z. Chen, N. A. K. Doan, S. Ruan, I. Langella, N. Swaminathan. Subgrid modelling of mixture fraction-progress variable correlation for LES of partially premixed flames: *a priori* DNS study. In preparation.

6. Z. Chen, S. Ruan and N. Swaminathan. Large eddy simulation of a gas turbine model combustor using a partially premixed flamelet approach. In preparation.

Conferences:

Peer reviewed

1. Z. Chen, S. Ruan and N. Swaminathan. Modelling of flame lift-off evolution: numerical implementation of density-pressure coupling. *10th Asia-Pacific Conference on Combustion (ASPACC)*, Beijing, China, 2015.

2. S. Ruan, Z. Chen and N. Swaminathan. Simulation of turbulent lifted jet flames and their transient propagation: a scaling analysis. *25th International Colloquium of Dynamic Explosive Reactive System (ICDERS)*, Leeds, UK, 2015.

Others

3. Z. Chen, S. Ruan and N. Swaminathan. RANS simulation of partially premixed turbulent flames. *Joint meeting of the British and Scandinavian-Nordic Sections of the Combustion Institute*, Cambridge, UK, 2014.

4. Z. Chen, S. Ruan and N. Swaminathan. Modelling of flame lift-off evolution: numerical implementation of density-pressure coupling. *15th International Conference on Numerical Combustion (ICNC)*, Avignon, France, 2015.

5. Z. Chen, S. Ruan and N. Swaminathan. RANS Simulation of partially premixed turbulent flames. *2nd International Education Forum of Academy for Co-creative Education of Environment and Energy Science (ACEEES),* Los Angeles, USA, 2013.

6. Z. Chen, S. Ruan and N. Swaminathan. Simulation of turbulent lifted jet flames. *3rd International Education Forum of Academy for Co-creative Education of Environment and Energy Science (ACEEES),* Perth, Australia, 2014.

7. Z. Chen, S. Ruan and N. Swaminathan. Large eddy simulation of partially premixed flames. *4th International Education Forum of Academy for Co-creative Education of Environment and Energy Science (ACEEES),* Hawaii, USA, 2015.

Appendix B. CFD Numerical discretisation

Generally in numerical simulations, the partial differential equations governing the system (see §3.1) are discretised into a set of coupled algebraic equations [Hirsch, 1991]. These algebraic equations are then solved at a finite number of spatial points in a prescribed closed computational domain at a given time step. This discretisation approach is commonly referred to as the Finite Volume Method (FVM), which is used for most of CFD codes including Fluent and OpenFOAM. This section briefly introduces the FVM discretisation methods and schemes used for the present work.

B.1 Finite volume method

The numerical discretisation procedure can usually be divided into two main sub-tasks, one for the computational domain and another one for the transport equations [Patankar, 1980]. The discretisation of the computational domain generates a numerical grid which comprises many sub-domains (or cells), and the transport equations are subsequently discretised and solved at the centroid of these sub-domains. Figure B.1 presents the schematic of a typical control volume (CV) sub-domain, where **P** and **N** denote respectively the centroids of the local and neighbour cells. $\underline{\mathbf{S}}$ is the face area normal vector representing the fluxes between the **P** and **N** cells, and **f** denotes the face centre. During the numerical simulation, all the information regarding the local cell value and its relation

with the neighbour cells can be expressed by $\mathbf{P}$, $\mathbf{f}$ and $\underline{\mathbf{S}}$. The shadowed surface can also be a boundary surface which needs to be prescribed depending on the physical problem in order to close the numerical system.

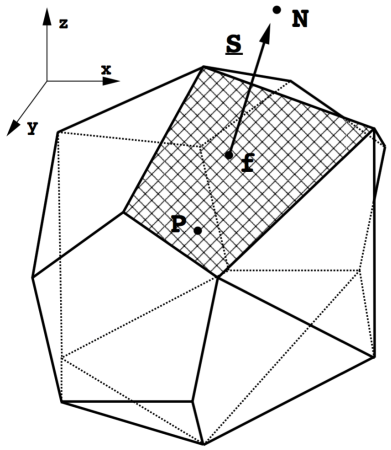

Figure B.1: Schematic of a CFD control volume [Jasak, 1996].

Discretisation of different terms in a transport equation representing different physical processes are treated separately. If we take the instantaneous conservation equation for species i given in Eq. (2.4), for example, it needs to be satisfied over the CV during a given time interval and thus one obtains the integral form of Eq. (2.4) written as [Ferziger & Perić, 1999; Hirsch, 1991]

$$\int_t^{t+\Delta t} \left[\underbrace{\frac{\partial}{\partial t}\int_{\mathrm{CV}} \rho Y_i dV}_{\text{temporal derivative}} + \underbrace{\int_{\mathrm{CV}} \nabla\cdot(\rho \boldsymbol{U} Y_i)\, dV}_{\text{convection}} - \underbrace{\int_{\mathrm{CV}} \nabla\cdot(\rho D \nabla Y_i)}_{\text{diffusion}} \right] dt \qquad \text{(B.1)}$$

$$= \int_t^{t+\Delta t} \left[\underbrace{\int_{\mathrm{CV}} \dot{\omega}_i dV}_{\text{reaction source}} \right] dt,$$

where Δt is the time-step size and dV denotes a numerical cell volume. Unfortunately, in this equation the convection and diffusion terms involving spatial gradients cannot be directly solved within the CV because the gradient information is not described using the local parameters discussed earlier in Fig. B.1.

Therefore, the generalised form of Gauss's theorem is used to transform these gradient operations to surface area and flux calculations. For instance, the divergence in the convection term can be calculated as [Patankar, 1980]

$$\int_{\mathrm{CV}} \nabla \cdot (\rho \boldsymbol{U} Y_i)\, dV = \oint_{\partial \mathrm{S}} (\rho \boldsymbol{U} Y_i) \cdot d\mathbf{S}, \tag{B.2}$$

where ∂S represents the closed surface bounding the CV and $d\mathbf{S}$ denotes an infinitesimal surface element with its normal pointing outwards of the CV. After the transformation and subsequent linearisation of Eq. (B.1) (see [Ferziger & Perić, 1999; Hirsch, 1991; Patankar, 1980] for detailed derivation), all the resulting terms appear in fully discretised forms which only require the values at the centroid and face centre of the CV. The latter, in common practice, are obtained from the centroid values in the surrounding CVs using appropriate numerical schemes, which will be discussed later.

Finally, the discretised equation is solved in each numerical cell over the entire computational domain leading to a system of algebraic equations expressed in a matrix form as

$$[\mathcal{C}][Y^{\mathrm{n}}_{i,\mathbf{P}}] = [\mathcal{S}], \tag{B.3}$$

where $[\mathcal{C}]$ is the matrix of coefficients and it can be further split into diagonal and off-diagonal parts. The source term $[\mathcal{S}]$ is often linearised as $[\mathcal{S}] = [\mathcal{S}_{\mathrm{u}}] + [\mathcal{S}_{\mathbf{p}}][Y^{\mathrm{n}}_{i,\mathbf{P}}]$ so that the coefficient of the linear part $[\mathcal{S}_{\mathbf{p}}]$ can be included in $[\mathcal{C}]$ implicitly in order to have a higher numerical stability [Ferziger & Perić, 1999; Hirsch, 1991].

Ideally, the numerical solution for the above system of linear algebraic equations may be obtained in a fully coupled form by calculating the inverse of $[\mathcal{C}]$: $[Y^{\mathrm{n}}_{i,\mathbf{P}}] = [\mathcal{C}]^{-1}[\mathcal{S}]$. However, for fluid flow problems where a segregated approach is used to solve the coupled equations such as the pressure-velocity equations, iterative solution algorithm is commonly used [Patankar, 1980]. Even so, one may still encounter convergence issues while solving the system particularly due to the numerical schemes used to compute the surface values. These numerical schemes can have a significant impact on the solution especially for LES which

requires higher order schemes.

B.2 Numerical schemes

B.2.1 Temporal schemes

Both explicit and implicit methods exist for temporal discretisation. Explicit methods evaluate the unknown values at the new time-step using the known information from the previous time step, and thus is also called *forward stepping* methods. On the contrary, implicit or *backward stepping* methods express the new time-step value in terms of the unknown information of the new time-step [Patankar, 1980]. The use of explicit discretisation is very limited in practical CFD applications. This is because it stringently requires the Courant-Friedrichs-Lewy (CFL) number [Courant *et al.*, 1928] to be smaller than unity. In reacting flow simulation, three different CFL numbers need to be considered, which correspond to the convection ($\mathrm{CFL_C}$), diffusion ($\mathrm{CFL_D}$) and reaction ($\mathrm{CFL_R}$) processes respectively:

$$\mathrm{CFL_C} = \frac{U\Delta t}{\Delta x}, \quad \mathrm{CFL_D} = \frac{D\Delta t}{\Delta x^2}, \quad \mathrm{CFL_R} = K_r \Delta t, \tag{B.4}$$

where Δt is the time-step size, Δx the grid size and U is the local flow velocity in the x-direction. D denotes the diffusivity and K_r is the chemical reaction rate in units of s^{-1}. In order to ensure a numerical stability, these three numbers need to satisfy the above condition individually and so

$$\max(\mathrm{CFL_C},\, \mathrm{CFL_D},\, \mathrm{CFL_R}) < 1. \tag{B.5}$$

This criterion is difficult to satisfy in practice and especially for steady-state flow calculations [Hirsch, 1991]. Therefore, the implicit approaches are commonly preferred especially for RANS and LES calculations as they allow a relatively large time-step size.

Specifically for the computational studies of this thesis, the first-order Euler

implicit scheme is used for the RANS simulations. For a variable ϕ, this scheme is expressed as [Patankar, 1980]

$$\phi^n = \phi^{n-1} + \mathscr{F}(\phi^n)\Delta t, \tag{B.6}$$

where the superscript ^{n} and $^{n-1}$ denote the new and previous time-steps respectively. $\mathscr{F}$ is a function of only the new time-step values. For LES calculations, a second-order *backward differencing* implicit scheme is applied for in order to obtain a higher numerical accuracy in time. This scheme is derived by considering the Taylor series expansion of ϕ in time around $\phi^n = \phi(t + \Delta t)$ [Ferziger & Perić, 1999]:

$$\phi(t) = \phi^{n-1} = \phi^n - \frac{\partial \phi^{n-1}}{\partial t}\Delta t + \frac{1}{2}\frac{\partial^2 \phi^{n-1}}{\partial t^2}\Delta t^2 + \mathcal{O}(\Delta t^3) + ... \tag{B.7}$$

Thus, the temporal derivative of ϕ can be expressed as

$$\frac{\partial \phi}{\partial t} \approx \frac{\phi^n - \phi^{n-1}}{\Delta t} + \frac{1}{2}\frac{\partial^2 \phi}{\partial t^2}\Delta t + \mathcal{O}(\Delta t^2). \tag{B.8}$$

Similarly, this approach is applied to an older time-step, $\phi(t - \Delta t) = \phi^{n-2}$, and one obtains

$$\frac{\partial \phi}{\partial t} \approx \frac{\phi^n - \phi^{n-2}}{2\Delta t} + \frac{\partial^2 \phi}{\partial t^2}\Delta t + \mathcal{O}(\Delta t^2). \tag{B.9}$$

Combining Eqs. (B.8) and (B.9), the second-order approximation of the temporal derivative of ϕ is obtained as

$$\frac{\partial \phi}{\partial t} = \frac{3\phi^n - 4\phi^{n-1} + \phi^{n-2}}{2\Delta t}, \tag{B.10}$$

which involves the information from three time-steps. Finally, the backward

differencing scheme is expressed as [Patankar, 1980]

$$\phi^n = \frac{2}{3}\phi^{n-1} - \frac{1}{6}\phi^{n-2} + \mathscr{F}(\phi^n)\Delta t. \tag{B.11}$$

See more details on these schemes in references [Ferziger & Perić, 1999; Hirsch, 1991; Patankar, 1980].

B.2.2 Spatial schemes

As noted in the previous section, spatial numerical schemes are required to determine the face centre values for the convection term and the gradient fluxes through the internal surface for the diffusion term in the discretised form of Eq. (B.1). It remains as a major challenge to find a convection scheme that provides a stable solution for the second term on the LHS of Eq. (B.1) without sacrificing the accuracy for high-fidelity computation such as LES.

To calculate the face value, ϕ_f, using the centroid values of two neighbouring cells, ϕ_P andϕ_N, an instinctive method is to interpolate these two values using the relative distance from the face to centroid, D_P and D_N [Patankar, 1980]:

$$\phi_\mathrm{f} = \frac{D_\mathrm{N}}{D_\mathrm{N} + D_\mathrm{P}}\phi_\mathrm{P} + \frac{D_\mathrm{P}}{D_\mathrm{N} + D_\mathrm{P}}\phi_\mathrm{N}, \tag{B.12}$$

and this approach is called the *Central Differencing* (CD) scheme. Although the CD scheme is simplistic and second-order accurate, it causes unphysical oscillations in the solution for convection-dominated high-Reynolds number turbulent flows [Hirsch, 1991]. This is particularly problematic for scalars having a physical boundedness such as mixture fraction and progress variable ranging from 0 to 1 as described in §3.1.1. By decreasing the accuracy to first order, the *Upwind Differencing* (UD) scheme guarantees the boundedness simply taking the centroid

value of the upstream cell for the face centre [Patankar, 1980]:

$$\phi_{\mathrm{f}} = \begin{cases} \phi_{\mathrm{P}}, & \text{if } F \geq 0 \\ \phi_{\mathrm{N}}, & \text{if } F < 0 \end{cases} \tag{B.13}$$

where value of F is positive when the local flow direction is from cell P to cell N and *vice versa*. This scheme is used for the RANS simulations in this work with sufficient accuracy. As for LES, however, the UD scheme is too dissipative to accurately capture the large-scale dynamic fluid motions. In order to keep both the physical boundedness and numerical accuracy at the same time, many oscillation-free flux-limited methods called *Total Variation Diminishing* (TVD) [Harten, 1983] schemes have been proposed. The total variation of the solution, $\mathcal{TV}$, defined as [Ferziger & Perić, 1999]

$$\mathcal{TV} = \sum_{f} |\phi_{\mathrm{N}} - \phi_{\mathrm{P}}| \tag{B.14}$$

represents the sum of the variation of ϕ between the local and all the neighbour cells. In TVD schemes, the value of $\mathcal{TV}$ is bounded by its value from the previous time-step: $\mathcal{TV}^n \leq \mathcal{TV}^{n-1}$. For the LES scalar convection in Eqs. (3.31)-(3.34), a second-order TVD scheme called *Limited linear* in the OpenFOAM library is used to ensure that these scalars are bounded on a physical basis. However, for the momentum equation, Eq. (3.25), the velocity is not physically bounded, and thus the CD scheme is applied.

References

Abdel-Gayed, R.G. & Bradley, D. (1989). Combustion regimes and the straining of turbulent premixed flames. *Combust. Flame*, **76**, 213–218. 22

Ahmed, S.F. & Mastorakos, E. (2006). Spark ignition of lifted turbulent jet flames. *Combust. Flame*, **146**, 215–231. xi, xii, xiv, xvi, xxi, 7, 25, 26, 63, 64, 67, 68, 69, 70, 72, 73, 74, 75, 93, 95, 96, 98, 100, 102, 104, 109, 110, 114, 115, 116, 118, 119, 121, 122, 125, 135, 136, 138, 139, 144, 145, 146, 147, 148, 149, 152, 153, 157, 158, 199, 200, 201

Anselmo-Filho, P., Hochgreb, S., Barlow, R.S. & Cant, R.S. (2009). Experimental measurements of geometric properties of turbulent stratified flames. *Proc. Combust. Inst.*, **32**, 1763–1770. 24

ANSYS-Fluent (2012). *ANSYS Fluent 13.0, ANSYS, Inc., Canonsburg, PA 15317, USA*. 60, 61, 118

Auzillon, P., Gicquel, O., Darabiha, N., Veynante, D. & Fiorina, B. (2012). A filtered tabulated chemistry model for LES of stratified flames. *Combust. Flame*, **159**, 2704–2717. 32

Auzillon, P., Riber, E., Gicquel, L.Y.M., Gicquel, O., Darabiha, N., Veynante, D. & Fiorina, B. (2013). Numerical investigation of a helicopter combustion chamber using LES and tabulated chemistry. *Comptes Rendus Mécanique*, **341**, 257–265. 32

Barlow, R.S. & Frank, J.H. (1998). Effects of turbulence on species mass fractions in methane/air jet flames. *Proc. Combust. Inst.*, **27**, 1087–1095. 34

Barlow, R.S., Dunn, M.J., Sweeney, M.S. & Hochgreb, S. (2012). Effects of preferential transport in turbulent bluff-body-stabilized lean premixed CH4/air flames. *Combust. Flame*, **159**, 2563–2575. 178

Barlow, R.S., Meares, S., Magnotti, G., Cutcher, H. & Masri, A.R. (2015). Local extinction and near-field structure in piloted turbulent CH4/air jet flames with inhomogeneous inlets. *Combust. Flame*, **162**, 3516–3540. 3

Batchelor, G.K. (1953). *The Theory of Homogeneous Turbulence*. Cambridge University Press. 15

Bekdemir, C., Somers, L.M.T. & de Goey, L.P.H. (2011). Modeling diesel engine combustion using pressure dependent flamelet generated manifolds. *Proc. Combust. Inst.*, **33**, 2887–2894. 36

Bilger, R.W. (1976). Structure of diffusion flames. *Combust. Sci. Technol.*, **13**, 155–170. 16

Bilger, R.W. (1993). Conditional moment closure for turbulent reacting flow. *Phys. Fluids*, **5**, 436–444. 29

Bilger, R.W., Stårner, S.H. & Kee, R.J. (1990). On reduced mechanisms for methane-air combustion in nonpremixed flames. *Combust. Flame*, **80**, 135–149. xviii, 17, 44, 140, 163, 178

Boger, M., Veynante, D., Boughanem, H. & Trouvé, A. (1998). Direct numerical simulation analysis of flame surface density concept for large eddy simulation of turbulent premixed combustion. *Proc. Combust. Inst.*, **27**, 917–925. 31, 32

Borghi, R. (1984). Mise au point sur la structure des flammes turbulentes. *Journal de chimie physique*, **81**, 361–370. 22

BP (2014). *Statistical Review of World Energy*. London. 2

Bradley, D., Gaskell, P.H. & Lau, A.K.C. (1990). A mixedness-reactedness flamelet model for turbulent diffusion flames. *Proc. Combust. Inst.*, **23**, 685–692. 5, 24, 26, 35, 39

Bradley, D., Gaskell, P.H. & Gu, X.J. (1998). The mathematical modeling of liftoff and blowoff of turbulent non-premixed methane jet flames at high strain rates. *Proc. Combust. Inst.*, **27**, 1199–1206. 26, 35, 39

Bray, K.N.C. (1980). Turbulent flows with premixed reactants. In P.A. Libby & F.A. Williams, eds., *Turbulent Reacting Flows*, 115–183, Springer Berlin Heidelberg. 35

Bray, K.N.C. & Libby, P.A. (1994). Recent developments in the BML model of premixed turbulent combustion. In P.A. Libby & F.A. Williams, eds., *Turbulent Reacting Flows*, 115–153, Academic Press Inc., New York. 31

Bray, K.N.C., Libby, P.A., Masuya, G. & Moss, J.B. (1981). Turbulence production in premixed turbulent flames. *Combust. Sci. Technol.*, **25**, 127–140. 42

Bray, K.N.C., Domingo, P. & Vervisch, L. (2005). Role of the progress variable in models for partially premixed turbulent combustion. *Combust. Flame*, **141**, 431–437. 5, 53, 54, 104

Broadwell, J.E., Dahm, W.J.A. & Mungal, M.G. (1984). Blowout of turbulent diffusion flames. *Proc. Combust. Inst.*, **20**, 303–310. 24, 25, 26, 111

Buckmaster, J. (2002). Edge-flames. *Prog. Energy Combust. Sci.*, **28**, 435–475. 24, 26, 111

Candel, S. & Poinsot, T. (1990). Flame stretch and the balance equation for the flame area. *Combust. Sci. Technol.*, **70**, 1–15. 30

Candel, S., Durox, D., Schuller, T., Bourgouin, J.-F. & Moeck, F.P. (2014). Dynamics of swirling flames. *Annu. Rev. Fluid Mech.*, **46**, 147–173. 84

Cant, R.S. & Mastorakos, E. (2008). *An Introduction to Turbulent Reacting Flows*. Imperial College Press. 12

Cavallo Marincola, F., Ma, T. & Kempf, A. (2013). Large eddy simulations of the Darmstadt turbulent stratified flame series. *Proc. Combust. Inst.*, **34**, 1307–1315. 31

Cessou, A., Maurey, C. & Stepowski, D. (2004). Parametric and statistical investigation of the behavior of a lifted flame over a turbulent free-jet structure. *Combust. Flame*, **137**, 458–477. 24

Chakraborty, N. & Mastorakos, E. (2006). Numerical investigation of edge flame propagation characteristics in turbulent mixing layers. *Phys. Fluids*, **18**, 105103. 124, 135

Chakraborty, N. & Swaminathan, N. (2011). Effects of lewis number on scalar variance transport in premixed flames. *Flow Turbul. Combust.*, **87**, 261–292. 193, 194

Chakraborty, N., Champion, M., Mura, A. & Swaminathan, N. (2011). Scalar-dissipation-rate approach. In N. Swaminathan & K.N.C. Bray, eds., *Turbulent Premixed Flames*, 74–102, Cambridge University Press, New York. 46

Charlette, F., Meneveau, C. & Veynante, D. (2002a). A power-law flame wrinkling model for LES of premixed turbulent combustion part i: non-dynamic formulation and initial tests. *Combust. Flame*, **131**, 159–180. 32

Charlette, F., Meneveau, C. & Veynante, D. (2002b). A power-law flame wrinkling model for LES of premixed turbulent combustion part ii: dynamic formulation. *Combust. Flame*, **131**, 181–197. 32

CHEMKIN (2013). *CHEMKIN-PRO 15131, Reaction Design: San Diego*. 20, 58

Chen, M., Herrmann, M. & Peters, N. (2000). Flamelet modeling of lifted turbulent methane/air and propane/air jet diffusion flames. *Proc. Combust. Inst.*, **28**, 167–174. 26, 30

Chen, Y. & Ihme, M. (2013). Large-eddy simulation of a piloted premixed jet burner. *Combust. Flame*, **160**, 2896–2910. 34

Chen, Z., Ruan, S. & Swaminathan, N. (2015). Simulation of turbulent lifted methane jet flames: effects of air-dilution and transient flame propagation. *Combust. Flame*, **162**, 703–716. xi, 20, 25, 34, 54, 57, 151, 158

Chen, Z., Reddy, V.M., Ruan, S., Doan, N.A.K., Roberts, W.L. & Swaminathan, N. (2016a). Simulation of MILD combustion using perfectly stirred reactor model. *Proc. Combust. Inst.*, doi: 10.1016/j.proci.2016.06.007. 203

Chen, Z., Ruan, S. & Swaminathan, N. (2016b). Numerical study of transient evolution of lifted jet flames: partially premixed flame propagation and influence of physical dimensions. *Combust. Theory Model.*, **20**, 592–612. 158

Colin, O., Ducros, F., Veynante, D. & Poinsot, T. (2000). A thickened flame model for large eddy simulations of turbulent premixed combustion. *Phys. Fluids*, **12**, 1843. 31

Courant, P., Pereira, J.C.F. & Lewy, H. (1928). Uber die partiellen differenzgle-ichungen der matematishen physik. *Matematishe Annalen*, **100**, 32–74. 210

Darabiha, N., Giovangigli, V., Trouvé, A., Candel, S. & Esposito, E. (1987). Coherent flame description of turbulent premixed ducted flames. In R. Borghi & S.N.B. Murthy, eds., *Turbulent Reacting Flows, Lecture Notes in Engineering 40*, 591–637, Springer-Verlag Berlin. 30

Darbyshire, O.R. & Swaminathan, N. (2012). A presumed joint pdf model for turbulent combustion with varying equivalence ratio. *Combust. Sci. Technol.*, **184**, 2036–2067. 44, 45, 55, 57, 106, 140, 158

Darbyshire, O.R., Swaminathan, N. & Hochgreb, S. (2010). The effects of small-scale mixing models on the prediction of turbulent premixed and stratified combustion. *Combust. Sci. Technol.*, **182**, 1141–1170. 46

Davidson, P.A. (2015). *Turbulence: an introduction for scientists and engineers*. Oxford University Press. 85

de Souza, C., Bastiaans, R.J.M., Geurts, B.J. & de Goey, L.P.H. (2011). LES and RANS of premixed combustion in a gas-turbine like combustor using the flamelet generated manifold approach. *Proc. ASME Turbo Expo*, **2**, 1119–1127. 36

Devaud, C.B. & Bray, K.N.C. (2003). Assessment of the applicability of conditional moment closure to a lifted turbulent flame: first order model. *Combust. Flame*, **132**, 102–114. 24, 26

Domingo, P., Vervisch, L. & Bray, K.N.C. (2002). Partially premixed flamelets in LES of nonpremixed turbulent combustion. *Combust. Theory Model.*, **6**, 529–551. 24, 26, 54, 104

Domingo, P., Vervisch, L. & Réveillon, J. (2005). DNS analysis of partially premixed combustion in spray and gaseous turbulent flame-bases stabilized in hot air. *Combust. Flame*, **140**, 172–195. 25, 54, 55

Domingo, P., Vervisch, L. & Veynante, D. (2008). Large-eddy simulation of a lifted methane jet flame in a vitiated coflow. *Combust. Flame*, **152**, 415–432. 25, 54

Dopazo, C. (1994). Recent development in pdf methods. In P.A. Libby & F.A. Williams, eds., *Turbulent Reacting Flows*, chap. 7, 375–474, Academic Press Inc. 37, 39

Dopazo, C. & O'Brien, E.E. (1974a). An approach to the autoignition of a turbulent mixture. *Acta Astronaut.*, **1**, 1239–1266. 37

Dopazo, C. & O'Brien, E.E. (1974b). Functional formulation of nonisothermal turbulent reactive flows. *Phys. Fluids*, **17**. 37

Driscoll, J.F. (2008). Turbulent premixed combustion: Flamelet structure and its effect on turbulent burning velocities. *Prog. Energy Combust. Sci.*, **34**, 91–134. 124

Dunstan, T.D., Swaminathan, N., Bray, K.N.C. & Cant, R.S. (2011). Geometrical properties and turbulent flame speed measurements in stationary premixed V-flames using Direct Numerical Simulation. *Flow Turbulence Combust.*, **87**, 237–259. 128

Dunstan, T.D., Swaminathan, N. & Bray, K.N.C. (2012). Influence of flame geometry on turbulent premixed flame propagation: a DNS investigation. *J. Fluid Mech.*, **709**, 191–222. 128

Dunstan, T.D., Minamoto, Y., Chakraborty, N. & Swaminathan, N. (2013). Scalar dissipation rate modelling for large eddy simulation of turbulent premixed flames. *Proc. Combust. Inst.*, **34**, 1193–1201. 51, 194, 197

Echekki, T. & Chen, J.H. (1997). Structure and propagation of methanol-air triple flames. *Combust. Flame*, **114**, 231–245. 24

Echekki, T. & Mastorakos, E. (2010). *Turbulent Combustion Modeling: Advances, New Trends and Perspectives*. Springer Netherlands. 29

Eickhoff, H., Lenze, B. & Leuckel, W. (1984). Experimental investigation on the stabilization mechanism of jet diffusion flames. *Proc. Combust. Inst.*, **20**, 311–318. 24, 111

Favier, V. & Vervisch, L. (1998). Investigating the effects of edge flames in liftoff in non-premixed turbulent combustion. *Proc. Combust. Inst.*, **27**, 1239–1245. 24, 25, 111

Favre, A. (1964). Statistical equations of turbulent gases. In *Problems of hydrodynamics and continuum mechanics*, 231–266, SIAM, Philadelphia. 12

Ferraris, S.A. & Wen, J.X. (2007). Large Eddy Simulation of a lifted turbulent jet flame. *Combust. Flame*, **150**, 320–339. 24, 26, 111, 112, 115, 151

Ferziger, J.H. & Perić, M. (1999). *Computational Methods for Fluid Dynamics*. Springer-Verlag Berlin Heidelberg. 49, 208, 209, 211, 212, 213

Fiorina, B., Baron, R., Gicquel, O., Thevenin, D., Carpentier, S. & Darabiha, N. (2003). Modelling non-adiabatic partially premixed flames using flame-prolongation of ildm. *Combust. Theory Model.*, **7**, 449–470. 20, 35, 44

Fiorina, B., Gicquel, O., Vervisch, L., Carpentier, S. & Darabiha, N. (2005). Approximating the chemical structure of partially premixed and diffusion counterflow flames using FPI flamelet tabulation. *Combust. Flame*, **140**, 147 – 160. 36, 39

Fiorina, B., Vicquelin, R., Auzillon, P., Darabiha, N., Gicquel, O. & Veynante, D. (2010). A filtered tabulated chemistry model for LES of premixed combustion. *Combust. Flame*, **157**, 465–475. 32

Fiorina, B., Mercier, R., Kuenne, G., Ketelheun, A., Avdić, Janicka, J., Geyer, D., Dreizler, A., Alenius, E., Duwig, C., Trisjono, P., Kleinheinz, K., Kang, S., Pitsch, H., Proch, E., Cavallo Marincola, F. & Kempf, A. (2015a). Challenging modeling strategies for LES of non-adiabatic turbulent stratified combustion. *Combust. Flame*, **162**, 4264–4282. 31, 32

Fiorina, B., Veynante, D. & Candel, S. (2015b). Modeling combustion chemistry in Large Eddy Simulation of turbulent flames. *Flow Turbulence Combust.*, **94**, 3–42. xi, 20, 24, 25, 44

Fox, R.O. (2003). *Computational Models for Turbulent Reacting Flows*. Cambridge University Press. 38

Franzelli, B., Riber, E., Gicquel, L.Y.M. & Poinsot, T. (2012). Large eddy simulation of combustion instabilities in a lean partially premixed swirled flame. *Combust. Flame*, **159**, 621–637. 27

Ge, Y., Cleary, M.J. & Klimenko, A.Y. (2013). A comparative study of Sandia flame series (D–F) using sparse-Lagrangian MMC modelling. *Proc. Combust. Inst.*, **34**, 1325–1332. 38

Germano, M., Piomelli, U., Moin, P. & Cabot, W.H. (1991). A dynamic subgrid-scale eddy viscosity model. *Phys. Fluids*, **3**, 1760. 49, 203

Gicquel, L.Y.M., Staffelbach, G. & Poinsot, T. (2012). Large eddy simulations of gaseous flames in gas turbine combustion chambers. *Prog. Energy Combust. Sci.*, **38**, 782–817. 27, 160

Gicquel, O., Darabiha, N. & Thevenin, D. (2000). Liminar premixed hydrogen/air counterflow flame simulations using flame prolongation of ILDM with differential diffusion. *Proc. Combust. Inst.*, **28**, 1901–1908. 16, 35

Glassman, I. (1987). *Combustion*. Academic Press Inc. 16, 21

Gregor, M.A., Seffrin, F., Fuest, F., Geyer, D. & Dreizler, A. (2009). Multi-scalar measurements in a premixed swirl burner using 1D Raman/Rayleigh scattering. *Proc. Combust. Inst.*, **32**, 1739–1746. 27

Gupta, A.K., Lilley, D.G. & Syred, N. (1984). *Swirl Flows*. Abacus Press, Tunbridge Wells, Kent. 160

Harten, A. (1983). High resolution schemes for hyperbolic conservation laws. *J. Comput. Phys.*, **49**, 357–393. 213

Haworth, D.C. (2010). Progress in probability density function methods for turbulent reacting flows. *Prog. Energy Combust. Sci.*, **36**, 168–259. 29, 37, 38, 39, 48

Hirsch, C. (1991). *Numerical computation of internal and external flows*. John Wiley and Sons, New York. 207, 208, 209, 210, 212

Ihme, M. & Pitsch, H. (2008a). Prediction of extinction and reignition in nonpremixed turbulent flames using a flamelet/progress variable model: 1. *a priori* study and presumed pdf closure. *Combust. Flame*, **155**, 70–89. 33, 34, 39

Ihme, M. & Pitsch, H. (2008b). Prediction of extinction and reignition in nonpremixed turbulent flames using a flamelet/progress variable model: 2. application in LES of Sandia flames D and E. *Combust. Flame*, **155**, 90–107. 33, 34, 39, 50, 194

Ihme, M. & See, Y.C. (2010). Prediction of autoignition in a lifted methane/air flame using an unsteady flamelet/progress variable model. *Combust. Flame*, **157**, 1850–1862. 34, 156

Ihme, M., Cha, C.M. & Pitsch, H. (2005). Prediction of local extinction and re-ignition effects in non-premixed turbulent combustion using a flamelet/progress variable approach. *Proc. Combust. Inst.*, **30**, 793–800. 33, 39

Ihme, M., Zhang, J., He, G. & Dally, B.B. (2012). Large-eddy simulation of a jet-in-hot-coflow burner operating in the oxygen-diluted combustion regime. *Flow Turbulence Combust.*, **89**, 449–464. 34

Im, H.G. & Chen, J.H. (2001). Effects of flow strain on triple flame propagation. *Combust. Flame*, **126**, 1384–1392. 124

Issa, R.I. (1986). Solution of the implicitly discretized fluid flow equations by operator-splitting. *J. Comput. Phys.*, **62**, 40–65. 62

Janicka, J. & Sadiki, A. (2005). Large eddy simulation of turbulent combustion systems. *Proc. Combust. Inst.*, **30**, 537–547. 5, 29

Jasak, H. (1996). *Error Analysis and Estimation for the Finite Volume Method with Applications to Fluid Flows*. Ph.D. thesis, Imperial College, University of London. xx, 208

Joedicke, A., Peters, N. & Mansour, M. (2005). The stabilization mechanism and structure of turbulent hydrocarbon lifted flames. *Proc. Combust. Inst.*, **30**, 901–909. 111

Jones, W.P. & Kakhi, M. (1998). Pdf modeling of finite-rate chemistry effects in turbulent nonpremixed jet flames. *Combust. Flame*, **115**, 210–229. 72

Jones, W.P. & Launder, B.E. (1972). The prediction of laminarization with a two-equation model of turbulence. *International Journal of Heat and Mass transfer*, **15**, 301. 43

Jones, W.P. & Prasad, V.N. (2010). Large Eddy Simulation of the Sandia Flame Series (D–F) using the Eulerian stochastic field method. *Combust. Flame*, **157**, 1621–1636. 38

Jones, W.P. & Prasad, V.N. (2011). LES-pdf simulation of a spark iginited turbulent methane jet. *Proc. Combust. Inst.*, **33**, 1355–1363. 26, 73, 139, 145, 150, 152, 153

Kalghatgi, G.T. (1984). Lift-off heights and visible lengths of vertical turbulent jet diffusion flames in still air. *Combust. Sci. Technol.*, **41**, 17–29. 24

Keck, O., Meier, W., Stricker, W. & Aigner, M. (2002). Establishment of a confined swirling natural gas/air flame as a standard flame: Temperature and species distributions from laser raman measurements. *Combust. Sci. Technol.*, **174**, 117–151. 177, 187

Kelman, J.B., Eltobaji, A.J. & Masri, A.R. (1998). Laser imaging in the stabilisation region of turbulent lifted flames. *Combust. Sci. Technol.*, **135**, 117–134. 26

Kerstein, A.R. (1988). A linear-eddy model of turbulent scalar transport and mixing. *Combust. Sci. Technol.*, **60**, 391–421. 38

Kim, I.S. & Mastorakos, E. (2005). Simulations of turbulent lifted jet flames with two-dimensional conditional moment closure. *Proc. Combust. Inst.*, **30**, 911–918. 26

Kioni, P.N., Rogg, B., Bray, K.N.C. & Liñán, A. (1993). Flame spread in laminar mixing layers: The triple flame. *Combust. Flame*, **95**, 276–290. 24, 111

Klimenko, A.Y. & Bilger, R.W. (1999). Conditional moment closure for turbulent combustion. *Prog. Energy Combust. Sci.*, **25**, 595–687. 29

Knudsen, E., Kim, S.H. & Pitsch, H. (2010). An analysis of premixed flamelet models for large eddy simulation of turbulent combustion. *Phys. Fluids*, **22**, 115109. 30

Kolla, H. & Swaminathan, N. (2010). Strained flamelets for turbulent premixed flames, i: Formulation and planar flame results. *Combust. Flame*, **157**, 943–954. 110

Kolla, H., Rogerson, J.W., Chakraborty, N. & Swaminathan, N. (2009). Scalar dissipation rate modeling and its validation. *Combust. Sci. Technol.*, **181**, 518–535. 46

Kolla, H., Rogerson, J.W. & Swaminathan, N. (2010). Validation of a turbulent flame speed model across combustion regimes. *Combust. Sci. Technol.*, **182**, 284–308. 110

Kolmogorov, A.N. (1941). The local structure of turbulence in incompressible viscous fluid for very large reynolds numbers. *C.R. Acad. Sci. USSR*, **30**, 301. 4, 15

Kronenburg, A. & Cleary, M.J. (2008). Multiple mapping conditioning for flames with partial premixing. *Combust. Flame*, **155**, 215 – 231. 38

Kronenburg, A. & Mastorakos, E (2011). The conditional moment closure model. In T. Echekki & E. Mastorakos, eds., *Turbulent Combustion Modeling*, 249–276, Springer. 29

Kuenne, G., Seffrin, F., Fuest, F., Stahler, T., Ketelheun, A., Geyer, D., Janicka, J. & Dreizler, A. (2012). Experimental and numerical analysis of a lean premixed stratified burner using 1D Raman/Rayleigh scattering and large eddy simulation. *Combust. Flame*, **159**, 2669–2689. 24, 32

Kuo, K.K. (1986). *Principles of Combustion*. John Wiley, New York. 10, 12, 21

Lacaze, G., Cuenot, B., Poinsot, T. & Oschwald, M. (2009a). Large eddy simulation of laser ignition and compressible reacting flow in a rocket-like configuration. *Combust. Flame*, **156**, 1166–1180. 145, 150, 153

Lacaze, G., Richardson, E. & Poinsot, T. (2009b). Large eddy simulation of spark ignition in a turbulent methane jet. *Combust. Flame*, **156**, 1993–2009. 26, 73, 98, 139

Lamouroux, J., Ihme, M., Fiorina, B. & Gicquel, O. (2014). Tabulated chemistry approach for diluted combustion regimes with internal recirculation and heat losses. *Combust. Flame*, **161**, 2120–2136. 34

Langella, I. (2015). *Large Eddy Simulation of Premixed Combution Using Flamelets*. Ph.D. thesis, University of Cambridge. 39, 51, 141

Langella, I. & Swaminathan, N. (2016). Unstrained and strained flamelets for les of premixed combustion. *Combust. Theory Model.*. 34, 37, 51, 191, 193, 194, 196, 197, 202, 203

Langella, I., Swaminathan, N., Gao, Y. & Chakraborty, N. (2015). Assessment of dynamic closure for premixed combustion large eddy simulation. *Combust. Theory Model.*, **19**, 628–656. 51

Law, C.K. (2006). *Combustion Physics*. Cambridge University Press. 2, 4, 19

Lawn, C.J. (2009). Lifted flames on fuel jets in co-flowing air. *Prog. Energy Combust. Sci.*, **35**, 1–30. 24, 111

Leigier, J.P., Poinsot, T. & Veynante, D. (2000). Dynamically thickened flame les model for premixed and non-premixed turbulent combustion. In *Proc. 2000 CTR Summer Program*, 157–168, Centre for Turbulence Research, NASA-Ames/Stanford University. 26

Li, B., Baudoin, E., Yu, R., Sun, Z.W., Li, Z.S., Bai, X.S., Aldén, M. & Mansour, M.S. (2009). Experimental and numerical study of a conical turbulent partially premixed flame. *Proc. Combust. Inst.*, **32**, 1811–1818. 3

Lilly, D.K. (1992). A proposed modification of the Germano subgridscale closure method. *Phys. Fluids*, **4**, 633. 49

Liñán, A. (1994). Ignition and flame spread in laminar mixing layer. In J. Buckmaster, T.L. Jackson & A. Kumar, eds., *Combustion in High Speed Flows*, Kluwer Academic Publishers. 24

Lucas Jr., R.E. (2002). *Lectures on Economic Growth*. Cambridge: Harvard University Press. 1

Lyons, K.M. (2007). Toward an understanding of the stabilization mechanisms of lifted turbulent jet flames: Experiments. *Prog. Energy Combust. Sci.*, **33**, 211–231. 24, 26, 111

Lyons, K.M. & Watson, K.A. (2000). Partially premixed combustion in lifted turbulent jets. *Combust. Sci. Technol.*, **156**, 97–105. 26

Ma, C.Y., Mahmuda, T., Fairweather, M., Hampartsoumian, E. & Gaskell, P.H. (2002). Prediction of lifted, non-premixed turbulent flames

using a mixedness-reactedness flamelet model with radiation heat loss. *Combust. Flame*, **128**, 60–73. 26

Ma, T., Stein, O.T., Chakraborty, N. & Kempf, A. (2013). *A posteriori* testing of algebraic flame surface density models for LES. *Combust. Theory Model.*, **17**, 431–482. 31

Maas, U. & Pope, S.B. (1992a). Implementaion of simplified chemical kinetics based on low-dimensional manifolds. *Proc. Combust. Inst.*, **24**, 719–729. 16, 35

Maas, U. & Pope, S.B. (1992b). Simplifying chemical kinetics: intrinsic low-dimensional manifolds in composition space. *Combust. Flame*, **88**, 239–264. 16, 35

Magnussen, B.F. & Hjertager, B.H. (1977). On mathematical modeling of turbulent combustion with special emphasis on soot formation and combustion. *Proc. Combust. Inst.*, **16**, 719–727. 29

Mansour, M.S. (2003). Stability characteristics of lifted turbulent partially premixed jet flames. *Combust. Flame*, **133**, 263–274. 24, 102, 121

Mantel, T. & Bilger, R.W. (1995). Some conditional statistics in a turbulent premixed flame derived from Direct Numerical Simulation. *Combust. Sci. Technol.*, **110-111**, 393–417. 46

Marble, F. & Broadwell, J.E. (1977). The coherent flame model of non-premixed turbulent combustion. *Project Squid TRW-9-PU (Project Squid Headquaters, Chaffee Hall, Puedue University, West Lafayette, IN)*. 30

Masri, A.R. (2015). Partial premixing and stratification in turbulent flame. *Proc. Combust. Inst.*, **35**, 1115–1136. 3, 5, 23, 24, 27, 29

Meares, S. & Masri, A.R. (2014). A modified piloted burner for stabilizing turbulent flames of inhomogeneous mixtures. *Combust. Flame*, **161**, 484–495. 3

Meier, W., Duan, X.R. & Weigand, P. (2006). Investigations of swirl flames in a gas turbine model combustor ii. turbulence–chemistry interactions. *Combust. Flame*, **144**, 225–236. xi, xii, xvii, xviii, xix, 7, 27, 28, 32, 67, 77, 78, 79, 80, 160, 161, 162, 163, 171, 172, 173, 174, 175, 176, 177, 178, 179, 180, 181, 182, 183, 184, 185, 186, 187, 188, 189, 190, 191, 194, 195, 197, 199, 202

Meier, W., Weigand, P., Duan, X.R. & Giezendanner-Thoben, R. (2007). Detailed characterization of the dynamics of thermoacoustic pulsations in a lean premixed swirl flame. *Combust. Flame*, **150**, 2–26. 27, 32

Meneveau, C. & Katz, J. (2000). Scale-invariance and turbulence models for large-eddy simulation. *Annu. Rev. Fluid Mech.*, **32**. 49

Mercier, R., Schmitt, T., Veynante, D. & Fiorina, B. (2015). The influence of combustion SGS submodels on the resolved flame propagation: application to the LES of the cambridge stratified flames. *Proc. Combust. Inst.*, **35**, 1259–1267. 32

Miake-Lye, R.C. & Hammer, J.A. (1989). Lifted turbulent jet flames: A stability criterion based on the jet large-scale structure. *Proc. Combust. Inst.*, **22**, 817–824. 25

Michel, J.-B., Colin, O., Angelberger, C. & Veynante, D. (2009). Using the tabulated diffusion flamelet model ADF-PCM to simulate a lifted methane-air jet flame. *Combust. Flame*, **156**, 1318–1331. 26

Minamoto, Y. & Swaminathan, N. (2014). Scalar gradient behaviour in MILD combustion. *Combust. Flame*, **161**, 1063–1075. 170

Mizobuchi, Y., Tachibana, S., Shinio, J., Ogawa, S. & Takeno, T. (2002). A numerical analysis of the structure of a turbulent hydrogen jet lifted flame. *Proc. Combust. Inst.*, **29**, 2009–2015. 6, 24, 25

Mizobuchi, Y., Shinjo, J., Ogawa, S. & Takeno, T. (2005). A numerical study on the formation of diffusion flame islands in a turbulent hydrogen jet lifted flame. *Proc. Combust. Inst.*, **30**, 611–619. 6

Moin, P., Squires, K., Cabot, W.H. & Lee, S. (1991). A dynamic subgrid-scale model for compressible turbulence and scalar transport. *Phys. Fluids*, **3**, 2746. 49

Mukhopadhyay, S., Bastiaans, R.J.M., van Oijen, J.A. & de Goey, L.P.H. (2014). Analysis of a filtered flamelet approach for coarse DNS of premixed combustion. *Fuel*, **144**, 388–399. 32

Müller, C.M., Breitbach, H. & Peters, N. (1994). Partially premixed turbulent flame propagation in jet flames. *Proc. Combust. Inst.*, **25**, 1099–1106. 24, 26, 30, 105, 121, 124, 126, 133, 151, 201

Mustata, Radu, Valiño, Luis, Jiménez, Carmen, Jones, W.P. & Bondi, S. (2006). A probability density function Eulerian Monte Carlo field method for large eddy simulations: Application to a turbulent piloted methane/air diffusion flame (sandia D). *Combust. Flame*, **145**, 88 – 104. 38

Najafi-Yazdi, A., Cuenot, B. & Mongeau, L. (2012). Systematic definition of progress variables and intrinsically low-dimensional, flamelet generated manifolds for chemistry tabulation. *Combust. Flame*, **159**, 1197–1204. 20

Navarro-Martinez, S. & Kronenburg, A. (2011). Flame stabilization mechanisms in lifted flames. *Flow Turbulence Combust.*, **87**, 377–406. 26

Nguyen, P.-D., Vervisch, L., Subramanian, V. & Domingo, P (2010). Multidimensional flamelet-generated manifolds for partially premixed combustion. *Combust. Flame*, **157**, 43–61. 36, 56

Open CFD (2013). *Open CFD Ltd. (ESI Group), Bracknell RG12 1BW, UK*. 60, 61, 167

Pantano, C. (2004). Direct simulation of non-premixed flame extinction in a methane–air jet with reduced chemistry. *J. Fluid Mech.*, **514**, 231–270. 124

Patankar, S.V. (1980). *Numerical hear transfer and fluid flow*. Taylor and Francis Inc. 62, 207, 209, 210, 211, 212, 213

Pellegrini, F. (2006). *Scotch 4.0 User's Guide*. Universite Bordeaux I, 351 cours de la Liberation, 33405 TALENCE, FRANCE. 63

Peters, N. (1984). Laminar diffusion flamelet models in non-premixed turbulent combustion. *Prog. Energy Combust. Sci.*, **10**, 319–339. 5, 17, 33

Peters, N. (1999). The turbulent burning velocity for large-scale and small-scale turbulence. *J. Fluid Mech.*, **384**, 107–132. xi, 22

Peters, N. (2000). *Turbulent Combustion*. Cambridge University Press. xi, 3, 5, 9, 15, 16, 17, 18, 19, 20, 23, 24, 26, 28, 29, 30, 33, 46, 111, 112, 124, 125, 127, 151

Peters, N. & Williams, F.A. (1983). Liftoff characteristics of turbulent jet diffusion flames. *AIAA J.*, **21**, 423–429. 24, 25, 111

Peters, N., Terhoeven, P., Chen, J.H. & Echekki, T. (1998). Statistics of flame displacement speeds from computations of 2-D unsteady methane-air flames. *Proc. Combust. Inst.*, **27**, 833–839. 127

Pierce, C.D. & Moin, P. (1998). A dynamic model for subgrid-scale variance and dissipation rate of a conserved scalar. *Phys. Fluids*, **10**, 3041. 194, 196

Pierce, C.D. & Moin, P. (2004). Progress-variable approach for large-eddy simulation of non-premixed turbulent combustion. *J. Fluid Mech.*, **504**, 73–97. 33

Pitsch, H. (2006). Large-eddy simulation of turbulent combustion. *Annu. Rev. Fluid Mech.*, **38**, 453–482. 5, 29, 36, 50, 51, 52

Pitsch, H. & Steiner, H. (2000). Large-eddy simulation of a turbulent piloted methane/air diffusion flame (sandia flame D). *Phys. Fluids*, **12**, 2541. 33, 48, 52

Pitts, W.M. (1988). Assessment of theories for the behavior and blowout of lifted turbulent jet diffusion flames. *Proc. Combust. Inst.*, **22**, 809–816. 24, 111

Poinsot, T. & Veynante, D. (2005). *Theoretical and Numerical Combustion*. Edwards, 2nd edn. 3, 5, 9, 10, 11, 12, 13, 16, 19, 22, 28, 29, 30, 31, 37, 38, 42, 43, 47, 48

Poinsot, T., Veynante, D. & Candel, S. (1990). Diagrams of premixed turbulent combustion based on direct simulation. *Proc. Combust. Inst.*, **23**, 613–619. 22

Pope, S.B. (1978). An explanation of the turbulent round-jet/plane-jet anomaly. *AIAA Journal*, **16**, 279–281. 72

Pope, S.B. (1985). Pdf methods for turbulent reactive flows. *Prog. Energy Combust. Sci.*, **11**, 119–192. 37, 38

Pope, S.B. (1988). The evolution of surfaces in turbulence. *Int. J. Eng. Sci.*, **26**, 445–469. 30

Pope, S.B. (1990). Computations of turbulent combustion: progress and challenges. *Proc. Combust. Inst.*, **23**, 591–612. 39

Pope, S.B. (1997). Computationally efficient implementation of combustion chemistry using in situ adaptive tabulation. *Combust. Theory Model.*, **1**, 41–63. 16

Pope, S.B. (2000). *Turbulent Flows*. Cambridge University Press. xii, 5, 15, 38, 39, 43, 47, 49, 51, 52, 72, 75

Pope, S.B. (2013). Small scales, many species and the manifold challenges of turbulent combustion. *Proc. Combust. Inst.*, **34**, 1–31. 13, 29, 33

Popp, S., Hunger, F., Hartl, S., Messig, D., Coriton, B., Frank, J.H., Fuest, F. & Hasse, C. (2015). LES flamelet-progress variable modeling and measurements of a turbulent partially-premixed dimethyl ether jet flame. *Combust. Flame*, **162**, 3016–3029. 34

Press, W.H. (1996). *Numerical recipes in FORTRAN 77: the art of scientific computing*. Cambridge University Press. 59

Ramaekers, W.J.S., van Oijen, J.A. & de Goey, L.P.H. (2009). A priori testing of flamelet generated manifolds for turbulent partially premixed methane/air flames. *Flow Turbulence Combust.*, **84**, 439–458. 36

Ribert, G., Champion, M. & Plion, P. (2004). Modeling turbulent reactive flows with variable equivalence ratio: Application to the calculation of a reactive shear layer. *Combust. Sci. Technol.*, **176**, 907–923. 45

Richards, C.D. & Pitts, W.M. (1993). Global density effects on the self-preservation behaviour of turbulent free jets. *J. Fluid Mech.*, **254**, 417–435. xii, 75, 76, 144

Richardson, L.F. (1922). *Weather Prediction by Numerical Process*. Cambridge University Press. 15

Robin, V., Mura, A., Champion, M. & Plion, P. (2006). A multi-dirac presumed pdf model for turbulent reactive flows with variable equivalence ratio. *Combust. Sci. Technol.*, **178**, 1843–1870. 45

Roux, S., Lartigue, G., Poinsot, T., Meier, U. & Bérat, C. (2005). Studies of mean and unsteady flow in a swirled combustor using experiments, acoustic analysis, and large eddy simulations. *Combust. Flame*, **141**, 40–54. 32

Ruan, S. (2012). *Turbulent Partially Premixed Combustion: DNS Analysis and RANS Simulation*. Ph.D. thesis, University of Cambridge. 40, 59, 60, 199, 200, 203

Ruan, S., Swaminathan, N., Bray, K.N.C., Mizobuchi, Y. & Takeno, T. (2012). Scalar and its dissipation in the near field of turbulent lifted jet flame. *Combust. Flame*, **159**, 591–608. 34, 45, 46, 54, 55, 56, 106

Ruan, S., Swaminathan, N. & Darbyshire, O.R. (2014a). Modelling of turbulent lifted jet flames using flamelets: *a priori* assessment and *a posteriori* validation. *Combust. Theory Model.*, **18**, 295–329. 5, 6, 34, 40, 44, 45, 46, 54, 55, 56, 57, 59, 60, 61, 95, 108, 110, 114, 118, 140, 151, 158

Ruan, S., Swaminathan, N. & Mizobuchi, Y. (2014b). Investigation of flame stretch in turbulent lifted jet flame. *Combust. Sci. Technol.*, **186**, 243–272. 24

Ruan, S., Swaminathan, N., Isono, M., Saitoh, T. & Saitoh, K (2015). Simulation of premixed combustion with varying equivalence ratio in gas turbine combustor. *J. Propulsion Power*, **31**, 861–871. 20, 140

Schefer, R.W. & Goix, P.J. (1998). Mechanism of flame stabilization in turbulent, lifted-jet flames. *Combust. Flame*, **112**, 559–574. 24, 111

Schefer, R.W., Namazian, M. & Kelly, J. (1994). Stabilization of lifted turbulent-jet flames. *Combust. Flame*, **99**, 75–86. 111

See, Y.C. & Ihme, M. (2014). LES investigation of flow field sensitivity in a gas turbine model combustor. *AIAA J.*, **0621**. 80, 82, 85, 194

See, Y.C. & Ihme, M. (2015). Large eddy simulation of a partially-premixed gas turbine model combustor. *Proc. Combust. Inst.*, **35**, 1225–1234. 27, 32, 34, 190

Seffrin, F., Fuest, F., Geyer, D. & Dreizler, A. (2010). Flow field studies of a new series of turbulent premixed stratified flames. *Combust. Flame*, **157**, 384–396. xi, 24, 25

Sen, B.A. & Menon, S. (2010). Linear eddy mixing based tabulation and artificial neural networks for large eddy simulations of turbulent flames. *Combust. Flame*, **157**, 62–74. 38

Smagorinsky, J. (1963). *Mon. Weather Rev.*, **91**, 99–164. 4, 49, 139

Spalding, D.B. (1979). *Combustion and Mass Transfer*. Elsevier Ltd. 35

Stårner, S.H., Bilger, R.W., Frank, J.H., Marran, D.F. & Long, M.B. (1996). Mixture fraction imaging in a lifted methane jet flame. *Combust. Flame*, **107**, 307–313. 111

Stavrianos, L.S. (1999). *The world to 1500 : a global history*. Upper Saddle River, N.J.: Prentice Hall. 1

Su, L.K., Sun, O.S. & Mungal, M.G. (2006). Experimental investigation of stabilization mechanisms in turbulent, lifted jet diffusion flames. *Combust. Flame*, **144**, 494–512. 24, 25, 26, 111, 115

Swaminathan, N. & Bray, K.N.C. (2005). Effect of dilatation on scalar dissipation in turbulent premixed flames. *Combust. Flame*, **143**, 549–565. 46, 51, 193

Swaminathan, N. & Bray, K.N.C., eds. (2011). *Turbulent premixed flames*. Cambridge University Press. 3, 5, 11, 23, 27, 28, 29, 34, 43, 124

Sweeney, M.S., Hochgreb, S., Dunn, M.J. & Barlow, R.S. (2012a). The structure of turbulent stratified and premixed methane/air flames i: Non-swirling flows. *Combust. Flame*, **159**, 2896–2911. 24

Sweeney, M.S., Hochgreb, S., Dunn, M.J. & Barlow, R.S. (2012b). The structure of turbulent stratified and premixed methane/air flames ii: Swirling flows. *Combust. Flame*, **159**, 2912–2929. 24

Syred, N. (2006). A review of oscillation mechanisms and the role of the precessing vortex core (PVC) in swirl combustion systems. *Prog. Energy Combust. Sci.*, **32**, 93–161. 85, 160

Tacke, M.M., Geyer, D., Hassel, E.P. & Janicka, J. (2000). A detailed investigation of the stabilisation point of lifted turbulent diffusion flames. *Proc. Combust. Inst.*, **27**, 1157–1165. 26

Tennekes, H. & Lumley, J.L. (1972). *A First Course in Turbulence*. The MIT Press, Cambridge, Massachusetts. 15

Tieszen, S.R., Stamps, D.W. & O'Hern, T.J. (1996). A heuristic model of turbulent mixing applied to blowout of turbulent jet diffusion flames. *Combust. Flame*, **106**, 442–466. xii, 74

Trisjono, P., Kleinheinz, K., Kang, S. & Pitsch, H. (2014). Large eddy simulation of stratified and sheared flames of a premixed turbulent stratified flame burner using a flamelet model with heat loss. *Flow Turbulence Combust.*, **92**, 201–235. 30

Upatnieks, A., Driscoll, J.F., Rasmussen, C.C. & Ceccio, S.L. (2004). Liftoff of turbulent jet flames-assessment of edge flame and other concepts using cinema-PIV. *Combust. Flame*, **138**, 252–272. 25

Valiño, L. (1998). A field Monte Carlo formulation for calculating the probability density function of a single scalar in a turbulent flow. *Flow Turbulence Combust.*, **60**, 157–172. 38

van Oijen, J.A. & de Goey, L.P.H. (2000). Modelling of premixed laminar flames using flamelet-generated manifolds. *Combust. Sci. Technol.*, **161**, 113–137. 16, 35

Vanquickenborne, L. & van Tiggelen, A. (1966). The stabilization mechanism of lifted diffusion flames. *Combust. Flame*, **10**, 59–69. 24, 25, 111

Vervisch, L. & Trouvé, A. (1998). Les modeling for lifted turbulent jet flames. In *Proc. 1998 CTR Summer Program*, 83–100, Centre for Turbulence Research, NASA-Ames/Stanford University. 26

Vervisch, L. & Veynante, D. (2000). Interlinks between approaches for modeling turbulent flames. *Proc. Combust. Inst.*, **28**, 175–183. 30

Vervisch, L., Hauguel, R., Domingo, P. & Rullaud, M. (2004). Three facets of turbulent combustion modelling: DNS of premixed V-flame, LES of lifted nonpremixed flame and RANS of jet-flame. *J. Turbulence*, **5**, 004. 26

Vervisch, L., Moureau, V., Domingo, P. & Veynante, D. (2011). Flame surface density and G equation. In N. Swaminathan & K. N. C. Bray, eds., *Turbulent premixed flames*, 60–74, Cambridge University Press, New York. 30, 31, 56

Veynante, D. & Vervisch, L. (2002). Turbulent combustion modeling. *Prog. Energy Combust. Sci.*, **28**, 193–266. 5, 29

Vreman, A.W., Albrecht, B.A., van Oijen, J.A., de Goey, L.P.H. & Bastiaans, R.J.M. (2008). Premixed and nonpremixed generated manifolds in Large Eddy Simulation of Sandia flame D and F. *Combust. Flame*, **153**, 394–416. 26, 36, 39

Wandel, A.P. & Lindstedt, R.P. (2013). Hybrid multiple mapping conditioning modeling of local extinction. *Proc. Combust. Inst.*, **34**, 1365 – 1372. 38

Watson, K.A., Lyons, K.M., Donbar, J.M. & Carter, C.D. (2003). On scalar dissipation and partially premixed flame propagation. *Combust. Sci. Technol.*, **175**, 649–664. 25, 111

Weigand, P., Meier, W., Duan, X.R., Stricker, W. & Aigner, M. (2006). Investigations of swirl flames in a gas turbine model combustor i. flow field, structures, temperature, and species distributions. *Combust. Flame*, **144**, 205–224. xii, xvii, xviii, xix, 7, 27, 32, 67, 77, 78, 79, 80, 84, 160, 161, 162, 163, 170, 171, 172, 173, 174, 175, 176, 177, 178, 179, 180, 181, 182, 183, 184, 185, 186, 187, 188, 189, 190, 191, 194, 197, 199, 202

Widenhorn, A., Noll, B. & Aigner, M. (2009). Numerical study of a non-reacting turbulent flow in a gas turbine model combustor. *AIAA Paper*, **2009-647**. xiii, 77, 80, 82, 85, 86, 88, 90, 92, 93

Wilcox, D.C. (2006). *Turbulence Modeling for CFD*. DCW Industries, Inc. 43, 69, 70, 117

Williams, F.A. (1975). Recent advances in theoretical descriptions of turbulent diffusion flames. In S.N.B. Murthy, ed., *Turbulent Mixing in Non-Reactive and Reactive Flows*, Plenum Press, New York. 5

Williams, F.A. (1985). *Combustion Theory*. The Benjamin/Cummings Publishing Company, Menlo, CA. xi, 10, 12, 13, 17, 18, 19, 30

Wohl, K., Kapp, N.M. & Gazley, C. (1949). The stability of open flames. *Symposium on Combustion and Flame, and Explosion Phenomena*, **3**, 3–21. 24, 111

Yoo, C.S. & Im, H.G. (2004). Transient dynamics of edge flames in a laminar nonpremixed hydrogen–air counterflow. *Proc. Combust. Inst.*, **30**, 349–356. 124

Yoo, C.S., Sankaran, R. & Chen, J.H. (2009). Three-dimensional Direct Numerical Simulation of a turbulent lifted hydrogen jet flame in heated coflow: flame stabilization and structure. *J. Fluid Mech.*, **640**, 453–481. 25

Yoo, C.S., Richardson, E.S., Sankaran, R. & Chen, J.H. (2011). A DNS study on the stabilization mechanism of a turbulent lifted ethylene jet flame in highly-heated coflow. *Proc. Combust. Inst.*, **33**, 1619–1627. 25